Trinity College Dublin
Coláiste na Tríonóide, Baile Átha Cliath
The University of Dublin

Electro-optic properties and applications of thermally-assisted conversion based few-layer MoS_2 devices

Nishtha Shelly

A thesis presented in partial fulfilment of the requirements

for the degree of

Doctor of Philosophy

School of Physics

Faculty of Engineering, Mathematics and Science

Trinity College

University of Dublin

Academic Supervisor: Professor David McCloskey

2025

Declaration

I declare that this thesis has not been submitted as an exercise for a degree at this or any other university and it is entirely my own work.

I agree to deposit this thesis in the University's open access institutional repository or allow the Library to do so on my behalf, subject to Irish Copyright Legislation and Trinity College Library conditions of use and acknowledgement.

I consent to the examiner retaining a copy of the thesis beyond the examining period, should they so wish (EU GDPR May 2018).

Signed: 

Date: 14/07/2025

ID No: 20335322

Abstract

The conventional methods of MoS_2 preparation are challenged in this work by integrating MoS_2 synthesis using a modified version of CVD technique in different stages of developing a multilayer stack. The modified technique used in this work is referred to as thermally-assisted conversion (TAC) that directly sulphurises a transition metal. This gets rid of the exfoliation and transferring process which can be very time consuming and incompatible with industrial processes and reduces the market value of scientifically known extraordinary materials like TMDs. This technique is also photolithographically compatible paving way for large scale synthesis of devices that aim to utilize the extraordinary properties of TMDs like MoS_2 but are limited by tricky transferring processes, thin film degradation, difficulty in patterning TMDs to a desired shape and contacting issues. Additionally, the conventionally utilized monolayers of MoS_2 exhibiting high absorption and hosting strongly bound room temperature excitons in the visible range of the electromagnetic spectrum were used as a reference to obtain similar performance from few-layer MoS_2 thin films. Given the direct correlation of MoS_2 excitons with its absorption, this work aimed at establishing active control on exciton properties and investigating the tunable optical properties of MoS_2 as a response to applied electrical bias. Depending upon the application, few-layer thin films of MoS_2 produced using the TAC process perform similar to monolayer MoS_2 for instance in the case of Fabry-Pérot based active modulation of refractive index. For photodetector applications, thicker films serve the purpose better especially when backed with metal reflector. This makes MoS_2 more desirable in the field of integrated photonics since much of the monolayer properties were shown to be retained even in few-layer MoS_2 films and thicker MoS_2 films were shown to be suitable for many sensor applications based on pyroelectricity, photodetection and bolometric detectors. This work reported photo-pyroelectricity in mixed/3R phase of MoS_2. A thorough analysis following this observation concluded that this mechanism too can be controlled which is dependent on laser frequency, modulation frequency, external applied bias and load. This work also presents a thorough electrical and optical characterization of TAC based few-layer MoS_2 films to understand light-matter interaction better in films beyond the monolayer limit.

Publications

Papers

[I] **N. Shelly**, E. Roy *et al.*, "Strong Absorption and Modulation in Deeply Subwavelength Transition Metal Dichalcogenide Thin Films." *In prep, 2025*

[II] **N. Shelly**, C. P. Murray, E. Roy, D. McCloskey, "Enhanced Photoconductivity in Ultrathin MoS_2 Films Using Lithography Free Structural Colour", *In prep, 2025*

[III] D. Khicher, E. Roy, **N. Shelly**, C. Murray, D. McCloskey, "Enhanced Coloration Efficiency and Cycling Stability in Ultrathin NiO_x Films Utilizing Zeroth Order Fabry – Perot Resonance", *Under review (ACS applied materials and interface)*

Posters

[I] **N. Shelly**, E. Roy, C. Murray, D. McCloskey, "Investigating effect of heat and light interaction on electrical properties of thin film MoS_2," *9th instalment of the Biennial Photonics Ireland Conference, Virtual, 2021*.

[II] **N. Shelly**, E. Roy, C. Murray, D. McCloskey, "Investigating effect of heat and light interaction on electrical properties of thin film MoS_2," *SFI Science Summit, Virtual, 2021*.

[III] **N. Shelly**, E. Roy, C. Murray, D. McCloskey, "Field Effect Modulation using Transparent Conductive Oxides and Multilayer Transition Metal Dichalcogenides", *43rd Conference of CLEO. San Jose California USA, 2023*.

[IV] E. Roy, **N. Shelly**, C. Murray, D, McCloskey, "Investigation of Field Effect Tuning of Refractive Index in Transparent Conducting Oxide Thin Film Fabry-Perot Cavity Structures", *META The 13th International Conference. Paris, 2023*.

[V] **N. Shelly**, C. Murray, D. McCloskey, "Electro-optic Modulation in Large Area Multilayer MoS_2 Pixel Arrays", *ItsHer Women in STEMM summit. Dublin, 2024.*

Acknowledgements

At a time when the world was fighting a pandemic, people were losing jobs and economies were crashing, my life found a new direction when I joined Prof. David McCloskey's group. I would therefore like to convey my deepest thanks to my supervisor for giving me a chance to learn and in realising my potential. He has guided me in every difficult direction that this project took over the course of 4 years and gave me every opportunity to enhance my skills be it in experimental work or theory. I could have not asked for a better PhD supervisor. I am also immensely grateful for having Christopher P. Murray in my group. He not just trained me for practically everything in the labs in CRANN and cleanroom but also mentored me and stood as a firm support in times of extreme burn out. He is absolutely an expert at what he does given his 30 years of industry experience and I feel very fortunate to have learnt from his precious experience. I will try my best to work according to his valuable advice and the skills he imparted in me. The gloomy days in Dublin could have been diffciult to manage amid the stresses of a PhD if it was not for my awesome group members. Dr. Kenny Yu was my first point of contact and go to person whenever I felt a little anxious, Evan Roy was always there for a good chat on geopolitics, history and science fiction and Dilkhush Khicher was the sunshine on a rainy cold Dublin day. I greatly appreciate their presence around me everyday in our labs and offices and I can't thank them enough for all their support. Also, many thanks to Dr. Erik Soderholm and Eoin Cotter for helping me out in setting up experiments and running to different labs to get missing components. A big thanks goes to Dr. Simon Corbett for training me in the CCD-DR technique and having the patience to answer my questions at odd times. A special thanks to Dr. David Caffrey, Dr. Riley Gatensby and Dr. Peter Gleeson for the engaging conversations during lunch, for teaching me and helping me repair tools, training me in Hall measurements and cleanroom equipment. A big shoutout to my landlady Geraldine Keane for taking care of me in times of sickness and baking delicious pastries regulalrly.

My biggest support system without whom none of this would be possible is firstly my father who gave up his dream of being a physicist to fulfil my dreams and my mother who gave up her teaching career to raise me. I will forever be indebted to your sacrifices. Lastly, I would like to express my thanks to Science Foundation Ireland for not only giving me an opportunity to partake in valuable research but for also being a medium in sealing my fate with my fiancé whom I wouldn't meet if I didn't move to Ireland. Thank you Dr. Manish Dama for being my safe house, thank you for everthing.

List of Acronyms & Chemical Abbreviations

Acronymns

2D	Two Dimensional
4PP	Four-point-probe
AFM	Atomic Force Microscopy
ALD	Atomic Layer Deposition
CCD	Charge-Coupled Device
CCD-DR	Charge-Coupled Device based Differential reflectance
CNT	Carbon Nanotube
C-V	Capacitance – Voltage
CVD	Chemical Vapour Deposition
CW	Continuous Wave
DC	Direct Current
DI	Deionized
EBL	Electron Beam Lithography
FDTR	Frequency Domain Thermoreflectance
FP	Fabry Pérot
FWHM	Full Width Half Maximum
IDE	Inter-digitated Electrode
IR	Infrared
I-V	Current – voltage
KHz	Kilohertz
KK	Kramers-Kronig
LIA	Lock-in Amplifier
LLID	Liquid-Liquid Interface Deposition
MHz	Megahertz
M-I-M	Metal-Insulator-Metal
MSE	Mean Square Error
M-S-M	Metal-Semiconductor-Metal
NIR	Near Infrared
NPVD	Nano Physical Vapour Deposition
PPC	Persistant photoconductivity
PV	Photovoltaics
PVD	Physical Vapour Deposition
RF	Radio Frequnecy
RMS	Root mean Square
sccm	Standard Cubic Centimeter Per Minute
S-D	Source-Drain
SE	Spectroscopic Ellipsometry
SEM	Scanning Electron Microscopy
SFI	Science Foundation Ireland
STM	Scanning Tunnnleing Microscopy
TAC	Thermally-Assisted Conversion
TCO	Transparent Conudctive Oxide
TCR	Temperature Coefficient of Resistance

THz	Terahertz
TIA	Trans-impedance amplifier
TLM	Transfer Length Method
TMD	Transition Metal Dichalcogenides
TMM	Transfer Matrix Method
UV	Ultraviolet
UV-Vis	Ultraviolet-Visible
VdW	Van Der Waals
w.r.t.	With respect to
XRD	X-Ray Diffraction

Chemical Abbreviations

Ag	Silver
Al	Aluminium
Al_2O_3	Alumina
Au	Gold
CdS	Cadmium Sulphide
hBN	Hexagonal Boron Nitride
HfO_2	Hafnia
ITO	Indium Tin Oxide
Mo	Molybdenum
MoS_2	Molybdenum Disulphide
Si	Silicon
Si_3N_4	Silicon Nitride
SiO_2	Silica
Ti	Titanium
WS_2	Tungsten Disulphide
Zn	Zinc
ZnO	Zinc Oxide
ZnSnO	Zinc Tin Oxide
ZnTe	Zinc Telluride

Table of Contents

This thesis is dedicated to my parents.

Chapter 1. Introduction

1.1 MoS_2 and its general properties

1.1.1 Stability considerations and disadvantages of thin film MoS_2

1.1.2 Electrical properties of MoS_2

1.1.3 Optical properties and origin of excitons

1.2 Light matter interaction

1.3 Effect of dielectric encapsulation

1.4 Role of excitons and gating effect on absorption of light

1.5 Applications

1.6 Thesis outline

To maximize the number of devices on a single chip as predicted by Moore's law, future devices need to be smaller while still being functional and efficient. However, user experience is limited by bandwidth according to Nielsen's law of internet bandwidth which claims that internet connectivity need increases by 50% every year [1]. To combat this, communication systems need external optical modulators with faster switching characteristics and higher bandwidth. Broadly, two modulator geometries are prevalent in the high speed communication technology - planar geometry and surface normal geometry [2]. Many advances have been made in the direction of the former with microring or Mach-Zehnder geometry based electro-optic modulators having bandwidth ranging from 2.7 GHz [3] to more than 25 GHz [4] and operating at visible to near infrared frequencies. Also, the latter is utilized in the long wavelength ranges of around 1.3 - 1.5 μm [5], [6] but is less explored in the visible range of electromagnetic spectrum. Surface normal modulators not just provide ease of fabrication, possibility of making two dimensional (2D) arrays and cost effectiveness but are also desirable for making optical interconnects [7], [8] hence aiding in optical signal and information systems. Advances in thin film material synthesis has opened new avenues to explore such designs by utilizing new materials in their 2D limit. M. A. Kats and F. Capasso showed strong optical absorption of visible light in metal backed Germanium films of thickness much smaller than the wavelength (λ_{inc}) incident light (sub-wavelength thick) [9]. Therefore, in the sub-wavelength limit of the visible light, high optical absorption can be achieved by opting for a high refractive index material which also has an extinction coefficient (k) comparable to its real part (n). A certain class of 2D materials namely Transition Metal Dichalcogenides (TMDs) having a stronger interaction with light compared to Germanium satisfy these conditions and thus are being researched on for their electro-optic properties. They are semiconducting in nature and possess a complex refractive index (n+ik) with a very high positive valued real part (n>4) as well as imaginary part i.e., 'extinction coefficient' or 'absorption coefficient' (k∼ 1-3) across a broad energy spectrum [10]; 'n' results in strong interference of light 'k' is responsible for its strong absorption.

Backing with a metal makes the interface of metal and sub-wavelength thick TMD absorber layer reflecting and causes a non-trivial phase shift between 0 and π in the propagation of light at the absorber layer/substrate interface which increases its path length. This happens at the thicknesses below $\frac{\lambda_{inc}}{4n}$. Due to the phase difference between reflected light waves, there is destructive interference at the TMD layer/air interface. This interference is even stronger in the case of TMD because of a large value of 'n' as mentioned previously. This

is because light bending and delay while travelling inside the medium is more due to higher phase change in its velocity. Additionally, due to the presence of the absorption coefficient 'k', TMD layer becomes a lossy thin film meaning there is high absorption of light inside it and it almost absorbs all the incoming and reflected light thereby not allowing any transmission. Such a stack device where light is absorbed each time it circulates within the film in a narrow range of wavelength is known to be based on the Fabry-Pérot cavity (FP) effect. A FP cavity is a resonant cavity with two parallel mirrors to enhance the optical gain of the incoming light by facilitating repetitive reflection (destructive interference) and transmission (constructive interference) thus providing a greater chance of light-matter interaction. ***Fig. 1.1*** illustrates this phenomenon aptly. Traditionally, FP cavities have been used to enhance optical response of CVD based micron sized MoS_2 monolayer flakes [11], [12] but this can also be achieved with large area few-layers. Such few-layer MoS_2 films with a large lateral area have been employed in the present work.

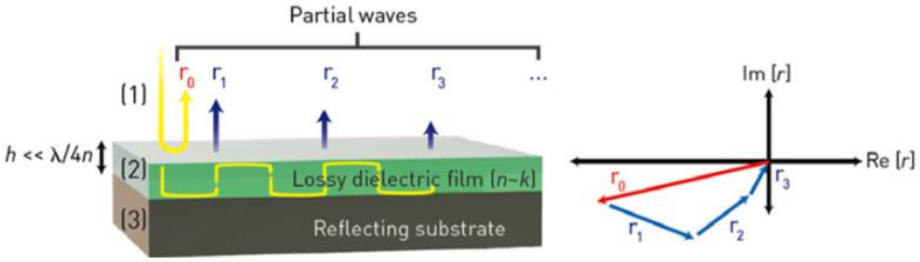

Fig. 1.1*: Light absorption using a lossy film of sub-wavelength thickness [9].*

Furthermore, due to reduced dielectric screening and strong Coulombic forces in d-orbital electrons of the transition metal, quasi-particles known as 'excitons' exist in the visible range at room temperature [13], [14]. These reasons make TMDs interesting materials for absorption-based modulators since absorption peaks near excitons' wavelengths [10] and active tuning of exciton properties in TMDs can be utilized [15] to realize electro-optic modulators.

Till date, absorption-based surface normal electro-optic modulators reported utilize monolayer TMDs. But synthesizing a high-quality monolayer film is difficult using conventional methods like CVD [16], [17], mechanical exfoliation [18], RF sputtering [19], [20], liquid phase exfoliation [21] and very recently a combination of hot pick up and stamp (dry) technique [22], [23], [24] and wetting polydimethylsiloxane (PDMS) technique [25], [26], [27]. These methods generally, don't provide a control on the placement of thin film

on the substrate (with an exception of the dry technique) and also the shape and size of the thin film which makes post processing like making contacts or characterization a difficult and time-consuming task. Therefore, main focus is put on pushing the thickness limit of the TMD beyond the monolayer limit and utilizing an alternative synthesis technique to obtain large lateral area films for easy device fabrication and characterization while still keeping the optical properties intact.

Objectives

This work elaborates on optimization of lithography-compatible, TMD based multi-layer stack for realization of surface normal electro-optic modulator via active control of excitons. Broadly, the objectives of this work are:

1. Synthesize a multi-layer stack based on Fabry-Pérot design using lossy thin films with metal backing.

2. Optimize stack design based on film quality, electrical and optical parameters by material characterization.

3. Test the multi-layer stack to probe the change in reflectivity.

This chapter aims to introduce one of the TMDs under consideration, Molybdenum Disulphide (MoS_2), its properties, structural defects, influence of defects on its electrical properties, interaction with light and finally its applications.

1.1 MoS_2 and its general properties

Apart from Graphene which is a layered 2D material made from graphite and has no bandgap, other materials with similar extraordinary optical, electrical, magnetic properties but having a finite bandgap unlike graphene have also been discovered. As introduced previously, TMDs are one such category of materials with the formula MX_2, where M is a transition metal (like Mo, W, Pt) and X is a chalcogen atom (like S, Se, Te). A unit cell of Molybdenum Disulphide (MoS_2) is shown in ***fig. 1.2***.

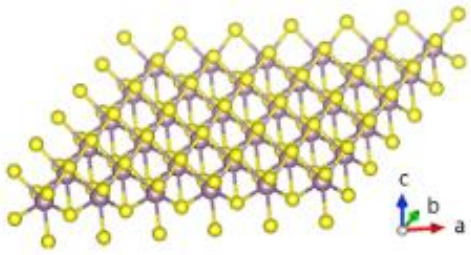

***Fig. 1.2**: Monolayer of MoS_2. Brown atom depicts Molybdenum (Mo) and yellow atom depicts Sulphur (S) [28].*

A summary of general properties of MoS_2 is tabulated in **tab. 1.1**. It is noteworthy how some physical properties vary depending upon the thickness of MoS_2, thereby, validating the significance of establishing control over synthesis of 2D materials.

***Table 1.1**: Physical properties of Molybdenum Disulphide*

Property	Value
Chemical Formula	MoS_2
Breakdown Current density (A/cm^2)	5×10^7 [29]
Lattice constant (Å)	DFT study: a=3.125 (1 layer), 3.126 (2 layers), 3.127 (bulk); c=12.066 [30] Experimental: a=3.15; c=12.3 [31]
Band gap (eV)	0.9 (bulk), 1.6 (monolayer) [32], [33]
Electron mobility (cm^2/V-s)	200-500 [34], 0.5-3 [35], ~ 200 [36] (monolayer)

Previously, graphene has been extensively used for a myriad of applications including nanolasers, electro-optic modulators, photodetectors and other optoelectronic devices. Now, there is an increased interest to achieve similar but better functionalities using TMD materials. Photoluminescence (PL) experiments on TMDs have shown that their bandgap ranges from near infrared to visible frequencies of the electromagnetic spectrum. This makes TMDs superior to graphene as the former covers a frequency range that is significant to advanced technological inventions [37]. On the other hand, graphene is a zero bandgap material and also requires time consuming, painstaking and non-scalable manufacturing processes. For instance, Chien Chung Lee et al., demonstrated the very first graphene based

electro-optic modulator [38] and even though CVD was used as the process of monolayer graphene sheet synthesis which is a scalable industry level process, yet the manufactured graphene suffered from the drawback of transfer process. CVD grown graphene requires the graphene to be grown first on copper foils and then later transferred onto the desired substrate which is in fact very tricky and requires skills of precision and handiwork. This is because while the graphene floats on liquid, the process of picking up a fragile monolayer or even a few multilayers and putting it on the substrate can often lead to twisting or breaking of sheets. Moreover, as noted by Cedric Huyghebaert et al., the interfacial interaction of graphene with polymers (like PMMA) and liquid (like water) may also impact electrical properties of graphene-based device [39] and local strain may result in alteration of local bandgap [40].

So, apart from attractive physical properties, TMDs are also preferred for ease of fabrication and scalable manufacturing processes with industrial relevance like direct RF sputtering and hot pick up and stamp technique as mentioned previously.

1.1.1 Stability considerations and disadvantages of thin film MoS_2

Also, from **tab. 1.1**, it is clear that MoS_2 is a very advantageous material for optoelectronics, but it has its disadvantages too. Controlling these disadvantages will lead to enhanced functionality of 2D TMD materials. Jian Gao et al., [41] have shown a time lapse comparison of WS_2 and MoS_2 monolayers on selected substrates for up to a year. They show that TMD monolayers adsorb organic molecules from air and oxidise at grain boundaries. They claim that the otherwise accepted opinion of TMDs being stable in ambient environment is in reality wrong and suggest a possible solution to it. The solution proposed by Jian Gao et al., is polymer encapsulation. Finally, their study shows a quantifiable effect of MoS_2 degradation in terms of reduced transistor current by 2 orders of magnitude and increased threshold voltage for the aged transistor devices made by MoS_2. Jian Gao et al., also noted that aged MoS_2 transistor devices show p-type doping which is induced by oxidation of MoS_2 sheets over time. Other DFT simulation studies on the other hand conducted along similar lines by Jana Martincová et al., [42] and Hongsheng Liu et al., [43] also conclude that monolayer MoS_2 is unstable in air due to exposed edge sites which get oxidised which is a result of low energetic barrier at Mo edges. Due to this, oxygen molecules are dissociated easily especially at Mo edges of MoS_2.

1.1.2 Electrical properties of MoS_2

Furthermore, mobility studies by Branimir Radisavljevic and Andras Kis reveal the presence of charge traps at the substrate-MoS_2 interface that reduce the room temperature mobility of MoS_2 devices [44]. They further report that dielectric environment effects the electron transport and hence link it to the electrical mobility of the TMD material. They show that encapsulation with high - κ dielectrics can compensate for the otherwise reduced mobilities by damping scattering from Coulombic impurities and improve the electrical mobility by an order of magnitude [45]. In fact, thin film MoS_2 transistor devices with top gated or back gated dielectric are relatively easier to fabricate as compared to graphene-based devices. Coating of dielectrics such as Al_2O_3 can be carried out directly on MoS_2 by commercially compatible fabrication processes like atomic layer deposition (ALD) at low temperatures [46] which enhances the measured room temperature mobility to more than 100 cm^2/V-s [47]. Also, a reduction in contact resistance was also reported by Aravindh Kumar et al., by comparing MoS_2 TLM structures with gold contacts before and after Al_2O_3 encapsulation [48].

1.1.3 Optical properties and origin of excitons

Optical spectra of different monolayer TMDs - MoS_2, $MoSe_2$, WS_2, WSe_2 have been obtained by different methods like Spectroscopic Ellipsometry (SE), Photo-luminescence (PL) measurements and Ultraviolet-visible (UV-Vis) spectroscopy [10], [33], [49], [50], [51], [52]. These measurements show that MoS_2 has an extraordinarily high real part of refractive index (n) of 6.5 at 450 nm. In fact, complex refractive indices of all monolayer TMDs (MX_2; M = Mo, W and X = S, Se) are feature-rich in the visible range of wavelengths and saturate from near infrared wavelength onwards to a high and constant value [33]. These features dominating the visible range are direct optical transitions [49] emanating due to Spin Orbit (S-O) coupling of the d-orbitals of the transition metal (say, Mo) at the K-point of the TMD. This S-O coupling induces splitting of the valence band maxima (VBM) (shown as $\nu 1$ and $\nu 2$ in ***fig. 1.3***) of which d_{xy} and $d_{x^2-y^2}$ Mo orbitals constitute its major part with very little contribution from the p_x and p_y orbitals of the Chalcogen atom (S or Se). The conduction band minimum (CBM) on the other hand is constituted mainly of d_{z^2} orbital of Mo and minor contributions from s-orbital of Mo, p_x and p_y orbitals of the Chalcogen atom [53], [54]. Direct optical transition from the spin split VBM to the CBM

gives rise to excitons (A and B in ***fig. 1.3***) in the TMDs and appear as strong features in the absorption spectrum and that of refractive index as mentioned previously. In fact, S-O coupling (Δ_{SO}) distinguishes TMDs (Δ_{SO} ~150 meV [33]) greatly from graphene (Δ_{SO} ~4 meV [55]) resulting in ~40 times stronger S-O coupling in TMDs than graphene. While the above-mentioned is true for monolayer MoS_2, for bilayer and multilayer MoS_2, VBM splitting is due to a combination of S-O coupling and interlayer interactions [56].

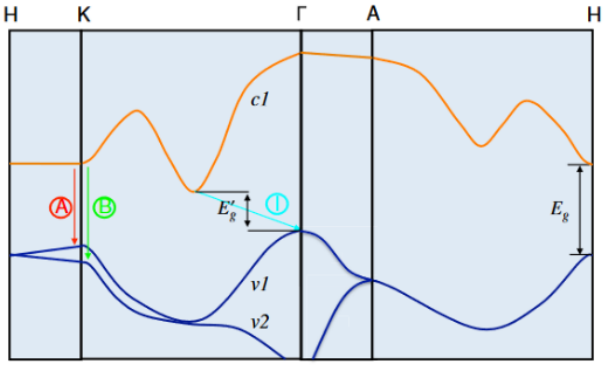

Fig. 1.3*: Bandstructure of bulk MoS_2 [49]. v1 and v2 are the split branches of the valence band.A and B are the excitonic transitions at K-point, E_g' represents the indirect bandgap of bulk MoS_2 and E_g the direct bandgap for monolayer MoS_2.*

1.2 Light matter interaction

In order to understand the significance of complex refractive index for better absorption in TMDs, it is important to understand the very process of refraction and derive an expression of refractive index 'n' based on the fundamental atomic quantities (such as electron density, mass, charge) rather than just being defined as a ratio of speeds in two media. The latter definition of refractive index does not justify the process of refraction, rather is an outcome of the refraction process. In the first instance, refractive index 'n' is very simply defined as:

$$n = \frac{c}{v} \qquad \textbf{(1-1)}$$

Where, n is the refractive index, c is the speed of light in vacuum and v is the speed of light in a medium. However, this description is quite basic and can be misleading when the subject of discussion is the physics occurring inside the very medium of reference. ***Eq. (1-1)*** only reveals the after effect of refraction i.e., the result of refraction which is the reduction in speed of light but does not give any information as to what brings about this reduction. Therefore, the further discussion is aimed at introducing a complete expression of 'n' that takes into account the absorption process in materials like TMDs.

An electric field (E_0) entering a medium of thickness 'z' interacts with its atoms which consists of electrons having mass 'm' and charge 'q_e'. This incoming electric field having an angular frequency 'ω' exerts an electric force on electrons due to which they start oscillating in the medium with a resonant frequency 'ω_0'and in turn produce fields - like new radiators. The field thus produced by a sheet of moving charges has velocity of its charges retarded in time by z/c times a constant A (= $\frac{\eta q e}{2\epsilon_0 c}$, where, η is number of atoms per unit area) [57]:

$$E = -A\left[i\omega \frac{q_e E_0}{m(\omega_0^2-\omega^2)} e^{i\omega(t-z/c)}\right] \qquad \textbf{(1-2)}$$

Upon applying equation of motion on electron oscillators and on comparing it with ***eq. (1-2)***, 'n' can be computed:

$$n = 1 + \frac{N q_e^2}{2\epsilon_0 m(\omega_0^2-\omega^2)} \qquad \textbf{(1-3)}$$

The above dispersion equation [57] defines 'n' based on atomic quantities and shows its dependence on frequency of light as well as the electron density in a medium. Frequency of electron oscillations differs among materials which gives them a unique refractive index. This also reveals the fact that while a material can be opaque to visible light, it might be transparent to other frequencies of light.

Furthermore, we also need to consider some damping because electrons cannot go on oscillating forever. This damping can be represented by the damping coefficient, 'γ' which accounts for 'absorption' of light in the medium. Also, there are more than one electron in a material and hence multiple oscillators (say, 'N_k' electrons per unit volume having natural frequency, 'ω_k' and damping coefficient 'γ_k'), therefore, ***eq. (1-3)*** now becomes:

$$n = 1 + \frac{q_e^2}{2\epsilon_0 m} \sum_k \frac{N_k}{\omega_k^2-\omega^2+i\gamma_k\omega} \qquad \textbf{(1-4)}$$

Eq. (1-4) [57] shows that refractive index is a complex quantity $n = n' - in''$. The effect of complex refractive index on the light that has passed through a medium of thickness Δz is shown in ***eq. (1-5)*** [57] below:

$$E_{lossy} = \underbrace{e^{-\omega n'' \Delta z/c}}_{1} \underbrace{e^{-i\omega(n'-1)\Delta z/c} E_0 e^{i\omega(t-z/c)}}_{2} \qquad \textbf{(1-5)}$$

E_{lossy} here refers to the electric field in the region beyond the medium through which light passes and the term takes consideration (qualitatively) the attenuation of transmitted light waves after having passed through the medium. While the second term is representative of light that passes through a lossless medium (for example, glass), term 1 is a negative exponent which represents the decrease in magnitude of the resultant electric field of light emerging out of a lossy, absorbing medium having a complex refractive index. Hence, the light wave loses its energy after having passed the material due to the presence of the damping factor introduced previously. Also, note that this reduction depends on n'' and Δz meaning that the greater the imaginary component of refractive index (n'') and the thickness of the material, the greater will be the absorption (or reduction in the magnitude of E). This 'n''' is actually 'k' introduced previously as the absorption coefficient.

1.3 Effect of dielectric encapsulation

There are also optical advantages of having a dielectric in the TMD device. Since the aim of this project is to investigate active light modulation meaning change in light interaction inside a TMD upon application of an external stimulus, therefore this work heavily relies on absorption of light and optical properties of TMDs. Transition metals (or d-band metals) are especially prone to adsorption processes like chemisorption and physisorption due to high density of states (DOS) near the Fermi level. Since s-bands are similarly filled across a transition metal period, therefore the interaction with an incoming adsorbing species seems similar across that period. The only difference arises from the d-band and since it is a narrow band, the interaction with an adsorbate, results in splitting to form anti-bonding and bonding states. The reactivity is therefore dependent on these interactions which further have a profound effect on the surface properties of TMDs [58], [59]. Thus, incorporating a dielectric buffer layer has shown to greatly alter and protect optical properties of monolayer TMDs [60] and this idea was further exploited in past studies to fully encapsulate the TMD monolayer with Hexagonal Boron Nitride (h-BN) which showed narrowing of the PL linewidth at room temperature and a greater narrowing at cryogenic temperatures [61], [62]. Furthermore, other dielectrics like Al_2O_3 and HfO_2 have also been used as gate dielectrics in multilayer MoS_2 based transistor devices to improve their electrical performance [63], [64], [65]. These experimental reports of increased electrical performance and enhanced PL signal of encapsulated TMDs can be explained by decrease in bandgap due to reduction in

Coulomb interaction of electrons caused by dielectric screening corroborated by J. Ryou et al.'s calculations [66].

1.4 Role of excitons and gating effect on absorption of light

Now that the process of refraction and its link with absorption in materials is established, the ways in which absorption can be controlled in materials having complex refractive index (like TMDs) can be discussed. A phenomenon that is exhibited in TMDs is that of exciton formation. Exciton is a stable state of an electron and a hole in unison held by Coulombic force. Presence of excitons (direct transitions at **K** points) at room temperature despite of the availability of a lower energy value of indirect transition is an explicit evidence of exciton stability in TMDs [49]. Absorption is seen to peak near exciton resonances [10], [49] and Y. Yu et al., have further extended this phenomenon to show tunability of reflectance (or absorption) in monolayer TMDs by gating them [15]. Tuning the absorption in turn is responsible for the modulation of refractive index according to Kramers-Kronig relations.

Furthermore, monolayer TMDs host intralayer excitons while bilayers, few layers and multilayer TMDs may host interlayer excitons as well depending upon the layer stacking i.e., polytypism (the most stable being 2H followed by 3R [67]). While it is shown that MoS_2 homobilayers of 2H stacking host interlayer excitons [68], 3R stacking does not [69], [70]. This is an important point of consideration since this project deals with few and multi-layered MoS_2 instead of being restricted to monolayers.

Building upon these findings, active electrical control over interlayer excitons has been experimentally achieved in up to bilayer TMDs [71], [72]. Here the application of an out-of-plane electric field brings about a change from symmetric to type-II band alignment (conduction band minimum lies in one of the materials and valence band maximum lies in the other material of the heterostructure) which is otherwise observed and studied in TMD heterostructures that also forms the basis of existence of interlayer excitons in them [73], [74], [75]. Alternatively, B. Chakraborty et al., and V. G. Kravets et al, have shown tunability in monolayer WS_2 [76] and MoS_2 [77] respectively by electrostatically inducing free carriers directly in the TMD layer and changing excitons' oscillator strengths.

Present work extends the above-mentioned ideas to large area few and multilayers of MoS_2 prepared with a photolithography compatible technique and a control over the shape and placement of the film on the Fabry-Pérot based cavity stack.

1.5 Applications

TMDs have taken the spotlight when it comes to manipulating light to suit many applications. For instance, open pore structure leads to larger available surface area in µm thick directly sputtered MoS_2 films which result in sustainable high capacitance measurements, reported by N. Choudhary et al. [19] and making MoS_2 a potential candidate for supercapacitors. MoS_2 thin films also serve as low cost and efficient electrocatalysts for hydrogen evolution reactions (HER) thus replacing Pt-based catalysts. Conventionally, only edge sites on MoS_2 flakes were believed to be catalytically active [78] but more recently, it has been reported that continuous monolayer MoS_2 film without edge sites is more catalytically active [79] having ~10 [80] – 55 [78] times higher current densities at 0.19 V. The HER activity is further enhanced by introducing Mo Frenkel defects in monolayer MoS_2 as shown by J. Xu et al. [81]. In fact, MoS_2 is not limited to energy storage and catalysis applications but also serves a useful platform for energy conversion. CVD grown few-layer MoS_2 has reportedly shown significantly high in-plane thermopower (Seebeck coefficient) ~ 742 µV/K at room temperature [82]. Though, lower than the previously reported thermopowers for CVD [17] and mechanically exfoliated [18] based monolayer MoS_2, but this is the first study to investigate thermo-electric (TE) properties of large area and few layers thick MoS_2 as well as measure cross-plane thermopower ~ 115 µV/K.

Y. Zhang et al., further reported combined photo-induced thermoelectric and photovoltaic effects in multilayer MoS_2 which makes it a good candidate for solar and photodetection applications too [83]. And indeed, MoS_2 photoelectric properties were investigated by C. Wu et al., and the study concluded that the same thickness of MoS_2 responds differently under different wavelengths of light [84]. Monolayer MoS_2 showed a higher photosensitivity when it was illuminated by a UV light source (365 nm) compared to when illuminated by 532 nm and 650 nm light. Based on this property of high photoresponse, TMD based phototransistors with active pixel control in the visible light range [65] and waveguide-led photodetectors in the infrared regime [85] have been successfully demonstrated by S. Hong et al. and Shayan Parhizkar et al. respectively justifying the versatality of 2D TMDs. They

further emphasized on the following: high carrier mobility which is theoretically calculated to be as high as 410 cm^2/V-s [86] (experimental: 2.7 cm^2/V-s to 3.7 cm^2/V-s [85]), easy back-end-of-line (BEOL) integration in optoelectronic circuits, stability in ambient conditions, the ability to transition between semiconducting and semi-metallic phase so as to attain a finite and zero band gap (based on application) by controlling layer thickness and compatibility with various other substrates.

Finally, S. Parhizkar et al., also proved the superiority of direct chalcogenization of transition metals by a less explored technique known as Thermally-Assisted Conversion (TAC) over wet transfer process as the former rendered conformal deposition of TMD films while the latter does not and in fact leads to wrinkles and breaking of the thin film near edges or waveguides. Therefore, we extend the use of the TAC technique to other TMDs like MoS_2 and compare all the devices based on electrical and optical characteristics.

1.6 Thesis Outline

Chapter 2 elaborates on the TMD synthesis process focussing on the TAC method used in this work. This is followed by a material and optical characterisation measurements for different stack design consisting of MoS_2. This includes optical characterization - spectroscopic ellipsometry, UV-Vis spectroscopy, XRD, Raman and photoluminescence spectroscopy. To learn about the surface morphology, atomic force microscopy and scanning electron microscopy were also performed and the results are presented for the same.

Chapter 3 deals with electrical characterization of MoS_2 films (based on thermally assisted conversion (TAC) method of synthesis) that includes capacitance - voltage (C-V), current - voltage (I-V) and resistance - temperature (R-T) measurements. It also discusses about the different material combinations and designs for both contacts and dielectrics that can be used to obtain the best performance for the TAC based TMD stack.

Chapter 4 includes differential reflectance (DR) results of stacks that include MoS_2 which was synthesised using the TAC process. DR results were obtained from our in-house CCD based DR measuring tool. The chapter further attempts to establish links between MoS_2 exciton dynamics and theory of tuning mechanisms with the experimentally obtained results to explain the underlying exciton-light mechanisms responsible for the change in reflectance upon gating the TMD stack.

Chapter 5 deals with photo-induced response of TAC based MoS_2 under a broad spectrum of light as well as when illuminated a focussed laser of fixed wavelength. An investigative study of pyroelectricity observed in TAC based MoS_2 films was carried out and the main parameters influencing this effect are discussed.

Chapter 6 finally concludes the main observations based on the experimental results obtained and future prospects in this field.

References

[1] J. Nielsen, "Nielsen's Law of Internet Bandwidth," *Nielsen Norman Group*, Apr. 1998.

[2] N. K. Dutta and K. Lu, "Optical Modulators," in *Encyclopedia of Optical and Photonic Engineering*, 2nd ed., Boca Raton: CRC Press, 2015.

[3] O. T. Celik *et al.*, "High-bandwidth CMOS-voltage-level electro-optic modulation of 780 nm light in thin-film lithium niobate," *Opt. Express, OE*, vol. 30, no. 13, pp. 23177–23186, Jun. 2022, doi: 10.1364/OE.460119.

[4] C. Li *et al.*, "High modulation efficiency and large bandwidth thin-film lithium niobate modulator for visible light," *Opt. Express, OE*, vol. 30, no. 20, pp. 36394–36402, Sep. 2022, doi: 10.1364/OE.469065.

[5] O. Tadanaga, T. Kagawa, Y. Itoh, C. Amano, and Y. M. andTakashi Kurokawa, "1.3-μm Surface-Normal Reflective Optical Modulators Based on the Wannier-Stark Effect in InP/InGaAsP Superlattices," *Jpn. J. Appl. Phys.*, vol. 38, no. 2S, p. 1278, Feb. 1999, doi: 10.1143/JJAP.38.1278.

[6] H. Mohseni, W. K. Chan, H. An, A. Ulmer, and D. Capewell, "Tunable surface-normal modulators operating near 1550 nm with a high-extinction ratio at high temperatures," *IEEE Photonics Technology Letters*, vol. 18, no. 1, pp. 214–216, Jan. 2006, doi: 10.1109/LPT.2005.861629.

[7] J. W. Goodman, F. J. Leonberger, S.-Y. Kung, and R. A. Athale, "Optical interconnections for VLSI systems," *Proceedings of the IEEE*, vol. 72, no. 7, pp. 850–866, Jul. 1984, doi: 10.1109/PROC.1984.12943.

[8] N. C. Helman, J. E. Roth, J. Altug, D. A. B. Miller, and D. P. Bour, "Low-voltage surface-normal InGaAsP/InP modulator for optical interconnects," in *The 17th Annual Meeting of the IEEELasers and Electro-Optics Society, 2004. LEOS 2004.*, Rio Grande, Puerto Rico: IEEE, 2004, pp. 461–462. doi: 10.1109/LEOS.2004.1363312.

[9] M. A. Kats and F. Capasso, "Optical absorbers based on strong interference in ultra-thin films," *Laser & Photonics Reviews*, vol. 10, no. 5, pp. 735–749, Sep. 2016, doi: 10.1002/lpor.201600098.

[10] C. Yim *et al.*, "Investigation of the optical properties of MoS_2 thin films using spectroscopic ellipsometry," *Applied Physics Letters*, vol. 104, no. 10, p. 103114, Mar. 2014, doi: 10.1063/1.4868108.

[11] H. Xu, "Enhanced light–matter interaction of a MoS_2 monolayer with a gold mirror layer," *RSC Adv.*, vol. 7, no. 37, pp. 23109–23113, Apr. 2017, doi: 10.1039/C6RA27691A.

[12] H. Y. Jeong *et al.*, "Optical Gain in MoS_2 via Coupling with Nanostructured Substrate: Fabry-Perot Interference and Plasmonic Excitation," *ACS Nano*, vol. 10, no. 9, pp. 8192–8198, Sep. 2016, doi: 10.1021/acsnano.6b03237.

[13] Y. Yu *et al.*, "Exciton-dominated Dielectric Function of Atomically Thin MoS_2 Films," *Sci Rep*, vol. 5, no. 1, Art. no. 1, Nov. 2015, doi: 10.1038/srep16996.

[14] K. F. Mak *et al.*, "Tightly bound trions in monolayer MoS_2," *Nat Mater*, vol. 12, no. 3, pp. 207–211, Mar. 2013, doi: 10.1038/nmat3505.

[15] Y. Yu, Y. Yu, L. Huang, H. Peng, L. Xiong, and L. Cao, "Giant Gating Tunability of Optical Refractive Index in Transition Metal Dichalcogenide Monolayers," *Nano Lett.*, vol. 17, no. 6, pp. 3613–3618, Jun. 2017, doi: 10.1021/acs.nanolett.7b00768.

[16] L. Seravalli and M. Bosi, "A Review on Chemical Vapour Deposition of Two-Dimensional MoS_2 Flakes," *Materials*, vol. 14, no. 24, Art. no. 24, Jan. 2021, doi: 10.3390/ma14247590.

[17] J. Wu, H. Schmidt, K. K. Amara, X. Xu, G. Eda, and B. Özyilmaz, "Large Thermoelectricity via Variable Range Hopping in Chemical Vapor Deposition Grown

Single-Layer MoS_2," *Nano Lett.*, vol. 14, no. 5, pp. 2730–2734, May 2014, doi: 10.1021/nl500666m.
[18] M. Buscema, M. Barkelid, V. Zwiller, H. S. J. Van Der Zant, G. A. Steele, and A. Castellanos-Gomez, "Large and Tunable Photothermoelectric Effect in Single-Layer MoS_2," *Nano Lett.*, vol. 13, no. 2, pp. 358–363, Feb. 2013, doi: 10.1021/nl303321g.
[19] N. Choudhary *et al.*, "Directly deposited MoS_2 thin film electrodes for high performance supercapacitors," *J. Mater. Chem. A*, vol. 3, no. 47, pp. 24049–24054, Nov. 2015, doi: 10.1039/C5TA08095A.
[20] E. Di Russo *et al.*, "Synthesis of Large-Area Crystalline MoS_2 by Sputter Deposition and Pulsed Laser Annealing," *ACS Appl. Electron. Mater.*, vol. 5, no. 5, pp. 2862–2875, May 2023, doi: 10.1021/acsaelm.3c00362.
[21] A. Thomas and K. B. Jinesh, "Excitons and Trions in MoS_2 Quantum Dots: The Influence of the Dispersing Medium," *ACS Omega*, vol. 7, no. 8, pp. 6531–6538, Feb. 2022, doi: 10.1021/acsomega.1c05432.
[22] P. J. Zomer, M. H. D. Guimarães, J. C. Brant, N. Tombros, and B. J. van Wees, "Fast pick up technique for high quality heterostructures of bilayer graphene and hexagonal boron nitride," *Applied Physics Letters*, vol. 105, no. 1, p. 013101, Jul. 2014, doi: 10.1063/1.4886096.
[23] F. Pizzocchero *et al.*, "The hot pick-up technique for batch assembly of van der Waals heterostructures," *Nat Commun*, vol. 7, p. 11894, Jun. 2016, doi: 10.1038/ncomms11894.
[24] A. Castellanos-Gomez *et al.*, "Deterministic transfer of two-dimensional materials by all-dry viscoelastic stamping," *2D Mater.*, vol. 1, no. 1, p. 011002, Apr. 2014, doi: 10.1088/2053-1583/1/1/011002.
[25] X. Ma *et al.*, "Capillary-Force-Assisted Clean-Stamp Transfer of Two-Dimensional Materials," *Nano Lett*, vol. 17, no. 11, pp. 6961–6967, Nov. 2017, doi: 10.1021/acs.nanolett.7b03449.
[26] Y. Zhang, Q. Liu, and B. Xu, "Liquid-assisted, etching-free, mechanical peeling of 2D materials," *Extreme Mechanics Letters*, vol. 16, pp. 33–40, Oct. 2017, doi: 10.1016/j.eml.2017.08.005.
[27] K. Buapan, R. Somphonsane, T. Chiawchan, and H. Ramamoorthy, "Versatile, Low-Cost, and Portable 2D Material Transfer Setup with a Facile and Highly Efficient DIY Inert-Atmosphere Glove Compartment Option," *ACS Omega*, vol. 6, no. 28, pp. 17952–17964, Jul. 2021, doi: 10.1021/acsomega.1c01582.
[28] H. Pan *et al.*, "Large-scale monolayer molybdenum disulfide (MoS_2) for mid-infrared photonics," *Nanophotonics*, vol. 9, no. 16, pp. 4703–4710, Nov. 2020, doi: 10.1515/nanoph-2020-0331.
[29] D. Lembke and A. Kis, "Breakdown of High-Performance Monolayer MoS_2 Transistors," *ACS Nano*, vol. 6, no. 11, pp. 10070–10075, Nov. 2012, doi: 10.1021/nn303772b.
[30] A. Molina-Sánchez and L. Wirtz, "Phonons in single-layer and few-layer MoS_2 and WS_2," *Phys. Rev. B*, vol. 84, no. 15, p. 155413, Oct. 2011, doi: 10.1103/PhysRevB.84.155413.
[31] N. Wakabayashi, H. G. Smith, and R. M. Nicklow, "Lattice dynamics of hexagonal MoS_2 studied by neutron scattering," *Phys. Rev. B*, vol. 12, no. 2, pp. 659–663, Jul. 1975, doi: 10.1103/PhysRevB.12.659.
[32] I. A. Rahman and A. Purqon, "First Principles Study of Molybdenum Disulfide Electronic Structure," *J. Phys.: Conf. Ser.*, vol. 877, no. 1, p. 012026, Jul. 2017, doi: 10.1088/1742-6596/877/1/012026.

[33] H.-L. Liu, C.-C. Shen, S.-H. Su, C.-L. Hsu, M.-Y. Li, and L.-J. Li, "Optical properties of monolayer transition metal dichalcogenides probed by spectroscopic ellipsometry," *Applied Physics Letters*, vol. 105, no. 20, p. 201905, Nov. 2014, doi: 10.1063/1.4901836.
[34] R. Fivaz and E. Mooser, "Mobility of Charge Carriers in Semiconducting Layer Structures," *Phys. Rev.*, vol. 163, no. 3, pp. 743–755, Nov. 1967, doi: 10.1103/PhysRev.163.743.
[35] K. S. Novoselov *et al.*, "Two-dimensional atomic crystals," *Proceedings of the National Academy of Sciences*, vol. 102, no. 30, pp. 10451–10453, Jul. 2005, doi: 10.1073/pnas.0502848102.
[36] B. Radisavljevic, A. Radenovic, J. Brivio, V. Giacometti, and A. Kis, "Single-layer MoS_2 transistors," *Nature Nanotech*, vol. 6, no. 3, Art. no. 3, Mar. 2011, doi: 10.1038/nnano.2010.279.
[37] C. Liu, J. Zheng, Y. Chen, T. Fryett, and A. Majumdar, "Van der Waals materials integrated nanophotonic devices [Invited]," *Opt. Mater. Express*, vol. 9, no. 2, p. 384, Feb. 2019, doi: 10.1364/OME.9.000384.
[38] C.-C. Lee, S. Suzuki, W. Xie, and T. R. Schibli, "Broadband graphene electro-optic modulators with sub-wavelength thickness," *Opt. Express, OE*, vol. 20, no. 5, pp. 5264–5269, Feb. 2012, doi: 10.1364/OE.20.005264.
[39] C. Huyghebaert *et al.*, "2D materials: roadmap to CMOS integration," in *2018 IEEE International Electron Devices Meeting (IEDM)*, Dec. 2018, p. 22.1.1-22.1.4. doi: 10.1109/IEDM.2018.8614679.
[40] B. G. Shin *et al.*, "Indirect Bandgap Puddles in Monolayer MoS_2 by Substrate-Induced Local Strain," *Advanced Materials*, vol. 28, no. 42, pp. 9378–9384, 2016, doi: 10.1002/adma.201602626.
[41] J. Gao, B. Li, J. Tan, P. Chow, T.-M. Lu, and N. Koratkar, "Aging of Transition Metal Dichalcogenide Monolayers," *ACS Nano*, vol. 10, no. 2, pp. 2628–2635, Feb. 2016, doi: 10.1021/acsnano.5b07677.
[42] J. Martincová, M. Otyepka, and P. Lazar, "Is Single Layer MoS_2 Stable in the Air?," *Chemistry – A European Journal*, vol. 23, no. 53, pp. 13233–13239, 2017, doi: 10.1002/chem.201702860.
[43] H. Liu, N. Han, and J. Zhao, "Atomistic insight into the oxidation of monolayer transition metal dichalcogenides: from structures to electronic properties," *RSC Adv.*, vol. 5, no. 23, pp. 17572–17581, Feb. 2015, doi: 10.1039/C4RA17320A.
[44] B. Radisavljevic and A. Kis, "Mobility engineering and a metal-insulator transition in monolayer MoS_2," *Nat Mater*, vol. 12, no. 9, pp. 815–820, Sep. 2013, doi: 10.1038/nmat3687.
[45] D. Jena and A. Konar, "Enhancement of Carrier Mobility in Semiconductor Nanostructures by Dielectric Engineering," *Phys. Rev. Lett.*, vol. 98, no. 13, p. 136805, Mar. 2007, doi: 10.1103/PhysRevLett.98.136805.
[46] H. Liu and P. D. Ye, "\hboxMoS_2 Dual-Gate MOSFET With Atomic-Layer-Deposited \hboxAl_2\hboxO_3 as Top-Gate Dielectric," *IEEE Electron Device Letters*, vol. 33, no. 4, pp. 546–548, Apr. 2012, doi: 10.1109/LED.2012.2184520.
[47] S. Kim *et al.*, "High-mobility and low-power thin-film transistors based on multilayer MoS_2 crystals," *Nat Commun*, vol. 3, no. 1, p. 1011, Aug. 2012, doi: 10.1038/ncomms2018.
[48] A. Kumar, A. Tang, H.-S. P. Wong, and K. Saraswat, "Improved Contacts to Synthetic Monolayer MoS_2 – A Statistical Study," in *2021 IEEE International Interconnect Technology Conference (IITC)*, Kyoto, Japan: IEEE, Jul. 2021, pp. 1–3. doi: 10.1109/IITC51362.2021.9537515.

[49] K. F. Mak, C. Lee, J. Hone, J. Shan, and T. F. Heinz, "Atomically Thin MoS 2 : A New Direct-Gap Semiconductor," *Phys. Rev. Lett.*, vol. 105, no. 13, p. 136805, Sep. 2010, doi: 10.1103/PhysRevLett.105.136805.
[50] A. Splendiani *et al.*, "Emerging Photoluminescence in Monolayer MoS_2," *Nano Lett.*, vol. 10, no. 4, pp. 1271–1275, Apr. 2010, doi: 10.1021/nl903868w.
[51] D. Y. Qiu, F. H. da Jornada, and S. G. Louie, "Optical spectrum of MoS_2: many-body effects and diversity of exciton states," *Phys Rev Lett*, vol. 111, no. 21, p. 216805, Nov. 2013, doi: 10.1103/PhysRevLett.111.216805.
[52] V. Forsberg *et al.*, "Exfoliated MoS_2 in Water without Additives," *PLOS ONE*, vol. 11, no. 4, p. e0154522, Apr. 2016, doi: 10.1371/journal.pone.0154522.
[53] R. Coehoorn, C. Haas, and R. A. de Groot, "Electronic structure of $MoSe_2$, MoS_2, and WSe_2. II. The nature of the optical band gaps," *Phys. Rev. B*, vol. 35, no. 12, pp. 6203–6206, Apr. 1987, doi: 10.1103/PhysRevB.35.6203.
[54] T. Cao *et al.*, "Valley-selective circular dichroism of monolayer molybdenum disulphide," *Nat Commun*, vol. 3, no. 1, Art. no. 1, Jun. 2012, doi: 10.1038/ncomms1882.
[55] Y. Yao, F. Ye, X.-L. Qi, S.-C. Zhang, and Z. Fang, "Spin-orbit gap of graphene: First-principles calculations," *Phys. Rev. B*, vol. 75, no. 4, p. 041401, Jan. 2007, doi: 10.1103/PhysRevB.75.041401.
[56] T. Cheiwchanchamnangij and W. R. L. Lambrecht, "Quasiparticle band structure calculation of monolayer, bilayer, and bulk MoS_2," *Phys. Rev. B*, vol. 85, no. 20, p. 205302, May 2012, doi: 10.1103/PhysRevB.85.205302.
[57] R. Feynman, "The Origin of the Refractive Index," in *The Feynman Lectures on Physics*, 1963.
[58] B. Hammer and J. K. Norskov, "Why gold is the noblest of all the metals," *Nature*, vol. 376, no. 6537, Art. no. 6537, Jul. 1995, doi: 10.1038/376238a0.
[59] L. G. M. Pettersson and A. Nilsson, "A Molecular Perspective on the d-Band Model: Synergy Between Experiment and Theory," *Top Catal*, vol. 57, no. 1–4, pp. 2–13, Feb. 2014, doi: 10.1007/s11244-013-0157-4.
[60] M. K. L. Man *et al.*, "Protecting the properties of monolayer MoS_2 on silicon based substrates with an atomically thin buffer," *Sci Rep*, vol. 6, no. 1, p. 20890, Feb. 2016, doi: 10.1038/srep20890.
[61] F. Cadiz *et al.*, "Excitonic Linewidth Approaching the Homogeneous Limit in MoS 2 -Based van der Waals Heterostructures," *Phys. Rev. X*, vol. 7, no. 2, p. 021026, May 2017, doi: 10.1103/PhysRevX.7.021026.
[62] S. Shree *et al.*, "High optical quality of MoS_2 monolayers grown by chemical vapor deposition," *2D Mater.*, vol. 7, no. 1, p. 015011, Nov. 2019, doi: 10.1088/2053-1583/ab4f1f.
[63] J. Zou, L. Wang, and F. Chen, "Improved performance of top-gated multilayer MoS_2 transistors with channel fully encapsulated by Al2O3 dielectric," *AIP Advances*, vol. 9, no. 9, p. 095061, Sep. 2019, doi: 10.1063/1.5119913.
[64] J. Xu *et al.*, "Effects of HfO2 encapsulation on electrical performances of few-layered MoS_2 transistor with ALD HfO2 as back-gate dielectric," *Nanotechnology*, vol. 29, no. 34, p. 345201, Aug. 2018, doi: 10.1088/1361-6528/aac853.
[65] S. Hong *et al.*, "Highly sensitive active pixel image sensor array driven by large-area bilayer MoS_2 transistor circuitry," *Nat Commun*, vol. 12, no. 1, p. 3559, Jun. 2021, doi: 10.1038/s41467-021-23711-x.
[66] J. Ryou, Y.-S. Kim, S. Kc, and K. Cho, "Monolayer MoS_2 Bandgap Modulation by Dielectric Environments and Tunable Bandgap Transistors," *Sci Rep*, vol. 6, no. 1, p. 29184, Jul. 2016, doi: 10.1038/srep29184.

[67] J. He, K. Hummer, and C. Franchini, "Stacking effects on the electronic and optical properties of bilayer transition metal dichalcogenides MoS_2, $MoSe_2$, WS_2, and WSe_2," *Phys. Rev. B*, vol. 89, no. 7, p. 075409, Feb. 2014, doi: 10.1103/PhysRevB.89.075409.
[68] T. Deilmann and K. S. Thygesen, "Interlayer Excitons with Large Optical Amplitudes in Layered van der Waals Materials," *Nano Lett*, vol. 18, no. 5, pp. 2984–2989, May 2018, doi: 10.1021/acs.nanolett.8b00438.
[69] I. C. Gerber *et al.*, "Interlayer excitons in bilayer MoS 2 with strong oscillator strength up to room temperature," *Phys. Rev. B*, vol. 99, no. 3, p. 035443, Jan. 2019, doi: 10.1103/PhysRevB.99.035443.
[70] I. Paradisanos *et al.*, "Controlling interlayer excitons in MoS_2 layers grown by chemical vapor deposition," *Nat Commun*, vol. 11, no. 1, Art. no. 1, May 2020, doi: 10.1038/s41467-020-16023-z.
[71] N. Peimyoo *et al.*, "Electrical tuning of optically active interlayer excitons in bilayer MoS_2," *Nat. Nanotechnol.*, vol. 16, no. 8, Art. no. 8, Aug. 2021, doi: 10.1038/s41565-021-00916-1.
[72] N. Leisgang *et al.*, "Giant Stark splitting of an exciton in bilayer MoS_2," *Nat. Nanotechnol.*, vol. 15, no. 11, pp. 901–907, Nov. 2020, doi: 10.1038/s41565-020-0750-1.
[73] H. Fang *et al.*, "Strong interlayer coupling in van der Waals heterostructures built from single-layer chalcogenides," *Proceedings of the National Academy of Sciences*, vol. 111, no. 17, pp. 6198–6202, Apr. 2014, doi: 10.1073/pnas.1405435111.
[74] P. Rivera *et al.*, "Valley-polarized exciton dynamics in a 2D semiconductor heterostructure," *Science*, vol. 351, no. 6274, pp. 688–691, Feb. 2016, doi: 10.1126/science.aac7820.
[75] S. Latini, K. T. Winther, T. Olsen, and K. S. Thygesen, "Interlayer Excitons and Band Alignment in MoS_2/hBN/WSe_2 van der Waals Heterostructures," *Nano Lett.*, vol. 17, no. 2, pp. 938–945, Feb. 2017, doi: 10.1021/acs.nanolett.6b04275.
[76] B. Chakraborty *et al.*, "Control of Strong Light–Matter Interaction in Monolayer WS2 through Electric Field Gating," *Nano Lett.*, vol. 18, no. 10, pp. 6455–6460, Oct. 2018, doi: 10.1021/acs.nanolett.8b02932.
[77] V. G. Kravets, F. Wu, G. H. Auton, T. Yu, S. Imaizumi, and A. N. Grigorenko, "Measurements of electrically tunable refractive index of MoS_2 monolayer and its usage in optical modulators," *npj 2D Mater Appl*, vol. 3, no. 1, p. 36, Sep. 2019, doi: 10.1038/s41699-019-0119-1.
[78] T. F. Jaramillo, K. P. Jørgensen, J. Bonde, J. H. Nielsen, S. Horch, and I. Chorkendorff, "Identification of active edge sites for electrochemical H2 evolution from MoS_2 nanocatalysts," *Science*, vol. 317, no. 5834, pp. 100–102, Jul. 2007, doi: 10.1126/science.1141483.
[79] G. Li *et al.*, "All The Catalytic Active Sites of MoS_2 for Hydrogen Evolution," *J Am Chem Soc*, vol. 138, no. 51, pp. 16632–16638, Dec. 2016, doi: 10.1021/jacs.6b05940.
[80] J. Kibsgaard, Z. Chen, B. N. Reinecke, and T. F. Jaramillo, "Engineering the surface structure of MoS_2 to preferentially expose active edge sites for electrocatalysis," *Nat Mater*, vol. 11, no. 11, pp. 963–969, Nov. 2012, doi: 10.1038/nmat3439.
[81] J. Xu *et al.*, "Frenkel-defected monolayer MoS_2 catalysts for efficient hydrogen evolution," *Nat Commun*, vol. 13, no. 1, p. 2193, Apr. 2022, doi: 10.1038/s41467-022-29929-7.
[82] M.-S. Kang *et al.*, "Large-scale MoS_2 thin films with a chemically formed holey structure for enhanced Seebeck thermopower and their anisotropic properties," *J.*

Mater. Chem. A, vol. 8, no. 17, pp. 8669–8677, May 2020, doi: 10.1039/D0TA02629H.

[83] Y. Zhang *et al.*, "Photothermoelectric and photovoltaic effects both present in MoS_2," *Sci Rep*, vol. 5, no. 1, p. 7938, Jan. 2015, doi: 10.1038/srep07938.

[84] C. Wu *et al.*, "Exploring the photoelectric properties of 2D MoS_2 thin films grown by CVD," *Journal of Materials Research*, vol. 37, pp. 3470–3480, Oct. 2022, doi: 10.1557/s43578-022-00720-0.

[85] S. Parhizkar *et al.*, "Two-Dimensional Platinum Diselenide Waveguide-Integrated Infrared Photodetectors," *ACS Photonics*, vol. 9, no. 3, pp. 859–867, Mar. 2022, doi: 10.1021/acsphotonics.1c01517.

[86] S. H. Mir, V. K. Yadav, and J. K. Singh, "Recent Advances in the Carrier Mobility of Two-Dimensional Materials: A Theoretical Perspective," *ACS Omega*, vol. 5, no. 24, pp. 14203–14211, Jun. 2020, doi: 10.1021/acsomega.0c01676.

Chapter 2. Thermally-assisted conversion (TAC) and optical characterisation of TAC based MoS_2

2.1 Introduction

2.2 Thermally-assisted conversion

2.2.1 Static coloration using metal backing

2.3 Raman spectroscopy measurements

2.3.1 Patterned MoS_2

2.3.1.1 Raman measurements on MoS_2 directly on Si/SiO_2 region vs MoS_2 on Au

2.3.1.2 Raman and PL mapping of patterned MoS_2 monolayers and bilayers

2.3.1.3 Resonant Raman measurements using 633 nm laser

2.4 Optical measurements using spectroscopic ellipsometry (SE) and UV-Vis

2.5 SEM and AFM measurements

2.6 X-ray diffraction

2.7 Summary and conclusions

2.1 Introduction

Many techniques have been utilised for synthesising 2D thin films of transition metal dichalcogenides (TMDs). Following the evolution of graphene synthesis from graphene nanoparticles to thin films, synthesis of TMDs like MoS_2 has also undergone its own synthesis evolution from solution processed methods like liquid exfoliation [1], [2], liquid-liquid interfacial thin-film assembly [3], mechanical exfoliation [4] to vapour phase sulphurisation methods like chemical vapour deposition (CVD) [5], [6], [7], dry transfer using viscoelastic stamping [8] to bypass the use of any wet solvents to dissolve polymer supports, hot pick up and stamp [9], [10] technique and etch-free MoS_2 synthesis using PMMA [11]. Another method though less explored but holds massive potential in large scale synthesis of thin films goes by the names – vapour phase sulphurisation or thermal vapour sulphurisation or thermally assisted conversion (TAC) [12], [13], [14]. Here pre-deposited Mo film on a substrate is sulphurised by sulphur vapour flowing over it. In a way, this method of synthesis can be considered to be a modified version of CVD. Y. Zhan et al., have highlighted the scalability of this modified CVD method of synthesis by showing uniform deposition of atomically thin MoS_2 layers on a SiO_2 substrate [15]. The significance of this technique is proven when SiO_2 is etched away to obtain 0.8 cm^2 continuous MoS_2 showing the lateral area of the film to be dependent on the substrate's lateral size. They further relate the starting Mo thickness with MoS_2 obtained after sulphurisation, claiming the starting Mo thickness as a useful parameter to control the thickness of the MoS_2 layer obtained at the end. D. Kong et. al., synthesised edge-terminated MoS_2 using the same setup and a rapid sulphurisation process [16]. MoS_2 based large area ammonia sensors were also synthesized using this vapour phase sulphurisation which proves that this can be the preferred method of synthesis to achieve MoS_2 film integration in a device [17].

In this chapter, our in-house modified version of this CVD-like technique is introduced where metal evaporated films (of Mo in this work, but generally, other transition metals can also be used) are sulphurised in a quartz tube in the presence of forming gas and sulphur vapour. This was setup by previous owners (Niall McEvoy's group) of our lab that included Dr. Riley Gatensby who assembled this setup and got it operational. The same setup is used to make MoS_2 films in this work. The samples include MoS_2 films just by themselves on a substrate as well as multilayer stacks that include MoS_2 films as one of the layers. In this work, this method will be referred to as – thermally assisted conversion (TAC).

2.2 Thermally-assisted conversion

This section presents the details of our in-house TAC process. Other sample preparation techniques like CVD, ALD and magnetron sputtering were also used to synthesize certain sample stacks presented in this work (other chapters) but that was done to compare the performance of MoS_2 synthesised by those methods with the TAC based MoS_2. So, main emphasis is put on detailing the TAC process in this section which is capable of producing thin TMD layers. Due to the reasons of film homogeneity and process scalability, a process that can be employed at the semiconductor industry level and very similar to CVD process is chosen. Thus, TAC is explored in this work. It converts a transition metal to a transition metal dichalcogenide (TMD). Here, the transition metal layer is deposited on a substrate using sputtering or metal evaporation techniques and then chalcogenized in a controlled temperature and pressure environment in a furnace. ***Fig. 2.1*** shows the step-by-step process of TAC.

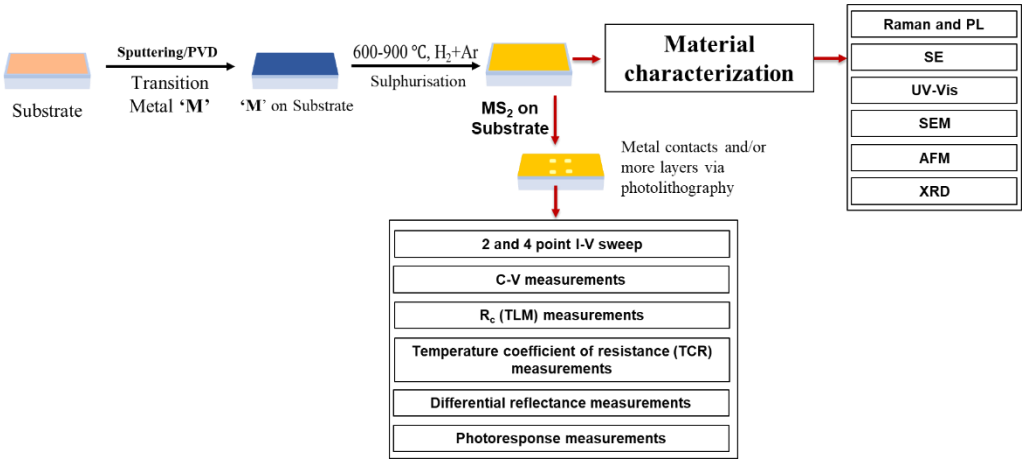

Fig. 2.1*: A schematic flow diagram of TAC process showing the steps of a transition metal (Mo) being chalcogenized (sulphurized) to form a transition metal dichalcogenide (MoS_2).*

In this process, the focus is on sulphides and especially Molybdenum Disulphide (MoS_2). All metal and dielectric depositions in this work were carried out using a tabletop magnetron sputtering tool capable of physical vapur deposition (PVD). The one used here was called the nano-PVD or nPVD system by Moorfield Nanotechnology Ltd., UK. Mo was deposited at 2% DC power and 5 sccm Ar flow rate in a vacuum chamber at a deposition pressure around the range 10^{-3} mbar and calibrated with a deposition rate of 0.03 nm/s. Calibration was done by depositing Mo for a long time around 600 s and then measuring under XRR and ellipsometry to confirm the thickness. Depositing Mo at 2% DC power and 5 sccm Ar in the nPVD sputtering tool for 600 s and 900 s resulted in around 18.4 nm and 28.4 nm

thick Mo films respectively confirmed by XRR. Deposition rate was thus calculated by dividing the measured thickness by the time of deposition which came out to be 0.03 nm/s. Room temperature was maintained during all metal depositions at the substrate holder plate. After having deposited the Mo metal on a suitable substrate, the sample placed on a ceramic boat which is then carefully inserted into the middle of the TAC furnace by sliding it using a long rod. Sulphur powder is kept alongside on a separate boat and the entire system is pumped down to 30 mTorr. At this point, no gas is flowing inside the tube and everything is around room temperature. Then the temperature is increased around 700-900 ℃ with Ar flowing in the tube. TAC process starts when the temperature at the sample boat reaches the set-point and a mixture of Hydrogen and Argon (Ar/H_2: 10%/90%) gas is made to flow inside the furnace that carries with it the sulphur molecules evaporated at the other end of the furnace. The heat generated by a halogen lamp around the sulphur boat sublimates the sulphur powder to sulphur vapour that flows towards the sample boat. This is pictorially represented in ***fig. 2.3(a)***. The melting point of sulphur is 112.8 ℃ and the halogen lamp provides enough heat for the sulphur powder to sublime. The sublimination temperature is measured via a thermocouple (TC-2) installed inside the sulphur boat and monitored from outside the setup. The actual in-house constructed setup is shown in ***fig. 2.2***. ***Fig. 2.2(a)*** shows the view from one end of the TAC setup showing a sulphur trap (S-trap) to protect the vacuum pump and the end of the tube (end-1) from where the sample boat is inserted. ***Fig. 2.2(b)*** shows the mid-section of the setup with the quartz tube passing through the benchtop furnace and its other end going through the halogen lamp. A thermocouple (TC-1) placed inside the furnace monitors and controls the temperature of the sample boat placed in the middle of the furnace. The sample is kept approximately in the common geometric centre of the tube and furnace shown in ***fig. 2.2(b)***. The furnace shown is open since it is at room temperature but lid is closed during the TAC process because a temperature of around 850℃ needs to be maintained in it. The last section of the setup is shown in ***fig. 2.2(c)*** which shows the placement of the halogen lamp near the other end (end-2) of the quartz tube. The sulphur boat is inserted from this end along with TC-2 readout cable.

Sulphurisation using TAC process produces thickness controlled, continuous, large area TMD thin films [12]. The large lateral area of the TMD depends on the area of the starting transition metal so wherever the transition metal is evaporated on the substrate, sulphurisation via TAC will convert the transition metal in that area to transition metal dichalcogenides.

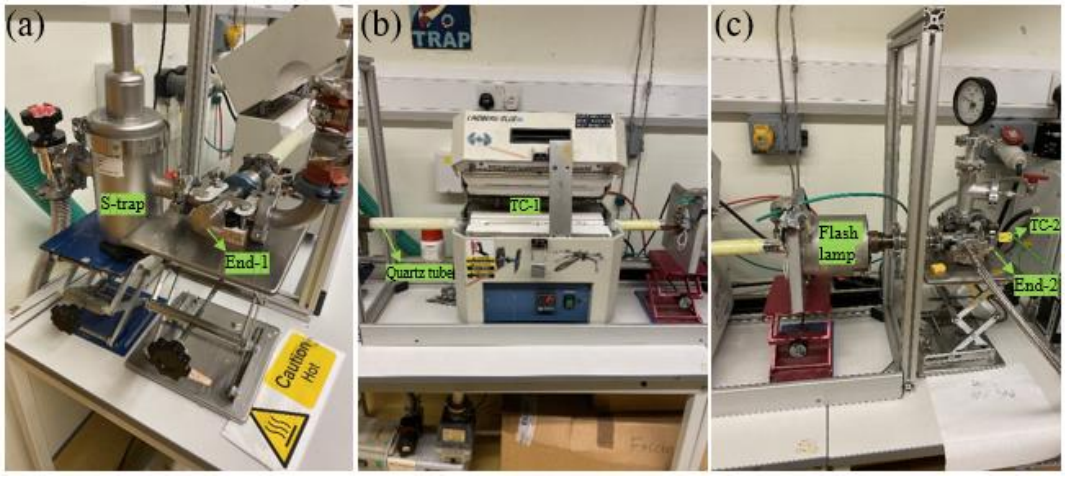

***Fig. 2.2**: **(a)** left hand-side section of the TAC setup showing S-trap and end-1 to insert the sample. **(b)** Mid-section of the setup showing the furnace and quartz tube passing through it where the sample boat is placed. **(c)** Right hand-side section of the setup showing halogen lamp to heat up the Sulphur boat, TC-2 and end-2.*

In the following sections, different samples will be referred to, which include TAC MoS_2 of different thicknesses, either by itself on a substrate or as a part of a stack with other layers. Some of these samples are restricted to just this chapter but some of them will also be discussed in other chapters. For convenience, **Table 2.1** lists all these samples including their synthesis details and most importantly a label to quickly identify them from this look up table whenever the sample name comes up in the chapter text.

***Table 2.1**: List of samples used in this chapter with details including stack structure, sulphurisation temperature and time*

Sample name	**Substrate**	**Stack structure**	**Starting Mo thickness (nm)**	**Starting Mo deposition time (s)**	**TAC temperature (℃)**	**TAC time (min)**
SC-A **SC-B** **SC-C** **SC-D** **SC-E**	Quartz	Substrate/MoS_2/ Au (100 nm)	1 2 3 4 5		750	30
SC-F **SC-G**	Quartz	Substrate/Au (100 nm) /Si_3N_4 (30 nm) /MoS_2		65 100	850	30
MoIDE17 **MoIDE21** **MoIDE30** **MoIDE60** **MoIDE120** **MoIDE150** **MoIDE200**	Si/SiO_2 (300nm)	Substrate/Ti (1 nm)/ Au IDEs (50 nm)/MoS_2		17 21 30 60 120 150 200	850	30
MoTLM150	Si/SiO_2 (300nm)	Substrate/MoS_2 (TLM bar) / Sn		150	750	30

		(10 nm)-Au (25 nm) TLM contacts				
A **B** **C**	Quartz	Substrate/MoS_2	1.5 1.3 0.8	57 46 30	850	30
Sample1	Si/SiO_2 (300nm)	Substrate/ HfO_2 (30 nm)/ MoS_2		30	750	5
Sample2	Quartz	Substrate/ Ti (1 nm)/Au (100 nm)/ HfO_2 (30 nm)/ MoS_2		21	750	5
Sample3 **Sample4**	Quartz	Substrate/MoS_2	3 10		750	40
Mod-A **Mod-B** **Mod-C**	Quartz	Substrate/ Ti (1 nm)/Au (100 nm)/ Si_3N_4 (30 nm)/ MoS_2		30 46 57	850	30
Sample5	Glass	Glass/ Indium Tin Oxide (185 nm) (commercially bought)				
Sample6	Sample5	Glass/ Indium Tin Oxide (185 nm)/MoS_2		35	750	30
Sample7	Sample5	Glass/ Indium Tin Oxide (185 nm)/Ti (0.5 nm)/ MoS_2		16	750	30
Sample8	Si_3N_4	Substrate/MoS_2		46	750	30
Sample9	Si_3N_4	Substrate/MoS_2		435	750	30
Sample10	Quartz	Substrate/MoS_2		46	750	30

It should be noted that in this table, TAC temperature and time varies across samples but other parameters like the pressure maintained inside the tube during TAC (~ 0.7 Torr), Ar/H_2 gas flow (150 sccm), sulphur furnace temperature (113℃) remain the same. Also, Mo deposition parameters inside the nano-PVD system remain the same to assume the same calibration for deposition rate. In reality, as the sputtering tool is used with time, it does not always deliver at its optimum capacity. Deposition rate of a sputtering target changes slightly due to deterioration of power over time which is supplied to the target. And so, the deposition rate must be calibrated regularly just as a procedural check. This is normal wear and tear of such tools and slight changes in the voltage, current and power to the sputtering target can bring about change in the amount of material being sputtered. Therefore, the samples used in this study had Mo sputtered with a deposition rate around 0.027-0.03 nm/s. For this reason, the thicknesses mentioned for Mo and/or MoS_2 in this thesis are approximated to a nearest value when relying purely on the calibrated deposition rate to calculate thickness. Since, thickness measurement was not performed at every stage of every stack, relying on the calibrated deposition rate is the easiest choice. And since the deposition rate did not

change much over time, Mo starting thickness can thus be used as a parameter to distinguish between different samples with confidence.

2.2.1 Static colouration using metal backing

A good example depicting the TAC process and ease of sulphurisation over a large area is shown in ***fig. 2.3(a)***. Here the transition metal, Mo was sputtered all over the 1 cm^2 quartz substrate and so after sulphurisation via TAC, MoS_2 is formed all over the area of the substrate. The reason of strong coloration in the samples ('SC-A to E' from tab. 2.1.) shown in ***fig. 2.3(b)*** is that MoS_2 is deposited on quartz (a transparent insulating substrate) and has Au metal coating on top of it. When the substrate is flipped over, what is viewed is the light passing through the quartz, interacting with MoS_2 and then reflected back from Au after it has changed its phase and path length. Therefore, what appears is coloured or tinted shades ranging from pale yellow, pink and blue depending upon the MoS_2 thickness as depicted in ***fig. 2.3(b)***. This coloration which is a function of MoS_2 thickness and occurs without using any active control or external stimulus is thus referred to as 'static coloration' in this work. It is also a good example which demonstrates film thickness control because the difference in the colour and shade among the samples shown depict the different starting thicknesses of the transition metal (Mo).

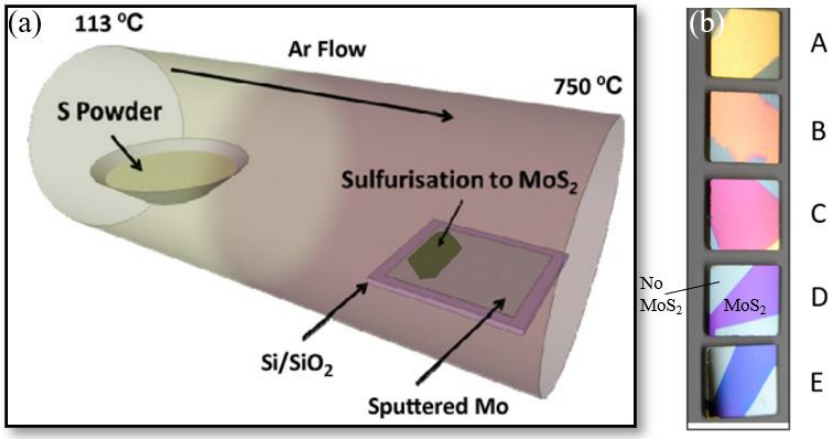

***Fig. 2.3**: **(a)** TAC process inside the closed furnace. The melting point of Sulphur is 112.8 °C therefore the halogen lamp provides sufficient heat for the Sulphur to evaporate which is carried towards the sample placed in the vicinity forming gas. **(b)** MoS_2 samples (samples 'SC-A to E' from tab. 2.1.) of different thicknesses showing coloration that is dependent on the thickness of starting metal (Mo). Here, samples A, B, C and D are shown with thicknesses 1 nm, 2 nm, 3 nm, 4 nm and 5 nm respectively.*

Sample A with a yellow tint is the thinnest MoS_2 since the Mo starting thickness was around 1 nm while sample E that shows deep blue colour had a 5 nm Mo deposited first which was then sulphurised to form around 17-layer thick MoS_2.

Another notable observation is around the corners of the substrate where the sample was taped off using Kapton tape for the metal depositions. Metal is only deposited in the areas with no Kapton tape and therefore colouration is observed only for those regions on the substrate that are backed by metal i.e., the middle regions of the substrate. Therefore, it becomes easier to observe this colouration due to the optical interference caused by metal backing, thus highlighting the regions with MoS_2 (seen as different colours and shades as mentioned previously) on quartz leaving out the corners because Kapton tape prevented the metal to be deposited in those regions and are clearly demarked from the MoS_2 regions.

Static colouration can also be achieved in patterned stacks as shown in ***fig. 2.4(c), (d)***. For reference, the same five samples ('SC-A to E' from tab. 2.1.) are shown in ***fig. 2.4(a)*** again with quartz substrate and varying starting Mo thicknesses along with their corresponding number of layers of MoS_2 obtained after the TAC. As mentioned previously, these samples show distinct colours according to their thickness i.e., number of layers and occurs due to optical interference between the TAC MoS_2 and Au deposited on them. Since these patterned layers (using photolithography) are deposited on a quartz substrate, the samples are also flipped and observed from the back side depicted in ***fig. 2.4(b)*** to observe the colouration due to interference.

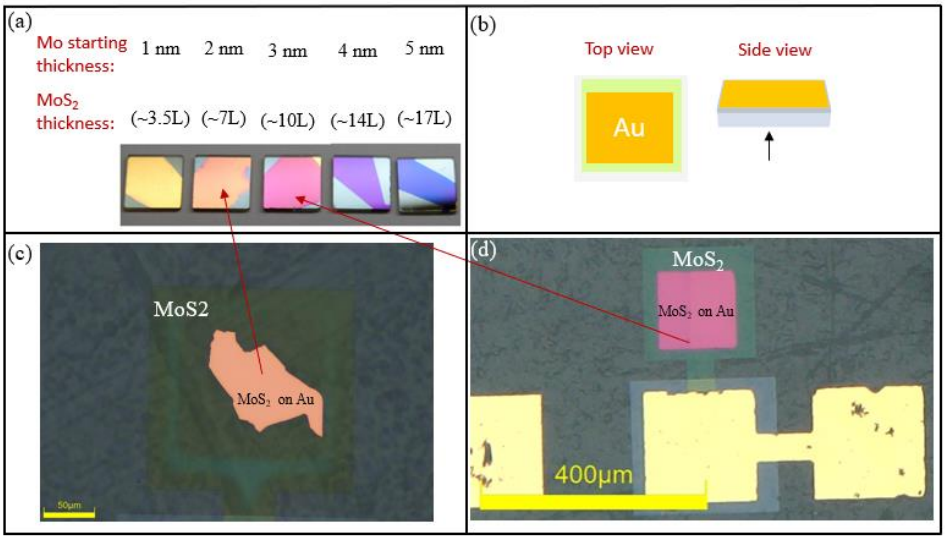

***Fig. 2.4**: **(a)** Samples with varying thicknesses backed by gold. **(b)** descriptive image of the samples in **(a)** showing top view and side view. The arrow shows the direction from which the sample is viewed when flipped. Similar design implemented in patterned samples viewed through quartz after flipping for **(c)** SC-F and **(d)** SC-G.*

Once again, in this case as well, the flipped side of the quartz substrate allows us to view MoS_2 on Au through it i.e., light passes through the quartz layer first, then MoS_2 and then experiences the MoS_2/Au interface and bounces back from Au coming out to show the static coloration phenomenon. Images were taken with the samples being flipped and showing static colouration while also proving successful MoS_2 deposition in a patterned area along with the desired optical interference caused by Au on it. The MoS_2 shown in ***fig. 2.4(c)*** (sample 'SC-F' from tab. 2.1.) got uniformly deposited on the photolithographically patterned square pad with initial Mo layer but the Au layer on top of it was not lifted off properly and so the colouration caused by the interference of the two layers is seen as an arbitrary shape consistent with the region where Au stayed after lift-off. Nonetheless, when compared with ***fig. 2.4(a)***, it matches the colour corresponding to 7L. In ***fig. 2.4(d)*** (sample 'SC-G' from tab. 2.1.), both the consecutive processes – 1) MoS_2 deposition using TAC followed by 2) Au lift-off – were done successfully and a clean patterned region was obtained. Here, the colour matches with 10L sample shown in ***fig. 2.4(a)***.

2.3 Raman spectroscopy measurements

Raman spectroscopy determines the chemical fingerprint of a material by measuring change in its vibrational state as a response to incoming monochromatic light. While most of the incident light scatters elastically from an atom, a tiny proportion of it on the other hand, undergoes inelastic scattering thereby placing the specimen's atoms in a new vibrational state. To preserve the total energy of the system consisting of incoming photon and specimen's atomic vibrations, the inelastically scattered photons thus acquire or lose energy which is probed in the form of its shift in frequency, wavelength or wavenumber in Raman spectroscopy measurements. This is represented as scattering intensity (counts) as a function of change in wavenumber (cm^{-1}) also known as a 'Raman spectrum'. Every material has certain vibrational modes which are different on surface than its bulk and this makes Raman spectroscopy highly surface sensitive as well. This is because Raman laser interacts with atomic vibrations (phonons) which are different on surface due to symmetry breaking and change in atomic arrangement compared to bulk. While in bulk, it can be visualized that atoms have satisfied bonds in all directions but on the surface, termination of bonds occurs due to symmetry breaking and so phonon activity also changes. In fact, Raman spectroscopy is an excellent method to carry out in-depth experimental study on electron-phonon

interaction and mobility-limiting property of phonons [18]. Additionally, phonons also determine thermal conductivity [19] and mechanical strength [20].

Raman spectroscopy in this work was performed using Witec Alpha 300R confocal Raman microscope with integrated 532 nm and 632 nm laser lines. Grating of 1800 lines/mm was chosen for Raman measurements.

The Raman spectra of TAC based MoS_2 samples with varying thicknesses is shown in ***fig. 2.5*** and ***fig. 2.6***. The ones in ***fig. 2.5*** were deposited on 50 nm Au inter-digitated electrode (IDEs), with inter-electrode spacing of the order of μm range and are from the sample group 'MoIDE17-MoIDE150' in tab. 2.1. Given the significant inter-electrode spacing between the IDEs, MoS_2 thus deposited as the last layer gets to be on top of Au IDEs as well as the inter-electrode region between IDEs i.e., directly on the substrate. So, the Raman spectra of the 6 MoS_2 samples (corresponding to Mo deposition time varying from 17s to 150s) shown in ***fig. 2.5(a)*** were taken from the interelectrode spacing regions or 'MoS_2 on substrate' region i.e., from the region in between the IDEs. A comparison of Raman spectra from the two regions will be discussed in ***sec. 2.3.1.1***. And the samples in ***fig. 2.6*** were deposited directly on Si/SiO_2 substrate and are from the sample group 'A-C' in tab. 2.1. For these Raman spectroscopy measurements, a laser source of 532 nm was used. The deposition time has been used as a parameter to distinguish between the samples, their spectra and qualtitatively characterize the samples in ***fig. 2.5(a)***. This is because the higher the deposition time, the higher is the starting Mo thickness as per the calibration calculations discussed in ***sec. 2.2*** and therefore higher is the MoS_2 thickness.

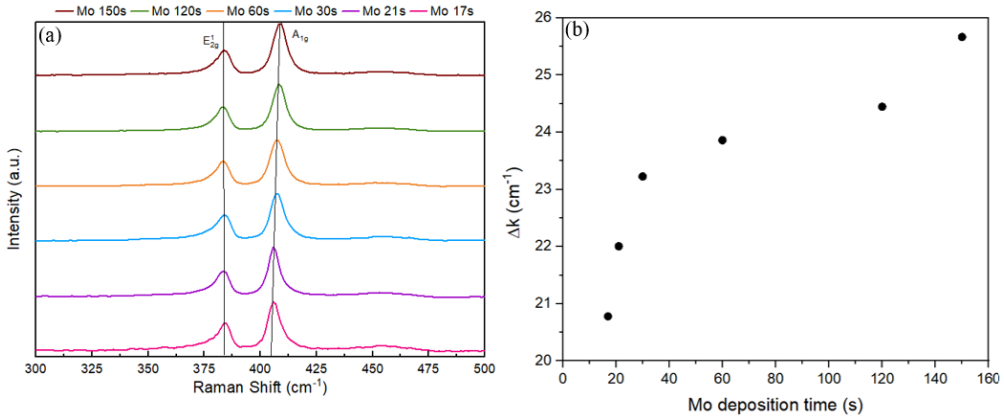

Fig. 2.5*: **(a)** Raman spectra of MoS_2 samples ('MoIDE17-MoIDE150' from tab. 2.1) formed from varying starting Mo deposition times on Si/SiO_2 **(b)** Difference between A_{1g} and E^1_{2g} peak positions from **(a)** plotted against Mo deposition time.*

Fig. 2.5(a) shows the two characteristic peaks of MoS_2 (marked by E^1_{2g} and A_{1g}) used to quickly identify the material. E^1_{2g} peak represents in-plane vibrations while A_{1g} represents out-of-plane vibrations. So, a high ratio of intensities of E^1_{2g} and A_{1g} peaks shows the extent to which the deposited MoS_2 layers are in-plane.

The evolution of the A_{1g} peak slightly drifting away from the E^1_{2g} peak signifies increase in MoS_2 thickness because the greater the difference (marked by Δk) between them, the thicker the MoS_2 film is. ***Fig. 2.5(b)*** shows this variation by plotting Δk as a function of increasing starting Mo deposition time. Raman spectroscopy here can be only used to characterize thickness of MoS_2 qualitatively and should not be used to quantify thickness because not all TAC based MoS_2 few-layer films are oriented in the same plane. Different modes (peaks) are enhanced when using different excitation light energies and UV enhances certain second order and inactive modes in 2D TMDs like B^1_{2g} because of its lower penetration depth in the material [21], [22], [23]. This gives more insight into the phonon activity in such materials and link between phonons and electronic structure of the material. The E^1_{2g} and A_{1g} peaks can be identified easily in the Raman spectra shown in ***fig. 2.5(a)*** and compares well with literature based on large lateral area synthesis of MoS_2 [24], [25]. The values of the peak locations match with the 'bulk' values mentioned in [21] which correspond to few-layer MoS_2 films of thickness more than 4 layers which is the case in this project. Therefore, these films are thin enough to be called 2D but are not atomically thin. Monolayer MoS_2 has also been produced in this work which will be discussed later.

A closer look reveals this slight drifting of A_{1g} peak from E^1_{2g} peak as plotted in ***fig. 2.6***. These TAC based MoS_2 films referred to as 'A', 'B' and 'C' in tab. 2.1 were deposited directly on a quartz substrate with starting Mo thickness of 1.5 nm, 1.3 nm and 0.8 nm respectively, (calculations based on calibration discussed previously and thickness measured by AFM and ellipsometry). A_{1g} peak of each of these measured samples was fit using a pseudo-Voight function to precisely obtain its position on the x-axis i.e., the Raman shift (cm^{-1}). The difference between the two characteristic peaks of MoS_2 i.e., $A_{1g} - E^1_{2g}$ depicted by 'Δk' relates to the thickness of MoS_2 films. As marked by dashed vertical lines in ***fig. 2.6***, the peak position of E^1_{2g} peak remains constant across the three thicknesses of the measured Raman spectra while A_{1g} peak undergoes a slight shift.

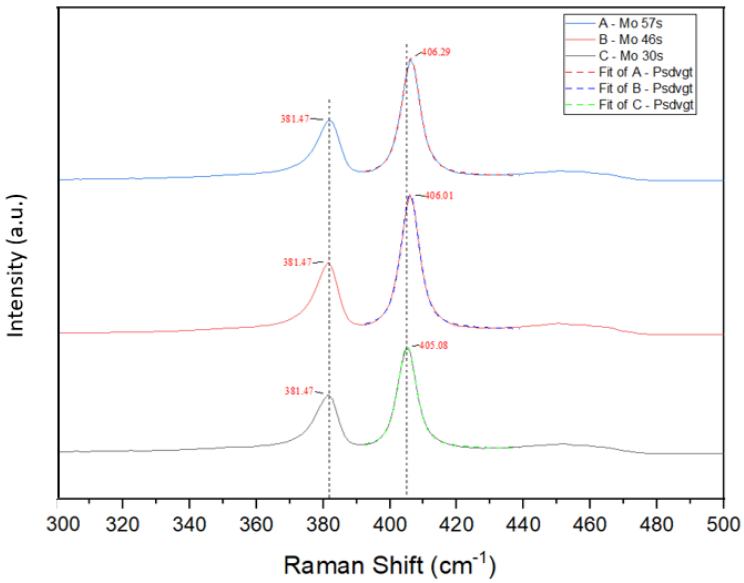

***Fig. 2.6**: Few-layer TAC based MoS_2 films showing slight deviation of the A_{1g} peak with increasing thickness.*

Assuming the peak positions marked by dashed lines for 'C' sample as reference, the A_{1g} peaks of both sample 'A' and 'B' are slightly shifted from it indicating increasing thickness of the samples. Apart from the peak positions, peak intensity ratios and FWHM also provide significant information about the deposited MoS_2 film. While peak ratio hints at the orientation of the grown MoS_2 film [26], [27], FWHM of the peaks indicates atomic order in their layers [28]. E^1_{2g} peak relates to in-plane vibrations of the MoS_2 molecules while A_{1g} peak is associated with their out-of-plane motion. So, the ratio of the intensities of the two peaks signifies which motion dominates the other or whether they are equal in which case the ratio is 1.

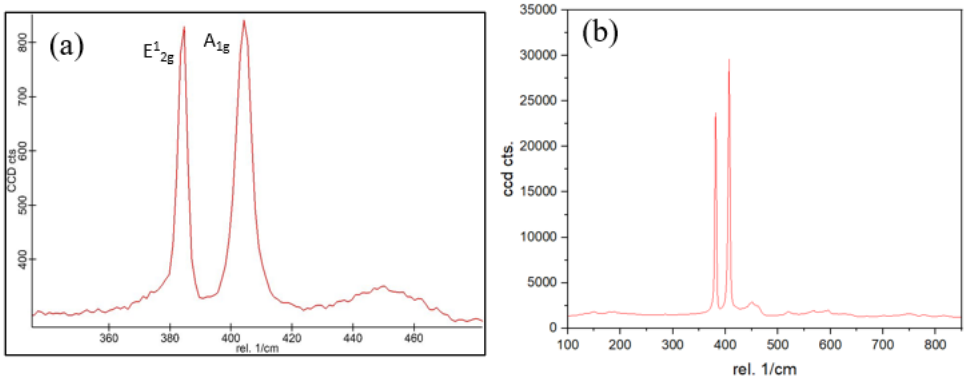

***Fig. 2.7**: MoS_2 prepared by (a) CVD and (b) Hot pick-up and stamp technique.*

Generally, this ratio equals to or tends to 1 for MoS_2 prepared by the CVD technique and hot-pickup-stamp technique. CVD MoS_2 was prepared in our furnace by Dr. Niall McEvoy's group and MoS_2 prepared using the hot pick-up technique was acquired from our collaborators – Dr. Jose Caridad's group in University of Salamanca, Spain. And then I performed Raman spectroscopy on them, results for which are shown in ***fig. 2.7(a), (b)*** respectively. These data sets are good for comparing with Raman results of TAC MoS_2.

The narrower the peaks are, the more pristine and ordered the deposited MoS_2 is and FWHM of the peaks quantifies this parameter. In the spectra shown in ***fig. 2.7***, it was observed that MoS_2 prepared by CVD has intensity of E^1_{2g} peak to be almost equal to that of A_{1g} but comparatively broader FWHM compared to MoS_2 prepared by hot pick-up and stamp technique while E^1_{2g} peak is slightly lower in intensity than the A_{1g} peak in this case.

2.3.1 Patterned MoS_2

Drawing attention back to TAC based MoS_2, the following results were obtained from patterned (using photolithography) TAC based MoS_2 samples measured under the 532 nm laser. 3 designs will be discussed here. Firstly, TAC MoS_2 was deposited on 50 nm thick Au source-drain (S-D) interdigitated electrodes (IDEs). This design will be explained in detail in chapter 3, sec. 3.2.2 ***(3-3.2.2)***. Si/SiO_2 substrate prepatterned with Au S-D IDEs was used for this sample and since MoS_2 was deposited over each IDE set (as per the design explained in detail in ***3-3.2.2***), there were regions with MoS_2 deposited directly on Si/SiO_2 and on Au IDEs. Raman measurements were carried out on both these regions. Note that a thin (~ 1 nm) film of Ti was deposited beneath Au to increase its adhesion with the substrate. Secondly, measurement was carried out for MoS_2 patterned as 5 µm wide bar using TAC on HfO_2 (30 nm) coated Si/ 300 nm SiO_2 substrate shown in ***fig. 2.9*** (top-left image). This is referred to as 'sample 1' in tab. 2.1. The pattern was obtained by utilizing standard photolithography processes and depositing the starting metal (Mo) followed by its sulphurisation. After sulphurisation, MoS_2 formed at sites where Mo was present i.e., the initial patterned bar of Mo became bar of MoS_2. Lastly TAC MoS_2 was deposited with the same methodology on top of patterned Au and HfO_2 (using photolithography). This is referred to as 'sample 2'in tab. 2.1. In this design, Au was patterned on quartz substrate as two square pads and a horizontal bar connecting the two for continuity and HfO_2 was patterned as another square pad on top of one of the Au pads. MoS_2 was included in this 3-

layer stack as the topmost layer. It overlaps the Au/ HfO_2 area and extends out perpendicular to the Au pattern. This stack is represented as: MoS_2/ HfO_2/Au/quartz and is shown in ***fig. 2.9*** (bottom-left image). This structure will be explained in detail in chapter 4 due to its use in active modulation of light but here this stack is simply characterized to show continuity and uniformity of TAC based MoS_2 prepared at high temperatures like 750℃ without causing damage to underlying layers – L1 and L2. This stack was measured under the same conditions as the one shown in ***fig. 2.9*** (top-left image).

2.3.1.1 Raman measurements on MoS_2 directly on Si/SiO_2 region vs on Au

Considering the sample with IDEs (MoIDE21 from tab. 2.1), as mentioned previously, there are regions where MoS_2 has Au directly beneath it and there are adjacent regions where MoS_2 has the substrate (Si/SiO_2) below it. Raman laser spot was first focussed on the region of MoS_2 with Au electrode beneath it and then on the region of MoS_2 lying directly on Si/SiO_2 substrate. The corresponding spectra for both the regions are shown in ***fig. 2.8(a)***, ***(b)*** respectively. The Raman spectrum corresponding to MoS_2 directly on the Si/SiO_2 substrate (***fig. 2.8 (b)***) is smoother and less noisy compared to the spectrum from MoS_2 on Au/Si/SiO_2 (***fig. 2.8(a)***).

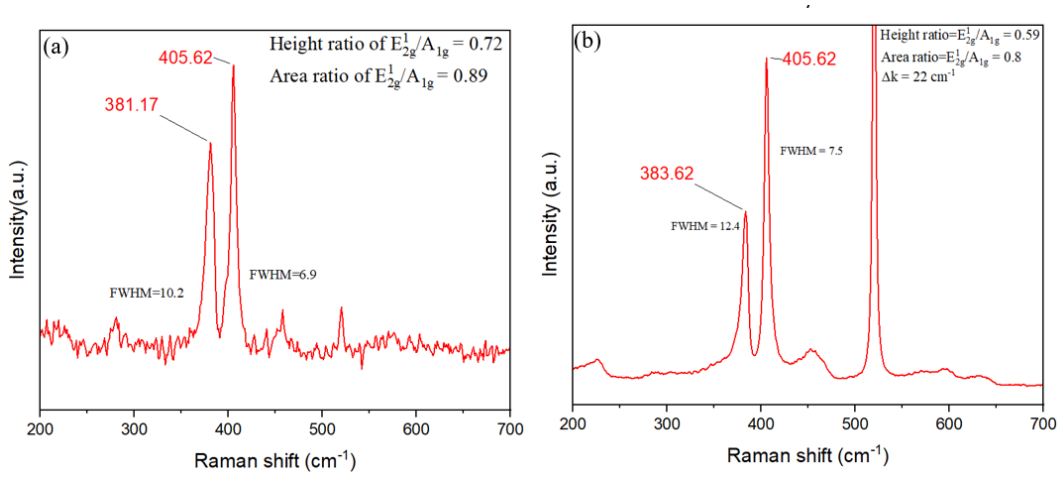

Fig. 2.8*: Raman single spectrum of 'MoIDE21' taken from* ***(a)*** *MoS_2 on Au (IDE) region and* ***(b)*** *MoS_2 on Si/SiO_2*

Both cases show the two characteristic peaks of MoS_2. The peak around 520 cm^{-1} corresponds to Si and so it is more prominent in the case where MoS_2 is deposited directly on Si/SiO_2 as seen in ***fig. 2.8(b)***. This peak reduces in the case where MoS_2 is deposited on the Au region as seen in ***fig. 2.8(a)***. There are some more differences in the two spectra in

terms of the FWHMs of each peak, peak intensity ratios and area ratios. The E^1_{2g} peak FWHM change is around 21.5% and A_{1g} peak FWHM change is around 8.7% which goes to show that MoS_2 on Au is more ordered and has better crystalline quality than when deposited directly on Si/SiO_2. Additionally, the relative difference in the heights of the two peaks also changes slightly when MoS_2 on Au is compared with MoS_2 directly on Si/SiO_2. Taking ratio of the peak intensities ($I_{E^1_{2g}}/I_{A_{1g}}$) as the measure of relative difference in peak heights in both the cases, it can be observed that in the case of MoS_2 directly on Si/SiO_2, E^1_{2g} peak is much smaller as compared to the E^1_{2g} peak in the case of MoS_2 on Au in reference to their respective A_{1g} peaks. Therefore, the intensity ratio in MoS_2 on Au is higher than that of MoS_2 on Si/SiO2. This hints at possibly more in-plane oriented deposition of MoS_2 on Au and less in-plane deposition of MoS_2 on Si/SiO_2.

2.3.1.2 Raman and PL mapping of patterned MoS_2 monolayers and bilayers

The results shown in ***fig. 2.8*** are for patterned MoS_2 of a large lateral area (4 mm^2) on top of Au IDEs. ***Fig. 3.8(a)*** shows the top view of this design and as mentioned earlier more details of this are mentioned in chapter 3, sec. 3.2.2 ***(3-3.2.2)***. But using photolithography to pattern TAC MoS_2 as a thin bar of width 5 µm was successfully implemented as shown in the microscopic image in ***fig. 2.9***. Its corresponding Raman spectrum is also shown and is represented by 'Sample 1' in ***fig. 2.9***.

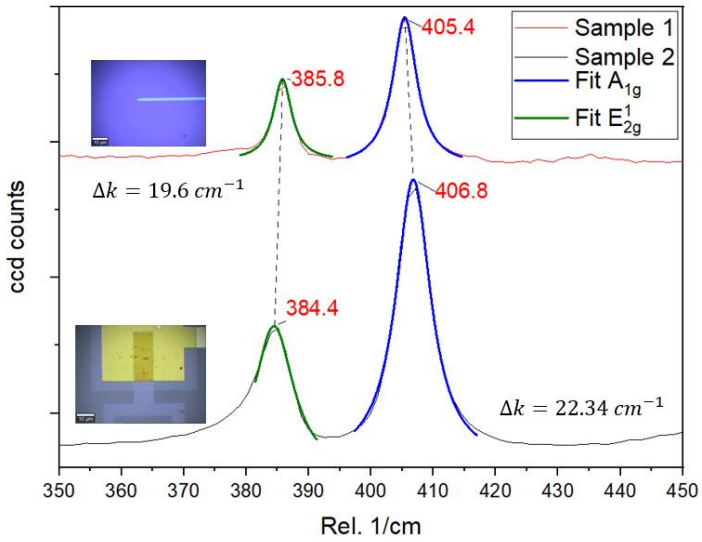

Fig. 2.9*: Raman single spectrum taken from* ***(a)*** *MoS_2 patterned as 5 µm wide bar on HfO_2 coated Si/SiO_2 substrate ('sample 1 from tab. 2.1') and* ***(b)*** *MoS_2 patterned as 50 µm wide box on HfO_2/Au on quartz ('sample 2 from tab. 2.1').*

Moreover, TAC based MoS_2 can also be patterned as a part of a multilayer stack without getting damaged itself or damaging other layers during the multi-step lithography processes that require spinning of photoresist and lift-off (corresponding spectrum represented by 'Sample 2' in ***fig. 2.9***). The single spectrum in 'sample 2' is taken from the spot marked by the red cross which is the region with all three layers overlapping: MoS_2/ HfO_2/Au on quartz substrate and is 50 µm wide. The difference in the two characteristic peaks, Δk is 19.6 cm^{-1} and 22.34 cm^{-1} for 'sample 1' and 'sample 2' respectively.

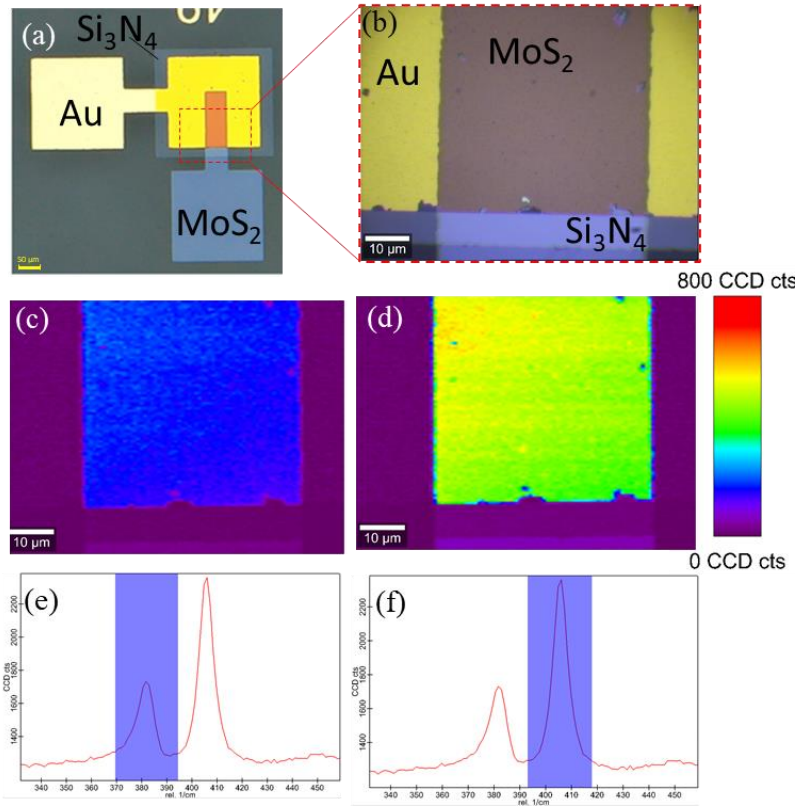

***Fig. 2.10**: **(a)** Optical image of a representative sample 'Mod-C' based on the same stack design as used in 'sample 2'. Orange region is the active area: MoS_2/Si_3N_4/Au. **(b)** Zoomed-in optical image of a section of the active area from a similar sample based on the stack design explained in **(a)**. **(c), (d)** Raman maps of the region shown in **(b)** maximised at the E^1_{2g} and A_{1g} peak positions depicted in **(e)** and **(f)** respectively.*

To investigate the stack structure introduced in sample 2 further, Raman mapping was done on the same design but a different stack having MoS_2 of thickness ~4 nm (measured by AFM). ***Fig. 2.10(a)*** shows one such stack with three layers. Layer 1 (L1) is 100 nm Au comprising of two square pads connected with a horizontal strip, layer 2 (L2) is a 30 nm Si_3N_4 square pad slightly bigger than the Au square pads and covering one of the Au pads entirely (right pad is covered by Si_3N_4 shown in ***fig. 2.10(a)***) and finally layer 3 (L3) of

MoS_2 consisting of a vertical bar shape (orange colour) on the middle of Au/Si_3N_4 square pad and extending out as a square pad in the bottom.

The image shown in ***fig. 2.10(a)*** is a zoomed-out image of how every device looks when this stack design is implemented using either of the photolithographic tools – Suss Mask aligner or Heidelberg direct writing. The latter gives cleaner edges though. Focussing on the orange active area (i.e., the area formed by intersection of the three layers) of the device, red dashed box in ***fig. 2.10(a)***, marks the area selected for Raman mapping. A zoomed-in optical image of this region in the device measured under Raman spectroscopy tool is shown in ***fig. 2.10(b)***, it was observed through Raman mapping of the focussed area (μm^2 range) that MoS_2 deposited via TAC in the overlapping regions of underlying Au and Si_3N_4 was continuous and uniform across the entire active area. This occurs clearly in the overlapping area i.e., the area of all 3 layers (Au, Si_3N_4, MoS_2) overlapping. Any area beyond this overlapping area does not contain one of the 3 layers and results in a height difference relative to the overlapping area which is being probed. As a result, no signal comes out of those areas because the laser is focussed to probe the signal from the height corresponding to the overlapping area of the 3 layers and anything beyond this goes out of focus for the laser spot.

This is observed in ***fig. 2.10(c), (d)*** which show the Raman maps of the area shown in ***fig. 2.10(b)*** maximised for intensity at E^1_{2g} (***fig. 2.10(e)***) and A_{1g} peak (***fig. 2.10(f)***) respectively. This maximisation at each peak is shown as blue boxes spanning a range of wavenumbers across the two characteristic peaks. The uniform colour in both cases (***fig. 2.10(c), (d)***) indicates uniform quality of MoS_2 across the entire area. As expected, the surrounding areas do not show any Raman signal indicating deposition of MoS_2 is only in the patterned region. 'Sample 1' was introduced in ***fig. 2.9***, and it showed Δk equal to 19.6 cm^{-1} indicating a monolayer of MoS_2 deposited as a 5 µm wide bar on Si/SiO_2 substrate covered entirely with 30 nm of HfO_2. A clearer and larger optical image of this is shown in ***fig. 2.11(a)*** while ***fig. 2.11(b)*** shows photoluminescence (PL) map of a portion of this MoS_2 bar marked by a red dashed box in ***fig. 2.11(a)***. A reference PL single spectrum measured at a random point on the MoS_2 bar is shown in ***fig. 2.11(c)*** and the PL map in ***fig. 2.11(b)*** is obtained by choosing to plot the maximum intensity of PL signal coming from the 1.9 eV peak to map out the PL intensity along the MoS_2 strip associated with only this peak.

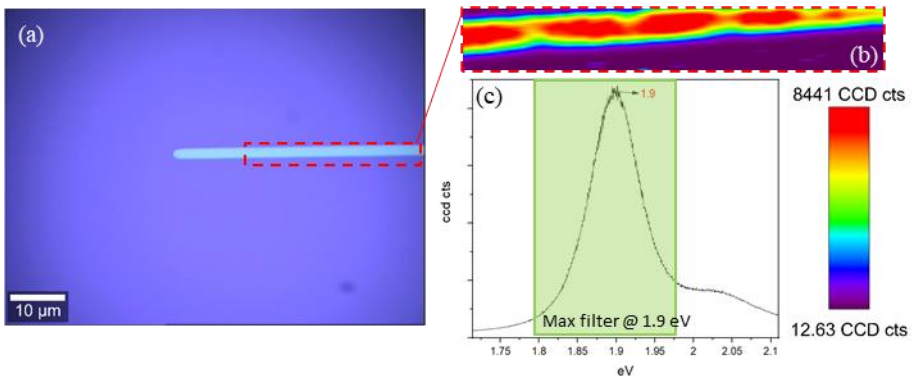

***Fig. 2.11**: **(a)** 5 µm wide bar of MoS_2/HfO_2 'sample 1 from tab. 2.1' on Si/SiO_2. **(b)** Corresponding uniform PL map maximised at PL peak around 1.9 eV. **(c)** Single spectrum from the bar showing a PL signal.*

It can be observed from the colour bar that the CCD counts are highest (red colour) along the middle part of the length of the bar and PL signal fades out towards the edges going down to the lowest number of counts (purple colour) for the regions corresponding to the substrate where MoS_2 is not present. A single PL spectrum was also taken for 'sample 2' described earlier and shown again (***fig. 2.12(a)***) with more clarity along with the red cross mark showing the point of measurement. The PL spectrum plotted in ***fig. 2.12(b)*** matches well with previous studies in literature [13], [24], [29].

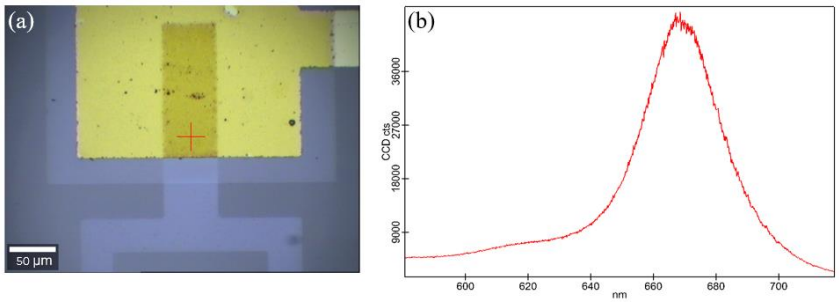

***Fig. 2.12**: **(a)** $MoS_2/HfO_2/Au$ 'sample 2 from tab. 2.1' multilayer stack with red cross marking the spot from where PL single spectrum is collected. **(b)** Plot of the corresponding PL single spectrum.*

Raman and PL mapping on both 'sample 1' and 'sample 2' prove that TAC is capable of producing monolayers and bilayers with large area film uniformity and continuity.

2.3.1.3 Resonant Raman measurements using 633 nm laser

While Raman measurement using 532 nm laser line reveals the thickness, orientation (edge enriched or in-plane layers) and atomic order in the deposited MoS_2, using 633 nm laser line

on the other hand reveals many other peaks in the spectrum not present with the 532 nm laser excitation. This is because 633 nm coincides with the band gap of MoS_2 and causes resonant Raman scattering [30], [31], [32], [33], thus revealing many other peaks. These peaks provide a greater insight into the electronic transitions at other symmetry points of the Brillouin zone in MoS_2 [34] and help in identifying defects [35].

To investigate TAC based MoS_2 further, it was also characterised under the Raman spectroscopy tool utilising the 633 nm laser line. 3 samples of varying thicknesses were measured. Their respective starting Mo deposition time serves as a qualitative parameter to distinguish between their thicknesses as well as their label to identify them. They are therefore marked as 'Mo 30s', 'Mo 46s' and 'Mo 57s' in ***fig. 2.13*** and referred to as 'Mod-A', 'Mod-B', 'Mod-C' respectively in tab. 2.1.

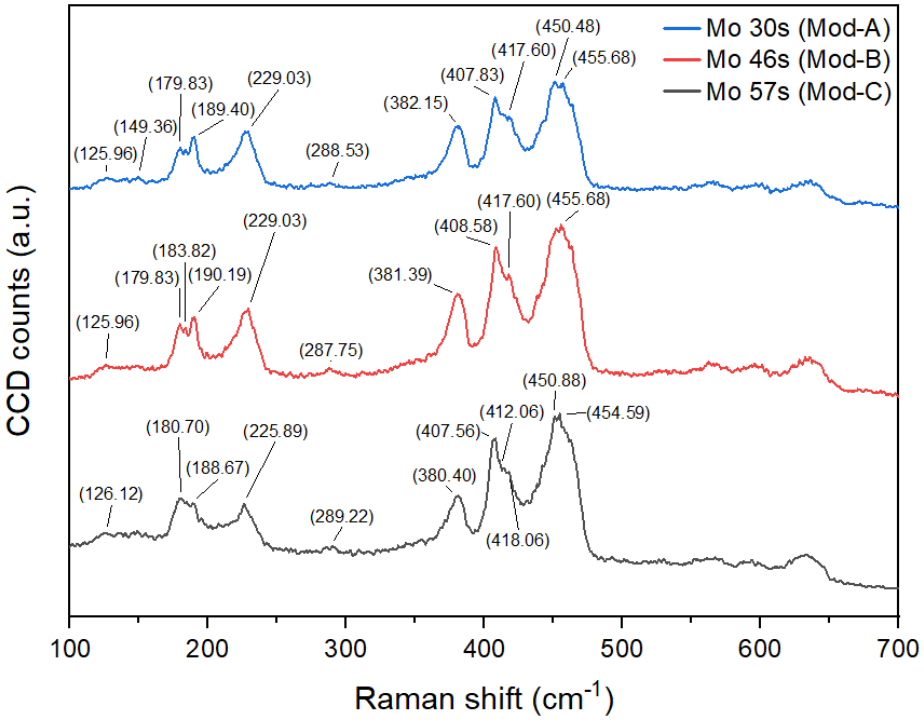

***Fig. 2.13*:** Raman spectra of varying thicknesses of TAC based MoS_2 under 633 nm laser line.

Apart from the characteristic peaks, many second order phonon scattering peaks and defect peaks (~180 cm^{-1}, ~229 cm^{-1}) can be seen. The occurrence of different phases (due to different synthesis methods) is called polytypism and has been widely reported in MoS_2 in the past [36], [37]. However, it is difficult to determine the phase from this data. The closest analysis was done by analysing Davydov splitting of the second characteristic peak ~407 cm^{-1}, which is a superposition of many other shoulder peaks. So, it will be referred to as 'A-

like peak'. W. Na et al., have shown that Davydov splitting of this peak depends on the stacking type [38]. By matching with their spectra that correspond to 2H, 3R and mixed phase MoS_2 samples, it seems that spectra presented in ***fig. 2.13***, hints at 3R or mixed phase of MoS_2. This is because the higher frequency side of the A-like peak has shoulder peaks while the lower frequency side of this peak is smooth. A further validation of this could have been obtained by analysing low frequency Raman spectrum which was unsuccessful in this case despite of obtaining a spectrum. This was because of the limited resolution of the tool used. The Raman spectra obtained for the MoS_2 samples of different thicknesses match well with previously reported studies [23], [38], [29], [33], [39]. The shoulder at the A-like peak has been assigned to a Raman inactive mode B_{1u} and the broad peak around 440 cm^{-1} is known to be due to formation of oxysulphide species [18] due to oxygen adsorption at MoS_2 edge sites which is supported by Raman measurements from 532 nm laser that showed a higher out-of-plane orientation of MoS_2.

2.4 Optical measurements using spectroscopic ellipsometry (SE) and UV-Vis

Spectroscopic Ellipsometry (SE) is a non-invasive and surface sensitive optical technique that is used to mainly deduce optical properties like complex refractive index ('n', 'k') and dielectric permittivity (ε). It requires linearly polarized light to be incident on the specimen and due to light-matter interaction, the amplitude and phase of the 's' and 'p' components of the linearly polarized incident light change with respect to each other thereby giving out an elliptically polarized light that hits the detector. These changes are recorded in the form of amplitude ratio (Ψ) and phase difference (Δ) of the 's' and 'p' components of the detected light. Ψ and Δ are measured as a function of light energy (the range varies with the instrument model) and a suitable model that associates optical parameters like **ε** with Ψ and Δ is used to fit the experimental data by varying the coefficients in the selected model and thickness of the specimen until a lowest mean squared error (MSE) is achieved. This results in a complex dielectric function that is further used to derive the complex refractive index from the model using Kramers-Kronig (KK) dispersion relations [40].

KK relations are a type of complex analytic functions that relate the real part of the function to its imaginary part. So, from SE measurements, once the imaginary part of complex dielectric function that relates to the absorption in a material is measured, it can be used to calculate the real part of the complex dielectric function that relates to refractive index. In

fact, change in the real part of refractive index Δn near absorption edge of a material i.e., the region in electromagnetic spectrum where the absorption (α) of a material changes rapidly, can be calculated by applying the KK dispersion relations from SE measurements which relates Δn with Δα. This has been previously shown for GaAs and GaInAs-InP material systems [41], [42] as well as monolayer and bulk MoS_2 [43]. This makes SE an extremely useful tool to calculate optical properties of a material directly. Ellipsometry can also be used for layer resolved determination of dielectric function of multilayers by fitting a suitable model for each of them. Therefore, this is a good technique to estimate thickness, surface roughness and uniformity of thin films. In this work, J.A Woollam Alpha SE system is used which allows to adjust to four angles of incidence: 60°, 70°, 75° and 90°. It uses a broadband linearly polarised light and quartz tungsten halogen lamp as the light source allowing wavelength range of 400 nm to 900 nm.

Non-destructive optical measurements like UV-Vis were also performed on TAC based MoS_2 by my colleague Dr. Evan Roy. Reflectance (%) was obtained via UV-Vis (Perkin Elmer LAMBDA 1050 UV/VIS/NIR) for two samples - 7 nm and 23 nm thick TAC based MoS_2 on quartz and is shown in ***fig. 2.14(a)***. They both clearly show excitonic dips in the visible range of the electromagnetic spectra. On the other hand, the added advantage with ellipsometry is that it is a layer resolved technique meaning that it can analyse multilayers in a stack separately from each other as discussed before. Here, a 4 nm TAC based MoS_2 sample was measured under a variable angle ellipsometer and the data was modelled on *CompleteEASE* - an integrated software with SE tool. The estimated thickness came out to be ~4.6 nm and extracted 'n' and 'k' spectra as shown in ***fig. 2.14(b)***. It also shows the positions of A and B excitons to be around 681 nm and 630 nm respectively.

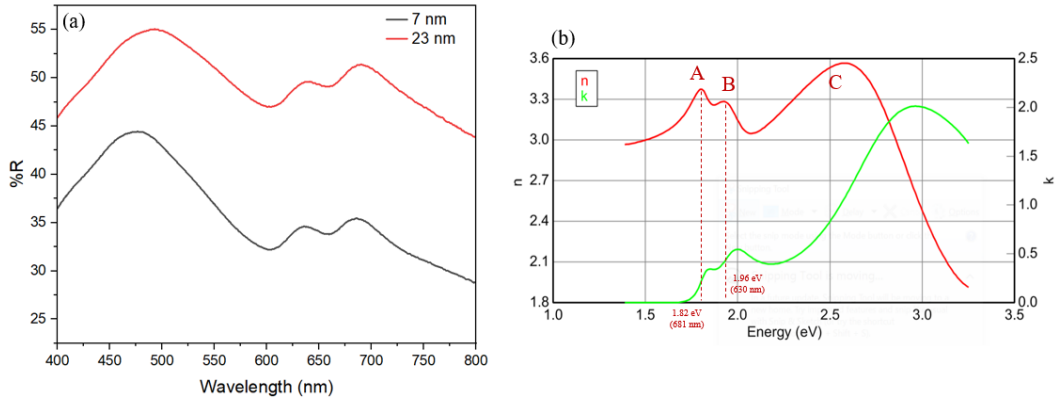

***Fig. 2.14**: **(a)** UV-Vis spectra of 7 nm and 23 nm MoS_2 on quartz. **(b)** 'n' and 'k' plots of 4 nm MoS_2 from ellipsometry measurement.*

2.5 SEM and AFM measurements

This subsection discusses some of the atomic force microscopy (AFM) and scanning electron microscopy (SEM) measurements to investigate and better understand the surface morphology of TAC based MoS_2 and its adhesion to substrates. Consider ***fig. 2.15(a)*** first which shows AFM image of a portion of MoS_2 (green) on Si/SiO_2 (blue) and 3 arbitrarily marked lines that correspond to line profiles shown in ***fig. 2.15(b)***. This portion is from the region between consecutive IDEs in sample 'MoIDE200' from tab. 2.1 where MoS_2 sits directly on top of Si/SiO_2. The deposition time of Mo to start with was 200s which leads to around 26 nm of MoS_2 after sulphurisation according to the 3 line profiles.

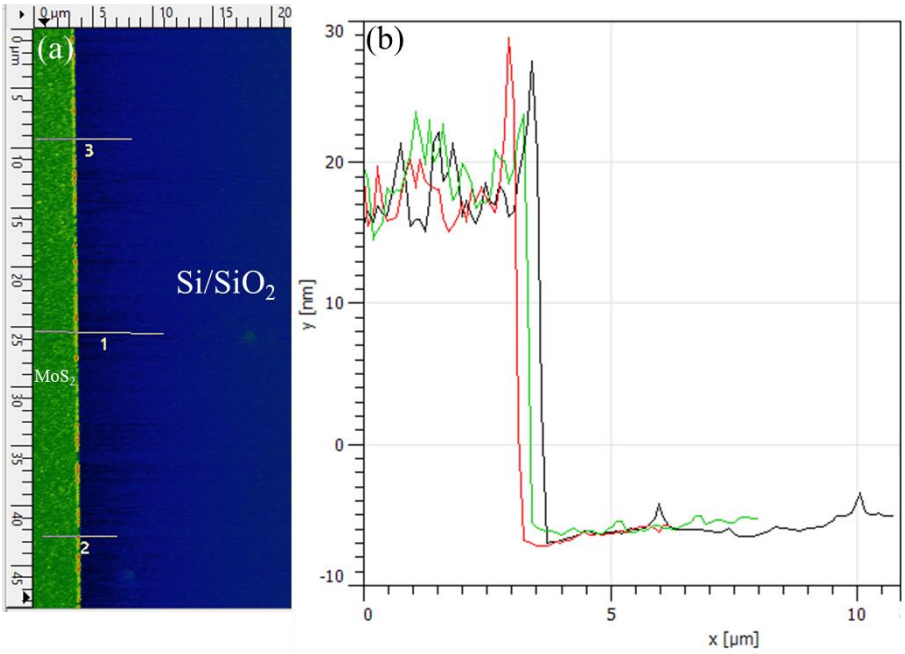

Fig. 2.15*: **(a)** AFM image of sample 'MoIDE200' from tab. 2.1- MoS_2 (green region) on Si/SiO_2 (blue region). **(b)** 3 height profiles across the MoS_2 edge on Si/SiO_2 showing ~26 nm of MoS_2 thickness.*

Apart from quartz and Si/SiO_2, MoS_2 deposition utilizing TAC method of synthesis was also tried on transparent conductive oxide substrates. Substrates of Indium Tin Oxide (ITO) coated on quartz were obtained from Biotain Crystal Co., Ltd. and they were investigated via AFM and SEM to understand their surface morphology right after unpacking them (as received) and then compared with the case after they had undergone sulphurisation conditions in the TAC furnace.

AFM and SEM images of an area of ITO substrates before and after being placed inside the TAC furnace is shown in ***fig. 2.16***. RMS roughness obtained from the red box region through AFM measurements (shown in ***fig. 2.16(a), (b)***) shows almost two times increase after being

exposed to TAC conditions inside the furnace for 10 mins and under 750℃. Similarly, ***fig. 2.16(c)***, ***(d)*** show the corresponding SEM images.

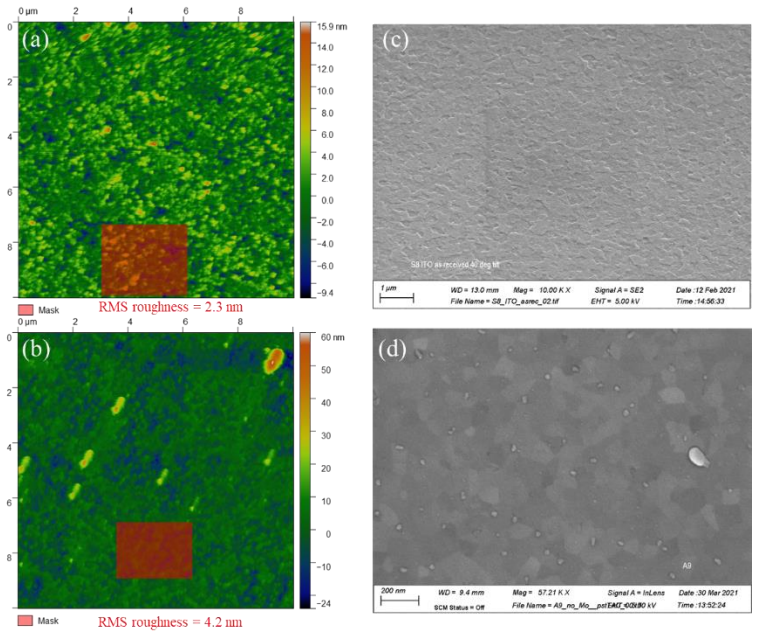

Fig. 2.16*: AFM images of* ***(a)*** *ITO substrate as received 'sample5' from tab. 2.1 and* ***(b)*** *ITO substrate after being inside the TAC furnace for 10 mins under 750℃. SEM images of* ***(c)*** *ITO substrate as received and* ***(d)*** *ITO substrate after being inside the TAC furnace for 10 mins under 750℃.*

Mo was then deposited on the ITO coated glass substrates and then sulphurised in the TAC furnace for 30 min at 750℃. The MoS_2 thus formed is approximately 35 nm thick with RMS roughness around 9.8 nm shown in ***fig. 2.17(a)***. Both AFM and SEM images (***fig. 2.17(a), (b)***) show more clustered islands compared to bare ITO substrate (***fig. 2.16(b)***).

To investigate the material that forms these clusters of significant height, energy dispersive x-ray (EDX) was performed on the region having clusters marked by 'spectrum 3' in ***fig. 2.17(c)*** and the region underneath it marked by 'spectrum 1' in ***fig. 2.17(d)***. The corresponding EDX plots are shown in ***fig. 2.17(e), (f)*** which indicate 'spectrum 3' region to be Molybdenum (Mo) and Sulphur (S) rich and 'spectrum 1' to be both Mo/S and Indium (In) rich. This means that the clusters are majorly formed by MoS_2 and the TAC based MoS_2 film is not continuous and uniform in this case.

To make the MoS_2 deposit uniformly on rough substrates like Biotain ITO, a thin adhesion layer of Titanium (Ti) was used before depositing MoS_2 on ITO. Generally, 5 nm or thicker Ti is used for adhesion purposes but 1 nm Ti layer suffices as well without diffusing through other layers and changing their properties [44].

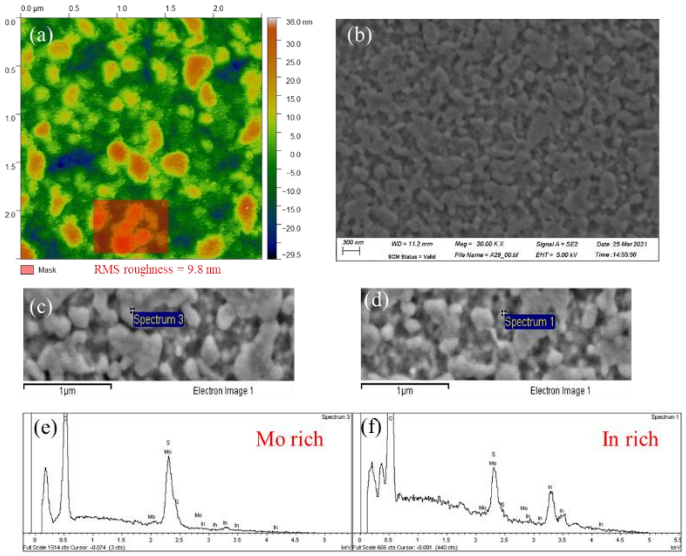

***Fig. 2.17**: Distinguishing between islands and background seen in **(a)** AFM image **(b)** SEM image of a 35 nm MoS_2 on ITO substrate 'sample6' from tab. 2.1 post TAC process of 30 mins at 750℃. Point chosen to probe **(c)** islands and **(d)** region under islands. **(e)** EDX spectrum from island regions in **(c)** and **(f)** region underneath the islands in **(d)**.*

This was shown by W. M. Abbott et. al., where they prevented dewetting of gold (Au) sputtered on substrates coated with different adhesion metals of extremely low thickness ~ 0.5 nm. They showed successful integration of 0.5 nm Ti sandwiched between Au and the substrate to make Au adhere more to the substrate at elevated temperature of 250℃ without changing the electrical properties of the combined Au/Ti layer structure. Here, the same concept is used not just for MoS_2 adhesion to tricky substrates like ITO that get porous at elevated temperatures but also for better adhesion of contact materials with MoS_2 which will be discussed in greater detail in ***ch. 3***.

Utilising the adhesive property of thin Ti film, protects the sputtered Mo from dewetting from the ITO substrate while undergoing the TAC process. ***Fig. 2.18*** shows AFM and SEM images of a ~16 nm MoS_2 deposited by TAC on an ITO substrate with 0.5 nm Ti adhesion layer sandwiched between ITO and MoS_2 ('sample7' from tab. 2.1). AFM image in ***fig. 2.18(a)*** shows the surface morphology of this sample and a region of this area highlighted by a red mask estimated the RMS roughness to be around 9.7 nm. When compared with the roughness of a 35 nm thick MoS_2 on ITO substrate without Ti adhesion layer shown in ***fig. 2.17(a)***, the roughness in this case is comparable to it. However, SEM images reveals that the MoS_2 formed after TAC in this case (having a 0.5 nm layer of Ti between ITO substrate and MoS_2) is more uniform and continuous (shown in ***fig. 2.18(b)***) and looks very different from the case where there is no Ti adhesion layer beneath MoS_2 (shown in ***fig. 2.17(b)***).

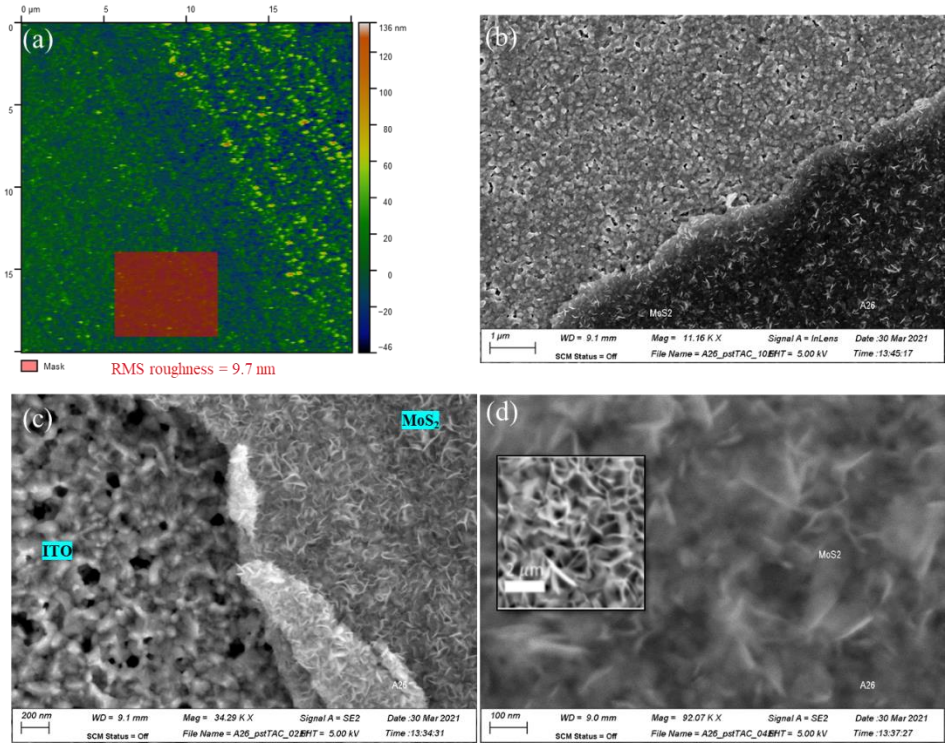

***Fig. 2.18**: **(a)** AFM image showing MoS_2 on ITO with a 0.5 nm Ti adhesion layer 'sample7'. **(b)-(d)** SEM images with different magnifications revealing the porous ITO substrate beneath MoS_2. Inset in **(d)**: SEM image of MoS_2 surface taken from ref. [27] for comparison.*

Even in the areas where it seems to chip off from ITO (as shown in ***fig. 2.18(c)***), it comes off as a continuous sheet thus revealing the extremely porous ITO substrate that causes this chip off after being subjected to elevated temperature and conditions of the TAC process. A magnified image of the same sample is shown in ***fig. 2.18(d)*** and for comparison, the inset shows a similar surface morphology of MoS_2 obtained from CVD process [27] that matches well with MoS_2 obtained from the TAC process.

2.6 X-ray diffraction

To confirm the phase and crystallinity of TAC based MoS_2, x-ray diffraction (XRD) was performed on 'MoIDE200'. It has been slightly difficult to obtain a measurable signal from TAC based MoS_2 and moreover differentiate between the two very naturally occurring phases of MoS_2 i.e., 2H (hexagonal) and 3R (rhombohedral) [45]. The XRD spectrum shown in ***fig. 2.19*** shows some peaks that are difficult to analyse but J. Strachan et. al., mention the range between ~40° – 50° where the peaks from the 2 polytypes can be distinguished [37]. Based on this, the peak around ~38° corresponding to the 3R phase is also seen in ***fig. 2.19***

marked as 38.32° while the peak around 40° corresponding to 2H phase is absent. Apart from this peak, other peaks corresponding to both the phases are present that are almost superimposed on each other which makes the further analysis difficult. So based on all these observations, it can be said that the data from this TAC based MoS_2 sample is consistent with both 2H and 3R phase or having a mixed phase. Additionally, it should be noted that the peak at 14.25°, that determines crystallinity and order along c-axis [46] is present but having a very low intensity. Polycrystallinity has also been reported in MoS_2 produced via similar techniques but with a different naming convention like thermal vapour sulphurisation (TVS) method discussed previously [47]. The spectrum matches well with studies reported previously [48], [49], [50], [51] and compared with XRD databases [52].

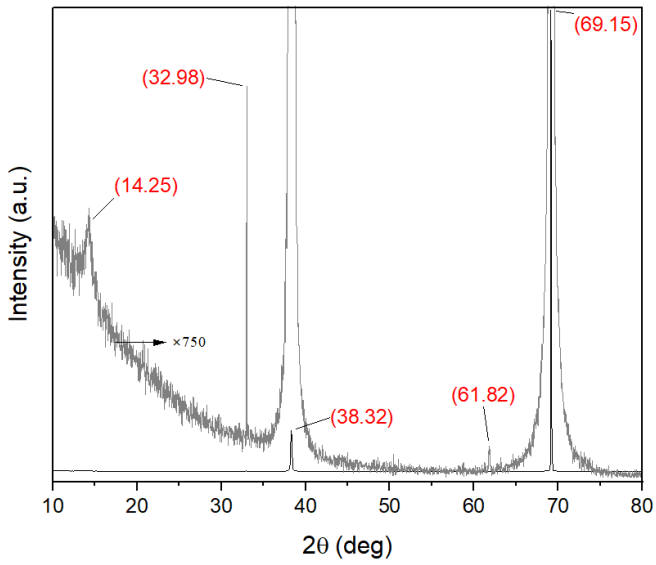

***Fig. 2.19**: XRD spectrum of a ~26 nm TAC based MoS_2 'MoIDE200'.*

2.7 Summary and conclusions

Many designs utilizing TAC MoS_2 were discussed above for their morphology, roughness, optical properties, crystal structure and stacking. It was also shown that TAC based TMDs like MoS_2 can be integrated as any layer in between a multilayer stack while still retaining its static coloration caused by other layers. The damage caused to underlying layers (like ITO) caused in the TAC furnace which affects MoS_2 deposition can be mitigated by increasing adhesion by using a thin Ti layer that renders a continuous MoS_2 deposition even when ITO beneath it becomes porous.

From Raman measurements, it seems that CVD MoS_2 is oriented more in-plane as compared to the one prepared by hot pick-up and stamp technique obtained by our collaborator- Dr. Jose Caridad's group in University of Salamanca. On the other hand, MoS_2 prepared by hot pick-up and stamp technique encapsulated by hBN from top and bottom appears more pristine and ordered than CVD MoS_2.

MoS_2 was also deposited on commercially bought rough substrates like ITO coated quartz with and without using 0.5 nm Ti adhesion layer. 16 nm TAC based MoS_2 was deposited with a Ti adhesion layer while 35 nm MoS_2 was deposited on the ITO substrates without Ti adhesion layer. Reducing the thickness to more than half and utilising a thin Ti adhesion film does not change the roughness but leads to a significant change in surface morphology and continuity of the MoS_2 film. The film looks more put together instead of separate islands above a porous substrate. Roughness is still less than what has been reported in past studies [27]. It was also shown that TAC method can produce transfer-free, site specific MoS_2 which is also compatible with standard photolithographic processes, easy integration in a large fabrication process requiring multilayer patterning. TAC few-layer films are continuous, and uniform over large areas (cm^2). Finally, it was shown that monolayers and bilayers of TAC based MoS_2 can be produced in patterned stacks as well.

References

[1] G. Cunningham *et al.*, "Photoconductivity of solution-processed MoS_2 films," *J. Mater. Chem. C*, vol. 1, no. 41, pp. 6899–6904, Oct. 2013, doi: 10.1039/C3TC31402B.

[2] J. N. Coleman *et al.*, "Two-Dimensional Nanosheets Produced by Liquid Exfoliation of Layered Materials," *Science*, vol. 331, no. 6017, pp. 568–571, Feb. 2011, doi: 10.1126/science.1194975.

[3] J. Neilson, M. P. Avery, and B. Derby, "Tiled Monolayer Films of 2D Molybdenum Disulfide Nanoflakes Assembled at Liquid/Liquid Interfaces," *ACS Appl. Mater. Interfaces*, vol. 12, no. 22, pp. 25125–25134, Jun. 2020, doi: 10.1021/acsami.0c03794.

[4] A. Ayari, E. Cobas, O. Ogundadegbe, and M. S. Fuhrer, "Realization and electrical characterization of ultrathin crystals of layered transition-metal dichalcogenides," *Journal of Applied Physics*, vol. 101, no. 1, p. 014507, Jan. 2007, doi: 10.1063/1.2407388.

[5] Z. Ai *et al.*, "A modified CVD method for the synthesis of monolayer MoS_2 and photoelectric improvement by HfO_2 passivation," *Nanotechnology*, vol. 34, no. 32, p. 325601, Aug. 2023, doi: 10.1088/1361-6528/acd1f6.

[6] S. Durairaj *et al.*, "Barrier-assisted vapor phase CVD of large-area MoS_2 monolayers with high spatial homogeneity," *Nanoscale Adv.*, vol. 2, no. 9, pp. 4106–4116, Sep. 2020, doi: 10.1039/D0NA00524J.

[7] M. O'Brien, N. McEvoy, D. Hanlon, T. Hallam, J. N. Coleman, and G. S. Duesberg, "Mapping of Low-Frequency Raman Modes in CVD-Grown Transition Metal Dichalcogenides: Layer Number, Stacking Orientation and Resonant Effects," *Sci Rep*, vol. 6, no. 1, p. 19476, Jan. 2016, doi: 10.1038/srep19476.

[8] A. Castellanos-Gomez *et al.*, "Deterministic transfer of two-dimensional materials by all-dry viscoelastic stamping," *2D Mater.*, vol. 1, no. 1, p. 011002, Apr. 2014, doi: 10.1088/2053-1583/1/1/011002.

[9] K. Buapan, R. Somphonsane, T. Chiawchan, and H. Ramamoorthy, "Versatile, Low-Cost, and Portable 2D Material Transfer Setup with a Facile and Highly Efficient DIY Inert-Atmosphere Glove Compartment Option," *ACS Omega*, vol. 6, no. 28, pp. 17952–17964, Jul. 2021, doi: 10.1021/acsomega.1c01582.

[10] F. Pizzocchero *et al.*, "The hot pick-up technique for batch assembly of van der Waals heterostructures," *Nat Commun*, vol. 7, no. 1, p. 11894, Jun. 2016, doi: 10.1038/ncomms11894.

[11] D. Ma *et al.*, "A universal etching-free transfer of MoS_2 films for applications in photodetectors," *Nano Res.*, vol. 8, no. 11, pp. 3662–3672, Nov. 2015, doi: 10.1007/s12274-015-0866-z.

[12] Y. Lee *et al.*, "Synthesis of wafer-scale uniform molybdenum disulfide films with control over the layer number using a gas phase sulfur precursor," *Nanoscale*, vol. 6, no. 5, p. 2821, 2014, doi: 10.1039/c3nr05993f.

[13] R. Gatensby *et al.*, "Controlled synthesis of transition metal dichalcogenide thin films for electronic applications," *Applied Surface Science*, vol. 297, pp. 139–146, Apr. 2014, doi: 10.1016/j.apsusc.2014.01.103.

[14] H. Liu, K. K. Ansah Antwi, J. Ying, S. Chua, and D. Chi, "Towards large area and continuous MoS_2 atomic layers via vapor-phase growth: thermal vapor sulfurization," *Nanotechnology*, vol. 25, no. 40, p. 405702, Oct. 2014, doi: 10.1088/0957-4484/25/40/405702.

[15] Y. Zhan, Z. Liu, S. Najmaei, P. M. Ajayan, and J. Lou, "Large-Area Vapor-Phase Growth and Characterization of MoS_2 Atomic Layers on a SiO_2 Substrate," *Small*, vol. 8, no. 7, pp. 966–971, Apr. 2012, doi: 10.1002/smll.201102654.

[16] D. Kong *et al.*, "Synthesis of MoS_2 and $MoSe_2$ Films with Vertically Aligned Layers," *Nano Lett.*, vol. 13, no. 3, pp. 1341–1347, Mar. 2013, doi: 10.1021/nl400258t.
[17] R. Gatensby *et al.*, "Controlled synthesis of transition metal dichalcogenide thin films for electronic applications," *Applied Surface Science*, vol. 297, pp. 139–146, Apr. 2014, doi: 10.1016/j.apsusc.2014.01.103.
[18] K. Kaasbjerg, K. S. Thygesen, and K. W. Jacobsen, "Phonon-limited mobility in n-type single-layer MoS_2 from first principles," *Phys. Rev. B*, vol. 85, no. 11, p. 115317, Mar. 2012, doi: 10.1103/PhysRevB.85.115317.
[19] X. Liu, G. Zhang, Q.-X. Pei, and Y.-W. Zhang, "Phonon thermal conductivity of monolayer MoS_2 sheet and nanoribbons," *Applied Physics Letters*, vol. 103, no. 13, p. 133113, Sep. 2013, doi: 10.1063/1.4823509.
[20] T. Li, "Ideal strength and phonon instability in single-layer MoS_2," *Phys. Rev. B*, vol. 85, no. 23, p. 235407, Jun. 2012, doi: 10.1103/PhysRevB.85.235407.
[21] H. Li *et al.*, "From Bulk to Monolayer MoS_2: Evolution of Raman Scattering," *Adv. Funct. Mater.*, vol. 22, no. 7, pp. 1385–1390, Apr. 2012, doi: 10.1002/adfm.201102111.
[22] M. Placidi *et al.*, "Multiwavelength excitation Raman scattering analysis of bulk and two-dimensional MoS_2: vibrational properties of atomically thin MoS_2 layers," *2D Mater.*, vol. 2, no. 3, p. 035006, Jul. 2015, doi: 10.1088/2053-1583/2/3/035006.
[23] J.-U. Lee, K. Kim, S. Han, G. H. Ryu, Z. Lee, and H. Cheong, "Raman Signatures of Polytypism in Molybdenum Disulfide," *ACS Nano*, vol. 10, no. 2, pp. 1948–1953, Feb. 2016, doi: 10.1021/acsnano.5b05831.
[24] S. Hong *et al.*, "Highly sensitive active pixel image sensor array driven by large-area bilayer MoS_2 transistor circuitry," *Nat Commun*, vol. 12, no. 1, p. 3559, Jun. 2021, doi: 10.1038/s41467-021-23711-x.
[25] J. Robertson, X. Liu, C. Yue, M. Escarra, and J. Wei, "Wafer-scale synthesis of monolayer and few-layer MoS_2 via thermal vapor sulfurization," *2D Mater.*, vol. 4, no. 4, p. 045007, Sep. 2017, doi: 10.1088/2053-1583/aa8678.
[26] D. Kong *et al.*, "Synthesis of MoS_2 and $MoSe_2$ Films with Vertically Aligned Layers," *Nano Lett.*, vol. 13, no. 3, pp. 1341–1347, Mar. 2013, doi: 10.1021/nl400258t.
[27] A. V. Agrawal *et al.*, "Controlled Growth of MoS_2 Flakes from in-Plane to Edge-Enriched 3D Network and Their Surface-Energy Studies," *ACS Appl. Nano Mater.*, vol. 1, no. 5, pp. 2356–2367, May 2018, doi: 10.1021/acsanm.8b00467.
[28] H. Park *et al.*, "Exceptionally Uniform and Scalable Multilayer MoS_2 Phototransistor Array Based on Large-Scale MoS_2 Grown by RF Sputtering, Electron Beam Irradiation, and Sulfurization," *ACS Appl. Mater. Interfaces*, vol. 12, no. 18, pp. 20645–20652, May 2020, doi: 10.1021/acsami.0c02393.
[29] R. Canton-Vitoria, T. Hotta, M. Xue, S. Zhang, and R. Kitaura, "Synthesis and Characterization of Transition Metal Dichalcogenide Nanoribbons Based on a Controllable O_2 Etching," *JACS Au*, vol. 3, no. 3, pp. 775–784, Mar. 2023, doi: 10.1021/jacsau.2c00536.
[30] B. Chakraborty, H. S. S. R. Matte, A. K. Sood, and C. N. R. Rao, "Layer-dependent resonant Raman scattering of a few layer MoS_2," *Journal of Raman Spectroscopy*, vol. 44, no. 1, pp. 92–96, 2013, doi: 10.1002/jrs.4147.
[31] T. Livneh and E. Sterer, "Resonant Raman scattering at exciton states tuned by pressure and temperature in 2H-MoS_2," *Phys. Rev. B*, vol. 81, no. 19, p. 195209, May 2010, doi: 10.1103/PhysRevB.81.195209.

[32] T. Sekine, K. Uchinokura, T. Nakashizu, E. Matsuura, and R. Yoshizaki, "Dispersive Raman Mode of Layered Compound 2H-MoS_2 under the Resonant Condition," *J. Phys. Soc. Jpn.*, vol. 53, no. 2, pp. 811–818, Feb. 1984, doi: 10.1143/JPSJ.53.811.
[33] O. A. Abbas, C.-C. Huang, D. W. Hewak, S. Mailis, and P. Sazio, "(INVITED) Opto-electronic properties of solution-synthesized MoS_2 metal-semiconductor-metal photodetector," *Optical Materials: X*, vol. 13, p. 100135, Jan. 2022, doi: 10.1016/j.omx.2022.100135.
[34] K. Gołasa *et al.*, "Multiphonon resonant Raman scattering in MoS_2," *Appl. Phys. Lett.*, vol. 104, no. 9, p. 092106, Mar. 2014, doi: 10.1063/1.4867502.
[35] R. G. Costa, A. do N. Barbosa, M. E. H. Maia da Costa, and F. L. Freire, "Resonance Raman spectroscopy of MoS_2 monolayers treated with nitrogen plasma," *Vibrational Spectroscopy*, vol. 123, p. 103454, Nov. 2022, doi: 10.1016/j.vibspec.2022.103454.
[36] S. Anghel *et al.*, "Identification of 2H and 3R polytypes of MoS_2 layered crystals using photoluminescence spectroscopy," Nov. 14, 2014, *arXiv*: arXiv:1411.3850. doi: 10.48550/arXiv.1411.3850.
[37] J. Strachan, A. F. Masters, and T. Maschmeyer, "3R-MoS_2 in Review: History, Status, and Outlook," *ACS Appl. Energy Mater.*, vol. 4, no. 8, pp. 7405–7418, Aug. 2021, doi: 10.1021/acsaem.1c00638.
[38] W. Na, K. Kim, J.-U. Lee, and H. Cheong, "Davydov splitting and polytypism in few-layer MoS_2," *2D Mater.*, vol. 6, no. 1, p. 015004, Oct. 2018, doi: 10.1088/2053-1583/aae61c.
[39] É. Blanco, P. Afanasiev, G. Berhault, D. Uzio, and S. Loridant, "Resonance Raman spectroscopy as a probe of the crystallite size of MoS_2 nanoparticles," *Comptes Rendus Chimie*, vol. 19, no. 10, pp. 1310–1314, Oct. 2016, doi: 10.1016/j.crci.2015.08.014.
[40] Y. Yu, Y. Yu, L. Huang, H. Peng, L. Xiong, and L. Cao, "Giant Gating Tunability of Optical Refractive Index in Transition Metal Dichalcogenide Monolayers," *Nano Lett.*, vol. 17, no. 6, pp. 3613–3618, Jun. 2017, doi: 10.1021/acs.nanolett.7b00768.
[41] F. Stern, "Dispersion of the Index of Refraction Near the Absorption Edge of Semiconductors," *Phys. Rev.*, vol. 133, no. 6A, pp. A1653–A1664, Mar. 1964, doi: 10.1103/PhysRev.133.A1653.
[42] C. Thirstrup, "Refractive index modulation based on excitonic effects in GaInAs-InP coupled asymmetric quantum wells," *IEEE J. Quantum Electron.*, vol. 31, no. 6, pp. 988–996, Jun. 1995, doi: 10.1109/3.387034.
[43] G. A. Ermolaev *et al.*, "Broadband optical properties of monolayer and bulk MoS_2," *npj 2D Mater Appl*, vol. 4, no. 1, p. 21, Jul. 2020, doi: 10.1038/s41699-020-0155-x.
[44] W. M. Abbott *et al.*, "Comparison of Metal Adhesion Layers for Au Films in Thermoplasmonic Applications," *ACS Appl. Mater. Interfaces*, vol. 12, no. 11, pp. 13503–13509, Mar. 2020, doi: 10.1021/acsami.9b22279.
[45] E. V. Belogub *et al.*, "Scroll-like and platy molybdenite-3R from the Ufaley metamorphic block, South Urals: EBSD, XRD, SEM, EPMA and ICP-MS study," *MinMag*, vol. 86, no. 3, pp. 422–435, Jun. 2022, doi: 10.1180/mgm.2022.35.
[46] M. Chhowalla and G. A. J. Amaratunga, "Thin Films of fullerene-like MoS_2 nanoparticles with ultra-low friction and wear," 2000.
[47] K. Hayashi, M. Kataoka, H. Jippo, J. Yamaguchi, M. Ohfuchi, and S. Sato, "Highly Sensitive NO_2 Detection by TVS-Grown Multilayer MoS_2 Films," *ACS Omega*, vol. 7, no. 2, pp. 1851–1860, Jan. 2022, doi: 10.1021/acsomega.1c05113.

[48] R. Kumar *et al.*, "Growth of MoS_2 –MoO_3 Hybrid Microflowers via Controlled Vapor Transport Process for Efficient Gas Sensing at Room Temperature," *Adv Materials Inter*, vol. 5, no. 10, p. 1800071, May 2018, doi: 10.1002/admi.201800071.
[49] A. M. A. Omar, A. Hassen, O. I. Metwalli, M. R. Saber, S. R. E. Mohamed, and A. S. G. Khalil, "Construction of 2D layered TiO_2 @MoS_2 heterostructure for efficient adsorption and photodegradation of organic dyes," *Nanotechnology*, vol. 32, no. 33, p. 335605, Aug. 2021, doi: 10.1088/1361-6528/abff8a.
[50] Y. Liu *et al.*, "U(VI) adsorption behaviour onto polypyrrole coated 3R-MoS_2 nanosheets prepared with the molten salt electrolysis method," *Int J Miner Metall Mater*, vol. 29, no. 3, pp. 479–489, Mar. 2022, doi: 10.1007/s12613-020-2154-5.
[51] J. Luxa, L. Spejchalová, I. Jakubec, and Z. Sofer, "MoS_2 stacking matters: 3R polytype significantly outperforms 2H MoS_2 for the hydrogen evolution reaction," *Nanoscale*, vol. 13, no. 46, pp. 19391–19398, 2021, doi: 10.1039/D1NR03284D.
[52] B. Lafuente, R. T. Downs, H. Yang, and N. Stone, "The power of databases: The RRUFF project," *De Gruyter*.

Chapter 3. Electrical properties and contact engineering

3.1 Introduction

For successful integration within an integrated circuit, a semiconductor-based device needs to have at least two metal contacts. This applies to our TAC based MoS_2 thin films as well where metal contacts are required not just for electrical characterization of the material but also for fabricating a working device out of it. However, this comes with its own complexities since unlike a metal-metal or semiconductor-semiconductor junction, metal-semiconductor junction is quite peculiar. This is because of the difference in energy bands of the two (depicted in ***fig. 3.1(a)***) and bringing them very close together to form an electrical contact for charge carriers to flow results in band bending at the interface and formation of a Schottky barrier. More specifically, the band bending depends on the work function $\boldsymbol{\varphi}$ of both metal ($\boldsymbol{\varphi_m}$) and semiconductor ($\boldsymbol{\varphi_s}$), temperature and doping level of the semiconductor. For instance, considering an n-type semiconductor, when $\boldsymbol{\varphi_m > \varphi_s}$, the metal-semiconductor contact (also known as Schottky contact) will result in rectifying contacts as shown in ***fig. 3.1(b)*** while in the case of $\varphi_m < \varphi_s$, a non-rectifying Ohmic contact is obtained where current is allowed to flow in both directions i.e. from semiconductor to metal and from metal to semiconductor across the junction (***fig. 3.2(a)***) [1]. Another way of obtaining such bi-directional current flow while still having a Schottky contact is by doping the semiconductor heavily which will reduce the width of the depletion region at the junction enough for electrons to quantum mechanically tunnel in both directions. This is represented by the second leftward pointed arrow and marked by **'2'** in ***fig. 3.2(b)***.

Theoretically, there are five main current transport mechanisms at a metal-semiconductor junction [2] (***fig. 3.2(b)***) but two out of them are especially relevant here - Thermionic Emission (TE) and Field Emission (FE) (or tunnelling). For moderately doped semiconductors, a metal-semiconductor junction experiences a rectifying (Schottky) contact where current transport is governed by the TE process while for heavily doped semiconductors, tunnelling dominates the current transport through the metal-semiconductor junction [2] as mentioned previously. This has been experimentally verified for a metal-MoS_2-metal device (metal = Au, Pd) in a study by N. Kaushik et al., where they showed that at low gate voltages, when charge density in the channel is low, current shows a higher dependence on temperature indicating TE as the main current transport mechanism whereas at larger back gate voltages, due to higher doping in the semiconductor channel, FE takes over and the current gets independent of temperature [3].

In yet another study the same was observed for a metal-carbon nanotube-metal device where active control over nature (rectifying or near-linear) of I-V characteristics was established by varying the gate bias voltage [4].

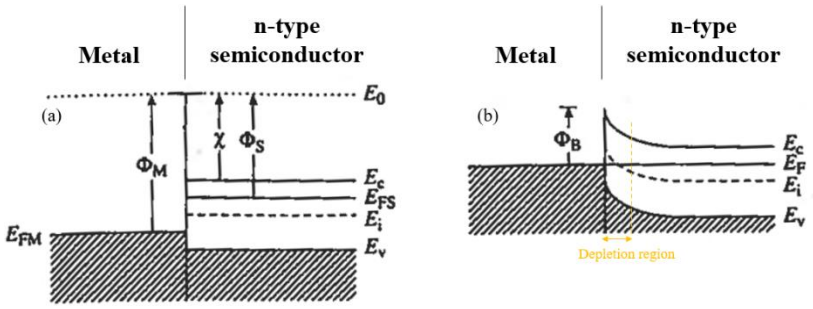

Fig. 3.1*: Formation of a Schottky junction for the case ($\varphi_m > \varphi_s$) when metal and semiconductor* ***(a)*** *just come in contact and* ***(b)*** *after reaching equilibrium [1].*

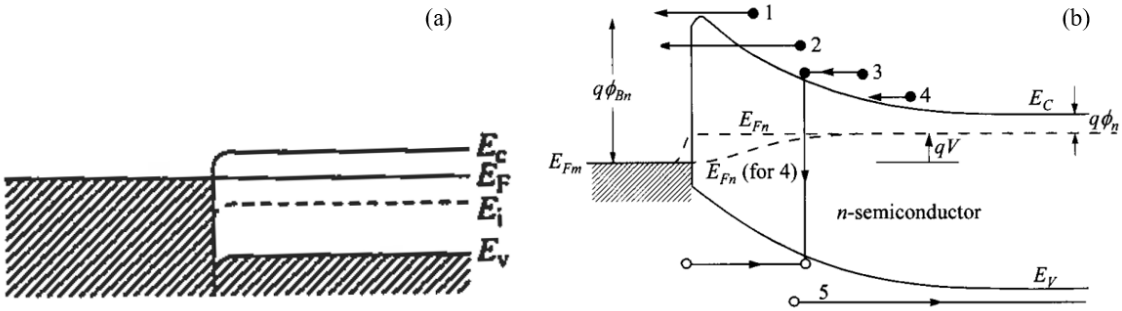

Fig. 3.2*: **(a)** Formation of a Schottky junction between a metal and n-type semiconductor after reaching equilibrium, for the case ($\varphi_m < \varphi_s$) [1]. **(b)** The five current transport mechanisms across a metal-semiconductor junction ($\varphi_m > \varphi_s$) under forward bias. (1) and (2) represent TE and FE processes respectively [2].*

While TE is intuitive to understand for Schottky contacts, Ohmic behaviour may seem to occur due to FE when thermal energy is much lower than E_{00} (an energy parameter that is directly proportional to $\sqrt{N}$; N=carrier density) [2] or when the contacts have different Schottky barrier heights i.e., they are a pair of asymmetric Schottky diodes. In such a case, I-V curve is dominated by the contact of higher Schottky barrier height and looks like a single Schottky diode characteristic i.e., as if having one Schottky contact and one Ohmic contact [5]. When in reality the other contact is also a Schottky contact just with a relatively lower barrier height compared to the other Schottky contact. In short, TE results in diode-like (rectifying) behaviour while FE or tunnelling forms Ohmic contact at a metal-semiconductor junction with a Schottky barrier, but the reverse i.e., when a contact appears to be Ohmic, FE being its transport mechanism may or may not be true. J. Osvald has shown

a thorough analysis of Schottky contacts having a very low Schottky barrier height and a high series resistance coming from a moderately doped semiconductor, but apparently showing Ohmic I-V (linear and symmetric) characteristics in a certain voltage range [6]. In some cases, absence of this knowledge may result in misleading analysis of electrical characterization but on the other hand, knowledge of this concept can be used to achieve near-Ohmic contacts in a certain voltage range while still using materials that result in Schottky contacts. Alternatively, observing Ohmic-like I-V characteristics in a structure which by conventional knowledge should show Schottky characteristics, should not be very surprising provided the structure's series resistance dominates the Schottky junction resistance. This is also observed in TAC based MoS_2 devices discussed in the sections to follow.

Double Schottky or back-to-back diode model perfectly considers the rectifying nature of both metal-MoS_2 contacts and the high resistance of especially TAC based MoS_2. This is modelled as a series resistor (MoS_2) sandwiched between two Schottky diodes (junction of the metal-MoS_2 contact) in the opposite direction to each other such that current flows in series through all three circuit elements and separate voltage drops are experienced by each [5], [7], [8], thus forming a metal-semiconductor-metal (MSM) structure. The following schematic in ***fig. 3.3(a)*** depicts this perfectly and the associated ***eq. (3-1)*** analytically explains this concept.

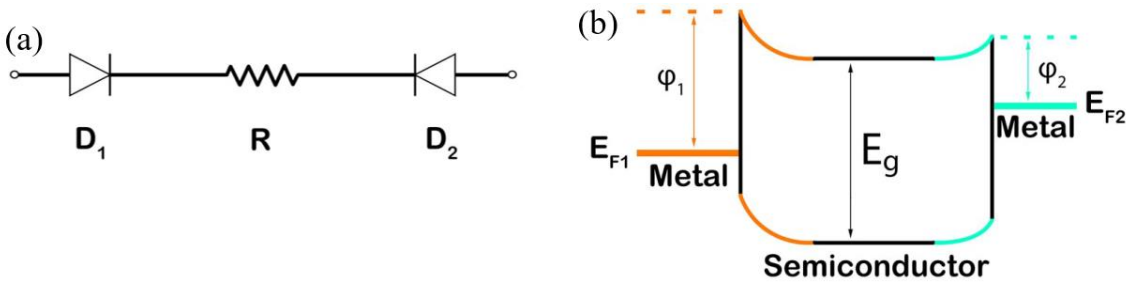

Fig. 3.3 (a) *Back-to-back double Schottky model for a MSM device with both rectifying contacts.* ***(b)*** *Energy band diagram showing band bending at the two junctions for an n-type semiconductor and metal with higher workfunction than it. Taken from [7].*

$$V = V_{D1} + V_{D2} + V_R = \frac{n_1}{\beta}\ln\left(\frac{I}{I_{01}} + 1\right) - \frac{n_2}{\beta}\ln\left(-\frac{I}{I_{02}} + 1\right) + R \cdot I \qquad \textbf{(3-1)}$$

Where V_{D1}, V_{D1}, V_R are voltage drops across diodes D1, D2 and resistor R respectively. $\beta = \frac{q}{k \cdot T}$ where *k* is the Boltzmann constant, T is the absolute temperature, q is the charge of an

electron and n_1, n_2 are the ideality factors of the two diodes. I_{01}, I_{02} are the saturation currents of D1 and D2 respectively that incorporate the effect of band bending and rectification at the junctions due to misalignment of fermi levels given by ***eq. (3-2)***. This misalignment is reflected by the difference in their respective work functions shown in ***fig. 3.1(a)*** with respect to semiconductor's electron affinity χ. The difference between $\boldsymbol{\varphi_m}$ in each case and χ leads to Schottky barrier height - SBH (φ_1, φ_2) formation at each junction depicted in ***fig. 3.3(b)*** and is related to saturation current as:

$$I_{01,02} = S \cdot A^* \cdot T^2 \cdot e^{-\beta \cdot \varphi_{1,2}} \qquad \textbf{(3-2)}$$

Where, **S** is the contact area and **A*** is the Richardson constant.

Finally, in order to experimentally measure and analyse these parameters (contact type, SBH, n), it is first essential to measure contact resistance (R_c) and sheet resistance (R_s) which are important figures-of-merit and easy to perform measurements using techniques like 4-point probe, current-voltage (I-V) sweeps, capacitance-voltage (C-V) sweeps, Hall bar measurements and transfer length method (TLM) measurements. These methods of characterization are discussed in the following sections and additionally, a study on temperature dependent resistance of TAC based MoS_2 is also included for a complete understanding of its electrical properties.

3.2 I-V measurements

Measuring the current through a device in response to a driving voltage is the simplest way to interrogate the electrical properties of the device and materials. For TAC based MoS_2 films, firstly it quickly verifies whether the metallic Mo sputtered films were fully sulphurised to form MoS_2 because the slope of the I-V sweep gives conductance which is comparatively low for partially sulphurised MoS_2 films as compared to fully sulphurised films.

Secondly, a deeper analysis reveals charge transport mechanism as discussed previously. Thirdly, it provides insight into contact-MoS_2 junction which is important to consider while integrating TMDs in a larger and integrated design of photonic circuits and devices as this junction is the most probable place for damage due to heat, degradation, and electrical failure to occur. Finally, I-V measurements under different light conditions helps

to understand light-matter interaction in TMDs in detail which will discussed in more depth in ***ch. 5***.

3.2.1 Four-point probe

The 4-point probe (***fig. 3.4***) used here is an easy to operate tool that presses down 4 equidistant probes (1 mm apart) on a large lateral area MoS_2 sample. Electrical resistivity and sheet resistance were measured using a 4-point probe. The aim is to pass a small amount of DC current of a few milli Amperes and sense voltage across the sample. From this information, resistance can be calculated and hence the electrical resistivity.

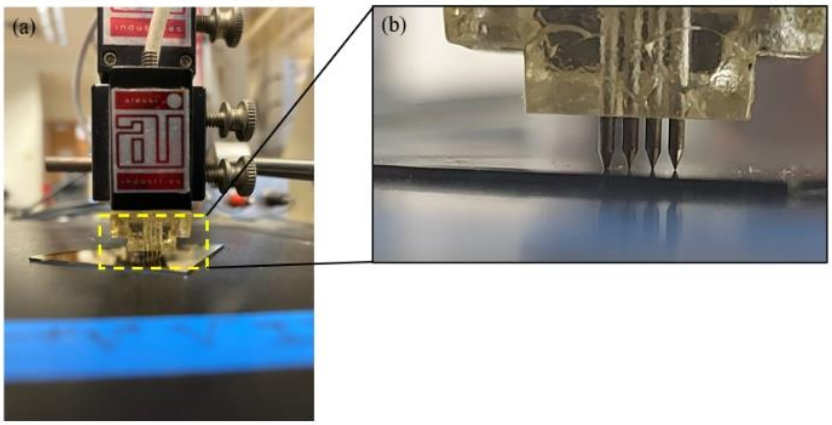

***Fig. 3.4**: **(a)** 4-point probe setup in our lab **(b)** zoomed-in picture of a piece of gold wafer under the 4-point probe tool.*

4-point probe technique is more advantageous than the 2-probe technique and is preferred because the latter uses the same probes for both sourcing current as well as measuring voltage as shown in ***fig. 3.5(a)***. This leads to erroneous results because the calculated sample resistance is accompanied by probe and contact resistance (***fig. 3.5(b)***). Whereas, in a 4-point probe method as shown in ***fig. 3.5*(c)**, this error is prevented by using separate probes for current source and voltage measurement, hence separating out the contact and probe resistance from sample resistance (***fig. 3.5(d)***). Therefore, the 4-point probe method of resistivity measurement gives more accurate results. This can then be used to calculate sheet resistance, R_s and resistivity, ρ of a thin film having thickness 't' less than half of the spacing between probes:

$$R_s = \frac{\pi}{\ln(2)}\frac{\Delta V}{I} \approx 4.53\frac{\Delta V}{I} \qquad \textbf{(3-3)}$$

$$\rho = R_s \cdot t \approx 4.53 \cdot t \cdot \frac{\Delta V}{I} \qquad \textbf{(3-4)}$$

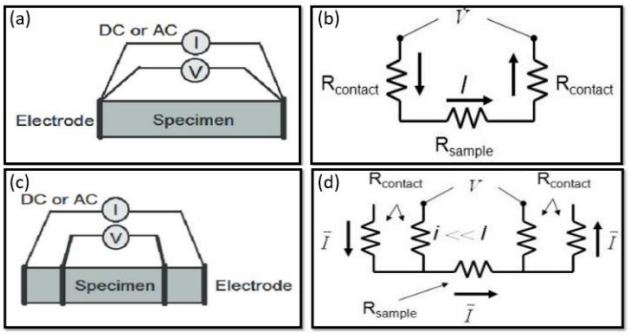

***Fig. 3.5**: **(a)** Schematic of 2-point probe arrangement. **(b)** Current is passed via 2 probes into the sample and voltage drop is measured across the sample via the same pair of probes. **(c)** Schematic of 4-point probe arrangement **(d)** Current is passed via the 2 outer probes into the sample and voltage drop is measured across the sample via the pair of inner probes.*

Based on the measured V, I values and ***eq. (3-3)***, ***(3-4)***, R_s and ρ respectively were obtained for large area TAC MoS_2 films shown in ***fig. 3.6***. Here, samples sulphurised at 750℃ and above seem to be forming insulating MoS_2 (with occasional outliers) and the ones sulphurised at lower temperatures like 450℃ and 600℃ seem to still be at an upper limit of semiconducting nature even after 60 minutes of sulphurisation as evident by their low sheet resistance.

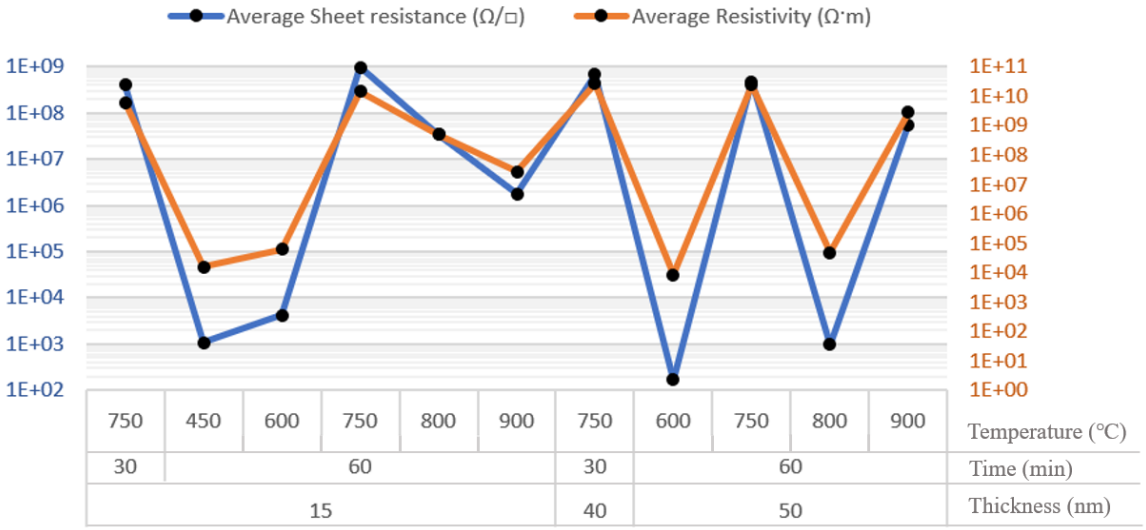

***Fig. 3.6**: Average sheet resistance (left axis) and resistivity (right axis) of thick (15 nm, 40 nm and 50 nm) MoS_2 films produced by TAC at different temperatures and durations.*

This can be attributed to partial sulphurisation of starting Mo film but might be advantageous for obtaining a semiconducting material produced at low temperatures. This can be used to

disrupt the conventional Si based semiconductor industry while reaping the benefits of extraordinary optical properties of MoS_2.

3.2.2 Two terminal I-V sweeps

The 4-point probe used here is a quick way to obtain a rough estimate of a material's conductance over a large lateral area, but it fails to deliver the same for patterned devices and laterally smaller area devices. For such microscale devices, patterned contacts were used for 2-terminal current-voltage (I-V) sweeps (discussed in this section) and transfer length method (TLM) of contact and sheet resistance measurements (discussed in ***sec. 3.4***). I-V sweeps of MoS_2 provide a great insight into its semiconducting properties, nature of contacts it forms (Schottky or Ohmic) and charge transport mechanisms apart from a simple measure of resistance. Keeping the substrate (Si/SiO_2 300 nm), MoS_2 thickness (15 nm), contact material and thickness (1 nm Ti/50 nm Au) the same for both, two contact designs are explored:

1. 2-point probe top electrodes: This is the simplest and most common design where contacts are lithographically patterned directly on top of the material that is to be measured at a desired channel length. Shown in ***fig. 3.7(a)***, are 4 such contacts on a thin MoS_2 bar and I-V sweeps can be performed utilising any pair from this set.

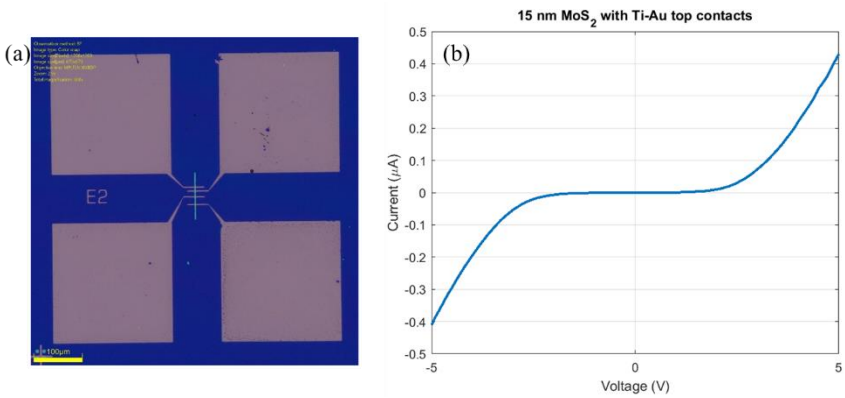

Fig. 3.7: (a) *Optical image of 15 nm MoS_2 of channel length = 2 μm on Si/SiO_2 (300 nm) substrate.* ***(b)*** *Schottky contacts are formed when 1 nm Ti/25 nm Au top contacts are used on MoS_2 shown in* ***(a)***.

2. Inter-digitated bottom-edge electrodes (IDE): This design was adopted from and for compatibility with electrical characterization tools from Ossila Ltd., UK. Ossila provides

a complete kit for measurement of current vs voltage and time with convenient extended contact design and a push-fit test board compatible with this design. The design consists of 5 sets of IDEs with varying inter-electrode spacing with each set.

The contacts were patterned and deposited first on the substrate and subsequently, MoS_2 was grown on them as layer-2 (***fig. 3.8(a)***) thus forming a bottom contact to MoS_2 which gets deposited directly on top of it and for MoS_2 that gets deposited in between the consecutive Au IDEs, the Au IDEs can be considered to be somewhat like side contacts. This is depicted in ***fig. 3.8(b)*** and was also discussed in chapter 2 and included in tab. 2.1 as 'MoIDE17-200'. This device under test (DUT) was then inserted in the push-fit test board and connected to a source measuring unit (SMU) interfaced with Ossila software to perform and record various electrical sweeps.

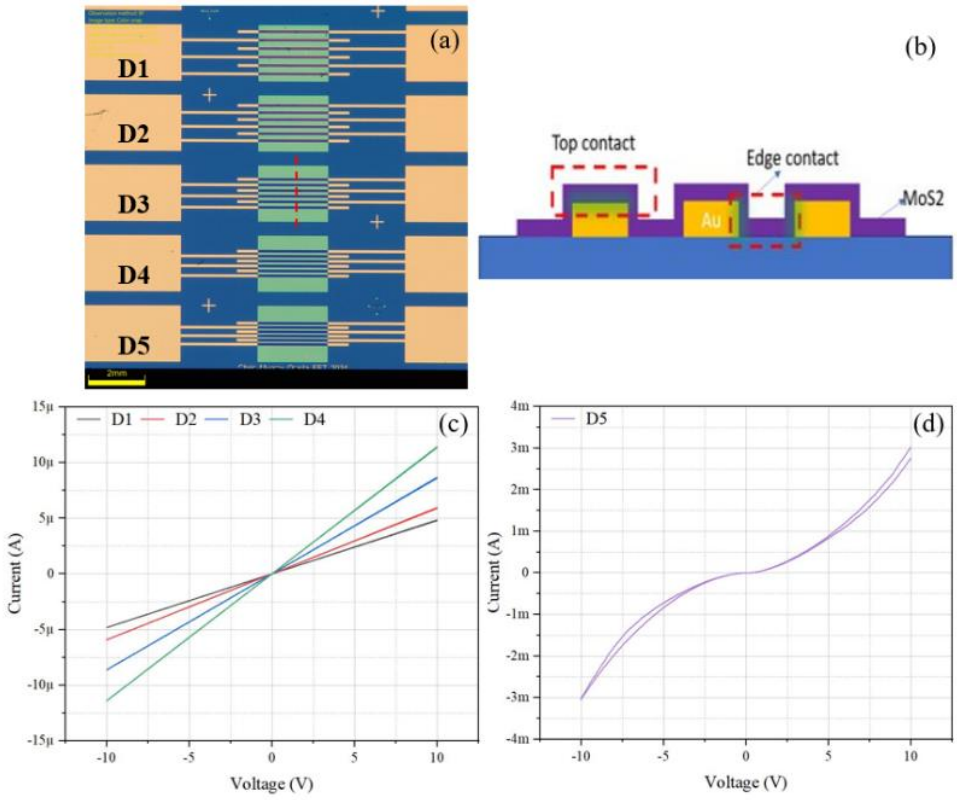

***Fig. 3.8**: **(a)** Optical image of 5 MoS_2 devices on Si/SiO_2 with IDE based on commercially available Ossila mask design. The 5 lime green boxes are MoS_2 devices of 15 nm thickness each, 2 mm x 2 mm (lateral area=4 mm^2) with varying inter-electrode spacing. The inter-electrode distances for devices D1, D2, D3, D4 and D5 are 200 µm, 150 µm, 100 µm, 75 µm, 50 µm respectively. **(b)** Side view of the cross-section (along the red dashed line in **(a)**) of a device depicting a not-to-scale hybrid inverted top-edge contact between Au (yellow) and MoS_2 (purple). **(c)** I-V sweeps of devices D1 to D4 **(d)** I-V sweep of D5.*

I-V sweeps from both the contact designs introduced above are discussed in the following part of this section. It should be noted that the first contact design (simple 2-terminal electrodes) consists of consecutive electrodes very closely spaced ~ 2 μm, 4 μm and 8 μm. while the IDE design consists of 5 sets of comb-like interdigitated electrodes with the least inter-electrode spacing of ~ 50 μm. So, this analysis is a good way to understand the transport mechanism in MoS_2 with different channel lengths and top vs top-edge (hybrid) contacts.

3.2.2.1 I-V sweep using simple 2-point probe top electrodes (channel length = 2 μm)

As observed by A. D. Bartolomeo et al., single Schottky diode model based on thermionic theory is not compatible with I-V characteristics (at zero gate bias) of a MoS_2 device having Ti/Au contacts [9]. These contacts are inherently rectifying in nature [10] and occur at both the contacts' junctions [11]. Local contact chemistry, MoS_2 defects as well as pressure at which Ti is evaporated as a contact govern parameters like SBH and ideality factor to a large extent [9] [12]. It is therefore advised to not use the single diode equation for such cases. Instead, A. Grillo and A. D. Bartolomeo proposed a model for a 2-terminal device which aptly describes conduction in it with both rectifying contacts [11] as opposed to assuming only one rectifying contact while the other to be Ohmic as in the case of a single diode model.

Experimental data presented in ***fig. 3.7(b)*** is compatible with these findings as 2-terminal Ti/Au contacts were evaporated at a pressure ranging from 10^{-8} to 10^{-7} mbar which leads to some degree of Ti oxidation [9], [11], [12] and these devices were stored at room temperature and pressure before measurement causing further degradation (oxidation) of MoS_2 /Ti interface. Therefore, the model proposed by A. Grillo and A. D. Bartolomeo is best suited here to calculate SBH and ideality factor.

Here, fitting of the I-V characteristics of a 15 nm MoS_2 sample was attempted according to ***eq. (3-1)*** to extract SBH and ideality factor 'n' but even though the fit got close to the shape of the experimentally measured I-V curve shown in ***fig. 3.7(b)***, 'n' was far from being realistic and the same order of magnitude of the current was not obtained. Perhaps, the error is arising from an erroneous relationship assumed between 'I_0' and 'T' as in ***eq. (3-2)*** since TAC based MoS_2 might not be following thermionic mechanism of electron transport even at room temperature.

3.2.2.2 I-V sweep using bottom-side IDE (channel length = 50 μm)

As described previously, I-V sweeps were performed on another set of 15 nm MoS_2 samples with IDE of varying inter-electrode distance to study the effect of channel length on current flow in multilayer MoS_2. Apart from having IDE, this set is different from the previous set (***sec. 3.2.2.1***) in having larger area (4 mm^2) MoS_2 boxes patterned by photolithography, having the same material and thickness of contacts (1 nm Ti/ 50 nm Au) acting like bottom contacts which makes 50 nm Au to be directly in contact with MoS_2. It can also be viewed as an inverted top or bottom-side hybrid contact (***fig. 3.8 (b)***) since Au (yellow) is deposited as layer-1 on the substrate (blue) and MoS_2 (purple) is grown on top of it making a contact with Au from its bottom surface. So, the important point to note is that here MoS_2 is being electrically contacted by a metal (Au in this case) at 2 surfaces forming a bottom-side hybrid contact instead of a pair of simple top electrodes where there is only 1 contact interface per electrode.

Following the tracks of work done by S. Walia et al., where they show Schottky contacts formation between few layer n-type MoS_2 and four metals (Al, W, Au, Pt) with different work functions but higher than that of MoS_2, which is exactly the case depicted in ***fig. 3.1***, it can be understood firstly, that Al contact offers the smallest barrier for current conduction through the junction and secondly, the most popular and conventionally used contact materials form rectifying Schottky contacts with n-type MoS_2 [13]. N. Kaushik et al., further claim that the TE mechanism of current transport dominates at Au-MoS_2 junction [3] which results in rectifying I-V characteristics as discussed previously.

It should also be noted that the lateral size of MoS_2 nanoflake in S. Walia et al.'s study is ~ 100 nm, so from this it can be inferred that the contacts were spaced not more than 100 nm apart. This inter-electrode spacing is way smaller than the spacing between electrodes of TAC based MoS_2 samples in ***fig. 3.7(a)*** and ***fig. 3.8(a)***. Yet, the rectifying trend is seen in the samples with inter-electrode spacing of 2 μm and 50 μm and in ***fig. 3.7(b)*** and ***fig. 3.8(d)*** respectively. It is therefore safe to say that TAC based MoS_2 films start showing clear rectifying characteristics in the applied bias range of $\pm$10V given that Au is used as a contact metal with an inter-electrode spacing equal to or below 50 μm. ***Fig. 3.7(b)*** and ***fig. 3.8(d)*** confirm that as one approaches the smaller limits of inter-electrode spacing, current is observed to be rectifying for both polarities of applied voltage indicating presence and domination of Schottky nature of both electrodes (source and drain) formed with MoS_2.

However, ***fig. 3.8(c)*** shows I-V sweeps of D1-D4 which are linear in the applied voltage range of 10V. They differ by an increasing slope with each device that indicates an increase in current as the interelectrode spacing decreases from 200 µm (D1) to 75 µm (D4). This indicates that MoS_2 is behaving like a highly resistive resistor (as expected) whose resistance keeps on decreasing as the distance (inter-electrode spacing, 'L') between a pair of electrodes decreases because resistance ∝ 'L'. Linear characteristics in a certain range of applied voltage don't necessarily mean Ohmic contacts because the barrier height might be low as compared to the series resistance at both contact interfaces and that gives an impression of linear sweep in that voltage range [5].

3.3 Capacitance – Voltage (C-V) measurements

Given that TAC based MoS_2 is a highly resistive material, it makes a good MSM device and an even better metal-insulator-metal (MIM) device. Therefore, capacitance vs voltage (C-V) measurement here becomes inevitable and more so since SBH extraction wasn't successful through I-V measurements. C-V measurement was performed across the devices by utilising consecutive IDEs as metal surfaces that encase the MoS_2 thin film as shown in ***fig. 3.8(b)***. This can be visualised as a metal-MoS_2-metal capacitor.

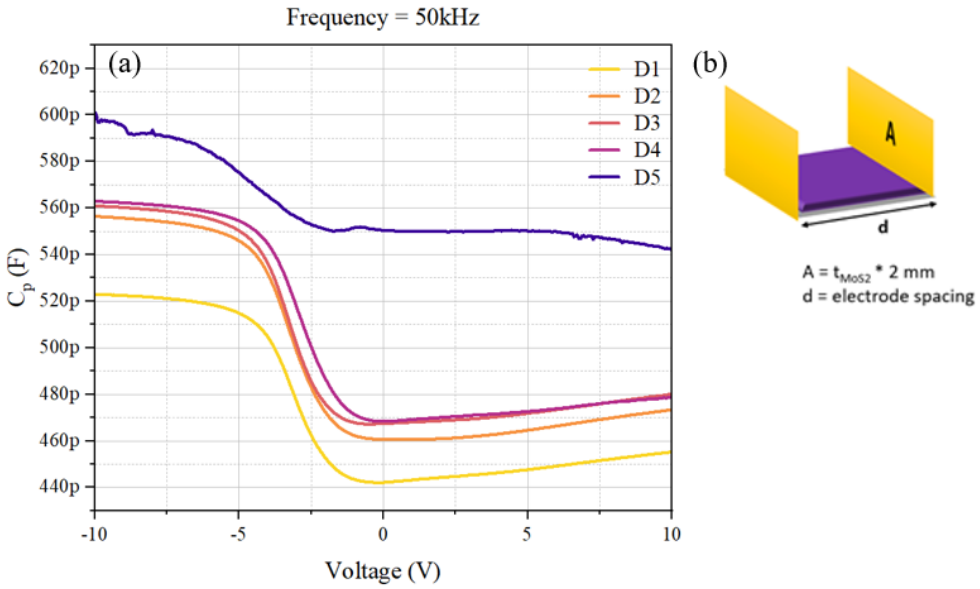

***Fig. 3.9**: **(a)** C-V plot for a 6 nm MoS_2 with IDE based design **(b)** a section of the structure showing highly resistive almost insulating MoS_2 (purple) sandwiched between metal (Au) electrodes.*

The structure in ***fig. 3.8(b)*** forms what is commonly known as interdigital capacitor (IDC) and was used for the C-V measurements shown in ***fig. 3.9(a).*** Capacitance was measured across these structures while sweeping voltage from negative to positive values. C-V measurement thus provides an avenue to delve again into SBH extraction and also understand the doping type and level of TAC based MoS_2 thin films.

R. Igreja and C. J. Dias have modelled a similar structure with 6 IDEs as bottom contacts to a sensitive layer on top of them for which capacitance is to be measured [14]. Using a conformal mapping technique, they proposed a generalised model for a multilayered material with IDEs to calculate the total capacitance while also taking into account the effect from all the N-layers, substrate as well as capacitance between electrodes and fringing effects at the outer electrodes. Other studies use similar techniques like capacitive transduction modelling to model coplanar IDC structures [15], [16], [17]. None of the methods were suitable to model this peculiar case presented here since the IDEs are sandwiched between two dielectric layers (SiO_2 and MoS_2) and the studies referenced above are for cases with complete dielectric encapsulation of the IDEs i.e., the dielectric above the IDEs is a very thick film exceeding the thickness of the electrodes which is not the case here since MoS_2 thickness (6 nm) is of the same order as that of the electrode thickness (50 nm). Also, unlike the case in [14], where substrate thickness (t_{SiO_2}) is much greater than the spatial wavelength (λ: distance between alternating electrode) of the unit cell shown in ***fig. 3.10(b)***, here it is the opposite, where λ (of the order of 1 mm) >> t_{SiO_2} (which is 300 nm).

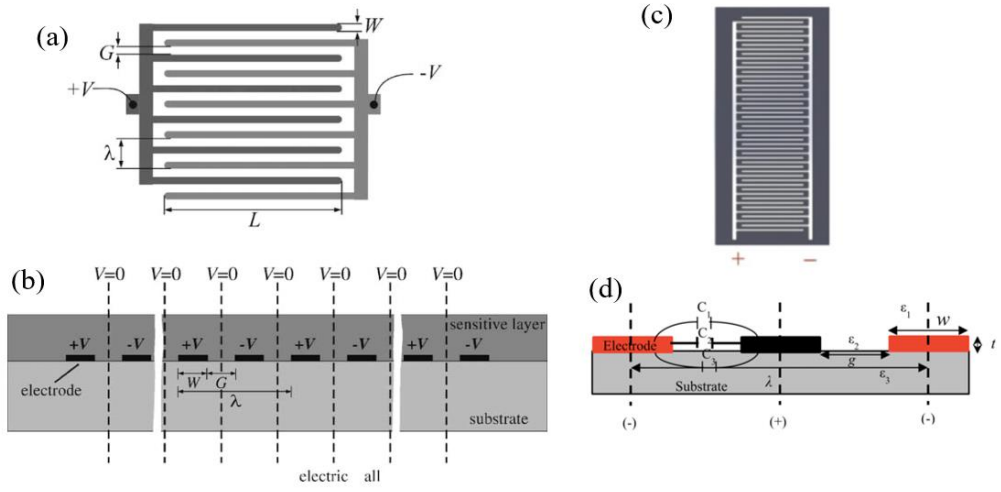

Fig. 3.10*: **(a)**, **(b)** taken from [14] and **(c)**, **(d)** taken from [18], show top view **(a)**, **(c)** and cross-sectional view **(b)**, **(d)** of IDC. Difference between **(b)** and **(d)** lies in the thickness of the MUT relative to the thickness of electrode.*

Therefore, another method was used to model the results shown in ***fig. 3.9(a)*** which considers the material under test (MUT) as a parallel plate capacitor (***fig. 3.9(b)***) and the interelectrode capacitances arising from curved electric field lines passing through MUT and substrate to be modelled by a method that utilises complete elliptic integral of the first kind (**K**) [18].

From the measurements, the trend seems to follow the capacitance of a parallel plate capacitor as seen from C-V curves for 5 devices differing only in their inter-electrode spacing with D1 having the highest and D5 the lowest in ***fig. 3.9(a)***. The curve seems to follow a shape characteristic of p-type doping (with accumulation region on the negative side and inversion region on the positive axis of applied voltage) and the transition from accumulation to inversion seems to be prominent until D4 and seems to get distorted for D5 with the least inter-electrode spacing. Another noticeable point is that capacitance increases with decreasing 'd' (interelectrode spacing) as expected for a parallel plate capacitor. Assuming that these curves are indeed indicating MoS_2 capacitance, which shows a p-type behaviour then this explains why certain devices show non-rectifying I-V characteristics when Ti/Au contacts are used which is the case when $\varphi_m > \varphi_s$ for a p-type semiconductor [1] (for example, D1-D4 as shown in ***fig. 3.8(c)***).
Utilising the equations in [18] and assuming dielectric constant of SiO_2 and MoS_2 to be 3.9 and 5 respectively, the capacitances for D1, D2, D3, D4 and D5 are calculated to be: 0.30 pF, 0.31 pF, 0.33 pF, 0.34 pF and 0.37 pF respectively. But back calculating dielectric constant for MoS_2 from the measured capacitance values, it turns out to be 12800, which seems extremely high and unrealistic. Perhaps some other effects are causing such a high measured capacitive value which are beyond the scope of this work.

3.4 Contact engineering

Making contacts to 2D MoS_2 thin films is tricky from the point of view of lithography as thicker metal contacts might chip off fragile thin films during lift off. This happened in some of the devices in this work, one of which was also showed in chapter 2 – ***fig. 2.4(c)***. Another consideration is fermi level pinning where the work function of the metal contact aligns with a defect induced energy level in between the band gap of MoS_2, thereby leaving the work function of the metal contact to be irrelevant [19], [20], [21]. This can bring disadvantages

to the overall device structure as it leads to high Schottky barrier and energy loss due to joule heating at the junctions as result of high contact resistance and might also damage the device due to current crowding. In this work, modulation of optical properties of MoS_2 greatly depend on its thickness and the modulation results along with their details will be discussed more in ***ch. 4***. That is why the implications of having suitable contacts that can form a low enough SBH for current to flow through our highly resistive TAC based MoS_2 are desirable and will be discussed. Contact engineering thus refers to selecting the most appropriate contact material, thickness and design of contacts that are to be deposited on a device (thin film MoS_2 in this case) in order to be able to measure the most out of the device while limiting the effects of contacts themselves on the device.

This section first explains the basics of transfer length method (TLM) and then presents contact resistance calculations using this method for two sets of samples that differ by choice of contact material and contact design.

3.4.1 Transfer length method (TLM)

As mentioned previously, a 4-point probe is an easy method to estimate a material's resistance quickly; however, it underestimates critical parameters like sheet resistance (R_{sh}) and contact resistance (R_c) due to current shunting between the inner sensing electrodes in most cases [22].

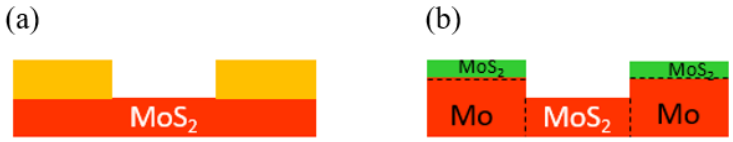

***Fig. 3.11**: **(a)** Standard top contact design **(b)** Phase engineered contacts by co-sulphurising bulk Mo along with thin Mo to form a thin film MoS_2 channel (middle red box) transitioning into metallic Mo phase whose topmost layers only form MoS_2 (green).*

TLM is therefore more suitable and accurate to determine R_c and R_{sh}. This sub-section will discuss the results obtained using TLM for two sets of samples based on:

1. Contact material- Here, top contacts using Sn/Au and Mo will be compared. Ti/Au top contacts are deliberately left out from comparison due to low current and rectifying behaviour which is difficult to analyse by this method.

2. Contact architecture - Here, standard top contact design will be compared with Mo co-sulphurised hybrid top-edge design shown in ***fig. 3.11(a)*** and ***(b)*** respectively.

Simply put, TLM is a method of estimating R_c and R_{sh}, also separates out both. A TLM design typically has 4 or more contacts on a material to be measured. These contacts are separated by increasing distance between them as shown in ***fig. 3.12(a)*** and resistance is measured between each consecutive pair. The resistance between each pair is plotted as a function of the distance (L1, L2...) between them in a plot referred to as R_{tot} vs length. ***Fig. 3.12(b)*** depicts this plot which should be linear, and it is extrapolated to the point of zero length resistor i.e., y-intercept which signifies the point where the contacts are right next to each other with no material in between them.

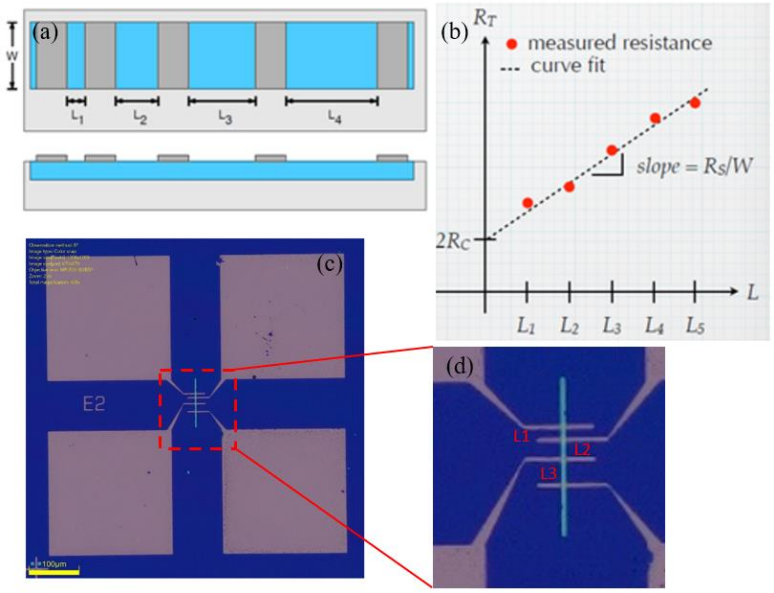

***Fig. 3.12**: **(a)** Arrangement of contacts for a TLM measurement showing increasing separation between consecutive contacts. The spacings are labelled as 'L1', 'L2', 'L3'and so on [23]. **(b)** Reciprocal of the **s**lope from I-V measurement between each consecutive pair of contacts corresponds to the resistance between them and is plotted against the corresponding spacing. The linear fit is extrapolated to zero-length resistance to calculate R_c and the slope is used to calculate R_{sh} [23]. **(c)** Optical image of a sample consisting of channel (teal blue) with Ti/Au TLM contacts extending out to larger area pads (faded brownish-copper colour) **(d)** Zoomed-in view showing the unequally spaced TLM contacts.*

So, total resistance is just a function of the contact resistance, R_c. The slope of this plot is used to calculate R_{sh}. ***Fig. 3.12(c)*** shows a TLM sample with 4 µm wide MoS_2 channel and four TLM contacts separated by distances L1, L2, L3 (shown in a zoomed-in image in ***fig. 3.12(d)***) and extended large area contact pads for ease of use with needle probes. The equations below explain this analytically and are used to calculate R_c and R_{sh}:

$$R_{tot} = 2R_M + 2R_C + R_{semi}$$

(3-5)

where, $\mathbf{R_M}$ is the resistance of metallic conductors, R_c is the contact resistance at the metal-semiconductor junction and R_{semi} is the resistance of the semiconductor (here, MoS_2) channel. R_M can be neglected here since it is very small compared to R_c and R_{semi}. So, R_{tot} can be written as:

$$R_{tot} = 2R_C + R_{semi}$$

(3-6)

And

$$R_{semi} = R_{sh}\frac{L}{W}$$

(3-7)

where, **W** is the width of the TLM channel. This implies that:

$$R_{tot} = 2R_C + R_{sh}\frac{L}{W}$$

(3-8)

Comparing ***eq. (3-8)*** to the general equation of a line: y=mx+c, where y= R_{tot} and x = L, c = $2R_c$ and m is the slope = $\frac{R_{sh}}{W}$. From here, contact resistance can be calculated as,

$$R_c = \frac{c}{2} = \frac{y - intercept}{2}$$

(3-9)

And

$$R_{sh} = W \cdot slope$$

(3-10)

Following sub-sections discuss the significance of using different contact materials and contact architecture and how they affect R_c of TAC based MoS_2 devices used here.

3.4.2 Choice of contact material

Conventionally, Au contacts have been used to contact devices owing to high conductivity and low contact resistance. However, as discussed previously, this introduces a level of complexity when the material to be contacted is a semiconductor and more so if it is MoS_2 - a well-known lubricant which makes adhesion difficult. Additionally, due to dewetting

property of Au, a layer as thin as 0.5 nm -1 nm of Ti is sufficient to aid in adhesion of Au with MoS_2 [24]. Alternatively, Ag paste can also be used but since it is solvent based, the paste can be very messy to apply and due to the high diffusion property of Ag particles, thin film layers can get shorted among themselves in a stack. So, sputtered Ti/Au was initially the best option to start with, but since it forms rectifying contacts with a high junction resistance with MoS_2, I-V characteristics in this case are not compatible with TLM analysis and determination of R_c. Therefore, following the statistical study done by A. Kumar et. al., where they experimentally characterised 720 MoS_2 transistors with In/Au and Sn/Au contacts [25], another set of devices was also made in this work, this time replacing Ti/Au top contacts with Sn/Au top contacts. A. Kumar et. al., reported low contact resistance materials made of low melting point metals like Indium (In) and Tin (Sn) that are less damaging to MoS_2 layers.

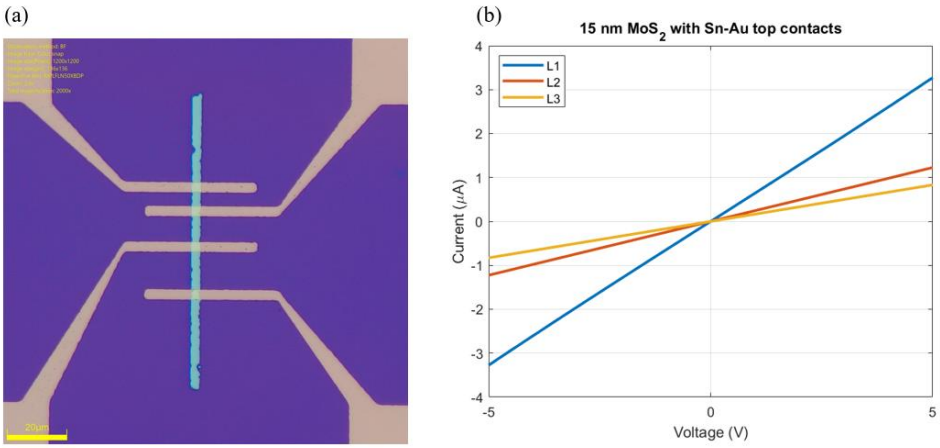

Fig. 3.13 (a) *Optical image of MoS_2 TLM bar ('MoTLM150' from tab. 2.1) with with increasing distance of TLM contacts on it.* ***(b)*** *I-V sweeps of channel lengths L1 = 2 µm, L2 = 6 µm, L3 = 10 µm on Si/SiO_2 (300 nm) substrate shows linear characteristics with 10 nm Sn/25 nm Au contacts.*

Fig. 3.13(a) shows a TLM arrangement of Sn/Au contacts patterned by UV-lithography and deposited by magnetron sputtering without breaking vacuum between Sn and Au deposition runs. The maximum current here corresponding to L1 = 2 µm at ±5V is almost 10 times higher than that in the case of 1 nm Ti/25 nm Au contacts shown in ***Fig. 3.7(b)***.

3.4.3 Choice of contact geometry

Various contact architectures have also been proposed from top, edge and a hybrid of top-side contacts. ***Sec. 3.2.2*** discussed standard top contacts on MoS_2 as this is the easiest to

make and serves as a good starting point. But later, a hybrid design of top-side contacts (***fig. 3.11(b)***) were made by co-sulphurisation of 75 nm thick Molybdenum (Mo) contacts along with the thin Mo channel which is to be measured by TLM after sulphurization. The procedure used to do this was to first deposit the TLM bar of desired thickness (much thinner than the contacts' thickness in the next step), then photolithography pattern of top contacts and deposition of Mo of much greater thickness followed by lift off. This gives a Mo TLM bar of a low thickness along with Mo contacts of relatively high thickness. The entire device (the TLM bar as well as the contacts) is now made up of Mo, just of different thicknesses. This entire device is then sulphurised in the TAC furnace and so each of the two Mo regions (thin TLM bar and thick contacts) becomes MoS_2. In essence the thin TLM bar sulphurises completely to form MoS_2 while only the top few layers sulphurise in the thick regions to form MoS_2. This is depicted in ***fig. 3.11***. The contacts thus have predominantly partially sulphurised Mo or regions of Mo not sulphurised at all at the bottom. So, the regions overlapping with TLM bar remain Mo (metallic) and so this can be viewed as Mo-MoS_2-Mo interface. Since the sulphurisation of the thin Mo TLM bar and thick Mo metal contacts is occurring together, therefore these contacts are being referred to as co-sulphurised contacts.

According to the current transport mechanisms at a metal-semiconductor junction, to obtain low R_c values, charge injection from the metal to the semiconductor should be as efficient as possible by either doping the semiconductor or lowering the Schottky barrier height or both [2]. Low R_c is desirable in a metal-MoS_2 device for applications pertaining to transistors, photodetectors and for any application where charge injection into MoS_2 or current readout is crucial. ***Fig. 3.14*** shows I-V sweeps of MoS_2 TLM bars for different channel lengths for three different contact materials – Ti/Au, Sn/Au, Mo. While Sn/Au and Mo contacts appear to have linear characteristics, Ti/Au shows non-linear characteristics. This is the reason that for R_c comparison, Ti/Au contact material was not considered. For a monolayer of MoS_2, Sn/Au contacts render an average R_c of around 1.3 kΩ·μm [25]. Here, at no gate bias, few layer TAC based MoS_2 has a mean R_c of ~ 1.22×10^3 kΩ·μm (using ***eq. 3.9***) when Sn/Au contacts are used. Mo top contacts are comparable to Sn/Au contacts with a mean R_c of ~ 1.44×10^3 kΩ·μm. However, Mo top-edge hybrid contacts made by co-sulphurising the contacts along with MoS_2 in the furnace showed an anomalous and unexpected behaviour by showing much greater R_c of ~ 65.8×10^3 kΩ·μm. These results are summarised in ***fig. 3.15***.

Several studies have reported different methods and analysis to determine R_c of a metal-MoS_2 contact. Most of them use a gate voltage to dope the active channel in MoS_2 to obtain a low value of R_c using different contact materials [22], [25], [26], [27], [28], [29]. One such experimental study introduced the concept of 'lateral access resistance' and showed that it has a profound effect on R_c and is independent of current transport mechanisms at the junction which greatly depend on doping, temperature and even deposition pressure of the contacts [22]. It goes on to explain that when Au contacts are deposited on multilayer MoS_2 under ultra-high vacuum ~ 10^{-9} Torr, it facilitates clean Au deposition and prevents any adsorbates to be trapped at the Au-MoS_2 interface resulting during the deposition resulting in higher mobility of charge under the contacts.

Furthermore, Kang et al., explain why Schottky theory based on work functions of the metal and MoS_2 is not sufficient and non-intuitive to understand certain abnormal observations at the metal-thin film TMDs interface. They show from an atomistic modelling perspective that ohmic contacts with high charge injection can be formed with MoS_2 despite using a high work function metal as long as MoS_2 under the contact is metallised forming an alloy with the metal contact due to d-orbital hybridization [30].

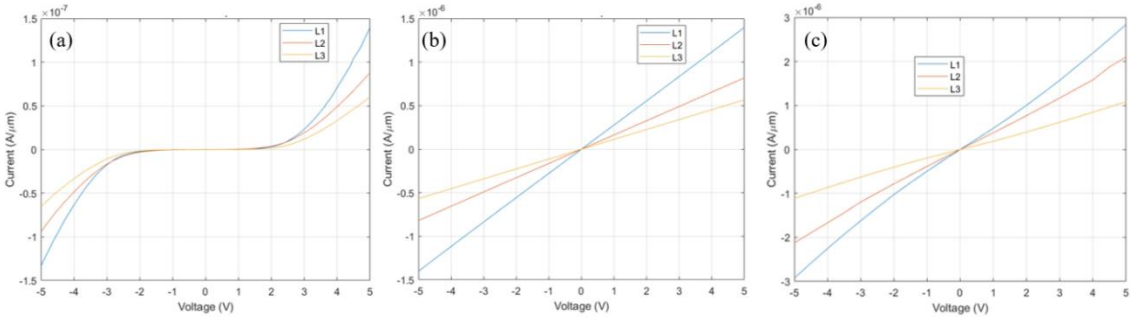

***Fig. 3.14**: I-V sweeps normalised by channel width (4 μm) using different materials used as contacts for multilayer MoS_2. **(a)** Ti/Au **(b)** Sn/Au **(c)** Mo patterned according to TLM arrangement where channel lengths are L1 = 2 μm, L2 = 6 μm, L3 = 10 μm.*

In another study, they also show how a high work function (4.5 eV) Mo contact forms a lower Schottky barrier (0.1 eV) as compared to Ti, a lower work function (4.3 eV) metal that forms a higher Schottky barrier (0.33 eV) with MoS_2 [31]. This is particularly interesting because in the case of TAC based multilayer MoS_2 presented here, Ti/Au contacts are much worse (high resistance) as compared to Mo top contacts. This is evident from the high resistance rectifying contacts formed by Ti/Au (as discussed in ***sec. 3.2***) and linear contacts

formed by Mo contacts that allow higher current to pass through as shown in ***fig. 3.14(a)*** and ***(c)*** respectively.

Combining the concept of orbital overlap and edge contacts being superior to top contacts for multilayer TMDs, R. Kappera et al., demonstrated phase engineered MoS_2 contacts for MoS_2 channel [27]. They used metallic 1T MoS_2 to contact semiconducting 2H MoS_2. Along similar lines, a third set of samples - top-edge hybrid Mo co-sulphurised contacts - was made as described previously and shown in ***fig. 3.11*** with the rationale that while TAC process can sulphurise Mo under ~ 20 nm completely, it only partially sulphurises very thick Mo. For Mo of thickness ~ 75 nm (used here), TAC process only sulphurises top few layers while leaving the bottom Mo as it is, and it is this Mo at the bottom which is in direct contact to the thin Mo channel that becomes the thin MoS_2 after sulphurisation and which is to be measured. This work was performed by by Mr. Christopher P. Murray (postdoc of the group) and Dr. G. S. Duesberg in a currently unpublished work. The fact that thin Mo (pre-sulphurisation) is a part of the thick Mo (that forms the hybrid contact), they are very intimately connected and should have a good orbital overlap even after they have been sulphurised. Therefore, these contacts were fabricated with the assumption that they will give the least contact resistance and will be the most compatible with MoS_2 TLM bar. However, the results show something different – Mo co-sulphurised (Mo-co) contacts showed much higher contact resistance than Mo and Sn-Au contacts (***fig. 3.15***).

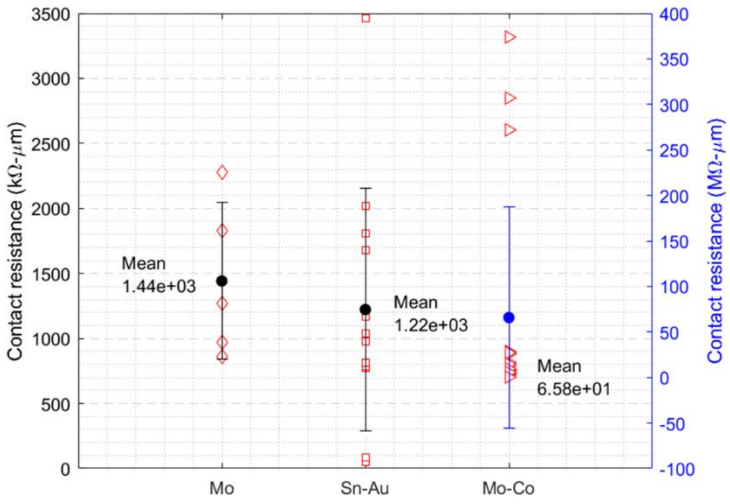

Fig. 3.15*: Measured contact resistances of devices with* ***(left)*** *Mo top contacts,* ***(middle)*** *Sn-Au top contacts and* ***(right)*** *Mo co-sulphurised hybrid top-edge contacts with their respective mean* R_c *values and standard deviation among the devices depicted by error bars.*

Two very possible reasons for this can be that since the entire device undergoes TAC process at 850°C, the partially sulphurised Mo that forms the contact might have lost its metallicity or undergone distortion in its structure and secondly, TAC produces polycrystalline MoS_2 and all layers are not uniformly arranged in a horizontal direction.

Fig. 3.15 shows R_c values of various devices for each set of contacts mentioned previously. From this, it can be concluded that 10 nm Sn/25 nm Au contacts worked best for TAC based multilayer films with the lowest R_c obtained with Sn/Au top contacts to be 53.8 kΩ·µm. It is to be noted that TAC based multilayer TMD films are not uniformly oriented in one direction so edge contacts would lose their efficiency of charge injection across all layers as they will lose access to direct in-plane contact with the individual layers [32]. Also, TLM measurements shown here were performed under room ambient conditions without using any dielectric encapsulation on MoS_2 and any gate bias.

Fig. 3.16 depicts the lowest R_c values plotted against MoS_2 thickness for each case (Mo top contacts, Mo co-sulphurised (Mo-co) contacts and Sn-Au top contacts). From this, it is seen that Mo-co contacts perform well under ~ 15 nm with R_c value of 11 nm thick MoS_2 being even lower than the R_c value of 1.5 nm thick MoS_2 with Mo top contacts, while R_c value of 15 nm MoS_2 with Mo top contact is somewhat comparable to 15 nm MoS_2 having Mo-co contacts. But R_c value of 15 nm MoS_2 with Sn-Au top contacts outperforms the other two contacts with the lowest R_c ~ 53.8 kΩ·µm.

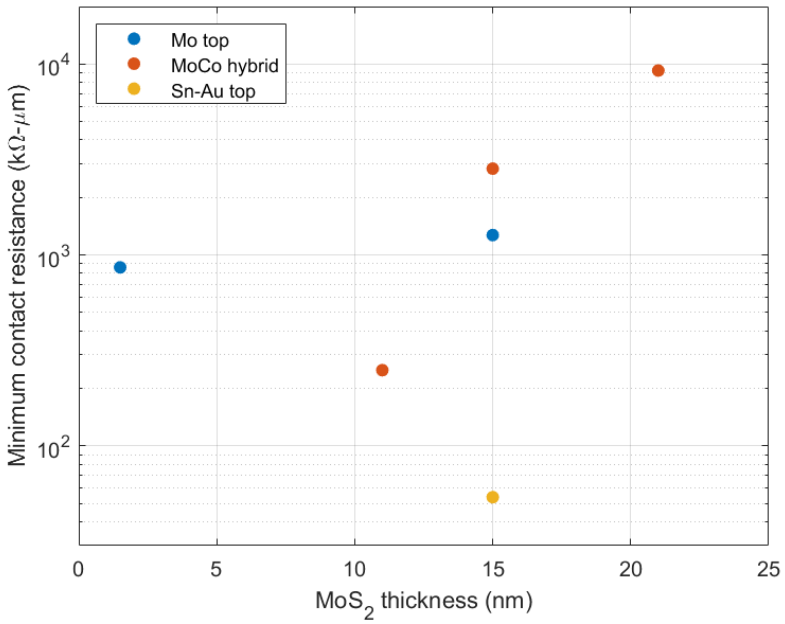

Fig. 3.16*: Lowest calculated contact resistances at different* MoS_2 *thicknesses for each of the contact material and contact geometry case.*

3.5 Thermal coefficient of resistance

Closed cycle refrigerator (CCR) setup with a helium cooled cold head (RDK-1xx) from Sumitomo Heavy Industries Ltd. suited to operate at a temperature range of 4 – 320 K, Lakeshore 331 temperature controller to sweep the temperature of the CCR with the sample placed inside it under vacuum and Keithley source meters were used to provide an electrical bias. The entire experiment setup including temperature sweep with simultaneous application of voltage bias and current readout was controlled remotely using LabView which was also used for data collection at the end of the experiment. ***Fig. 3.17(a)*** shows resistance as a function of temperature R(T) for 3 nm and 30 nm on MoS_2 on Si_3N_4 and 3 nm MoS_2 on quartz.

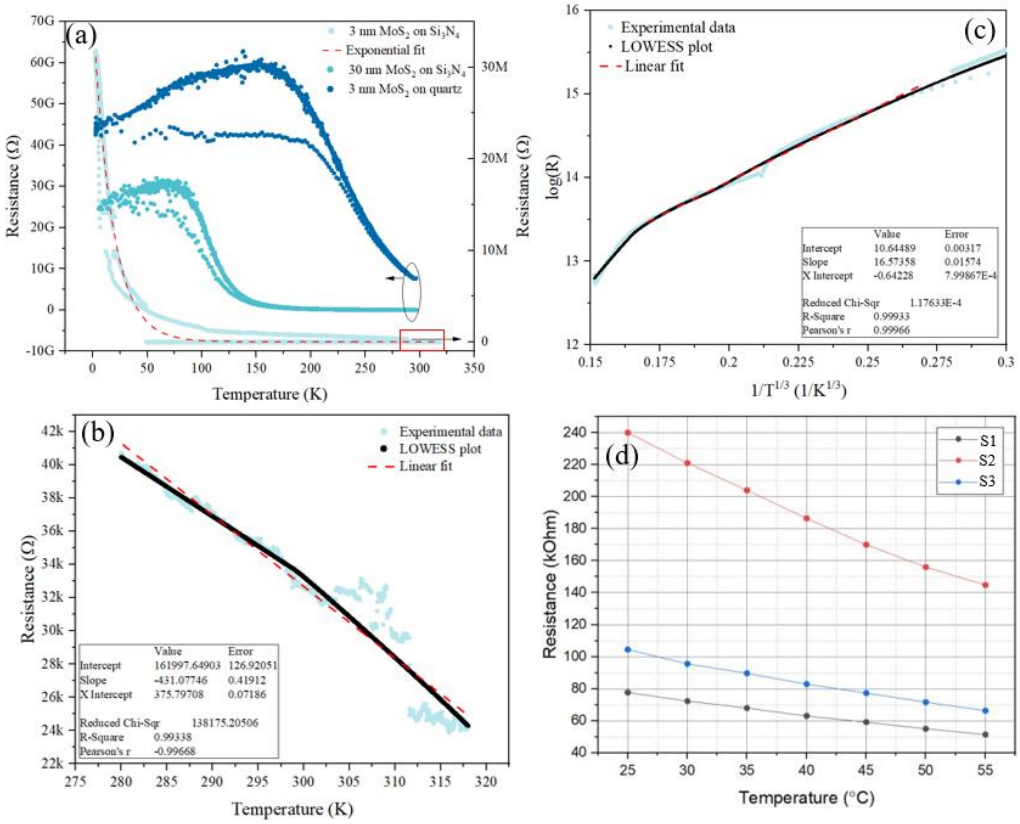

Fig. 3.17*: **(a)**Temperature dependent resistance plots for MoS_2 of different thicknesses on Si_3N_4 and quartz substrates ('sample8-10' from tab. 2.1). Exponential fit for 3 nm MoS_2 on Si_3N_4 substrate ('sample8' from tab. 2.1) is shown with red dashed curve. **(b)** Zoomed-in plot and linear fit after smoothing of 'sample8' in the temperature range marked by red box in **(a)**. **(c)** Logarithm of resistance showing dependence on temperature (for 'sample8') based on Mott-VRH theory. **(d)** Resistance vs temperature plots of thicker TAC based samples showing similar behaviour as in **(b)** upon heating on a hot plate in ambient temperature and pressure.*

These unpatterned samples were made on 1 cm^2 large area substrates and mounted on a carrier plate placed inside a cryogenic chamber capable of creating vacuum and sweeping

temperature down to 5 K and up to 323.15 K (50 ℃). Thin conducting wires were pasted using Ag paste on the samples' surfaces in a 4-point probe type of arrangement on the sample surface and left to dry. These thin wires extending out of the sample surface can then be soldered onto the built-in electrodes on the carrier plate which extend out of the vacuum chamber and are connected to a Keithley source and measurement unit outside the chamber. This is used to control applied voltage or current from outside when the chamber is under vacuum.

A bias of 100V was applied to the outer probes and current was measured between the inner probes at each temperature point while temperature was swept from room temperature to 5 K and back to room temperature for 3 nm and 30 nm MoS_2 on quartz and Si_3N_4 respectively while the 3 nm MoS_2 on quartz sample was swept from room temperature to 5 K and back to room temperature and even beyond i.e., ~ 50 ℃). While the plot corresponding to 'sample8' clearly shows a typical semiconducting behaviour of resistance with decrease in temperature, the other two plots corresponding to 'sample9' and 'sample10' start showing some saturation around 70 K and 200 K. ***Fig. 3.17(b)*** shows the resistance variation in the temperature range going above room temperature marked by red box in ***fig. 3.17(a)***. After applying locally weighted scatter plot smoothing (LOWESS) – an in-built functionality in Origin pro plotting software – which reduces the influence of outliers on the bulk of meaningful trend in a data, the plot was linearly fit to obtain the slope which gives a change in resistance over a range of temperature. This was done because the measured data looked scattered in certain temperature ranges and extracting meaningful trend was difficult. This technique makes it easy to visualise trends in noisy data like the one here by smoothing fluctuations and outliers in data. Temperature coefficient of resistance (TCR), 'α' relates temperature 'T' and resistance 'R' as: $\alpha = \frac{1}{R_a}\left(\frac{R-R_a}{T-T_a}\right) = \frac{1}{R_a}\left(\frac{\Delta R}{\Delta T}\right)$ where, T_a is reference temperature and R_a is the resistance at reference temperature (T_a). $\frac{\Delta R}{\Delta T}$ is the slope of the R(T) plot shown in ***fig. 3.17(b)*** and is used to calculate TCR for 3 nm MoS_2 on Si_3N_4 in the temperature range shown in ***fig. 3.17(b)***. This gives $\alpha_{MoS_2} = \frac{-431}{25\times10^3} = -0.01724\ K^{-1}$ or -1.724 $\%K^{-1}$.

The negative sign here indicates that MoS_2 is semiconducting since its resistance increases exponentially with decreasing temperature as is also evident from the fit of 3 nm MoS_2 on quartz in ***fig. 3.17(a).***

Additionally, thicker samples of TAC based MoS_2 - S1, S2, S3 were made, and they were heated (post-deposition) on a hotplate under ambient pressure conditions and resistance was measured at different points in temperature. The details of the TAC process are mentioned in ***tab. 3.1*** and the plots of R(T) for these samples are shown in ***fig. 3.17(d)***. Anneal time in ***tab. 3.1*** refers to the in-furnace annealing time of the samples at their respective deposition temperature without forming gas ($Ar+H_2$) but only Ar gas. For the samples S1, S2 and S3 the TCR calculated is 1.12, 1.33 and 1.2 % ^oC respectively.

Table 3.1*: TAC details of MoS_2 samples that underwent post-deposition heating in ambient pressure conditions for measurement of R(T).*

Sample	MoS_2 thickness (nm)	Deposition temperature (℃)	Deposition time (min)	Annealing time (min)
S1	15	800	30	30
S2	55	750	30	-
S3	55	900	30	30

While disordered solids are known to follow Mott-variable range hopping (VRH) at low temperatures, there are contradicting studies about transport mechanisms in MoS_2 at low temperature. Transport studies are important to understand behaviour of charge mobility in 2D field effect transistors (FETs) [33].

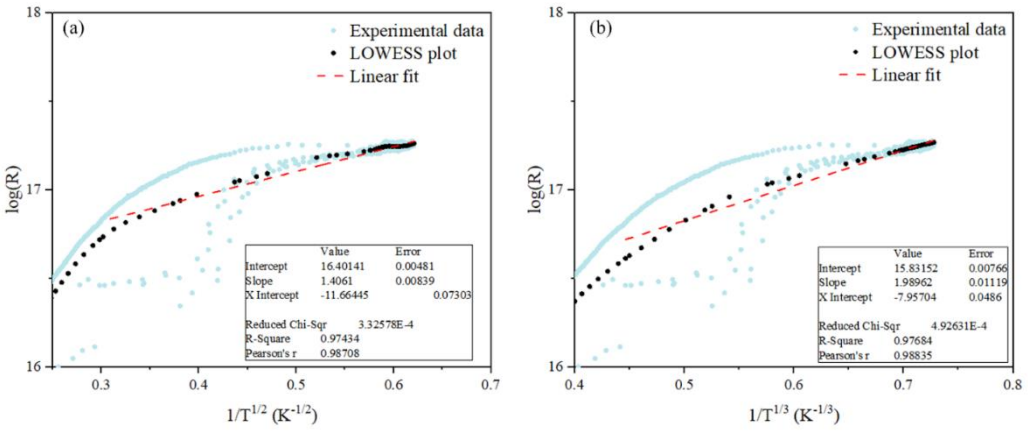

Fig. 3.18*: **(a)** Logarithm of resistance against **(a)** $T^{-1/2}$ and **(b)** $T^{-1/3}$ is plotted that shows ES-VRH and Mott-VRH mechanism of carrier transport respectively. The data seems to fit more closely to ES-VRH model.*

Fig. 3.17(c) shows log(R) vs $T^{-1/3}$ for ~ 296 K (room temperature) to 50 K (mid temperature range) for 'sample8' and fits very well to Mott-VRH but plotting the data for very low temperature range ~ 2.7 K to 11 K, the data fits slightly better to Efros-Shklovskii (ES) VRH than Mott-VRH as shown by linear fits of log(R) vs $T^{-1/2}$ and log(R) vs $T^{-1/3}$ respectively in ***fig. 3.18(a)***, ***(b)***. J. Xue et al., reported MoS_2 nanoflakes to fit Mott-VRH trend more than ES-VRH in the 6 K to 25 K temperature range [34]. Contrary to this, N. Papadopoulos et al., claim ES-VRH dominated behaviour for 1T/1T' MoS_2 [35] which is also backed by study done by Jana Hrda. The data presented in this section and log (R) fits to both $T^{-1/2}$ and $T^{-1/3}$, can be used to conclude that TAC based MoS_2 also seems to follow ES-VRH transport mechanism at low temperatures.

3.6 Conclusion

4-point probe data of multilayer MoS_2 samples were presented that reveal an optimum temperature of sulphurisation using TAC process to be around 750-850℃. Any temperature below this is not able to fully sulphurise the transition metal (Mo) and the resulting MoS_2 largely remains metallic perhaps due to sulphurisation of only its topmost layers. It can also be inferred that temperature plays a bigger role than time for the TAC process since films sulphurised at lower temperatures than 750℃ for as long as 60 mins show much lower sheet resistance and resistivity compared to when sulphurised at 750℃ or higher temperature possibly due to partial conversion of Mo into MoS_2 leaving behind significant metallicity coming from Mo. This corroborates well with studies on TAC based MoS_2 performed by another group [36].

The semiconducting nature of TAC based MoS_2 is also proven by resistivity vs temperature measurements where measured resistivity data fits exponentially as a function of decreasing temperature. It further shows that at mid-room temperature, MoS_2 seems to use Mott-VRH mechanism for current transport but at very low temperatures, it is more aligned to follow ES-VRH mechanism. The data becomes very noisy at such temperatures for the samples measured here so an accurate distinction between the two mechanisms was difficult to observe, perhaps these measurements can be repeated with thinner MoS_2 and with a slower scan rate at low temperatures to study the transport mechanism at low temperatures better.

Other I-V measurements were carried out at room temperature which showed Ti/Au top contacts to be rectifying when deposited on ~ 15 nm thick MoS_2 and spaced ~ 2 um apart. The most probable reason for this lies in fermi level pinning mechanism at the MoS_2-contact interface. Such curves follow a typical back-to-back double Schottky diode model that consists of a series resistance sandwiched between them which has also been studied previously. More knowledge of modelling techniques is required to successfully extract a realistic value of ideality factor and Schottky barrier height which when combined with the knowledge of transport mechanism and whether n-type or p-type nature of MoS_2 can provide greater insight in to TAC based TMD materials.

I-V sweeps were also done using an IDE design that serves as bottom-edge hybrid contacts to MoS_2. The material used was Ti/Au and since this layer was deposited prior to MoS_2 sulphurisation, the contact interfaces thus consisted of Au/MoS_2. Such a design was implemented to be compatible with Ossila's I-V and solar tool kit that includes easy to use push-fit test boards and integrated SMUs interfaced with a measuring software. The same IDE design was used to fabricate IDC structures to carry out C-V measurements on a 6 nm MoS_2. The C-V curves showed accumulation region at the negative voltage bias and inversion at positive voltage bias thus indicating its p-type nature.

Finally, not just the contact design but also contact materials were engineered to form the best contacts with TAC based MoS_2 with the aim to achieve as low contact resistance as possible. For this, other materials apart from Ti/Au were used, like – Sn/Au top contacts, Mo top contacts and Mo co-sulphurised top-edge contacts. After a comparison of all of them thorough I-V characterisation and TLM calculations, the best performing contact design and material for TAC based MoS_2 studied here was found to be Sn/Au top contacts that formed Ohmic contacts in a voltage range of -10V to 10V as well as gave the lowest R_c ~ 53.8 $k\Omega \cdot \mu m$.

Some inherent properties of TAC based multilayer MoS_2, like layers not being oriented in the same direction and fermi level pinning with metal contacts make it especially difficult to analyse TLM results. Nonetheless, this study sheds light on characterising multilayer MoS_2 films using conventional methods of characterisation to the best of the capability and scope of this project and serves as a platform for future advanced studies.

References

[1] R. F. Pierret, *Semiconductor Device Fundamentals*. 1996.

[2] S. M. Sze and K. K. Ng, *Physics of semiconductor devices*, 3rd ed. Hoboken, N.J: Wiley-Interscience, 2007.

[3] N. Kaushik *et al.*, "Schottky barrier heights for Au and Pd contacts to MoS_2," *Applied Physics Letters*, vol. 105, no. 11, p. 113505, Sep. 2014, doi: 10.1063/1.4895767.

[4] C. Lu, L. An, Q. Fu, J. Liu, H. Zhang, and J. Murduck, "Schottky diodes from asymmetric metal-nanotube contacts," *Appl. Phys. Lett.*, 2014.

[5] J. Osvald, "Back-to-back connected asymmetric Schottky diodes with series resistance as a single diode," *Physica Status Solidi (a)*, vol. 212, no. 12, pp. 2754–2758, Dec. 2015, doi: 10.1002/pssa.201532374.

[6] J. Osvald, "Ohmic contacts to moderately doped semiconductors—are they really Ohmic or low-barrier Schottky contacts?," *Semicond. Sci. Technol.*, vol. 20, no. 6, pp. 611–614, Jun. 2005, doi: 10.1088/0268-1242/20/6/022.

[7] Z. Wang *et al.*, "Extraction and Analysis of the Characteristic Parameters in Back-to-Back Connected Asymmetric Schottky Diode," *Physica Status Solidi (a)*, vol. 217, no. 8, p. 1901018, Apr. 2020, doi: 10.1002/pssa.201901018.

[8] J.-R. Chen *et al.*, "Control of Schottky Barriers in Single Layer MoS_2 Transistors with Ferromagnetic Contacts," *Nano Lett.*, vol. 13, no. 7, pp. 3106–3110, Jul. 2013, doi: 10.1021/nl4010157.

[9] A. Di Bartolomeo *et al.*, "Asymmetric Schottky Contacts in Bilayer MoS_2 Field Effect Transistors," *Adv Funct Materials*, vol. 28, no. 28, p. 1800657, Jul. 2018, doi: 10.1002/adfm.201800657.

[10] S. McDonnell, R. Addou, C. Buie, R. M. Wallace, and C. L. Hinkle, "Defect-Dominated Doping and Contact Resistance in MoS_2," *ACS Nano*, vol. 8, no. 3, pp. 2880–2888, Mar. 2014, doi: 10.1021/nn500044q.

[11] A. Grillo and A. Di Bartolomeo, "A Current–Voltage Model for Double Schottky Barrier Devices," *Adv Elect Materials*, vol. 7, no. 2, p. 2000979, Feb. 2021, doi: 10.1002/aelm.202000979.

[12] S. McDonnell, C. Smyth, C. L. Hinkle, and R. M. Wallace, "MoS_2 –Titanium Contact Interface Reactions," *ACS Appl. Mater. Interfaces*, vol. 8, no. 12, pp. 8289–8294, Mar. 2016, doi: 10.1021/acsami.6b00275.

[13] S. Walia *et al.*, "Characterization of metal contacts for two-dimensional MoS_2 nanoflakes," *Applied Physics Letters*, vol. 103, no. 23, p. 232105, Dec. 2013, doi: 10.1063/1.4840317.

[14] R. Igreja and C. J. Dias, "Analytical evaluation of the interdigital electrodes capacitance for a multi-layered structure," *Sensors and Actuators A: Physical*, vol. 112, no. 2–3, pp. 291–301, May 2004, doi: 10.1016/j.sna.2004.01.040.

[15] Y. Wang, N. Chong, Y. L. Cheng, H. L. W. Chan, and C. L. Choy, "Dependence of capacitance on electrode configuration for ferroelectric films with interdigital electrodes," *Microelectronic Engineering*, vol. 66, no. 1–4, pp. 880–886, Apr. 2003, doi: 10.1016/S0167-9317(02)01015-8.

[16] Huey-Daw Wu, Zhihang Zhang, F. Barnes, C. M. Jackson, A. Kain, and J. D. Cuchiaro, "Voltage tunable capacitors using high temperature superconductors and ferroelectrics," *IEEE Trans. Appl. Supercond.*, vol. 4, no. 3, pp. 156–160, Sep. 1994, doi: 10.1109/77.317831.

[17] L. Y. Zhang *et al.*, "Discrimination of colorectal cancer cell lines using microwave biosensors," *Sensors and Actuators A: Physical*, vol. 216, pp. 405–416, Sep. 2014, doi: 10.1016/j.sna.2014.03.022.

[18] R. E. Rachmanita *et al.*, "The high capacitance for electrode structure of interdigital capacitor thin film models," 2019.
[19] C. Gong, L. Colombo, R. M. Wallace, and K. Cho, "The Unusual Mechanism of Partial Fermi Level Pinning at Metal–MoS_2 Interfaces," *Nano Lett.*, vol. 14, no. 4, pp. 1714–1720, Apr. 2014, doi: 10.1021/nl403465v.
[20] E. Pollmann *et al.*, "Large-Area, Two-Dimensional MoS_2 Exfoliated on Gold: Direct Experimental Access to the Metal–Semiconductor Interface," *ACS Omega*, vol. 6, no. 24, pp. 15929–15939, Jun. 2021, doi: 10.1021/acsomega.1c01570.
[21] C. Kim *et al.*, "Fermi Level Pinning at Electrical Metal Contacts of Monolayer Molybdenum Dichalcogenides," *ACS Nano*, vol. 11, no. 2, pp. 1588–1596, Feb. 2017, doi: 10.1021/acsnano.6b07159.
[22] C. D. English, G. Shine, V. E. Dorgan, K. C. Saraswat, and E. Pop, "Improved Contacts to MoS_2 Transistors by Ultra-High Vacuum Metal Deposition," *Nano Lett.*, vol. 16, no. 6, pp. 3824–3830, Jun. 2016, doi: 10.1021/acs.nanolett.6b01309.
[23] C. B. Honsberg and S. G. Bowden, "TLM measurement," Photovoltaics Education Website. [Online]. Available: https://www.pveducation.org/pvcdrom/tlm-measurement
[24] W. M. Abbott *et al.*, "Comparison of Metal Adhesion Layers for Au Films in Thermoplasmonic Applications," *ACS Appl. Mater. Interfaces*, vol. 12, no. 11, pp. 13503–13509, Mar. 2020, doi: 10.1021/acsami.9b22279.
[25] A. Kumar *et al.*, *Sub-200 Ω·μm Alloyed Contacts to Synthetic Monolayer* MoS_2. 2021, p. 7.3.4. doi: 10.1109/IEDM19574.2021.9720609.
[26] A. Kumar, A. Tang, H.-S. P. Wong, and K. Saraswat, "Improved Contacts to Synthetic Monolayer MoS_2 – A Statistical Study," in *2021 IEEE International Interconnect Technology Conference (IITC)*, Kyoto, Japan: IEEE, Jul. 2021, pp. 1–3. doi: 10.1109/IITC51362.2021.9537515.
[27] R. Kappera *et al.*, "Phase-engineered low-resistance contacts for ultrathin MoS_2 transistors," *Nature Mater*, vol. 13, no. 12, pp. 1128–1134, Dec. 2014, doi: 10.1038/nmat4080.
[28] A. Allain, J. Kang, K. Banerjee, and A. Kis, "Electrical contacts to two-dimensional semiconductors," *Nature Mater*, vol. 14, no. 12, pp. 1195–1205, Dec. 2015, doi: 10.1038/nmat4452.
[29] L. Luo *et al.*, "Ultra-low power consumption flexible sensing electronics by dendritic bilayer MoS," *InfoMat*, vol. n/a, no. n/a, p. e12605, doi: 10.1002/inf2.12605.
[30] J. Kang, W. Liu, D. Sarkar, D. Jena, and K. Banerjee, "Computational Study of Metal Contacts to Monolayer Transition-Metal Dichalcogenide Semiconductors," *Phys. Rev. X*, vol. 4, no. 3, p. 031005, Jul. 2014, doi: 10.1103/PhysRevX.4.031005.
[31] J. Kang, W. Liu, and K. Banerjee, "High-performance MoS_2 transistors with low-resistance molybdenum contacts," *Applied Physics Letters*, vol. 104, no. 9, p. 093106, Mar. 2014, doi: 10.1063/1.4866340.
[32] F. Straß, C. Schedel, and M. Scheele, "Edge contacts accelerate the response of MoS_2 photodetectors," *Nanoscale Adv*, vol. 5, no. 13, pp. 3494–3499, doi: 10.1039/d3na00223c.
[33] A. Cerdeira, M. Estrada, A. Mounir, T. Grasser, and B. Iñiguez, "Analysis of the mobility behavior of MoS_2 2D FETs," *Solid-State Electronics*, vol. 224, p. 109032, Feb. 2025, doi: 10.1016/j.sse.2024.109032.
[34] J. Xue, S. Huang, J.-Y. Wang, and H. Q. Xu, "Mott variable-range hopping transport in a MoS_2 nanoflake," *RSC Adv.*, vol. 9, no. 31, pp. 17885–17890, Jun. 2019, doi: 10.1039/C9RA03150B.

[35] N. Papadopoulos, G. A. Steele, and H. S. J. van der Zant, “Efros-Shklovskii variable range hopping and nonlinear transport in 1T/1T’ -MoS_2,” *Phys. Rev. B*, vol. 96, no. 23, p. 235436, Dec. 2017, doi: 10.1103/PhysRevB.96.235436.
[36] M. Sojková *et al.*, “Tuning the orientation of few-layer MoS_2 films using one-zone sulfurization,” *RSC Adv.*, vol. 9, no. 51, pp. 29645–29651, Sep. 2019, doi: 10.1039/C9RA06770A.

Chapter 4. Electrical modulation in few-layer TAC MoS_2 films

4.1 Introduction

In this chapter we will investigate the active control on exciton properties which directly influence the change in reflection from MoS_2 thin films. MoS_2 is a lossy semiconductor in the visible range with a relatively high refractive index and extinction coefficient. As such they exhibit strong optical interference effects and can support what is known as a zeroth order Fabry Perot mode [1]. This mode can be used to achieve total destructive interference with films that are much thinner than usual ~ 10 nm when they are deposited on a metallic substrate [2]. MoS_2 has strong exitonic features in its n and k values in the visible range which can be seen even at room temperature and these excitons give access to optical interferences brought about by FP cavities. The position and width of these excitonic features can be controlled by external bias. When combined with the interference effects in these thin films we can enhance the change in reflectivity and investigate the possibility of using these nanoscale films as optical modulators. Surface normal design is achieved by stacking layers on top of each other and allows for such interference effects. Therefore, this geometry is used which also opens up new research directions to fabricate surface normal photodetectors, tuneable optical filters, opto-electronic modulators etc. in the future. The novelty in doing so is purely based on the naturally occurring excitons in MoS_2 coupled with a less explored optical interference effect with respect to TMD films but mostly discussed in reference to transparent dielectrics.

While FP interference is more relevant to transparent and absorbing dielectrics [3] and 1^{st} order FP modes have been utilised for various applications, 0^{th} order FP mode hasn't been implemented yet. As C. Bueno-Blanco et. al., have modelled MoS_2 in various different stack designs, they show 0^{th} order FP interference at the MoS_2 and metal of finite optical conductivity to be of enormous use [4].

This chapter aims to explore light-matter interaction and active light manipulation in TAC based MoS_2 by utilising 0^{th} and 1^{st} order FP modes facilitated by sub-wavelength thick MoS_2. While the light-matter interaction is intrinsic to thin TMD films because of the presence of room temperature excitons which facilitate strong absorption [5], [6], [7] in the visible spectrum, active manipulation of light can be achieved by:

1. Inducing change in exciton properties by an externally applied voltage.
2. Performing the experiments around exciton resonances to observe maximum change in response to the external stimulus.

3. Maximize absorption and minimize reflection by integrating thin MoS_2 films in a FP cavity design.

As discussed in ***ch. 1***, externally applied voltage can change exciton oscillator strength, induce more free carriers and change the overall band alignment of a monolayer TMD with respect to its electrical contacts. The work presented in this chapter takes off from here to push the capability of MoS_2 beyond its monolayer limit and achieve change in its optical properties like absorption (or reflectance) in few-layer, large lateral area (μm^2 to mm^2) upon application of in-plane as well as cross-plane voltage bias (electric field). The CCD based differential reflectance technique (CCD-DR) is our in-house setup to visually detect this change in reflectance upon an external voltage stimulus.

4.2 CCD-DR setup and explanation

The in-house setup to measure local reflectivity change was initially used for application of thermoreflectance imaging and so most of the working principle explained here is based on conventional and modified CCD based thermoreflectance (CCD-TR) technique [8], [9]. The thermoreflectance technique is actually about evaluating change in refractive index which is assumed to be related to change in local temperature.

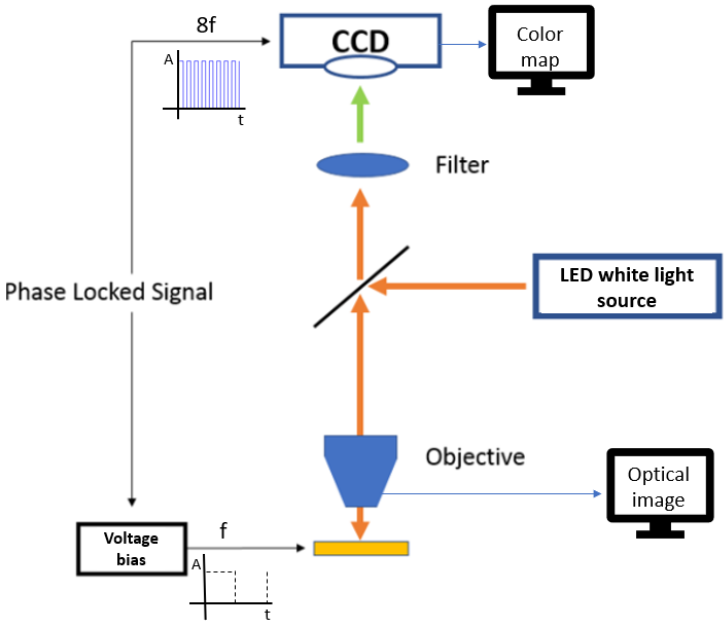

Fig. 4.1*: Schematic depicting the optical arrangement of the CCD-DR setup.*

As such this is more generally classified as a differential reflectance technique. The schematic of this setup is shown in ***fig. 4.1***. Its spatial resolution is ~250 nm and is sensitive enough to pick up change in reflectance signals as low as 1E-4.

The region of interest (ROI) on the DUT is adjusted under the objective with needle probes contacting it and the white light source brightness is set to a value that illuminates the ROI sufficiently without saturating it. The CCD camera is triggered at 8 times the frequency of the driving signal (voltage bias) and captures instantaneous images (of the ROI) averaged over 5000 frames. Each on and off cycle of the driving voltage is divided into 4 parts (or bins) and the captured instantaneous images are categorized into each bin over the course of one voltage cycle i.e., 8 bins per cycle in total. The resulting data thus consists of ROI's spatial map of reflectance in response to voltage's on and off-state. The off-state here, refers to 0V bias while the on-state refers to a non-zero voltage amplitude that differs according to the DUT. Since voltage signal is used as the cause of change in reflectance in this work instead of a thermal input, voltage bringing out this change in the TAC MoS_2 based stack had to be calibrated first and this is also the reason that CCD-differential reflectance (CCD-DR) terminology is used here instead of CCD-TR.

The reflectance data of the captured instantaneous images in the first bin (in the on-state), is subtracted from the first bin (in the off state) during post processing of the data. Like this, data of each bin in the on cycle is subtracted from the bins of the off cycle for comparison. This gives the change in reflectance (ΔR) at each pixel of the ROI. When plotted against the 2-D coordinates of the ROI, this gives a colour map of ΔR in response to the applied alternating voltage signal under a suitable light illumination.

4.3 Differential reflectance in CVD MoS_2

The very first signature of differential reflectance under the CCD-DR setup was observed in CVD based single layers of MoS_2 procured from Dr. Niall McEvoy's group. This MoS_2 was grown in the same setup as shown in ***ch. 2*** and used the same apparatus as used for TAC MoS_2. The difference being in the precursor used, arrangement of the substrate inside the furnace relative to the precursor, inert gas flow rate and temperature. The characteristic triangular flakes of MoS_2 can be seen in the optical image shown in ***fig. 4.2(a)***. Contact pads were patterned using electron-beam lithography (EBL) and gold was deposited later. Due to the underlying alignment marks (+ symbol), the two contact pads that were otherwise

supposed to be electrically isolated from each other form a conducting path between themselves as one of the alignment markers shorted them. Therefore, electrically biasing one of them with a needle probe (using substrate as back contact for ground) as shown in ***fig. 4.2(a)*** also contacts the adjacent pad and so all the CVD MoS_2 flakes beneath them get electrically biased. Observing this under the CCD-DR setup where white light uniformly illuminated the region shown in ***fig. 4.2(a)***, while a 10 V bipolar square wave biased the MoS_2 flakes and the CCD camera captured reflectance images in the on and off cycle of the square wave after the light passed through a filter in the range of 600-650 nm, a surface map showing the differential reflectance was obtained as can be seen in ***fig. 4.2(b)***. It is noteworthy that all the flakes beneath the biased pads show change in reflectance in response to an electrical bias whereas the isolated flakes around them show no change at all. This proves that when observed at a wavelength around A-exciton, change in reflectance of around 0.3% can be uniformly obtained across the biased MoS_2 flakes. This change is attributed to the trion (quasiparticle of an exciton + electron) formation. This will be explained in detail further in this chapter. These MoS_2 flakes had relatively high electrical conductivity so the charge uniformly distributes across many flakes which are physically (and electrically) in contact.

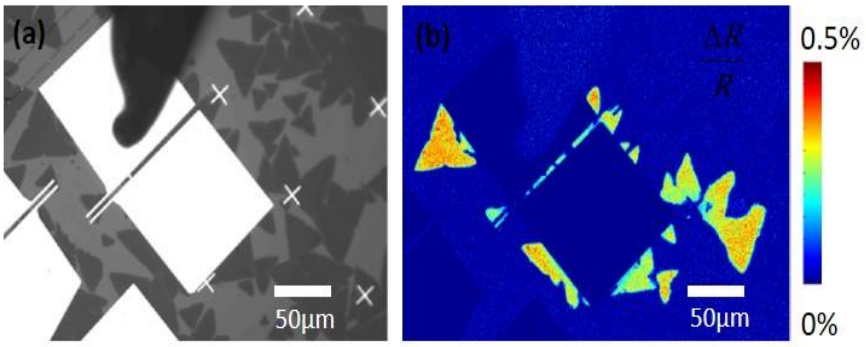

Fig. 4.2*: (a) Optical micrograph of top contacted 2D material single layer MoS_2 on 300nm SiO_2 with highly p-doped Silicon substrate as back gate (b) Differential reflectance image with 10Vpp bipolar square wave applied.*

Another sample was prepared by CVD method with MoO_3 seed layer deposited first and then sulphurised in the furnace to form very pristine MoS_2. The dark regions seen at the centre in some of the flakes in ***fig. 4.3(a)*** is the underlying seed layer. Similar experiment was repeated with this sample but this time using two contact pads for in-plane or lateral CCD-DR measurements across an isolated flake. The pads chosen were the farthest apart from each other and a 5V square wave was applied while the ROI was uniformly illuminated

with white light and CCD-DR images were captured with a narrowband filter of 650 nm. ***Fig. 4.3(b)*** shows a clear down-scaling of DR with the increasing distance from the positive potential electrode (top edge of the image) to the ground potential electrode (bottom left of the image). The flake intended to be contacted did not show any DR but all the flakes in a cluster under the biased contact pad show around 0.2% change in the reflectance.

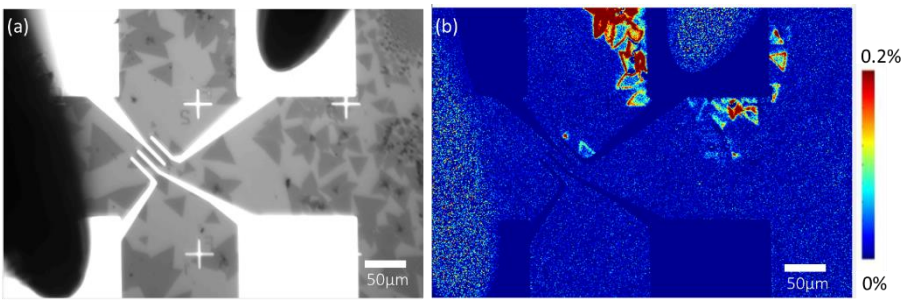

Fig. 4.3*: MoO_3 seed layer first which is then sulphurised in a CVD furnace to form very pristine MoS_2 (dark areas are the seed layer)- just not large area but TAC has that advantage.*

This hints at voltage dependence for DR and can be explored further to understand it in the context of exciton tuning. It can be observed that the DR is restricted to small area (limited by flake dimensions) and its location is dependent on the randomness of the CVD grown MoS_2 flakes. Also, isolating a single flake for this application is not just difficult but very time consuming. Furthermore, patterning such small lateral area flakes required e-beam lithography which is much more cumbersome than photolithography.

Therefore, there is a need to explore other synthesis methods to produce MoS_2 with similar pristine level, better compatibility with patterning techniques and photolithography, the ability to be deposited at any desired location, and have continuous and larger area films. All this was achieved using TAC based MoS_2 films along with additional novelty that these films were not limited to single layers but were made to be a few layers thick so as to push the limit of active exciton tuning beyond the monolayer limit.

4.4 Differential reflectance in TAC based MoS_2

Theoretically, excitons in MoS_2 stay bound up to ~ 7 layers of thickness as shown in ***fig. 4.4***. Y. Yu et al., have depicted this geometric confinement of excitons in MoS_2 by fitting their experimental results to a suitable model based on quantum confinement [5]. Exciton is most strongly bound when the thickness of MoS_2 film is less than its radius i.e., single layer as shown in ***fig. 4.4(b)*** which is a possible reason for strong exciton-based effects in

monolayer MoS_2. This study however, gave us a large enough window to fabricate few-layer MoS_2 devices to show amplitude modulation of reflectance beyond the single layer limit.

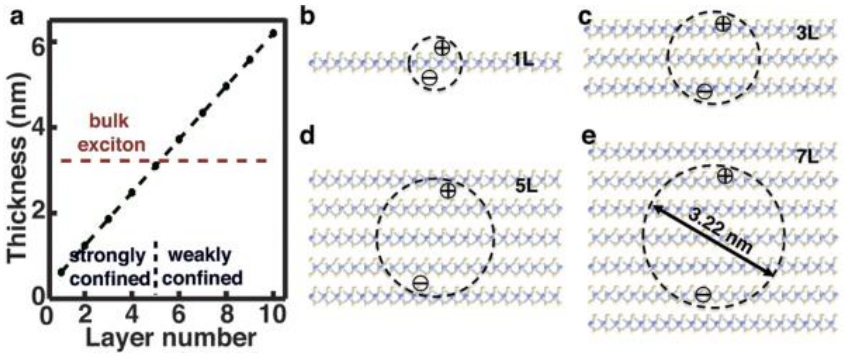

Fig. 4.4*: Taken from* [5], ***(a)*** *shows the exciton confinement strength as a function of MoS_2 thickness which can be visualised as in* ***(b)-(e)****.*

Another important consideration in the design of few-layer TAC based MoS_2 devices for DR application taken into account here is the effect of dielectric encapsulation. To limit the negative effects of ambient environment on MoS_2, especially in the in-plane DR measurement, where DR measured is over a longer distance (on the order of µm) across the surface of MoS_2 as compared to cross-plane measurements which are performed across the MoS_2 thickness in the range of nm. Cross-plane measurement not just ensures shorter distance for the electric field strength resulting from the applied bias but also limits the surface effects since the applied electric field travels inside the plane of the thin film but surface effects become more prominent in the measurement when it is applied in-plane. The in-plane design consists of electrical contacts around µm distance apart which reduces the electric field strength for the same bias applied when compared to the cross-plane case. Additionally, top surface layer has a greater effect in this case than the underlying layers of the thin film. Therefore, it becomes more important to protect this top layer from oxidation and other ambient adsorbates from damaging the surface when it is under in-plane DR measurement. Here, dielectric encapsulation plays a very important role and Al_2O_3 has been used to coat the top surface of a ~3-4 nm TAC based MoS_2 film presented in ***section 4.4.2.1.*** However, before diving into the in-plane measurements, it was more intuitive to perform out-of-plane or cross-plane DR measurements using TAC based MoS_2, FP cavity design and exciton absorption theory.

4.4.1 Cross plane topology

Incorporating a dielectric layer makes the FP cavity a first order one and V. G. Kravets et. al., have shown tuning of reflection spectra at ~665 nm in such a stack consisting of a monolayer of MoS_2 (deposited by CVD) on Si_3N_4/Au [10]. Similarly, ~ 3-4 nm MoS_2 was prepared by TAC on pre-patterned and deposited Si_3N_4 (~30 nm thick) on Au according to a custom-made mask. The custom-made mask was designed to achieve layer by layer patterning and deposition of the stack layers consisting of TAC based MoS_2 in tandem with a metal back reflector and a sandwiched layer of dielectric between the metal and MoS_2. This design was introduced in chapter 2 (***sec. 2.3.1***). As a recap, the explanation of the mask design is: first layer (L1) pattern consisted of two square pads with horizontal bar connecting the two for continuity, then second layer (L2) patterned as another bigger square pad on top of one of the L1 square pads to completely cover it. Finally, the third layer (L3) was included which overlaps L1 and L2 in such a way that part of it lies directly on top of L1 and L2 while the rest of the part extends out perpendicular to L1 pattern. The top view of this stack is shown in ***fig. 4.6(b)***. Au being L1 in this case, its thickness was chosen to be 100 nm with a 1 nm Ti adhesion layer so that Au stays intact after subsequent lithography steps and can survive TAC furnace temperature of 850°C. Si_3N_4 formed L2 and MoS_2 was L3. This stack is represented as: MoS_2/Si_3N_4/Au/quartz. AFM line scans in ***fig. 4.5*** show the thicknesses of MoS_2 and Si_3N_4 designed to be 3 nm and 31 nm respectively using our nanoPVD sputtering tool.

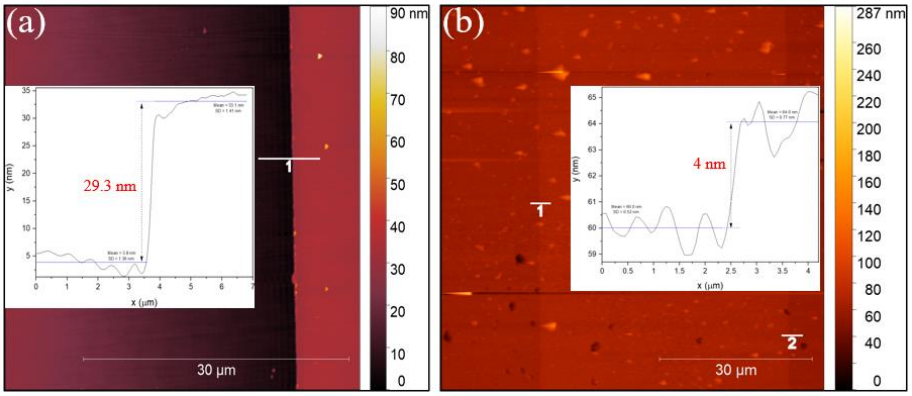

Fig. 4.5*: AFM images showing* ***(a)*** *L2 (Si_3N_4) thickness and* ***(b)*** *L3 (MoS_2) thickness.*

As mentioned previously, since this stack was being made for a measurement requiring cross-plane contacts, therefore, it was very necessary to do so without damaging the active area (overlapping region of L1, L2 and L3) and the stack's optical interference. The contacts used in this setup were sharp needle probes that can pierce through the active area if the

needle probes are made to land directly on it. For this, photomask was designed keeping in mind that first layer (100 nm Au) and the MoS_2 layers should be easily accessible for electrical contacting.

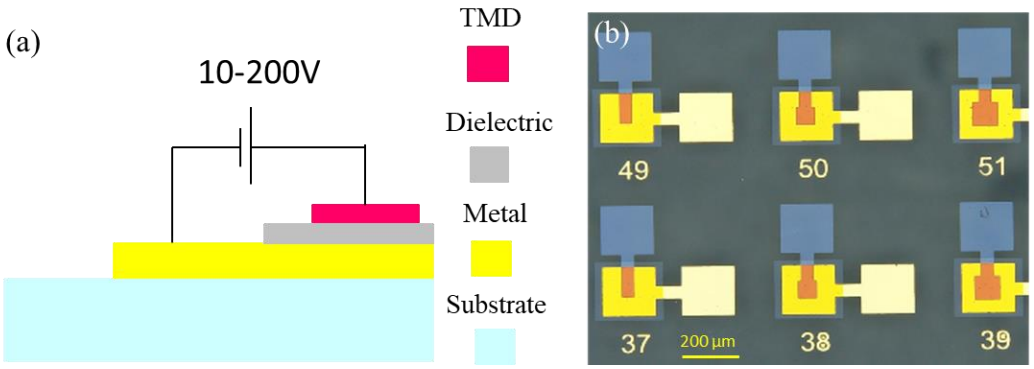

***Fig. 4.6**: **(a)** order of layers in the stack starting from quartz substrate, then Au as the metal reflector followed by Si_3N_4 as the dielectric and finally MoS_2 (pink). **(b)** Top view of the stack with different sizes of the active area across the pixel array and showing extended portions of L1: Au and L3: MoS_2.*

Therefore, both of these layers were extended out of the active area region and were designed to be placed laterally perpendicular to each other so as to avoid overlap. The sandwiched Si_3N_4 layer was designed to have larger area than both these layers to prevent shorting as mentioned earlier. The arrangement of layers and top view of the stack are shown in ***fig. 4.6(a), (b)*** respectively. The width of the active areas in the pixel array are 50 µm, 75 µm, 100 µm, 150 µm. Orange colour is due to optical interference of all 3 layers (L1: Au, L2: Si_3N_4, L3: MoS_2) and golden-yellow colour is due to optical interference between L1: Au and L2: Si_3N_4.

4.4.1.1 Case-1: MoS_2 biased

Voltage bias was applied between L1 (Au) and L3 (MoS_2) as shown in ***fig. 4.6(a)*** ranging from as low as 10 V to as high as 200 V. It was good to see the stability of unencapsulated few-layer TAC based MoS_2 being measured under ambient conditions to survive such large voltages without getting damaged. Due to small active area and limited resources, SE could be only performed for unbiased and un-patterned stacks (having the same layer arrangement), though it would be the best-case scenario if the sample shown in ***fig. 4.6*** was measured while being biased.

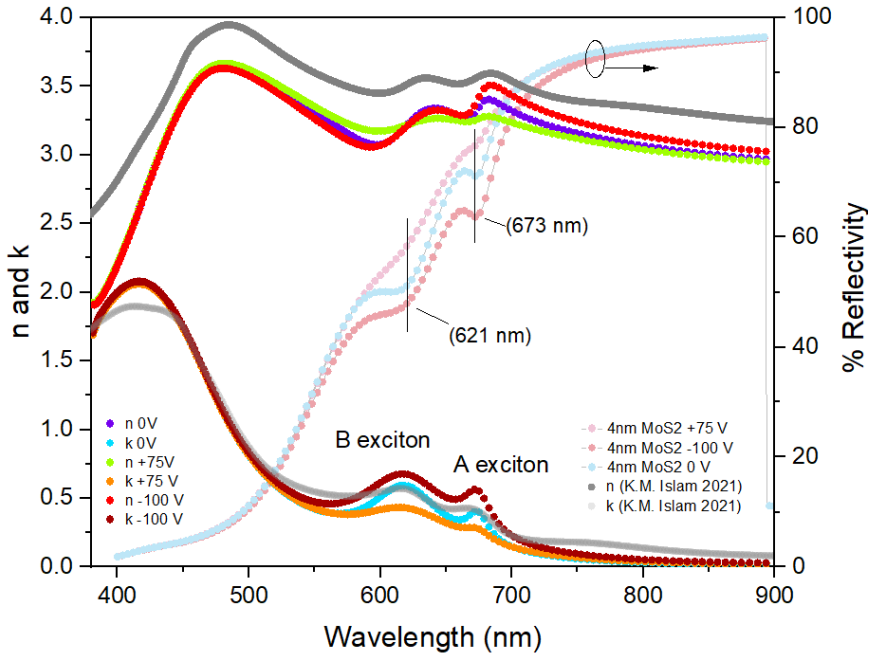

***Fig. 4.7**: (left axis) Experimentally extracted n, k values for unbiased 4 nm MoS_2 on Si_3N_4/Au fit to the model presented in* [11] *along with simulated n, k spectra of biased 4 nm MoS_2 based on ellipsometric model in* [10]. *(right) Simulated reflectivity spectra of biased 4 nm MoS_2/Si_3N_4/Au showing dips around ~670 nm.*

Yet making the best use of the available facilities, unbiased sample was measured under the ellipsometer described in ***2-2.4*** and the data was fit according to a multi-Lorentzian function to extract 'n' and 'k' plotted as purple and cyan colour curves in ***fig. 4.7***. The closest match to these curves was found in K. M. Islam et. al.'s work [11] where they provided 'n' and 'k' values extracted from ellipsometry performed on monolayer, thin and few-layer thick MoS_2 films. The dark grey and light grey curves show 'n' and 'k' values respectively across the visible spectrum for thin MoS_2 films. Using TMM and multi-Lorentzian model (that relates the dielectric function with a material's electric dipoles in response to oscillating electric field) used in [10], the experimentally extracted 'n', 'k' values were simulated for the positive and negative biased cases (colleague Evan Roy's PhD work). A Lorentzian model treats electron – nucleus system as a small mass attached to a large mass via a spring. It takes into consideration the oscillations of electrons' motion around the nucleus in response to electromagnetic radiation. Oscillation of electrons with respect to nucleus creates an atomic dipole 'p' which in this case can be interpreted as an exciton and relates to the dielectric function 'ε_r' through:

$$\varepsilon_r = 1 + \frac{Np}{\varepsilon_0 E} \qquad \textbf{(4-1)}$$

Where 'N' is the number of dipoles, 'p' is the dipole moment, 'ε_0' is permittivity of free space and E is the electric field (from electromagnetic radiation) driving the oscillations of electrons. Furthermore, this relationship can be expressed in terms of refractive index as well given the direct relation between refractive index and dielectric function (n=$\sqrt{\varepsilon_r}$). The Lorentzian model thus takes into consideration the excitons' oscillator strength 'f' (the strength of exciton coupling with electromagnetic field), linewidth 'Γ_x' that accounts for all kinds of damping mechanisms (radiative decay, scattering etc.), exciton resonant energy 'E_x' and background permittivity 'ϵ_∞' to relate with complex dielectric function '$\epsilon(E)$' [12]:

$$\epsilon(E) = \epsilon_\infty + \frac{f E_x^2}{E_x^2 - E^2 - i\Gamma_x E} \qquad \textbf{(4-2)}$$

Fig. 4.7 shows the change in amplitude and width of the exciton peaks indicating a strong change in absorption (and reflection) when thin MoS_2 films are subjected to externally applied bias. Expected change in reflection from the TMM calculations was large (~10%) that is evident from the plots associated with the right axis (% reflectivity). This is of course large compared to what was experimentally obtained as will be discussed in the sections to follow. Possible reasons will also be discussed later but in short, the main reason for the mismatch between calculated change in reflectivity compared to experimentally obtained data is that in simulations, pristine, continuous thin films with no defects are considered while in reality this is very difficult to obtain. Especially in this project, MoS_2 thin films were incorporated in multilayer stack devices without any dielectric encapsulation and were measured under ambient temperature and pressure conditions to test their feasibility as a commercially available device that can be used in real life applications.

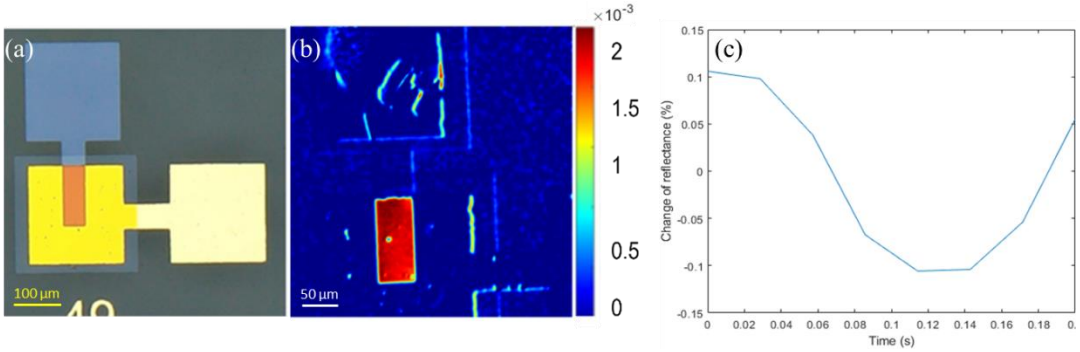

***Fig. 4.8**: **(a)** Top view of the stack (ROI) with the smallest active area (orange region). **(b)** Corresponding change in reflectance in the active area. The colour bar depicts the magnitude in the order of 1E-3. **(c)** Evolution of change in reflectance with time follows the 40 V p-p sine wave driving signal.*

Such a device was experimentally tested by measuring the DR of the stack described previously and shown in ***fig. 4.6*** biased with a sine wave with different amplitudes ranging from 10-200V. Time varying voltage is required to compare reflectance images from the on cycle to off cycle as explained in ***sec. 4.2***.

An optical filter of 670 nm was chosen since simulated reflectivity (%) in ***fig. 4.7*** shows change around exciton dips and is seen to be more pronounced ~ 670 nm. Out of all the sizes of active area shown in ***fig. 4.6(b)***, only the smallest of the lot (50 µm wide) showed change in reflectance. This is clearly observed through CCD-DR measurement when the active area (orange colour region in ***fig. 4.8(a)***) formed from the overlap of L1, L2 and L3 showed a clear change in reflectance ~ 2E-3 (red region in ***fig. 4.8(b)***) with 670 nm filter (10 nm bandwidth) on white light source, leaving the rest of the ROI predominantly at zero change (blue background in ***fig. 4.8(b)***). The voltage signal used to drive this process was a sine wave of frequency 5 Hz, 40 V p-p amplitude phase synchronised with the camera triggered at 8 times the voltage frequency i.e., 40 Hz. The CCD-DR signal follows the voltage signal as seen in the plot ***fig. 4.8(c)*** which was picked from a random point in the active area (orange region) in ***fig. 4.8(a).*** Similarly, change of reflectance was probed under the above explained setup and settings at different voltage biases. ***Fig. 4.9*** shows the percentage change in reflectance of the active area in (orange region in ***fig. 4.8 (a)***) as a function of changing amplitude of the driving voltage signal (sine wave with a frequency of 5 Hz). At the largest applied voltage of 200 V, ~ 0.32 % change in reflectance was observed in the 1st order FP based stack design formed from overlap and optical interference between Au back reflector, Si_3N_4 and 4 nm MoS_2.

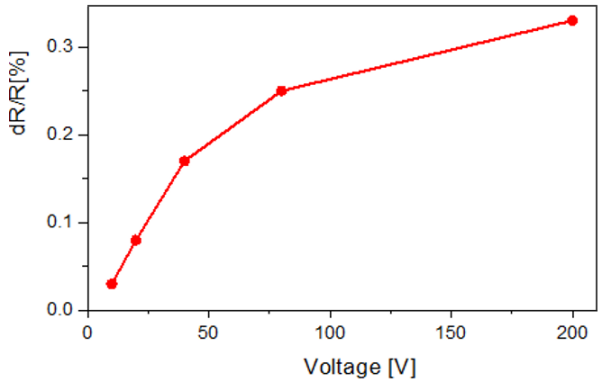

Fig. 4.9*: Change in reflectance increases with increasing applied bias keeping the same illumination settings.*

Another notable observation was quality of dielectric (Si_3N_4 in this case) sandwiched between the L3: MoS_2 and L1: Au. If not continuous and/or of the correct thickness, then it

can result in shorting between the two layers or fail to provide the desired optical interference needed for light trapping inside the cavity. This results in a reduced signal and was especially the cause of failure for larger active area devices in the pixel array. In fact, this even showed up in certain smallest (50 µm wide) devices, where the change in reflectance signal fell continuously as it went away from the biasing electrode. Shown in ***fig. 4.10 (a)*** is one such device from the array with two needle probes contacting L1 and L3 each. Probe near the top edge of the image is placed on L1 extended Au pad and the probe at the left edge of the image is placed on L3 extended pad of MoS_2 with an additional Au contact pad to achieve a better electrical contact between the needle probe and MoS_2. ***Fig.* 4.10(b)** shows change in reflectance in the active area falling across its length. It is maximum around the edge nearest to the electrode at x=~1000 µm mark after which its magnitude decreases to zero as it reaches the farthest edge of the active area length around x=1500 mark. Such issues can be mitigated by using better quality of dielectric perhaps deposited using less aggressive methods like atomic layer deposition (ALD) instead of sputtering that was used here so that the dielectric can electrically isolate L1: Au and L3: MoS_2 successfully.

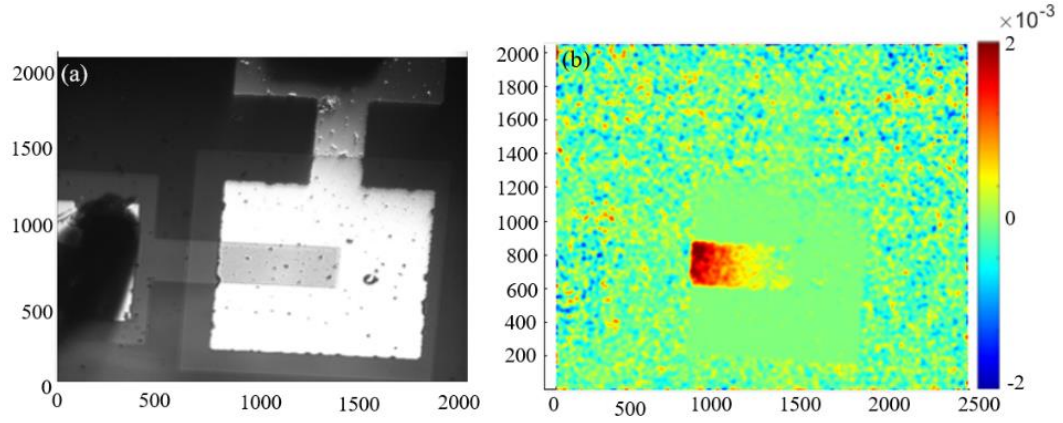

***Fig. 4.10**: **(a)** Gray-scale image of the ROI. **(b)** Corresponding DR map showing reduction in DR signal as a function of increasing needle probe distance in the active area.*

4.4.1.2 Case-2: Au biased

Lastly, electric configuration was changed slightly, i.e., Au layer forming the bottom reflector was biased with the driving signal (square wave of p-p amplitude =160 V) and MoS_2 layer was connected to the negative (ground) electrode.

Fig. 4.11*(c)** shows this layer arrangement which is the same as before (shown in ***fig. 4.8(a), ***fig. 4.10(a)***) but the biased and ground electrodes are switched. Among the array consisting of different sized active region pads, 75 µm wide pad is shown in ***fig. 4.11(a)*** and ***fig. 4.11(b)*** shows a maximum of around 0.06% change in reflectance observed upon measuring under the CCD-DR setup with the same settings. The spatial colour map in ***fig. 4.11(b)*** is also seen to follow the frequency of the driving voltage bias shown in ***fig. 4.11(d)***. Here, yet again leaking through the dielectric is visibly evident.

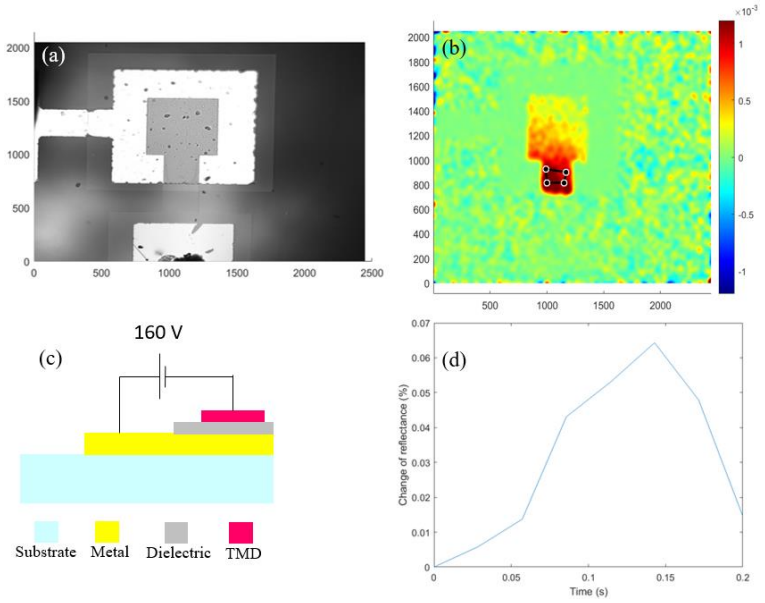

***Fig. 4.11**: **(a)** Gray-scale image showing top view of the ROI. **(b)** CCD-DR signal of the ROI measured with 670 nm filter. **(c)** Layer arrangement and electrical bias configuration, this time biasing Au layer with the driving signal. **(d)** % change in reflectance following the driving signal frequency.*

Lastly, this stack was measured under 630 nm optical filter as well with a 10 V p-p square wave. This was done to test the contribution from the B-exciton which reportedly shows low tunability with charge modulation [10]. The change in reflectance under this setting is shown in ***fig. 4.12***. it can be noted that the signal is the weakest in this case compared to the results shown before and what will be also presented in subsequent sections. This corroborates with V. G. Kravets et. al.'s findings [10] and can also be attributed to either low quality of dielectric beneath it or insufficient thickness of dielectric responsible for the optical interference that can happen due to non-uniform evaporation of this layer during the fabrication process or phonon-assisted polariton scattering [13], [14], [15] or a mix of all these concerns.

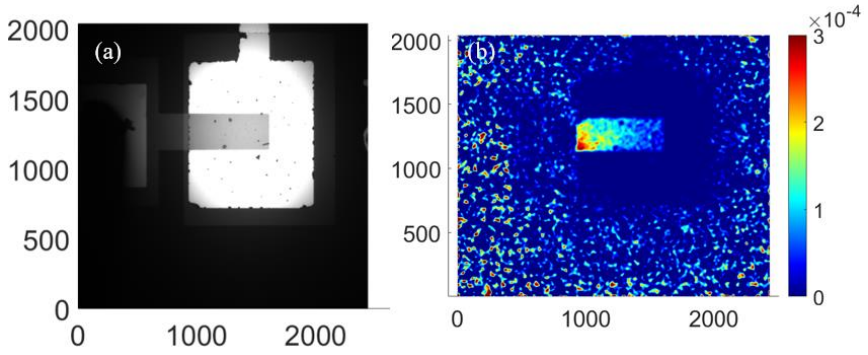

***Fig. 4.12**: **(a)** Optical image of the ROI under test illuminated by light passing through a 630 nm optical filter. **(b)** Corresponding DR spatial map across the ROI obtained by aplying 10 V p-p time varying square wave.*

4.4.2 In-plane topology

Using a similar approach but slightly different execution, MoS_2 of two different thicknesses were deposited on two different substrates and layer arrangements. The first one presented in ***sec. 4.4.2.1*** was deposited directly on unpatterned quartz substrate followed by top electrode patterning and deposition and then top dielectric encapsulation of the entire substrate area. On the other hand, the stack presented in ***sec. 4.4.2.2*** was based on Ossila's FET design but only the layer consisting of source-drain IDEs was used to achieve the desired function and the gate layer was not used. In this sample stack, Si/300 nm SiO_2 substrate was used followed by S-D IDEs and then MoS_2 as the last layer giving alternate regions of two different optical interferences as explained later in that section.

4.4.2.1 TAC based MoS_2 on quartz substrate

MoS_2 of the same thickness (~3-4 nm) as in ***sec. 4.4.1*** was deposited directly on a $1cm^2$ quartz substrate followed by 50 nm Au top interdigitated electrodes (IDEs) and Al_2O_3 encapsulation to protect the large area MoS_2 surface as shown in ***fig. 4.13(a)***. Two needle probes were placed on the extended contact pads piercing through the Al_2O_3 encapsulation and reaching the Au contact pads. An optical filter of 640 nm was placed between the white light source and the CCD camera and a voltage bias of square waveform with an amplitude of 5 V was applied across the two electrodes.

Given the high sensitivity of the CCD-DR setup to probe change in reflectance, it was able to measure a signal as low as ~5E-4 shown in ***fig. 4.13(b)*** upon the application of electrical bias.

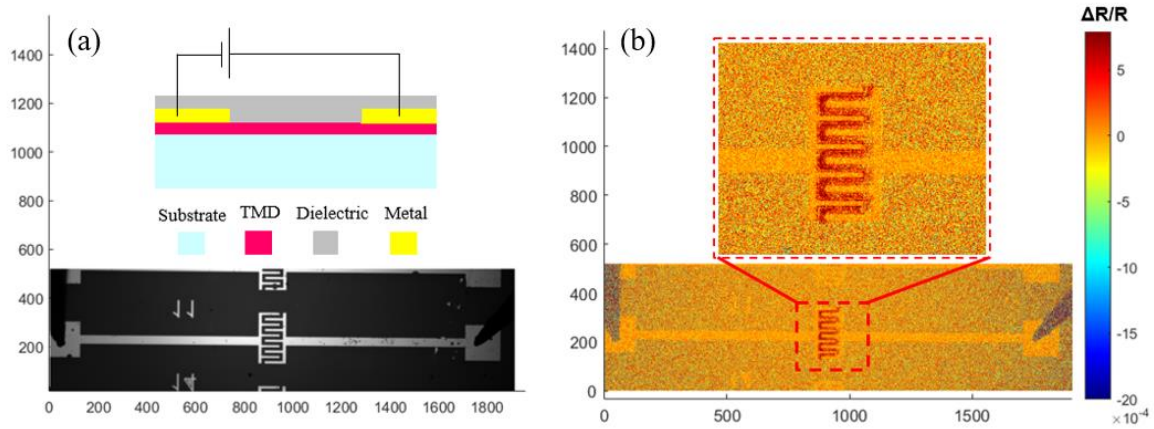

***Fig. 4.13**: **(a)** layer by layer arrangement of the stack (Top) and gray sclae image showing top view of the contacted stack (bottom). **(b)** Change in reflectance signal observed between the IDEs shown in red colour.*

4.4.2.2 TAC based MoS_2 on Si/SiO_2 substrate using Ossila design

In this sub-section, the sample set presented utilizes MoS_2 in 1st order FP cavity. 50 nm Au IDEs were patterned and deposited on a Si/300 nm SiO_2 substrate and then 6 nm thick MoS_2 produced by TAC was deposited on top of them. This created two regions of different optical interference; first one consisting of substrate/L1/L2: $Si/SiO_2/Au/MoS_2$ and the second region consisting of substrate/L2: $Si/SiO_2/MoS_2$. The IDEs were biased as in the previous sub-section thus also directly biasing the MoS_2 above them.

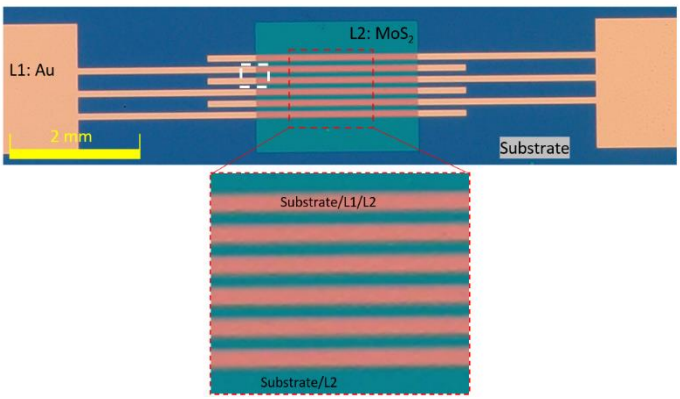

***Fig. 4.14**: Ossila design-based device with alternating regions of 1st order FP stacks produced using different combination of layers.*

As shown in ***fig. 4.14***, the optical image shows the top view of this stack with a zoomed-in section showing the alternating regions of different 1st order FP cavities formed due to optical interference between different layers. The blue region is MoS_2 optically interfering directly with the substrate while the pink region is caused due to interference between MoS_2,

Au and substrate. The former will be referred to as stack-1 and the latter as stack-2 for convenience.

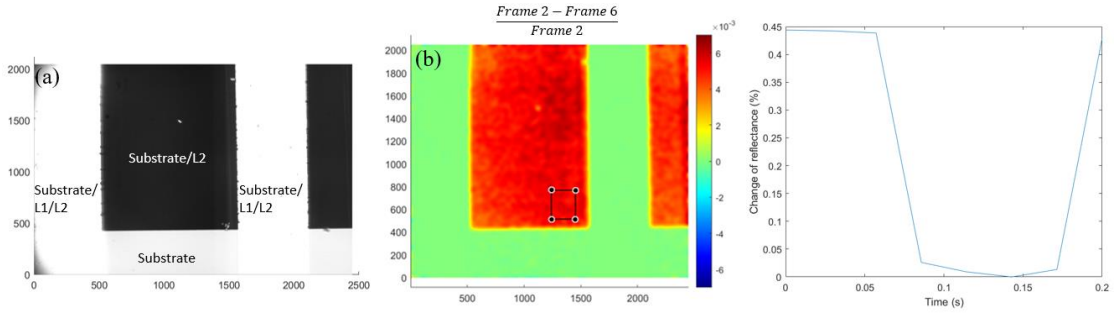

***Fig. 4.15**: **(a)** Grey sale image of ROI with marked regions to identify the alternating stacks making 1st order FP by varying layer arrangement. **(b)** Spatial colour map produced after CCD-DR measurement with 670 nm filter and 160 V square wave driving signal. **(c)** % change in reflectance of the region outlined by a black square in **(b)** that also follows the driving signal frequency.*

Outlined by white dashed square in ***fig. 4.14***, is roughly the chosen ROI measured under the CCD-DR setup. A grey scale image of this ROI is shown in ***fig. 4.15(a)*** that clearly shows strong reflection (saturated bright regions) of white light from the L2 regions backed by L1 (Au IDEs) on the substrate and a strong absorption evident from dark area between the two IDEs in the region comprising of L2 (MoS_2) directly on substrate.

This sample also shows an unexpected CCD-DR signal from the region forming stack-1 (MoS_2 on Si/SiO_2) i.e., the dark region in ***fig. 4.15(a)***. Even reducing the source white light's intensity so that the regions forming stack-2 are not saturated by light anymore, did not produce any DR signal from them under the same settings. It was also noteworthy that illuminating the stack-1 region with maximum intensity of light (from the same source) that would otherwise completely saturate the samples presented before in this chapter, failed to increase the brightness significantly in this case. This is also a proof of strong light absorption caused possibly due to the 1st order FP or the Salisbury screen effect. This measurement was repeated for the different amplitudes of the driving voltage signal and each time, similar result was obtained with the strongest change in reflectance observed for higher applied voltages.

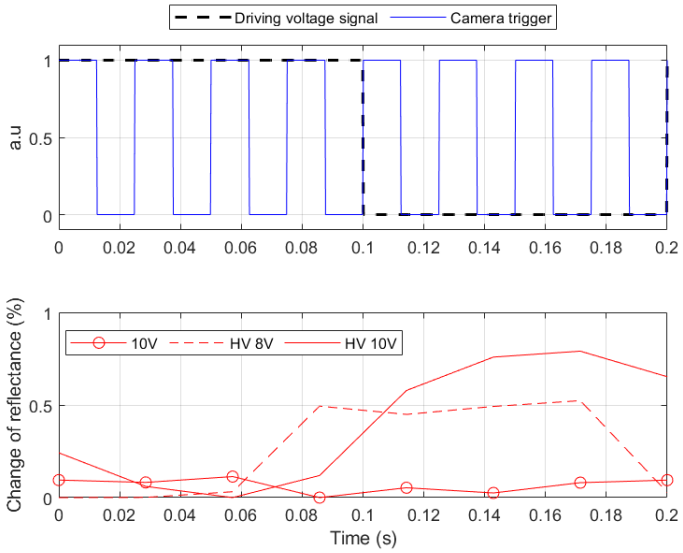

***Fig. 4.16**: Waveforms as a function of time of (top tile) driving voltage and CCD camera and (bottom tile) the measured DR responses at 10 V, 160 V and 200 V.*

Top tile in ***fig. 4.16*** shows an example of camera triggered at 8 times the frequency of the driving signal as also explained in previous sections and the bottom tile shows the % change in reflectance as a function of time for three different amplitudes of the driving voltage. 'HV' refers to 'high voltage' to distinguish between the voltages applied with and without using a voltage amplifier. The gain of the amplifier used was 20x therefore 'HV' mentioned before an amplitude value (which was the input from the signal generator) means that the voltage amplitude obtained after passing through the amplifier was 20 times the mentioned amplitude value and this amplified square wave was used as the input bias to the device for CCD-DR measurement. The bottom tile thus shows the time variation of the %change in reflectance as a response to square wave input of amplitude 10 V, 160 V (20 x 8 V) and 200 V (20 x 10 V).

4.5 Possible mechanisms of exciton tuning in TAC based MoS_2 stacks

The previous section (***sec. 4.4***) showed a visual representation of change in reflectance in few-layer MoS_2 films upon electrostatically gating the stack: $MoS_2/Si_3N_4/Au$. The change in reflectance observed can be attributed to exciton tuning in MoS_2 and can be explained by change in exciton properties upon gating. Energetically, excitons lie close to the conduction band that is in between the valence band maximum (VBM) and conduction band minimum (CBM). According to ***eq. 4-2***, a change in excitons' oscillator strength and linewidth can lead to a change in overall complex permittivity. V. G. Kravets et. al., experimentally

showed the variation of optical constants near exciton bands as a response to gate voltage [10]. They observed increasing gate voltage applied in the out-of-plane direction of the MoS_2 monolayer causes decrease in exciton (A and B) absorption intensities with a significant change observed in *f* (oscillator strength) and γ (or 'Γ' as used in ***eq. 4-2*** – spectral width or damping factor). They also showed that 'n' and 'k' are tuneable only in the spectral range of 580-750 nm beyond which they are independent of gate voltage. This tunability appears only near the exciton resonances and is caused due to a decrease in *f* and broadening of γ (spectral width i.e., exciton bands) of the A and B excitonic transitions brought about by charge injection. This explains the measured DR in this work which is also a result of gating the MoS_2/Si_3N_4/Au stack. This is also validated by Y. Yu et al., where they observed change in refractive index due to gating (charge injection) in monolayer WS_2 caused mainly by change in *f* and γ [16]. The reduction in *f* due to charge injection is explained by Pauli blocking effect [17] and change in exciton orbital wavefunction [18]. Pauli blocking or phase space filling theory is governed by Pauli-exclusion principle according to which excitons and conduction electrons should energetically reside in different region of the phase space and this dynamic gets disturbed upon charge injection causing reduction in *f*. In contrast, γ broadens due to increased collisions and Coulomb scattering as charge injection increases [17]. Another point to consider is that in all the stacks showing DR presented above, show the results around A-exciton resonance i.e., ~ 670 nm. This is supported by [10], [16] which show that tunability is easier to achieve around A-exciton. The red and blueshifts (caused by Pauli blocking and/or inelastic interactions between exciton and free charge carriers) are accounted in experiment by using a 670 nm filter with 10 nm bandwidth. D. Vella et. al.'s experimental work narrows down the above explained mechanism and points out a clear distinction between change in reflectance due to 1) motion of free carriers (brought about in their device by in-plane electric field without injecting charge carriers) to be mainly due to change in linewidth and 2) charge modulation by applying a gate voltage to their capacitively coupled device to being caused by transfer of oscillator strength from an uncharged (neutral) exciton to a negatively charged exciton (trion) [19]. While the change in reflectance in the former case showed spatial dependence on the magnitude and polarity of their driving signal, the latter was independent of all this. The latter result therefore supports light modulation in the MoS_2/Si_3N_4/Au stack caused by change in excitons' oscillator strength as observed in ***sec. 4.4.1***. This result showing change in reflectance due to gating is of significant use for applications pertaining to visible range of the electromagnetic spectrum which also happens to coincide with the spectral range of MoS_2 excitons.

The measurements show uniform change in reflectance across the active area (overlap of MoS_2, Si_3N_4 and Au). For certain failed devices (not shown) where Si_3N_4 was damaged, any kind of shorting between bottom Au layer to the top MoS_2 layer after passing through Si_3N_4 layer would show up as current hotspots (regions of extremely high current density) in the CCD-DR measurement. These current hotspots would not appear with such small order and magnitude especially at the high voltages used on these devices and would present themselves at twice the frequency of that of the applied driving voltage signal. If the measurement was left running, this would also damage the device stack significantly in other areas and the results were not reproducible. However, in the work presented here, a working device was measured multiple times over the course of weeks and months (in some cases) under different CCD-DR settings without showing any signs of damage.

The differential reflectance signal can be further enhanced by ensuring sustainable photon interaction with excitons and reducing polariton scattering that are caused by acoustic phonons [13] especially longitudinal acoustic phonons in the vicinity of **K** and **M** points in the Brillouin zone [14] and are the main causes of dispersive Raman scattering or translational motion of excitons. This leads to valley depolarisation and so the incident light frequency should be chosen carefully to access excitons for interaction with light because excess kinetic energy in the form of light energy or thermal energy can result in intervalley scattering of excitons. T. Sekine et. al., clearly point out that when the incident light is slightly above the 1s level of A or B exciton, it gives rise to dispersive Raman peaks attributed to phonon scattering [13] and G. Kioseoglou et. al, further quantified this excess energy to be equal to twice the energy of the lowest phonon available in the MoS_2 system which is 0.06 eV [15]. While this is true for single layer MoS_2, this is still relevant for few-layer MoS_2 at least qualitatively. This gives us a frequency window in the vicinity of the excitons beyond which accessing excitons to tune their properties and using them for opto-electronic applications can become cumbersome. This is a possible explanation for observing a weak DR signal with a 630 nm filter as shown in ***fig. 4.12*** which corresponds to 1.968 eV which is well above the A-exciton energy level (1.842 eV) as shown in ***fig. 4.7*** and surpasses the threshold value of 0.06 eV assuming that this remains the same for few-layer MoS_2 films as well. Though not very strong, yet B-exciton contributes to the DR signal since the difference in B-exciton energy and light passing through the 640 nm filter is 1.99-1.968 eV which equals to 0.022 eV meaning that the condition for 100% valley depolarization has not been met yet and therefore despite the difficulty in B-exciton tuning

reported previously, it results in a week CCD-DR signal. This also adds on to the explanation as to why exciton tuning beyond the exciton energy vicinity is not possible and more so at the room temperature where phonon effects are more pronounced.

4.6 Conclusion

This chapter showed a direct visualisation of change in reflectance using our in-house CCD camera based differential reflectance setup via false colour spatial maps. Different topologies of the stack design were used keeping the thickness of MoS_2 below 4 nm to take the advantage of exciton confinement that dictates high absorption in MoS_2. To enhance the absorption further, FP cavity design was used to facilitate light trapping to give MoS_2 the best chance to interact with photons as much as possible. Change in reflectance was actively achieved by applying a time varying voltage signal. The application of a voltage bias is responsible for charge injection in both cases of the cross-plane topology where first the time-varying voltage driving signal was applied directly to the MoS_2 thin film and then to the Au back reflector; both layers were separated by Si_3N_4 layer in both cases. Charge modulation facilitates significant change in exciton properties like spectral width and oscillator strength thereby causing change in absorption and light-matter interaction in MoS_2. Both the cases showed change in reflectance of similar magnitude and order (~0.2%) without causing any damage to MoS_2 in the first case even after applying voltage as high as 200 V. A slightly better result was obtained in the in-plane topology with the highest change in reflectance ~ 0.75% was observed at 200 V. Here the region of stack that gave this result consisted of MoS_2 directly on Si/SiO_2 substrate forming a yet another 1^{st} order FP cavity like the cases discussed in the previous topology. Another design where MoS_2 was not backed by any reflector and directly deposited on a quartz substrate was also implemented which was presented in the in-plane topology section and a very small signal (0.05%) was detected. In conclusion, TAC based large area (mm^2) MoS_2 on Si/SiO_2 substrate showed a slightly higher % change in reflectance than CVD MoS_2 deposited on the same substrate. This is a proof of concept that TAC based large area, continuous MoS_2 films which are compatible with photolithography processes can be used in a patterned stack at any stage or deposited directly on a substrate. Moreover, TAC based MoS_2 films produce equivalent or similar % change in reflectance compared to CVD MoS_2 flakes which is also uniform across the MoS_2 based active area.

References

[1] M. A. Kats and F. Capasso, "Optical absorbers based on strong interference in ultra-thin films," *Laser & Photonics Reviews*, vol. 10, no. 5, pp. 735–749, Sep. 2016, doi: 10.1002/lpor.201600098.

[2] M. A. Kats *et al.*, "Ultra-thin perfect absorber employing a tunable phase change material," *Applied Physics Letters*, vol. 101, no. 22, p. 221101, Nov. 2012, doi: 10.1063/1.4767646.

[3] C. Bueno-Blanco, S. A. Svatek, and E. Antolin, "High broadband light absorption in ultrathin MoS_2 homojunction solar cells," *Opt. Express*, vol. 30, no. 23, p. 42678, Nov. 2022, doi: 10.1364/OE.469931.

[4] M. A. Kats, R. Blanchard, P. Genevet, and F. Capasso, "Nanometre optical coatings based on strong interference effects in highly absorbing media," *Nature Mater*, vol. 12, no. 1, pp. 20–24, Jan. 2013, doi: 10.1038/nmat3443.

[5] Y. Yu *et al.*, "Exciton-dominated Dielectric Function of Atomically Thin MoS_2 Films," *Sci Rep*, vol. 5, no. 1, p. 16996, Nov. 2015, doi: 10.1038/srep16996.

[6] K. M. Islam, R. Synowicki, T. Ismael, I. Oguntoye, N. Grinalds, and M. D. Escarra, "In-Plane and Out-of-Plane Optical Properties of Monolayer, Few-Layer, and Thin-Film MoS_2 from 190 to 1700 nm and Their Application in Photonic Device Design," *Advanced Photonics Research*, vol. 2, no. 5, p. 2000180, May 2021, doi: 10.1002/adpr.202000180.

[7] M. Li, Q. Li, M. L. Brongersma, and H. A. Atwater, "Optical devices as thin as atoms," *Science*, vol. 386, no. 6727, pp. 1226–1228, Dec. 2024, doi: 10.1126/science.adk7707.

[8] E. Matatagui, A. G. Thompson, and M. Cardona, "Thermoreflectance in Semiconductors," *Phys. Rev.*, vol. 176, no. 3, pp. 950–960, Dec. 1968, doi: 10.1103/PhysRev.176.950.

[9] M. Farzaneh *et al.*, "CCD-based thermoreflectance microscopy: principles and applications," *J. Phys. D: Appl. Phys.*, vol. 42, no. 14, p. 143001, Jul. 2009, doi: 10.1088/0022-3727/42/14/143001.

[10] V. G. Kravets, F. Wu, G. H. Auton, T. Yu, S. Imaizumi, and A. N. Grigorenko, "Measurements of electrically tunable refractive index of MoS_2 monolayer and its usage in optical modulators," *npj 2D Mater Appl*, vol. 3, no. 1, p. 36, Sep. 2019, doi: 10.1038/s41699-019-0119-1.

[11] K. M. Islam, R. Synowicki, T. Ismael, I. Oguntoye, N. Grinalds, and M. D. Escarra, "In-Plane and Out-of-Plane Optical Properties of Monolayer, Few-Layer, and Thin-Film MoS_2 from 190 to 1700 nm and Their Application in Photonic Device Design," *Advanced Photonics Research*, vol. 2, no. 5, p. 2000180, May 2021, doi: 10.1002/adpr.202000180.

[12] J. Lynch, L. Guarneri, D. Jariwala, and J. van de Groep, "Exciton resonances for atomically-thin optics," *Journal of Applied Physics*, vol. 132, no. 9, p. 091102, Sep. 2022, doi: 10.1063/5.0101317.

[13] T. Sekine, K. Uchinokura, T. Nakashizu, E. Matsuura, and R. Yoshizaki, "Dispersive Raman Mode of Layered Compound 2H-MoS_2 under the Resonant Condition," *J. Phys. Soc. Jpn.*, vol. 53, no. 2, pp. 811–818, Feb. 1984, doi: 10.1143/JPSJ.53.811.

[14] B. R. Carvalho *et al.*, "Intervalley scattering by acoustic phonons in two-dimensional MoS_2 revealed by double-resonance Raman spectroscopy," *Nat Commun*, vol. 8, no. 1, p. 14670, Mar. 2017, doi: 10.1038/ncomms14670.

[15] G. Kioseoglou, A. T. Hanbicki, M. Currie, A. L. Friedman, and B. T. Jonker, "Optical polarization and intervalley scattering in single layers of MoS_2 and $MoSe_2$," *Sci Rep*, vol. 6, no. 1, p. 25041, Apr. 2016, doi: 10.1038/srep25041.
[16] Y. Yu, Y. Yu, L. Huang, H. Peng, L. Xiong, and L. Cao, "Giant Gating Tunability of Optical Refractive Index in Transition Metal Dichalcogenide Monolayers," *Nano Lett.*, vol. 17, no. 6, pp. 3613–3618, Jun. 2017, doi: 10.1021/acs.nanolett.7b00768.
[17] S. Schmitt-Rink, D. S. Chemla, and D. A. B. Miller, "Theory of transient excitonic optical nonlinearities in semiconductor quantum-well structures," *Phys. Rev. B*, vol. 32, no. 10, pp. 6601–6609, Nov. 1985, doi: 10.1103/PhysRevB.32.6601.
[18] P. Lefebvre, P. Christol, H. Mathieu, and S. Glutsch, "Confined excitons in semiconductors: Correlation between binding energy and spectral absorption shape," *Phys. Rev. B*, vol. 52, no. 8, pp. 5756–5759, Aug. 1995, doi: 10.1103/PhysRevB.52.5756.
[19] D. Vella *et al.*, "In-Plane Field-Driven Excitonic Electro-Optic Modulation in Monolayer Semiconductor," *Advanced Optical Materials*, vol. 10, no. 4, p. 2102132, Feb. 2022, doi: 10.1002/adom.202102132.

Chapter 5. Photo-induced response in MoS_2

5.1 Introduction

This chapter aims to explore the photo-induced response in multilayer large area MoS_2 produced using several approaches including chemical vapour deposition (CVD), liquid phase exfoliation (LPE), and thermally assisted conversion (TAC) process. There are several mechanisms evident simultaneously in the film which lead to a complex optoelectronic response. These include photoconductivity, photovoltaic effect, photothermal effect and photobolometric effect to name a few. The CVD process results in high quality single and few layer MoS_2 however there is little control over the position on the sample where the MoS_2 forms. LPE allows easy production of large area multilayer films however these consist of many flakes of different thicknesses and lateral sizes resulting in defect dominated slow photoresponse. We show that the TAC process provides a compromise between the previous two methods in terms of photoresponse. At the same time, we can accurately position the thickness-controlled TAC MoS_2 using photolithography. This allows us to do a more complete study of the photo response in terms of electrode geometry, film thickness and steady-state versus transient response. We show that TAC films demonstrate a unique combination of photoconductive, photovoltaic and pyroelectric response. Combined with resonantly enhanced absorption in ultrathin films this could lead to interesting device applications such as broadband pyroelectric sensors with fast response time.

5.1.1 Photoconductivity (PC)

Photoconductivity is the change of the electrical conductivity of a material in response to a light stimulus. A semiconducting material such as MoS_2 becomes more conductive when exposed to light with energy greater than the bandgap. This is due to emission of photo-electrons which can then contribute to the electrical conduction. The change in conductivity is directly proportional to the number of photons absorbed by a material. Materials with a high absorption coefficient are desirable to create thin film photoconductive sensors. Several parameters are considered as figures of merit to assess the performance of a photoconductive device. The basic and most important ones considered in this work are described as follows:

1) **Responsivity** relates the optical power input (P_{opt}) to the photoinduced electrical current output (I_{ph}) as:

$$R = \frac{I_{ph}}{P_{opt}} [A/W]$$

(5-1)

Previous studies have reported photoresponsivity using MoS_2 ranging from as low as 5.8×10^{-6} A/W [1] to as high as 273 A/W [2]. Z. Yin et al., reported a photoresponsivity of 7.5 mA/W for single layer MoS_2 at very low optical power (80μW) and V_{ds} =1V but by gating MoS_2 [1] and D.S. Tsai et al., reported a photoresponsivity of 0.57 A/W for few layer MoS_2 in a MSM design created by using top interdigitated electrodes (IDE) [2]. It is clear that the synthesis process and device geometry have a large effect on the photoresponse.

2) **Sensitivity** is the ratio of photoconductivity (or photocurrent, I_{ph}) to dark conductivity (dark current, I_{dark}) i.e., current measured in the illuminated/light and dark conditions respectively.

$$S = \frac{I_{ph}}{I_{dark}}$$

(5-2)

3) **Response time (rise and fall)**: This is the time it takes for a photoactive material to respond to change in intensity of light stimulus. It is measured as the time taken for the sample to reach 90% of its final value under a step impulse (rise time) or decay to 10% of its original value on switching off the light source. The response time can have both fast and slow components depending on the underlying effect and defects in the material. Operating across light modulation frequencies can therefore allow us to use different underlying photoresponse mechanisms. The rise and fall times are important for use as a fast detector. Usually, the sensitivity is linked to the response time because higher sensitivity results in slower response for photoconductors.

5.1.2 Photovoltaic (PV) effect

Due to the presence of room temperature excitons in the visible range of the electromagnetic spectrum, MoS_2 is very sensitive to light illumination, contact material and design. PV in MoS_2 is greatly governed by the effectiveness of the source-drain contacts to separate the photo-electrons from holes. But the energy levels where the photo-electrons reside is governed by light intensity, wavelength and whether it is continuous or pulsed.

Also, MoS_2 shows a mix of mechanisms altogether that can be difficult to separate out. These effects are Photovoltaic (PV) [3], Photo-thermoelectric (PTE) [4], photo-bolometric

(PB) [5], piezo-PV [6] and photoconductivity (PC) [7], pyro-phototronic [8]. In this work, some of these effects are investigated for TAC based MoS_2.

5.1.3 Photothermal (PT) effect

Photothermal effects are where the absorbed light in the thin film generates heat which in turn changes the electrons' response. There are a broad range of compound effects which can be generally classed as photothermal. The ones relevant to this work are briefly described below:

5.1.3.1 Photo-thermoelectric (PTE) effect

In the photo-thermoelectric effect, light absorbed unevenly in the sample creates a temperature gradient. The temperature gradient generates a voltage due to the Seebeck effect which if connected to load can drive a small current. Usually, Seebeck effect is small in the range of a few hundred μV/K yet several studies have utilised this effect to fabricate self-powered photodetectors. Y. Zhang et. al., reported that in multilayer MoS_2 based transistors, PTE and PV effects work in tandem with each other [9] while M. He et. al., utilised the PTE effect in MoS_2 to fabricate PTE based flexible nanogenerators (PTENG) [10]. P. -Y. Huang proposed a polarisation sensitive photodetector and demonstrated a self-powered single walled CNT-MoS_2 based PTE detector in the visible range of electromagnetic spectrum [11]. M. Buscema et. al., on the other hand, claimed that most of the photoresponse in monolayer MoS_2 is attributed to PTE than PV (separation of charge carriers) [12]. Their mechanically exfoliated single layer MoS_2 flake showed a Seebeck coefficient between -4×10^2 μV/K to -1×10^5 μV/K tuned by an externally applied bias.

5.1.3.2 Photo-bolometric (PB) effect

From ***3-3.5,*** strong temperature dependence on resistance of TAC based MoS_2 thin films was shown and a high TCR was also calculated. Thus, a conclusion that temperature variation causes change in electrical conductivity of MoS_2 thin films was established without requiring any temperature gradient. This is known as a bolometric effect and when light induces variation in temperature that brings about a change in electrical conductivity, then this is regarded as photo-bolometric effect. This is especially found to occur in TCOs where hot carriers generate photocurrent i.e., when light is absorbed strongly by the TCO, it increases the temperature of the electrons which is directly proportional to the photocurrent

generated [13], [14]. J. Y. Wu et. al., have claimed PB effect to be the main cause of negative photocurrent in MoS_2 based phototransistors [15]. The NIR radiation in their case, induced lattice heating leading to the PB effect. In another instance, MoS_2 nanoflowers were used to enhance the sensitivity of CNT based infrared sensors by utilising the PB effect in MoS_2 [16]. The otherwise outstanding candidates for IR detection i.e., CNTs, suffer from low TCR with the exception of SWCNTs which are neither scalable nor cost effective. When combined with MoS_2, CNT-MoS_2 system achieved this goal by up to 18 folds. Their choice for MoS_2 was based on strong broadband absorption of up to 85% observed in extremely (thin 20 nm) MoS_2 porous films [17]. The work presented in this thesis does not consider 20 nm to be extremely thin because TAC based MoS_2 can produce even thinner films which has been shown in previous chapters and such films have been used to produce results presented in the subsequent sections.

Both PTE and PV based photodetectors are self-powered since they have a built-in electric field to drive the photogenerated carriers but PB based ones are not. They need an external bias to drive hot electrons, which adds a layer of disadvantage to PB based sensors.

5.1.3.3 Pyroelectric effect

In ancient times, civilizations in India, Greece and Ceylon were studying and reporting that transient change in temperature w.r.t time results in transient voltage spikes [18], [19]. In fact, ‘pyro’ means ‘fire’ in Greek probably hinting at ‘heat’ property of fire. A subset of piezoelectric materials naturally shows this property and such materials are known as pyroelectric materials. Non-centrosymmetry is a pre-requisite condition for being piezoelectric and thus also for pyroelectric materials. This non-centrosymmetry leads to spontaneous pyroelectric polarisation and materials that satisfy these conditions fall under the ferroelectric sub-group [19]. Pyroelectric effect has been observed in the recent past as well and has been reported for a multitude of applications like a multifunctional nanogenerator [20], photo-pyroelectric sensors [21], [22], pyro-thermoelectric generators [23], [24], neuromorphic sensors [25] and biomedical applications like optical synapses to bio-mimic eye retina [26]. Heat induced by virtue of light illumination, environmental conditions (changes in ambient temperature, bodily heat, heat plate, resistive heating) can cause transient electricity spikes. This is an extremely useful property for wearable electronics, biomedical devices powered by body heat, space applications and heat recovery

from an electric vehicle's internal mechanical and electronic apparatus to drive other systems thus increasing automobile efficiency.

5.1.4 Resonant effects in thin films

Absorption can be enhanced by using photonic resonances such as Fabry-Pérot (FP) cavities [27], [28]. In this work we see evidence of 0^{th} order FP resonances in ultrathin (~10 nm) MoS_2 layers. The resonances resulting from non-trivial phase shift on reflection from the absorbing thin film and can result in destructive interference of the reflected light even in deeply sub-wavelength films [29]. In general, they require a lossy dielectric film with reflective metal backing however we can also get strong absorption with MoS_2 of a sub-wavelength thickness with reflective backing. Additionally, another absorbing layer can be added by utilising a lossy dielectric film between metal reflecting layer and MoS_2 layer which is similar to a Salisbury screen concept [30]. We are particularly interested in MoS_2 based devices in the visible range where room temperature excitons generate sharp features in the absorption spectrum. This not just provides a platform to explore active light modulation as discussed in ***ch. 4*** but also leads to the enhancement of photodetection using high light absorption by MoS_2 in the visible spectrum.

5.2 Photoresponse in CVD grown MoS_2

CVD MoS_2 flakes were procured from Dr. Niall McEvoy's group. These flakes are known to appear randomly and discontinuously on the substrate which makes it difficult to make devices out of them.

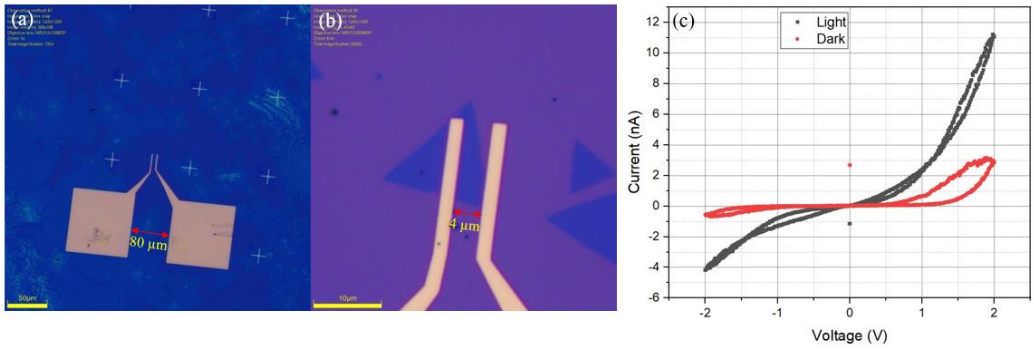

***Fig. 5.1**: **(a)** EBL contacts on CVD MoS_2 flakes with extended contact pads for easy measurement. **(b)** Zoomed-in image of one isolated flake with EBL contacts 4 μm apart. **(c)** I-V sweep showing increase in current upon light illumination (black) compared to dark case (red) when measurement was done in the dark.*

CVD grown MoS_2 flakes have lateral dimensions on the order of tens of microns which makes placing electrical contacts difficult and must be done on a flake-by-flake basis. Therefore, great efforts have been made recently to extend these films to large area [31], [32], [33]. For these samples gold electrical contacts were deposited using EBL patterning shown in ***fig. 5.1(a)*** and **(b)**. ***Fig. 5.1(a)*** shows EBL contacts with extended square contact pads to land needle probes easily and ***fig. 5.1(b)*** shows a zoomed-in optical picture of the same clearly showing triangle MoS_2 flakes where one of the isolated flakes is used for placing EBL contacts. I-V sweeps were carried out in dark and white light conditions. These two sweeps are shown in ***fig. 5.1(c)*** for comparison and show a double Schottky type of trend indicating asymmetric rectifying contacts with CVD MoS_2. Furthermore, current upon illumination increases slightly but it is in nA range in both cases. Lastly, some hysteresis is also observed in both cases which was not investigated at that time and at present the sample has been degraded, so not much can be said about it at this point. However, relying on past studies, this trend looks like electromigration mechanism [34] most probably caused due to atomic defects [35].

5.3 Photoresponse in Liquid-liquid interface deposited (LLID) MoS_2

Another novel method of MoS_2 synthesis is electrochemical exfoliation combined with liquid -liquid interfaces assembly techniques. Langmuir Schaefer [36] and Langmuir Blodgett methods use liquids of different densities to form an interface. Here, electrochemically exfoliated MoS_2 particles settle towards this interface and form horizontal nanosheet films with conformal junctions after which the substrate is carefully retrieved out of the liquid-liquid interface and is left for drying. Post-deposition annealing makes it further adhere to the substrate and remove the residual liquid solvents [37], [38]. Courtesy of our collaboration with Prof. Jonathan Coleman's group in School of Physics, we were able to get some MoS_2 prepared by this dipping process onto pre-patterned substrates on request. The liquid-liquid techniques are required in order to make the films thin and uniform enough for comparison with CVD and TAC based films. ***Fig. 5.2*** shows the layer-by-layer process of making a sample of MoS_2 deposited by liquid-liquid interface exfoliation on our pre-patterned substrates for photoresponse study. The preliminary patterned structure is shown in ***fig. 5.2 (a)***, ***(b)*** where Ti/Au 100 nm square pads were deposited as the first layer. This mask design is reused from the modulation stack design (***4-4.4.1.1***) where one of the pads is used for the active area and the other pad is used as the extended pad for safe landing of needle contact probes to avoid damage to the active layer structure. It should be noted that

this mask design was also the very first one to be made and an error of not mirroring the numbers in the design stage resulted in the actual mask to have mirrored numbers. therefore, samples made using this mask have mirrored numbers which should not be confused with a flipped sample. This mask was used to deposit the first layer (L1: Ti 1 nm/Au 100 nm) and second layer (L2: 30 nm Si_3N_4) for many samples like the ones shown in ***fig. 5.2(a)*** and (***b).***

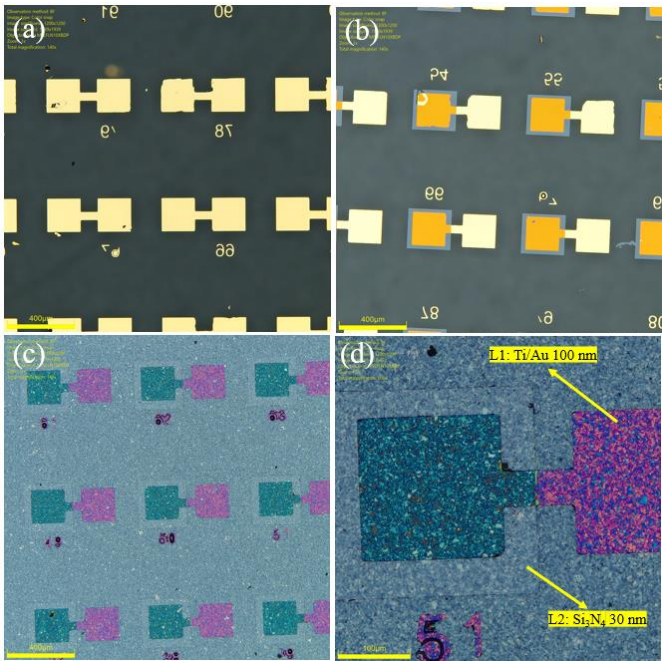

Fig. 5.2*: **(a)** Layer 1: Ti/Au 100 nm deposition. One of the square pads is used to form the active area of the structure while the other square is used as an extended electric contact. **(b)** Layer 2: Si_3N_4 deposition on the active area. **(c)** Layer 3: All over MoS_2 deposited by liquid-liquid exfoliation. **(d)** Zoomed-in image from **(c)** showing MoS_2 coloration effects due to interference with L1: Ti/Au (pinkish-purple areas on the right-side square) and L2/L1: Si_3N_4 on Au (teal-emerald-blue area on the inner square on left side).*

MoS_2 deposited by liquid interface exfoliation results in grainy textured MoS_2 which consists of a size range of different MoS_2 particles with different orientations. Flakes of varying thickness can be easily identified since they optical interfere from the metallic background resulting in slightly different coloration or shades. It can be noticed in ***fig. 5.2(d)***, that certain regions in the square pad on the right side show a range of MoS_2 coloration from deep pink or magenta to bluish-purple to light blue. This is another proof of FP interference of TMDs with metal backing.

Needle probes were placed on either side of the pink-purple square consisting of ~ 15-20 nm MoS_2 on 100 nm of Au (Region 1). Then voltage of 5 V, 10 V was applied and current vs time was recorded which is shown in ***fig. 5.3***. The photoresponse of these structures is very slow on the order of seconds as they are very defective and have a lot of junctions.

Compared to photoconductivity in [7], where MoS_2 was prepared by a similar solution processed method, here when backed with Au metal, it exhibited a higher photocurrent. G. Cunningham et al. presented photoconductivity results for a 6 μm thick MoS_2 sandwiched between ITO and Au electrodes to make a vertical stack and therefore photocurrent vs time plots correspond to this out-of-plane arrangement and ~5.5 nA of photocurrent is obtained at 15 V and 1100 W/m^2 of illumination in their case. However, in our case presented here, MoS_2 is much thinner (~15 nm) having a gold backing, so FP effects appear more prominent. This is a possible reason as to why much higher photocurrents (~100 nA, 380 nA) are obtained in the case of LLID MoS_2 shown in ***fig. 5.3(b)*** at 5 V and 10 V under a class-3 laser of 405 nm and 4.5 mW of illumination.

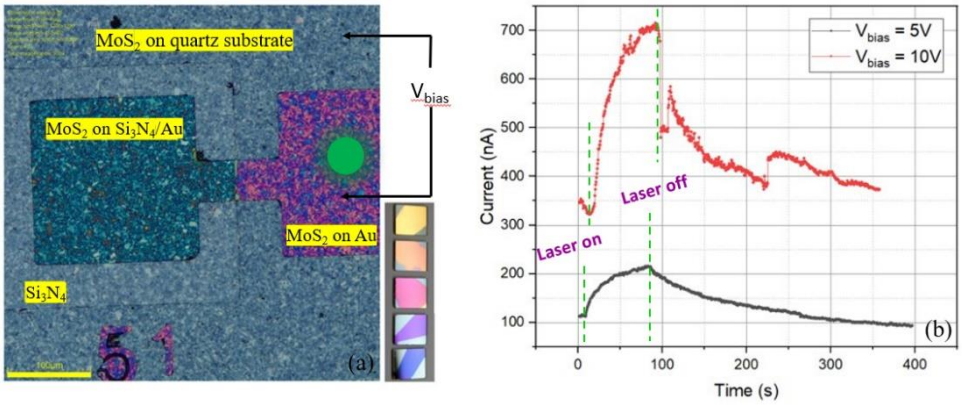

***Fig. 5.3**: **(a)** Representative setup showing the position of two needle probes used for biasing (5 V and 10 V) the MoS_2 (topmost layer) deposited by LLID on pre-patterned substrates under 405 nm laser shown by a green circle. A vertical bar of 5 samples of TAC based MoS_2 with Au backing is shown as a colour match chart at bottom right of it. **(b)** Time vs current plot associated with the region described in **(a)** showing rise in current when the laser is turned on and then fall in the current when laser is turned off for both biases.*

5.4 Photoresponse in TAC MoS_2

Before delving into details of the different experiments performed and the results obtained, a summary of the samples used in this section and subsequent sections is given in tab. 5.1.

Table 5.1: Samples consisting of TAC MoS_2 and used for photoresponse measurements

Sample name	Substrate	Stack structure	Starting Mo deposition time (s)	TAC temperature (℃)	TAC time (min)
SS1A6 **SS1A9** **SS1A15** **SS1A20** **SS1A30**	Si/SiO_2	Substrate/Ti (1 nm)-Au (50 nm) IDEs/MoS_2	6 9 15 20 30	850	30

SS1B6 **SS1B9** **SS1B15** **SS1B20** **SS1B30**	Si/SiO_2	Substrate/Ti (1 nm)-Au (100 nm) IDEs/MoS_2	6 9 15 20 30	850	30
SS2	Quartz	Substrate/Ti (1 nm)-Au (100 nm)/Si_3N_4 (30 nm)/MoS_2	100	850	30
SS3	Quartz	Substrate/Ti (1 nm)-Au (100 nm) vertical strip/ MoS_2 / Ti (1 nm)-Au (100 nm) S-D horizontal contacts	150	850	30

For photoresponse measurements on TAC MoS_2 films, three sets of samples were prepared to show different aspects of photoresponsivity in TAC based MoS_2. The first set of samples – **sample set-1** consists of 'SS1A' series and 'SS1B' series from ***tab. 5.1***. This set utilised the IDE mask design (based on Ossila Ltd., U.K. design) as also discussed in ***3-3.2.2.2*** with 5 devices of varying inter-electrode spacing and with extended S-D contacts for easy measurement using push-fit test boards and SMUs. One of the representative samples of this set is shown in ***fig. 5.4(a)***. Here, once again, Ti/Au (50 nm, 100 nm) S-D contacts formed the first layer and MoS_2 (of thickness varying from ~6 nm to ~ 30 nm) was deposited on top of them as the second layer. The samples with 50 nm Ti/Au contacts are 'SS1A6 to SS1A30' in ***tab. 5.1*** and samples with 100 nm Ti/Au contacts are 'SS1B6 to SS1B30' in ***tab. 5.1***. The lateral distances are the interelectrode spacing between the IDEs. The novelty here is similar to photoresponsivity studies performed on electrodeposited MoS_2 [39] by N. M. Abdelazim et. al. They electrodeposited multilayer, site selective and scalable MoS_2 films onto patterned electrodes with insulating top surface but conductive side edges. Similar to TAC based MoS_2 presented in this work, their MoS_2 was not just photolithographically compatible but also did not cause any harm to pre-existing patterned layers. Their photocurrent is however still lower than what has been observed in some of the devices presented in this work which will be discussed in more detail in sections to follow. This is possibly because devices based on the design of this sample set utilizes the enhanced absorption of MoS_2 backed by Au in some regions and Si/SiO_2 in other regions as will be explained in subsequent sections.

The second set of samples: **sample set-2** ('SS2' from ***tab. 5.1***) have the same structure as that of LLID samples in ***sec. 5.3.*** As before, 1.5 cm^2 quartz substrate is used to pattern and deposit layer 1 (Ti/Au 100 nm) and layer 2 (Si_3N_4 ~30 nm) using the same mask. The only

difference is in layer 3 which this time is TAC based MoS_2 (***fig. 5.4(b)***) deposited all over the substrate. Finally, a third set of samples: **sample set-3** ('SS3' from ***tab. 5.1***) was prepared as a part of an extended study from the second set of samples. Here, another custom-made mask was used that consisted of 7 horizontal strips of TAC MoS_2 with 5 of them having a running vertical strip of gold underneath which is thick enough to facilitate FP interference in the sub-nanometre thick MoS_2 strips and rest 2 out of the 7 horizontal strips were left without any metal backing. Then layer 3 of source drain contacts with a common drain for all the devices was deposited. These S-D contacts were extended out till the edge of the 1.5 x 2.5 cm^2 quartz substrate for making an easy electrical contact with an edge connector whose conducting legs are punched into a breadboard.

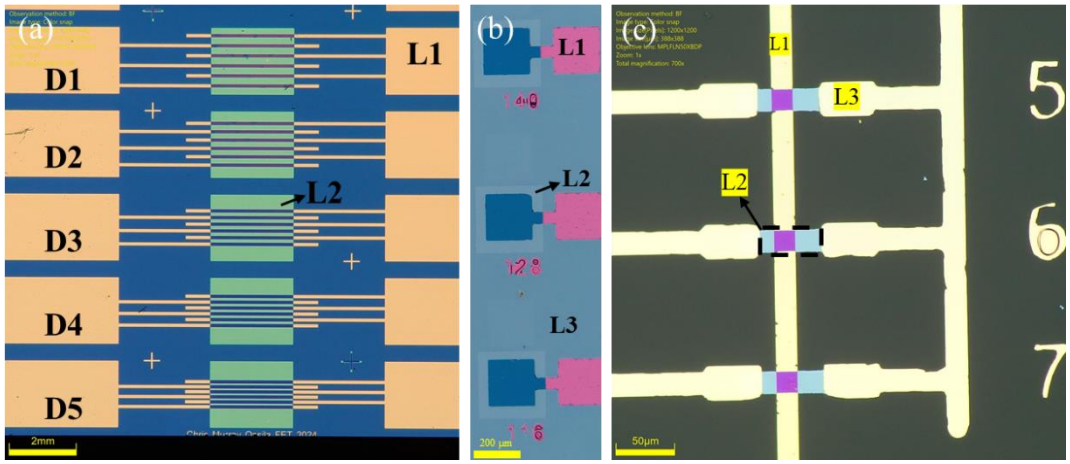

Fig. 5.4*: Optical microscope images showing the top view of* ***(a)*** *sample set-1* ***(b)*** *sample set-2* ***(c)*** *sample set-3.*

Different devices can be biased separately by using jumper wires corresponding to the source contact of each device. This setup is shown in ***fig. 5.18***. And one of the representative samples used for measuring under this setup is shown in ***fig. 5.4(c)***. The purple square is the area consisting of 15 nm MoS_2 on 1 nm Ti/100 nm Au which is around ~10 µm wide.

The following sections present photo-induced response for each of the three sets of TAC based MoS_2 samples described above subjected to:

1) Broad area white light continuous wave (CW) illumination which was achieved using Ossila's solar simulator
2) Focused 405 nm laser illumination
3) Square wave modulated illumination using 511 nm diode laser.

5.4.1 CW illumination

5.4.1.1 Sample set-1: IDE design

The first step of investigating photo-induced response in TAC based MoS_2 was to measure current 'I' vs voltage 'V' (I-V) sweeps of samples prepared from Ossila's variable IDE mask design (as discussed previously) under dark condition and then upon illumination from Ossila's solar simulator. Samples of varying MoS_2 thickness based on the bottom-side hybrid IDE contact design were kept under the solar simulator one at a time. With the solar simulator turned off initially, I-V sweep was recorded from 10 V to –10 V and then it was repeated with the solar simulator turned on. This was done for all the devices (D1 to D5) of all the samples of MoS_2 with thicknesses of 6 nm, 9 nm, 15 nm and 20 nm (SS1B6-20). The solar simulator was set to provide its 100% irradiance output i.e., 1 sun (1000 W/m^2) at AM 1.5G. In the following sections, this is the default setting used everywhere unless specified. For some reason, the first set of these samples couldn't sustain large negative voltages.

The contacts broke down (burnt out) if swept beyond ~ -3 V towards negative direction. So, another set of samples with the same design were measured from –3 V to 10V and they seemed to remain stable after multiple I-V sweeps in both dark as well as light conditions. ***Fig. 5.5(a)*** shows I-V sweeps of D1-D4 of a 9 nm TAC based MoS_2 sample under dark condition. Since D5 has the shortest inter-electrode spacing, its I-V sweep is non-linear (red curve in ***fig. 5.5(c)***) unlike D1-D4 which were linear. Similarly, such sweeps were repeated next with the solar simulator turned on. A comparison of current under light conditions (referred to as 'light current' for simplicity) vs. current measured in dark conditions (referred to as 'dark current' for simplicity) at 10 V bias is represented in the form of bar graphs for D1-D4 in ***fig. 5.5(b)*** and D5 in ***fig. 5.5(d)***.

Non-linear behaviour of I-V sweeps was observed for all the thicknesses of MoS_2 in this sample set. ***Fig. 5.5(e)*** shows light current increasing non-linearly as a function of voltage and monotonically as a function of thickness until 15 nm after which I-V sweeps corresponding to 20 nm thickness falls between that of 6 nm and 9 nm as can be seen by the green curve in ***fig. 5.5(e)***. A more representative picture of this argument is shown in ***fig. 5.5(f)*** where both dark and light current for 20 nm MoS_2 decrease as compared to the 15 nm MoS_2 and more generally the dark current peaked for 9 nm MoS_2 after which it decreases for higher thicknesses and photocurrent follows the trend of light current across the thicknesses shown. Another noticeable parameter is the photo-to-dark current ratio (PDCR)

which is the ratio of photocurrent (teal blue bar graph in ***fig. 5.5(f)***) and dark current (black bar graph in ***fig. 5.5(f)***. A transition from PDCR < 1 to PDCR > 1 is seen when thickness surpasses 15 nm.

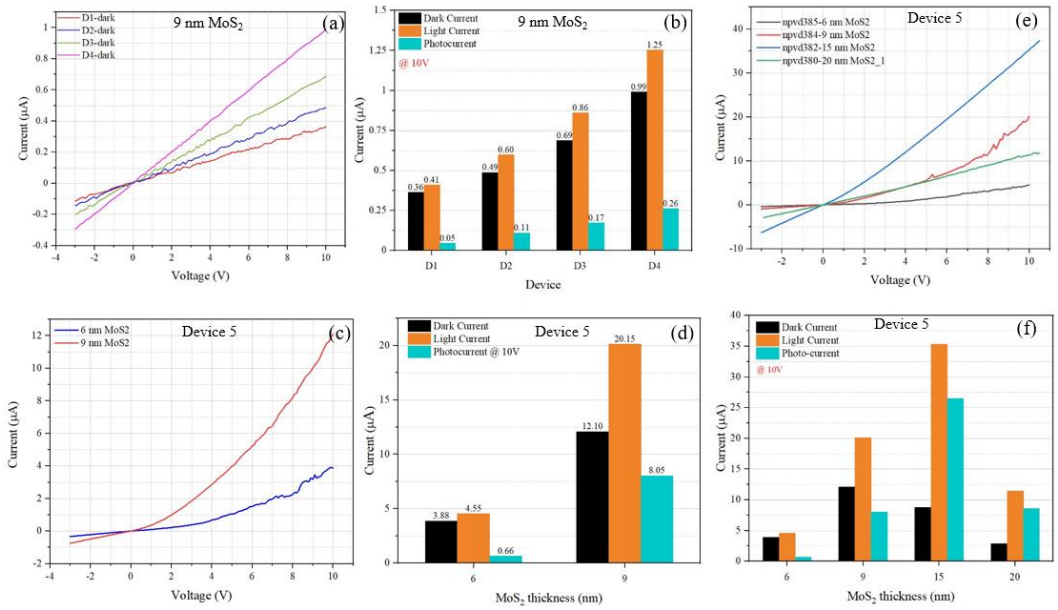

Fig. 5.5*: **(a)** Dark I-V sweeps of 9 nm MoS_2 ('SS1B9' from tab. 5.1) sample with IDE devices of varying inter-electrode spacing. **(b)** Dark current, light current and photocurrent for each device at 10 V for the same sample in **(a)**. **(c)** Dark I-V sweeps of D5 for 6 nm and 9 nm MoS_2 'SS1B6,9'. **(d)** Dark current, light current and photocurrent for D5 at 10 V for the same samples as in **(c)**. **(e)** Light I-V sweeps of D5 for varying MoS_2 thicknesses. **(f)** Dark current, light current and photocurrent for D5 at 10 V for the same samples as in **(e)**.*

A special case is device 5 of a ~ 12 nm MoS_2 film deposited on 50 nm Au IDEs, shown in ***fig. 5.6*** where the substrate edge was chipped off taking away part of the active area. This left only a pair of undamaged electrodes to collect the photogenerated carriers while the entire area marked by white dashed box is used to generate photocarriers.

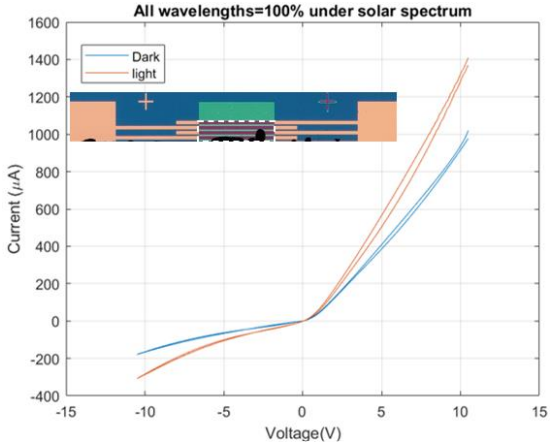

Fig. 5.6*: I-V sweep of a damaged device with asymmetrical contacts and reduced illuminated area compared to an undamaged device.*

A combination of asymmetry in the contacts, reduced effective area and expected optical interferences (0^{th} order FP and Salisbury effect) mentioned previously in ***sec. 5.1.4*** lead to an extremely large photocurrent ~ 390 µA at an optical input of 0.1 A/W. The effective illuminated area is calculated to be around 0.0096 cm^2, and responsivity, R is calculated as:

$$R = \frac{390\ \mu A}{0.1\frac{W}{cm^2} * 0.0096\ cm^2} = 0.4063\ A/W$$

Like the previous experiment (in ***sec. 5.3***), 'I' as a function of 't' was also measured in the same set of samples under both light and dark conditions. Here the Ossila IDE design based MoS_2 sample set is further divided into two kinds: 1) 100 nm Au S-D contacts (SS1B series in ***tab. 5.1***) and 2) 50 nm Au S-D contacts (SS1A series in ***tab. 5.1***). With the solar simulator turned off initially and a voltage bias of 10 V applied to the S-D electrodes, the measurement of 'I' vs 't' was recorded using Ossila's software and after the dark current settled, solar simulator was turned on until the photo-induced current reached its peak after which the solar simulator was again turned off to let the current fall to its dark current value. This was done for devices D3 and D5 of TAC based MoS_2 samples of both the sub-sets (SS1A and SS1B series). ***Fig. 5.7*** shows I-t plots of D3 and D5 of sample SS1B6 (***fig. 5.7(a), (b)***) and sample SS1A6 (***fig. 5.7(c), (d)***). In the I-t plots of D3 (***fig. 5.7(a), (c)***) for both SS1A6 and SS1B6, not much difference is observed but in the case of D5 (***fig. 5.7(b), (d)***) where inter-electrode spacing is the smallest (50 µm), an increase of almost 100 times in the order of magnitude is seen for SS1A6 compared to SS1B6.

Rapid band-to-band transitions due to freeing of electrons from holes and transitioning to the conduction band [3], [42], [43] are marked by '1' and '3' and comparatively slower rise and decay are marked by '2' and '4' respectively in ***fig. 5.7(b)***.

Both stage-1 and 3 are rapid band-to-band transitions occurring the very next instant the light is turned on and off respectively. Stage-2 and 4 are attributed to persistent photoconductivity (PPC) arising from both extrinsic (charge trapping at the MoS_2-substrate interface [44], [45], ambient conditions [46], [47]) and intrinsic effects (structural disorder [48] and defects like Sulphur vacancies that introduce mid-gap localized donor states [49]). All these are possible sources of PPC in TAC based MoS_2 and the measurements presented

here as well since no post-deposition treatment was done on these devices and no encapsulating dielectric layer was deposited to protect them from oxidation.

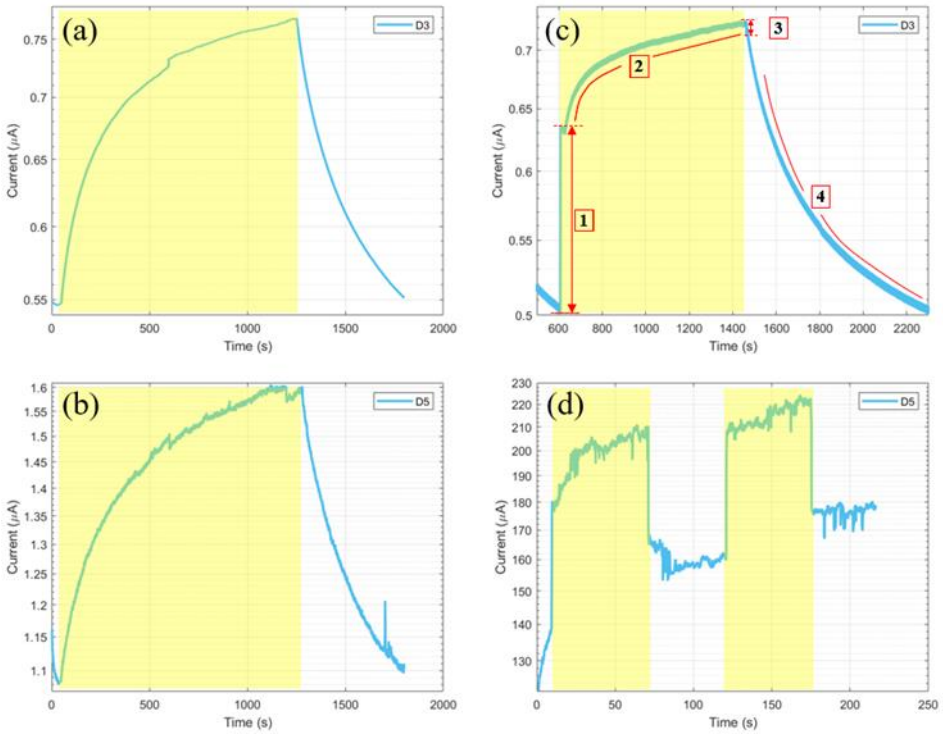

***Fig. 5.7**: Time response of 6 nm MoS_2 with 100 nm Au S-D contacts, **(a)** device 3 **(b)** device 5. 6 nm MoS_2, 50 nm Au S-D contacts, **(c)** device 3 **(d)** device 5.*

Moreover, these measurements were carried out in air and at room temperature and pressure (humid) carrying water and oxygen in abundance. This analysis is based on the random local potential fluctuations (RLPF) model which arise due to both extrinsic and intrinsic sources.

The only device that does not follow this trend is D5 of 6 nm MoS_2 on 50 nm Au S-D electrodes (SS1A6) shown in ***fig. 5.7(d)***. Upon close inspection, it can be seen that this device also has more than 100 times higher current as mentioned previously and stage-3 component is more pronounced in this case as compared to others. Perhaps, if the measurement after turning the light off after stage-3 was left to run without starting the second cycle of measurement, slow decay of current (stage-4) and a sustained PPC effect could have been observed. It can still be observed slightly upon noticing that the current doesn't completely fall to its dark current value after turning the light off and the fact that the current shows an upwards trend in the second cycle for both on and off states is indicative of a PPC effect.

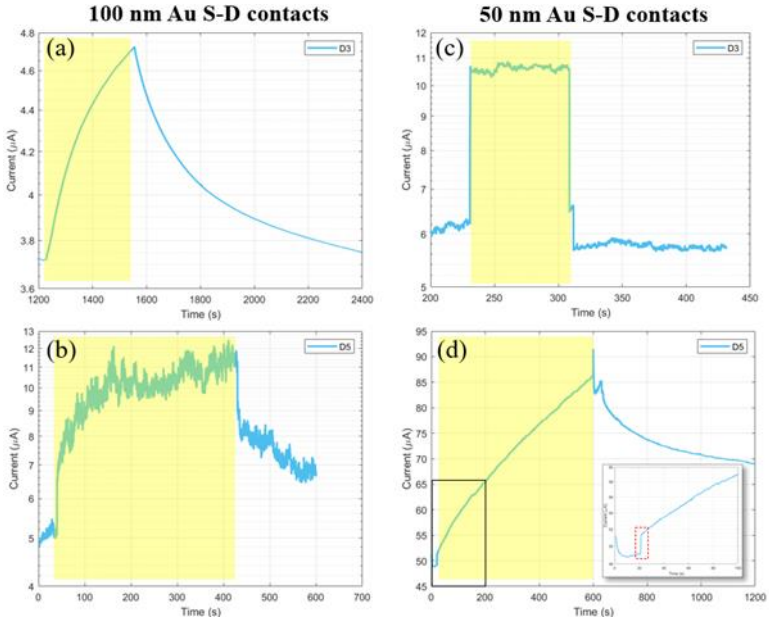

Fig. 5.8*: Time response of 15 nm MoS_2 with 100 nm Au S-D contacts (sample 'SS1B15' from tab. 5.1),* ***(a)*** *device 3* ***(b)*** *device 5. 15 nm MoS_2, 50 nm Au S-D contacts (sample 'SS1A15' from tab. 5.1),* ***(c)*** *device 3* ***(d)*** *device 5. Inset shows zoomed-in part marked by black rectangle. Red rectangle shows the rapid band-to-band transition region*

These observations also hold valid for the same devices of thicker TAC based MoS_2 shown in ***fig. 5.8***. Sample 'SS1A15' from ***tab. 5.1*** -15 nm MoS_2 on 50 nm Au S-D (D5) contacts gives the highest light current shown in ***fig. 5.8(d)***, however accompanied by slow rise and decay. Stage-1 rapid transitions corresponds to almost 2 μA which is still higher than light current obtained from stage-2 of 15 nm MoS_2 on 100 nm Au S-D (D3) ***fig. 5.8(a)***. The spike in current around 600s is due to movement of the apparatus while switching the illumination off and not representative of the actual measurement. Measurement shown in ***fig. 5.8(d***) was performed in ambient air. To validate the effect of surrounding atmosphere and investigate the effect of oxidation on bare MoS_2 devices without any protective dielectric encapsulation, the same device - D5 of 15 nm MoS_2 on 50 nm Au S-D (sample 'SS1A15' from ***tab. 5.1***) was exposed to 30s of ozone treatment using Ossila UV ozone cleaner. This resulted in lowering of the current shown in ***fig. 5.9*** upon same illumination and bias settings used for ***fig. 5.8(d)***. This result proved how excess oxygen has a damaging effect on MoS_2 based photodetectors and for optimum performance, encapsulation with a transparent dielectric is the best way forward. Alternatively, devices without encapsulation can be used in ambient air with controlled oxygen content only for a limited time.

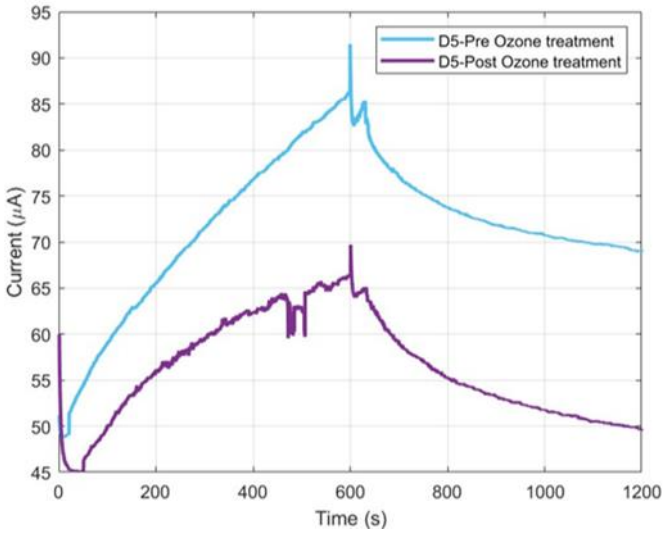

***Fig. 5.9**: I-t response of 15 nm MoS_2 (D5) on 50 nm Au S-D interdigitated contacts (sample 'SS1A15' from tab. 5.1) measured before and after ozone treatment. Both measurements were done under the same bias and illumination conditions.*

It is noteworthy that the observed photocurrent is dependent on the MoS_2 thickness as well as enhanced absorption in MoS_2 due to metal backing. MoS_2 by itself on a transparent substrate like quartz has the absorption spectra shown in ***fig. 5.10(a)*** but with a metal backing like 100 nm Au on S/SiO_2 substrate, the absorption spectrum changes as in ***fig. 5.10(b)*** to match more to the energy spectrum of the sun (***fig. 5.10(c)***) and absorb more of its incident visible radiation. The effect of Si is negligible compared to Au which means that the enhanced absorption in MoS_2 is mainly due to the underlying Au layer. Effect of this phenomenon is also realised in photocurrent measurements for different thicknesses of MoS_2 shown in ***fig. 5.11(a)-(c)*** where same device is measured for MoS_2 of different thicknesses and is deposited on 100 nm Au layer on Si/300 nm SiO_2 nm substrate.

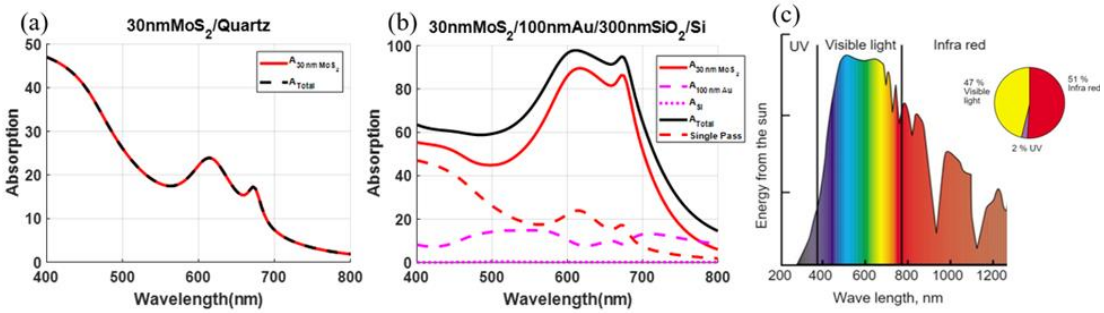

***Fig. 5.10**: TMM simulation of 30 nm MoS_2 absorption on **(a)** quartz and on **(b)** 100 nm Au. **(c)** solar irradiance spectrum.*

Their associated TMM simulations of absorption spectra and stack layers are shown in ***fig. 5.11(d)-(f)*** where it is evident that not only the total absorption (A_{total}) peak increases but also its spread across the wavelength range increases with increasing MoS_2 thickness. ***Fig. 5.12*** shows photocurrent ($I_{light} - I_{dark}$) measured as a function of solar simulator's individual wavelengths set at 100% illumination one by one for a 6 nm MoS_2 film on 50 nm Au/ 300 nm SiO_2/ Si substrate.

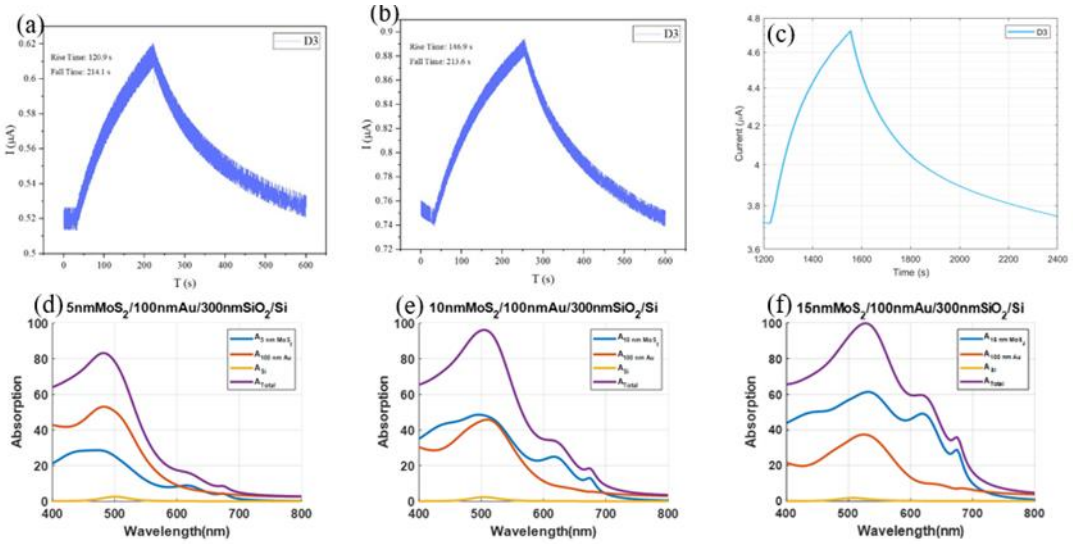

Fig. 5.11*: I-t plots* ***(a)-(c)*** *of 5 nm, 10 nm and 15 nm MoS_2 and their respective absorption spectra simulated by TMM* ***(d)-(f)****.*

Given the assumption that most of the absorbed light (simulated) from the solar simulator is converted to photocurrent (measured), the measured trend seems to closely follow its simulated counterpart in ***fig. 5.11(d)***. This trend also matches the spectral response of MoS_2 in a metal-semiconductor-metal (MSM) structure in O. A. Abbas's study [50] (just like the MSM structure presented here) and MoS_2-on-ZnO heterojunction photodetector [2].

From ***fig. 5.12***, the responsivity, 'R' calculated at 600 nm, no gate bias and a smaller drain voltage (10 V) for TAC based MoS_2 compares well with what has been reported previously [50], [51]. With I_{ph} (130 µA), area of MoS_2-D5 (0.085 cm^2) and light intensity (0.1 W/cm^2), 'R' for TAC based MSM MoS_2 structure presented here is

$$R = \frac{130\ \mu A}{0.1\ \frac{W}{cm^2} \cdot 0.085\ cm^2} = 0.015\ A/W$$

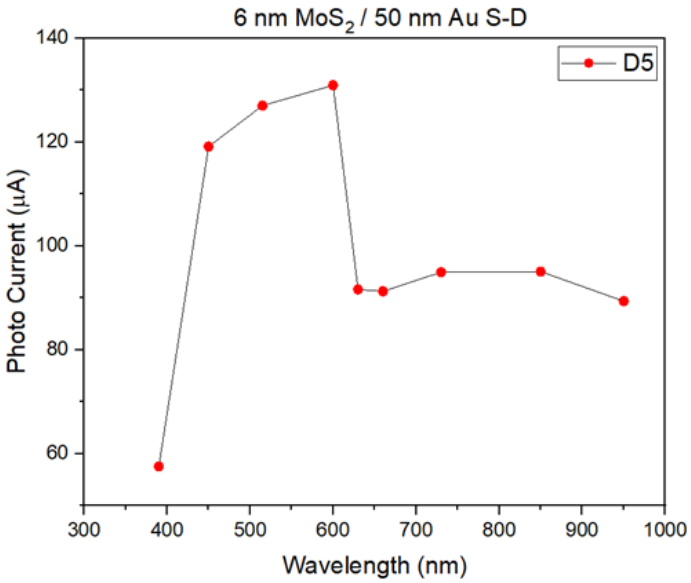

***Fig. 5.12**: Spectral response of MSM structure using TAC based 6 nm MoS_2 as the semiconductor and 50 nm Au as the interdigitated metal contacts. Laterally, they form a MSM structure.*

For a complete picture to understand the effect of MoS_2 thickness and metal backing on its optical properties, the evolution of MoS_2 absorption spectra as a function of its thickness in the stacks: MoS_2/100 nm Au/300 nm SiO_2/Si and MoS_2/50 nm Au/300 nm SiO_2/Si are shown in ***fig. 5.13*** and ***fig. 5.14***.

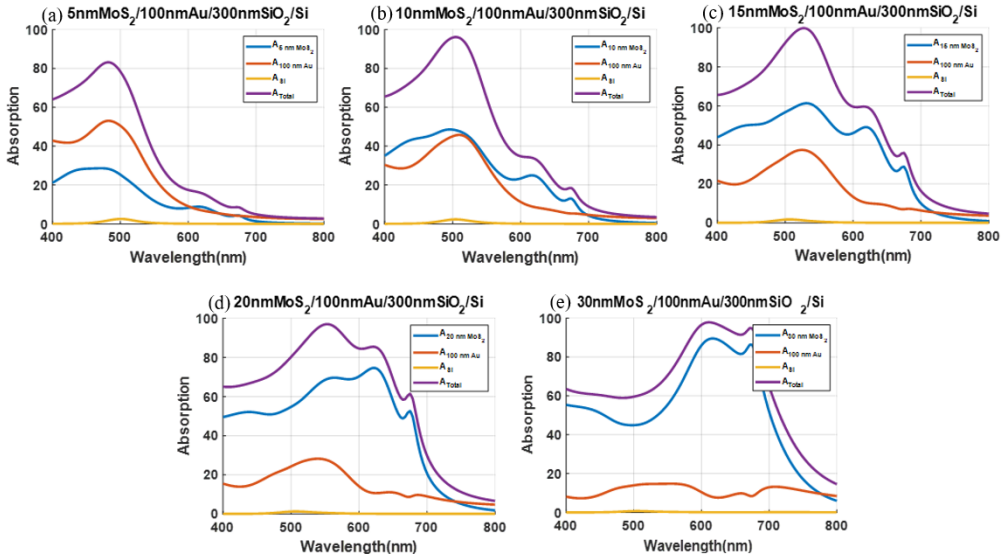

***Fig. 5.13**: Layer resolved TMM simulations of **(a)** 5 nm **(b)** 10 nm **(c)** 15 nm **(d)** 20 nm **(e)** 30 nm MoS_2 absorption on 100 nm Au/300 nm SiO_2/Si*

MoS_2 is more absorbing across the visible wavelength range for thicker (MoS_2 ~ 15 nm and above) films and Au backing gives a further push to the absorption around ~520 nm. The highest total absorption bump again seems to mimic Au absorption for films less than 15 nm in thickness. Doubling MoS_2 thickness makes a huge difference.

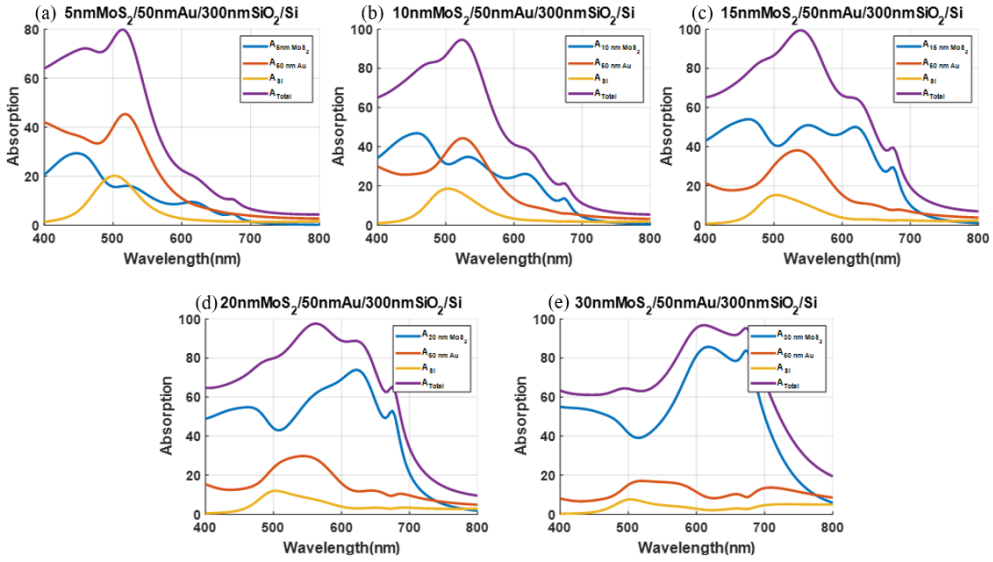

***Fig. 5.14**: Layer resolved TMM simulations of **(a)** 5 nm **(b)** 10 nm **(c)** 15 nm **(d)** 20 nm **(e)** 30 nm MoS_2 absorption on 50 nm Au/300 nm SiO_2/Si.*

Comparing ***fig. 5.13(c)*** and ***fig. 5.14(c)*** with ***fig. 5.13(e)*** and ***fig. 5.14(e)*** respectively, highest total absorption peak shifts towards 600-700 nm and overall spread also increases across the visible range for 30 nm MoS_2 in both 50 nm Au and 100 nm Au metal backing cases.

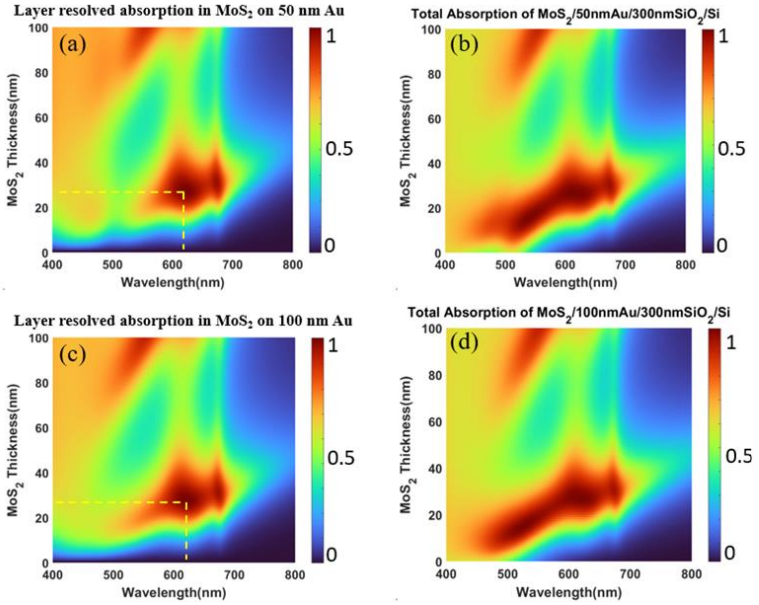

***Fig. 5.15**: TMM surface plots summarising **(a)**, **(c)** layer resolved absorption in MoS_2 on 50 nm and 100 nm Au respectively and **(b)**, **(d)** total absorption of MoS_2 on Au/SiO_2/Si stack as a function of varying MoS_2 thicknesses across the visible electromagnetic spectrum.*

Also, total absorption seems to rely more on MoS_2 than Au for films thicker than 15 nm. The best-case scenario for maximising absorption in such a stack is to have 25-30 nm thick TAC based MoS_2 and illuminating it with light of wavelength around 600 nm as shown in ***fig. 5.15***.

5.4.1.1.1 Investigation of photocurrent scaling with geometrical parameters of IDE design

Finally, the solar spectrum was used to study the scaling of light current density with the area of each device. Referring to ***fig. 3.8(a)*** in ***Ch. 3***, the area 'A' of MoS_2 can be considered in two ways for calculations. The first way is to consider the entire square block confined within the MoS_2 deposited layer (light blue area: 2 mm × 2 mm) which makes the area to be constant in calculations for each device. The second way is to consider the area confined within the first (topmost) electrode and the last (bottom-most) electrode for each device. This scales the area according to the inter-electrode spacing of each device respectively. Assuming MoS_2 in each device behaves like a resistor (MSM model or 2 diode model considers MoS_2 as a resistor with resistance 'r'), current density can be expressed as:

$$r = \frac{V}{I} = \rho \frac{L}{A}$$

$$\Rightarrow \frac{I}{A} = J \propto \frac{1}{L}$$

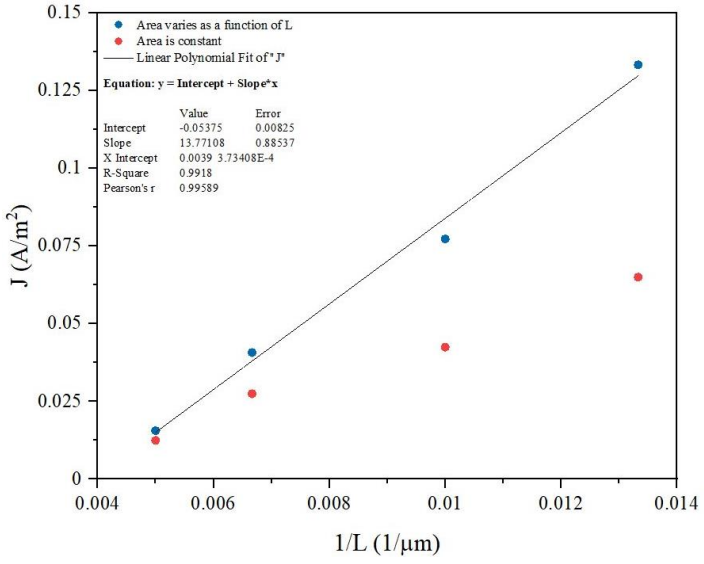

Fig. 5.16*: Current density calculated from measured light current under white light default solar spectrum considering constant area (red) and as a function of 'L' of each device (blue).*

Current density 'J' varies linearly with the inverse of electrode spacing 'L' which is also shown by the linear fit of blue scatter plot in ***fig. 5.16*** when the active area is considered to be a function of electrode spacing i.e., the active area is bound between the topmost and the bottom-most electrode in each device.

5.4.1.2 Sample set-2: LLID design

An imitation of experiment presented in ***sec. 5.3*** was performed but this time with TAC based MoS_2 (sample 'SS2' from ***tab. 5.1***). Just like samples shown in ***fig. 5.2***, Au extended pads and Si_3N_4 square pads were prepatterned as layer-1 (L1) and layer-2 (L2) respectively, over which Mo was deposited using sputtering and then sulphurised in the TAC furnace to form MoS_2 as the top layer (L3). ***Fig. 5.17(b)*** shows pale yellow L1 extended across both columns and L2 as a faded blue square on top of the left extended pad of L1 causing orange coloration in the overlapping area. It is interesting to note that the rest of the area left outside of the orange overlapping area appearing as faded blue also forms a Salisbury screen (metal (Si)-dielectric (SiO_2/Si_3N_4)-metal (Mo)). L3 is formed by depositing Mo all over both the layers. The entire sample was then sulphurised to convert Mo (L3) into MoS_2 covering the entire area of the 1.5 cm^2 sample shown in ***fig. 5.17(c)***.

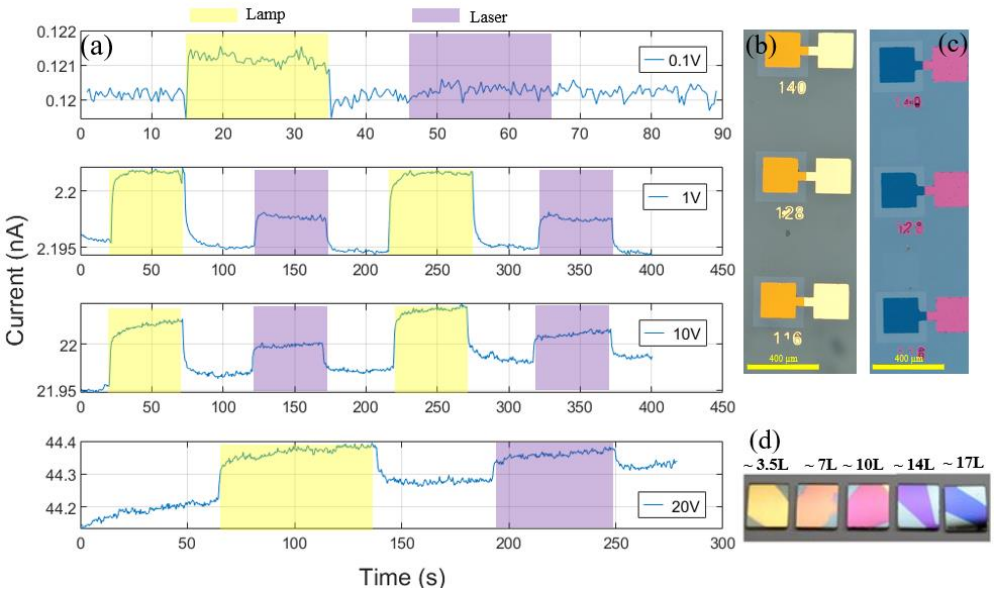

***Fig. 5.17**: **(a)** I-t plots at different biases under 405 nm laser and white light lamp turned on and off manually (yellow and purple shaded regions show lamp and laser on state respectively). **(b)** DUTs pre-sulphurisation i.e., L1 as Ti/Au (pale yellow), L2 as Si_3N_4 (big squares covering the extended Au pad on left column) and L3 as Mo deposited all over the surface. **(c)** same DUTs post-sulphurisation. **(d)** L3 changes to MoS_2 of thickness between ~10-14L layers (~10-11 nm).*

The pink colour corresponds to interference between L1 and L3 (0^{th} order FP), dark blue colour corresponds to interference effect caused by L1, L2 and L3 (1^{st} order FP). ***Fig. 5.17(d)*** shows a set of TAC based MoS_2 samples of different thicknesses backed by Au metal to compare with coloration seen in the patterned samples post sulphurisation (***fig. 5.17(c)***). Probes were placed on the pink squares of device 140 and device 116 to bias L3 (MoS_2) lying directly on top of L1 (Au) of device 128. The bias values applied were 0.1 V, 1 V, 10 V, 20 V and device 128 was illuminated by lamp and laser as indicated in ***fig. 5.17(a)***. When laser was used, 405 nm laser spot was focussed roughly in the centre of device 128. Photoconductivity of TAC based MoS_2 on prepatterned Au pixels was then measured by recording current response each time lamp/laser was turned on and off with respect to time as shown in ***fig. 5.17(a)***. Though low in magnitude, the response time is faster than what was observed in LLID based MoS_2 (***fig. 5.3***). Compared to ***fig. 5.3*** (LLID based MoS_2), low current is observed in ***fig. 5.17(a)*** (TAC based MoS_2) because the probes are stationed much farther apart from the illumination spot as described previously which increases the overall resistance thereby causing a decrease in the measured photocurrent. Also, the photocurrent arising here is purely out of the 0^{th} order FP optical effect since the Au underneath MoS_2 on device 128 which is illuminated is kept electrically unbiased.

5.4.1.3 Sample set-3: Observation of NPC in TAC based MoS_2 films

Fig. **5.19** shows TAC based MoS_2 sample with laterally confined dimensions ~ 10 µm and this is the optimum dimension for which MoS_2 can be patterned in a multilayer structure successfully for our experiments[1]. This is sample 'SS3' from ***tab. 5.1***. The custom design shown in ***fig. 5.19(a)*** consists of a common drain for all devices and separate source contacts for each device. Devices D3 to D7 have a 100 nm Au strip running vertically beneath them responsible for causing thickness dependent coloration in MoS_2 (***fig. 5.19(b)***) while D1 and D2 are left without metal backing. All the individual source electrodes, common drain electrode and vertical strip (for optical interference) are brought out to the edge of the substrate (***fig. 5.18(b)***) with increasing lateral dimension to be compatible with the pitch of a right-angled PCB edge connector[2].

[1]The minimum TAC based MoS_2 width patterned using UV-lithography in my experiments was 5 µm but was not very robust at vulnerable regions like near overlapping layers and hence, they did not survive the patterning process of further layers and became discontinuous especially where there was an abrupt change in the dimensions. Hence 10 µm is referred to be optimum as it survived all the processes.

[2]The vertical strip was not electrically connected to anything for these experiments. The custom-made mask is a general-purpose design that gives the provision of making FETs where this vertical strip is used as a gate and dielectric layer that covers all the 7 devices

Shown in ***fig. 5.18(a)*** is an edge connector purchased from RS components that was used in these experiments and the custom-made general-purpose mask was designed according to the specifications of this edge connector. Only the top row of pins shown in ***fig. 5.18(a)*** was used to electrically extend the common drain and devices 1 through 7 shown in ***fig. 5.18(b)*** out of the sample to a studier platform like breadboard or PCB. The pitch of the spring-loaded pins that clutch onto the sample when inserted and holds it in place is used to design the spacing (red dashed box in ***fig. 5.18(b)***) between the S-D contacts. The inner width (blue arrow in ***fig. 5.18(a)***) of the connector decides the total width of the sample's substrate, height of the connector which is the distance between the bottom pins row and top pins row (yellow arrow in ***fig. 5.18(a)***) determines the thickness of the chosen substrate (quartz in this case). Given the micron scale of the devices, conventional probes connected to SMUs and other lab equipment are tricky to use on these devices. This edge connector is used for easy electrical connection of fragile and small devices to SMUs and can be made compatible with a variety of probes like crocodile clips, needle probes, banana cables, BnC etc.

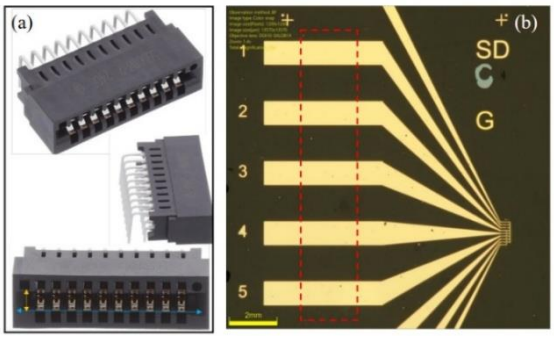

Fig. 5.18*: **(a)** Edge connectors from RS components **(b)** Zoomed-out view of sample set 3 showing extended contact reaching the edge of the substrate.*

Once the sample is lodged into this edge connector from the front, the spring-loaded metal clasps make robust electrical connection with the extended Au electrodes of the sample and these metal clasps come out from behind of the connector in the form of PCB or breadboard mountable pins. These pins represent the common drain and 7 source electrodes which were biased using a source meter via jumper wires, crocodile clips and copper tape. After mounting the sample successfully, it is ready for measurement and can now be placed under Keithley 4200A-SCS parameter analyser integrated with a 405 nm laser of 4.5 mW power. Spot size was smaller than the active area (purple square region –MoS_2 on Au), aligned at its centre and then current vs time plots were recorded for laser on and off. This setup was a

preventing shorting between the vertical gate electrode, S-D electrodes and MoS_2 active layers is not shown here and purposefully skipped in the fabrication of devices for this experiment.

part of another group's lab (Prof. John Boland) and so its components were used as they were setup already i.e., laser spot size was not varied, laser intensity was fixed for all the experiments and optical alignment was not touched.

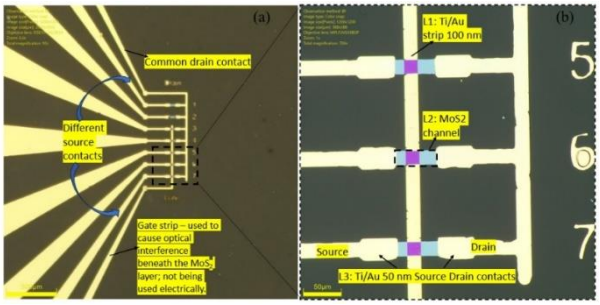

Fig. 5.19*: Zoomed-in view of sample set 3 showing* ***(a)*** *Source contacts, common drain, gate strip* ***(b)*** *MoS_2 active area (purple).*

Interestingly, instead of increase in current upon illumination, which was expected before starting the experiment, a decrease in current was observed every time laser was turned on and then it attempted to recover to its original magnitude when the laser was switched off. ***Fig. 5.20*** shows these trends and this phenomenon has been reported previously by others and referred to as 'negative photo-conductivity (NPC)'.

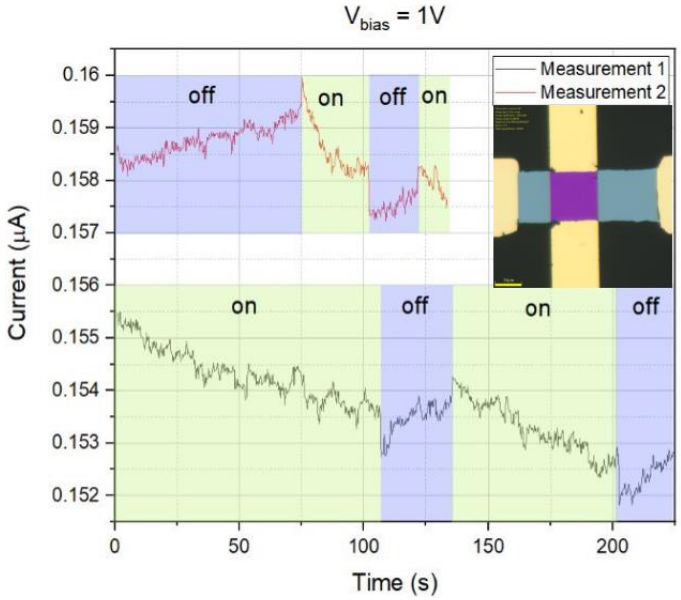

Fig. 5.20*: NPC observed in two trials for a 15 nm TAC based MoS_2 deposited on an electrically disconnected Au strip (sample 'SS3' from tab. 5.1) to facilitate optical interference.*

H. Jawa et al. attributed this to recombination of photogenerated electrons with holes of black phosphorous (BP) in a BP/MoS_2 heterostructure based FET. They also showed thickness and wavelength dependent reversible switching of PPC to NPC in their FET [40]. On the other hand, X. Xiao et al, argue that NPC generation is caused due to charge trapping

in the defect state of their CVD MoS_2 when the illuminated light energy is not enough to excite the free carriers in the split valence band to the conduction band and therefore, they get trapped in the mid-gap defect states [41]. In the TAC based MoS_2 results shown in ***fig. 5.20***, NPC is observed in a simple S-D design contacting the active area i.e., without applying any gate voltage, at room temperature and under an illumination of 405 nm i.e., ~ 3 eV. This is strange since the band gap shouldn't be beyond this range which means some other reason is causing NPC here. The most probable reason for this to happen then is PB effect [15] coming into play given the small lateral distance between source-drain contacts and a focussed laser illuminating and heating the active area especially when backed by Au strip.

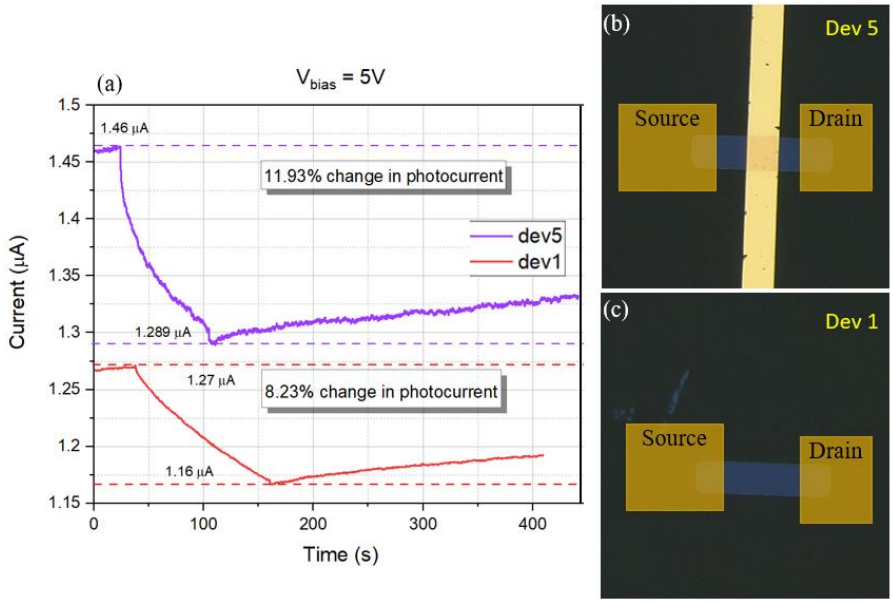

***Fig. 5.21**: **(a)** negative photoresponse for dev.5 and dev. 1. Optical image of **(b)** dev. 5 (with Au back-strip) and (c) dev.1 (without Au back-strip).*

Another interesting result was the enhancement of NPC effect with Au backing. ***Fig. 5.21(a)*** shows a comparison between two devices (dev. 5 and dev. 1) where the MoS_2 horizontal strip with and without Au backing is measured using two probes under an illumination of 405 nm laser. When laser is turned on to focus roughly on the centre of the MoS_2 horizontal strip in dev. 5 (***fig. 5.21(b)***), enhancement in NPC effect is observed as compared to the case in dev. 1 (***fig. 5.21(c)***) where MoS_2 horizontal strip has no Au backing and sits directly on the quartz substrate. MoS_2 is extremely thin here ~2 nm which should interact strongly with light especially when backed with Au due to 0^{th} order FP effect which explains this enhancement.

5.4.2 Modulated illumination

This work initially aimed to measure the frequency domain and transient PV and PC response of MoS_2 in conjunction with a lock-in amplifier (HF2LI-Zurich Instruments) and a trans-impedance amplifier (HF2TA – Zurich Instruments).

Initial hypothesis was to first obtain an amplified PV signal from an unbiased sample and then measure the amplified signal consisting of both PV and PC components when the sample is biased. PC component can then be isolated by subtracting the PV portion that would appear as a DC offset. However, there were far more impediments than expected in executing the same since illuminating from a focused laser would cause local heating that gave rise to bolometric and thermoelectric effects. Since thermoelectricity requires a temperature gradient, likelihood of TE effects being involved in the measured signal are as high as bolometric (ρ-T measurements discussed in ***ch. 3***) effects (which requires rate of change of temperature, $\frac{\Delta T}{\Delta t}$) since the focused laser spot spreads as a gaussian on MoS_2 surface and the probing contacts are at the edge of the sample. This means that due to the localised laser spot, any photo-generated electron undergoes non-uniform heating (or a temperature gradient, $\frac{\Delta T}{\Delta x}$) at the sample surface before reaching the point of contact with the probe. In summary, the interplay between heat and photon induced current due to the difference in points of generation and collection of induced current is explained in the following sections. According to TMM simulations (all TMM simulations were performed by my colleague Dr. Evan Roy), at 511 nm, ~15-20 nm thick MoS_2 seems to be the optimum for maximum absorption of the wavelength when backed with Au (***fig. 5.22(a)***) as compared to being directly deposited on SiO_2 (***fig. 5.22(b)***). This situation is best explored under a frequency modulated laser illumination because it can be focussed to illuminate a small area on the sample thus creating both temperature gradient spatially on the surface of the device as well as temperature change w.r.t time.

With all these points in mind, the measurement was carried out on various TAC based MoS_2 samples with varying thicknesses based on Ossila's IDE design (**sample set-1:** SS1A series) with a frequency modulated laser (511 nm) using our in-house system. This setup consists of a single mode CW diode laser from Toptica Photonics iBEAM SMART with an integrated software to control the laser intensity and communicate with the LIA that can frequency modulate the laser signal to a desired set frequency lying in the range DC to 50 MHz. The setup is also capable of recording time as well as frequency response of the connected device

in response to the laser on/off cycle. On top of these components, a TIA was added later on to enhance the signal to noise ratio of the measured signal from the TAC based MoS_2 device. Time resolved measurements utilising this setup showed repeated positive and negative current spikes on the LIA at the start of each on and off cycle of the laser beam. These were consistent across different samples and strongly dependent on laser, LIA and TIA settings and independent of external electronic circuitry and its associated R-C time constant. This was the main motivation to investigate TAC based MoS_2 of varying thicknesses under such a setup.

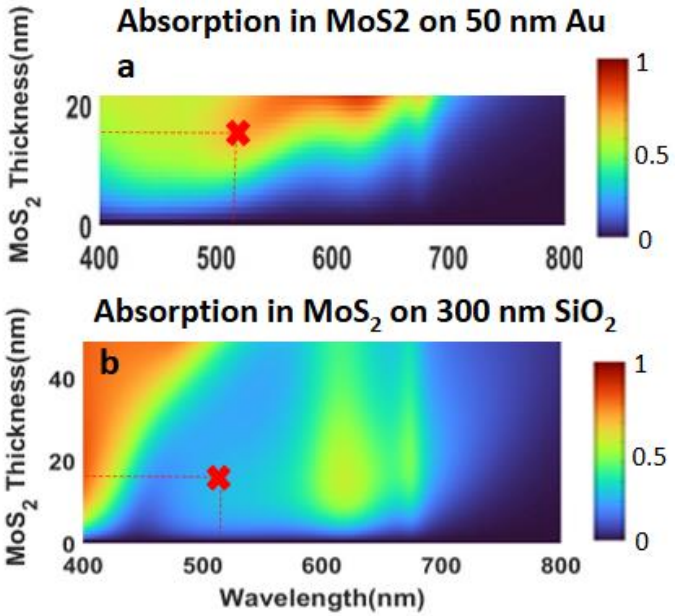

***Fig. 5.22**: TMM surface plots summarising absorption in MoS_2 of varying thicknesses across the visible electromagnetic spectrum **(a)** with Au backing compared to **(b)** being on a transparent dielectric layer of SiO_2.*

Since ***fig. 5.22*** hints at a possible interesting effect, therefore, preliminary characterizations were done before delving deeper into it. So, frequency responses of each device (D1-D5) of a ~20 nm thick MoS_2 sample were measured under 511 nm laser illumination at varying laser intensities. Since some of the devices of this sample got damaged (contacts burnt out after I-V sweep under the solar simulator and bad lift off resulting in broken IDEs), therefore frequency response of only D1 under varying laser intensities is shown in ***fig. 5.23***. Under no externally applied voltage (Auxiliary input (AuxInp) of the TIA = 0 V), ~ 15 nA flows from the device and through the load resistance (TIA resistance, R1 = 100 MΩ) which gets shifted to higher frequencies as the laser intensity is increased from 10 mW to 100 mW. A noticeable feature in this frequency response is a dip around 500 Hz which indicates two parallel processes leading to this PV effect. Measuring the time response of this device under

a laser illumination modulating at 2 kHz for varying R1 values, an interesting trend was observed. 'Demod signal (V)' is the output voltage signal from TIA after undergoing the gain (G1) amplifier stage. So, the output current from the device is calculated by dividing 'demod signal (V)' by R1 and G1 of the TIA.

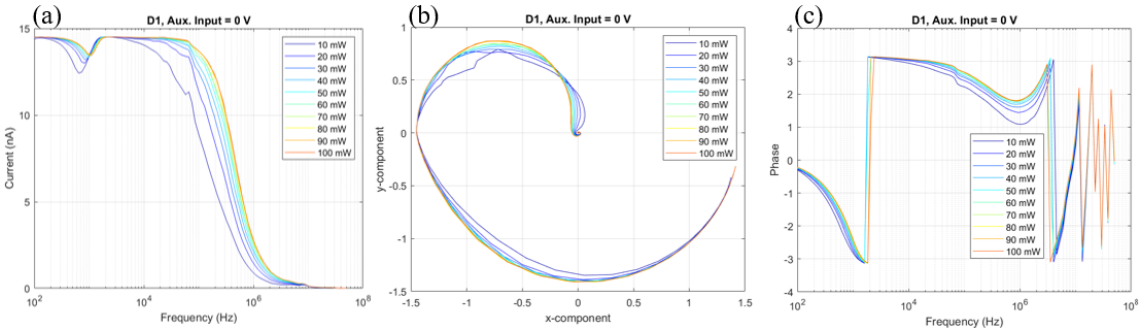

***Fig. 5.23**: **(a)** Frequency response of current **(b)** in-phase (x) vs. quadrature (y) component **(c)** frequency response of the phase of the measured signal of a 20 nm TAC based MoS_2 (SS1A20) with TIA settings: R1= 100M, G1 = 10, opamp offset=10mV, AuxInp=0V.*

For instance, taking the example of the plots shown in ***fig. 5.24(a)***, setting the gain, G1=10, the lowest R1=10k corresponds to a current from the device to be around 2 µA while the highest R1 = 100M leads to a current output from the device to be around 1 nA, both of which fall in the bounds of what is permissible according to the TIA's manual as seen in the snapshot in ***fig. 5.24(b)***. Some other plots presented in this chapter already have this back calculation done and so directly show the calculated current on the y-axis.

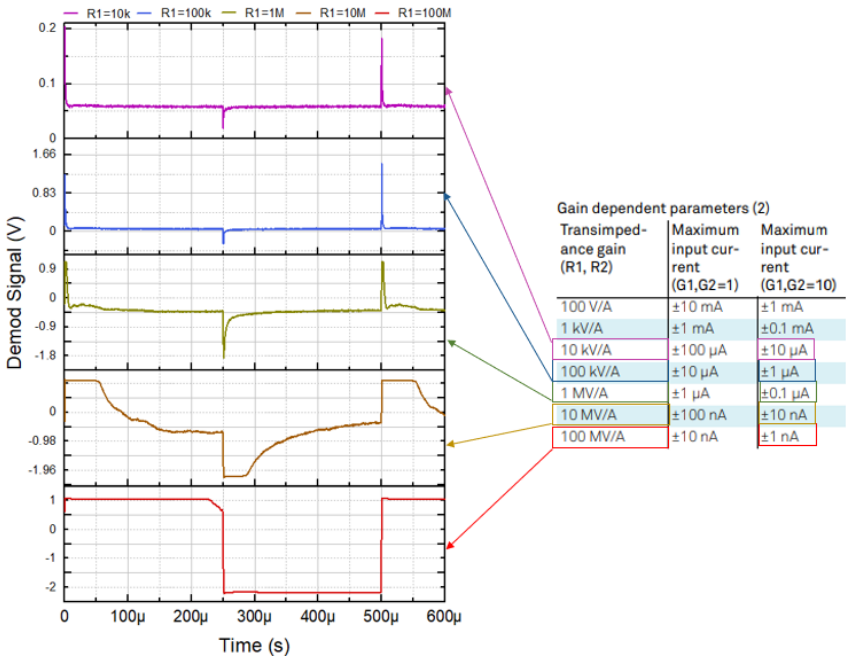

***Fig. 5.24**: **(a)** 20 nm MoS_2 (SS1A20) illuminated by 511 nm laser modulated at 2 kHz and 100 mW power under varying R1 settings and constant G1=10. **(b)** Screenshot of the TIA parameters and range of input current.*

An interesting observation while performing these experiments was that at lower R1 values, a transient peak in the output signal is noticed which is camouflaged otherwise at higher R1 values. This camouflaged transient peak lead further exploration under biased/unbiased conditions, different laser intensities and for lower thicknesses of TAC based MoS_2. ***Fig. 5.24*** presents this observation along with a snapshot of the TIA's manual that explains how the output signal from the TIA is dependent on the two parameters: R1 and G1. This peak is also influenced by laser modulation frequency. ***Fig. 5.25(a)*** and ***fig. 5.25(b)*** show the appearance of this peak for smaller modulation frequencies at 100 mW and 10 mW respectively. These waveforms were compared with [8] where the same observations were reported.

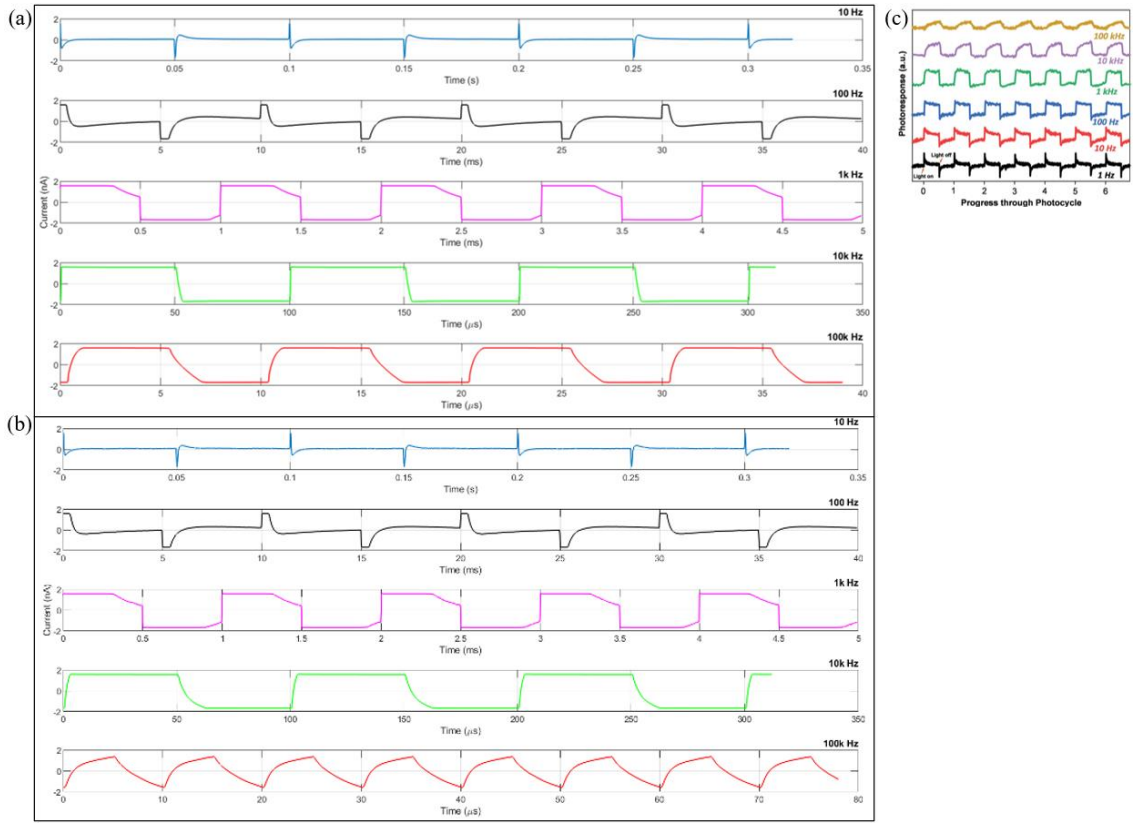

Fig. 5.25*: Time response of unbiased 20 nm MoS_2 (SS1A20) (D1) at varying laser frequencies and fixed TIA settings: R1=100 MΩ, G1=10 under* ***(a)*** *100 mW and* ***(b)*** *10 mW.* ***(c)*** *Photoresponse taken from [8] for comparison.*

Finally, in an attempt to explore what happens to the photo-induced response in the same sample (~20 nm) and device (D1) upon applying an external bias, same measurement was performed at 200 kHz, 20 mW laser intensity, R1=1M and G1=10. ***Fig. 5.26(a)*** shows the drifting of the plot vertically from its reference position (corresponding to AuxInp = 0V plot) when it is biased. Sustenance of the steady state photo-induced signal evident from flattening of the top of the curve (black) for a longer on-cycle duration at negative biases

(AuxInp = -2V) is also interesting to note. ***Fig. 5.26(b)*** shows a similar trend in slightly thinner sample ~15 nm with extremely fast photoresponse to rising and falling laser signal. The shortest transient response time is 0.19 µs under external bias and this transient response can be completely curbed thereby increasing the steady state response in the laser on-cycle by applying 10 V (topmost tile).

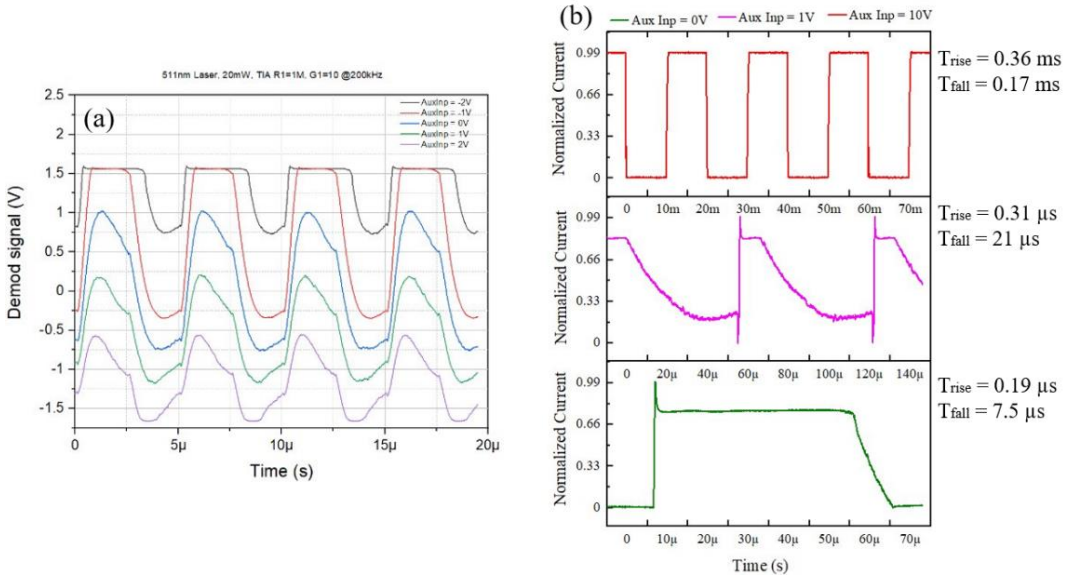

Fig. 5.26: *I-t plots (w.r.t modulating laser of 511 nm) of* ***(a)*** *D1 of ~20 nm sample (SS1A20) biased at -2V, -1V, 0V, 1V, 2V at 20 mW illumination and (b) D3 of ~15 nm biased at 0 V (bottom), 1 V (middle) and 10 V (top) with their respective rising and falling times at 30 mW illumination.*

Such a trend was also observed in thinner TAC based MoS_2 even though the absorption of light should be slightly lower according to the TMM simulations. ***Fig. 5.27*** shows the frequency responses under various biased conditions for a 6 nm TAC based MoS_2 film on 50 nm Au S-D contacts.

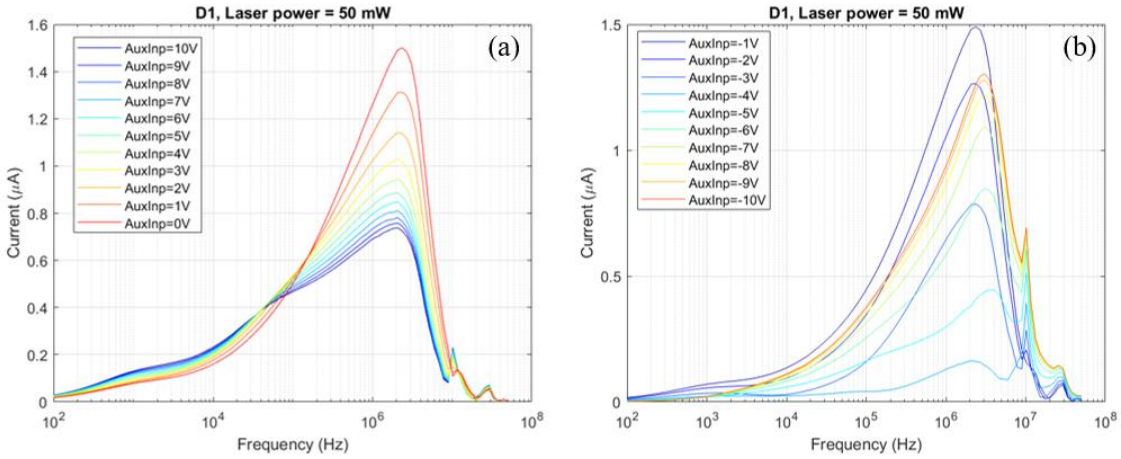

Fig. 5.27*: Frequency response of 6 nm TAC based MoS_2 on 50 nm Au S-D IDEs (SS1A6) with 50 mW laser power as a function of (a) positive externally applied voltage from 0 to 10V and (b) negative externally applied voltage from -1 to -10V.*

It is noteworthy that this response is very different from ~20 nm thick TAC based MoS_2 (same device- D1) shown in ***fig. 5.23*** where the device showed a significant signal at lower frequencies too but in the case presented in ***fig. 5.27***, the signal is very low in low frequency range whereas it peaks around 1 MHz. The current signal is higher in this case since the TIA resistance R1 chosen is 10k which is lower than the case in ***fig. 5.23*** while G1 remains the same as before.

5.4.2.1 Time response of unbiased MoS_2 with varying laser power

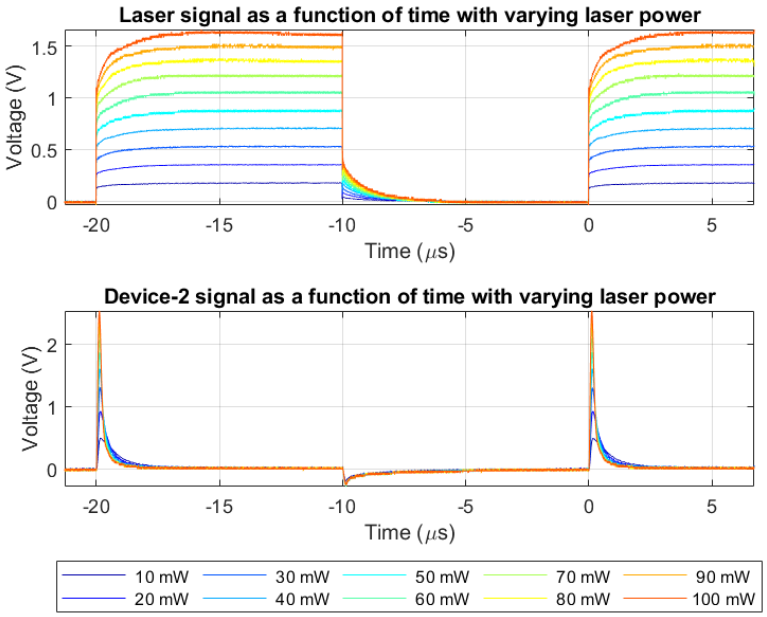

Fig. 5.28*: Photoresponse after passing through a TIA connected to an unbiased 6 nm MoS_2 (SS1A6) illuminated by a 50 kHz modulated laser of 511 nm.*

The evolution of a photo-induced signal from an unbiased 6 nm MoS_2 device connected to a TIA as a response to varying intensity of frequency modulated 511 nm laser using a LIA is shown in ***fig. 5.28*** in the bottom tile. The top tile shows the laser input signal of varying intensity and the device signal is seen to be in sync with it. Sharp transient peaks are observed in the output corresponding to each alternating on state of the laser input similar to the trend observed for thicker MoS_2 films discussed before. The amplitude of the output signal is also observed to increase along with an increase in laser intensity. Compared to thicker TAC based MoS_2 devices, the transient peak amplitude is comparable under same laser intensity but the steady state signal is much lower around similar modulating frequencies. For instance, steady state signal almost overpowers the transient peak in 20 nm

MoS_2 from 10 kHz frequency onwards as shown in ***fig. 5.25(b)*** while, here in ***fig. 5.28*** steady state signal is almost negligible when illuminated with an alternating laser even at a frequency of 50 kHz.

5.4.2.2 Time response of biased MoS_2

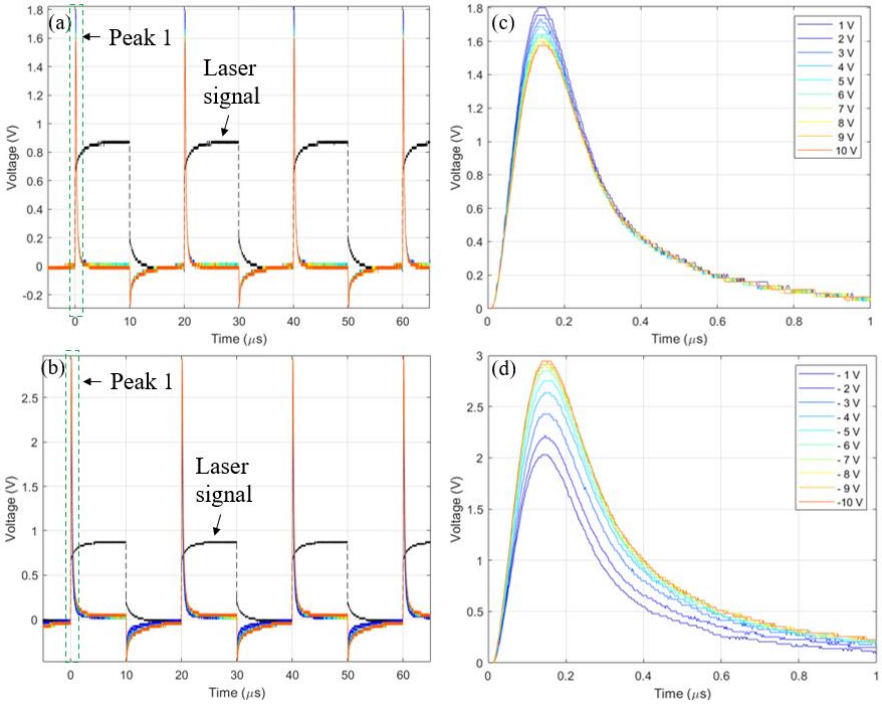

Fig. 5.29*: Positively* ***(a)*** *and negatively* ***(b)*** *biased 6 nm MoS_2 (SS1A6) in sync with the alternating laser signal depicted by black dashed plot. Zoomed-in plot of peak 1 marked by green dashed box in* ***(a, b)*** *showing a small change in its transient photo-induced peak amplitude with varying positive* ***(c)*** *and negative* ***(d)*** *electrical bias.*

At the same set laser frequency of 50 kHz, the same sample in ***fig. 5.28*** was now biased in steps first in the positive direction and then in the negative direction to investigate the evolution of its response under both light and electrical stimulus. Shown in ***fig. 5.29(a),(b)*** are output voltage signals from the TIA connected to the device as a function of laser on and off shown as dashed black plot. Only a slight change is seen in the peak for a positive applied bias ***fig. 5.29(c)*** where it decreases by 0.2 V with increasing bias but there is almost an increase of a Volt when the negative bias increases from -1 V to -10 V (***fig. 5.29(d)***). However, no change is seen in the ratio of transient peak versus the steady state signal with applied bias where the latter remains negligible throughout.

5.4.3 Discussion

5.4.3.1 Origin of spontaneous polarization in MoS_2

The observations presented in the above sections though performed under different conditions of TIA gain, bias and laser intensity yet had one thing in common – a transient peak at the rising and falling edge of each on and off cycle respectively followed by a slowly decaying trailing photo-sensitive signal. According to initial assumption, this transient peak was unexpected and only a steady state photo-induced signal was expected indicating direct evidence of photoconductivity. However, occurrence of the transient part of the output signal upon laser illumination indicates that other phenomena are at work beyond simple photoconductivity. A similar MSM device structure (Pd-MoS_2-Pd) used to study photoresponse in CVD based monolayer MoS_2 concluded the involvement of thermal to electrical conversion besides optical to electrical conversion but no further explanation was given about it [42].

Considering that highly focussed laser spot can induce local heating in the MSM device (**sample set-1**) and given the sensitivity of TAC MoS_2 to temperature changes (both rate and gradient), a significant thermal to electrical conversion process seems quite inevitable. To confirm that the observed spikes are related to only the TAC based MoS_2 and not to the substrate (Si/SiO_2 300 nm), 50 nm Au S-D IDEs or a combination of the two, two samples (plain substrate - Si/SiO_2 and Si/SiO_2 with Au IDEs) without TAC MoS_2 were measured under the same settings (LIA and TIA) and conditions (laser intensity and modulation) using the Ossila push fit test board and no signal was observed out of them. Then to confirm that the spikes in the TAC MoS_2 samples were indeed due to a thermal effect and not a secondary unexplained optical effect, the samples were illuminated from the back (substrate facing the laser) so that they are heated but not illuminated and the spikes occurred again. This confirmed that the spikey transient signal is due to a process occurring in TAC based MoS_2 region of the device and is associated with heating caused by laser illumination.

This hints at a possible pyroelectric effect being present given that heat can activate polarization in its crystal structure or its vicinity and the time resolved measurements discussed previously reveal a possible pyro-photo-thermoelectric combined mechanism. Based on this assumption and hypothesis, light-induced pyroelectricity has been investigated further in TAC based MoS_2 films.

S. Liu et al., explained the pyro-photo-thermoelectric effects working in tandem to produce the 4-stage photoresponse in wurtzite structured CdS with asymmetric Ag contacts and the effect of laser wavelength, power and bias on their sample [55]. Similar studies by D. Bhattacharya et al., used MoS_2 nanosheets to create flexible, wearable and self-poled piezoelectric nanogenerators [56] while A. Abnavi et al., reported laser driven pyro-phototronic spikes at the water-MoS_2 interface caused by heating due to laser illumination [10]. Here again, they show the 4-stage time response at both unbiased and biased conditions as a function of light intensity, polarization and pulse frequencies measured in air. I-t response of unbiased ZnO/ZnTe core/shell nanorods was measured in [57] under light illumination (2.13 mW/cm^2) at frequency of 20 Hz showing transient peaks upon turning light illumination on, which overpower the steady state PV signal present otherwise. Application of a voltage bias reduces these transient (pyroelectric) peaks and increases the steady-state PC signal.

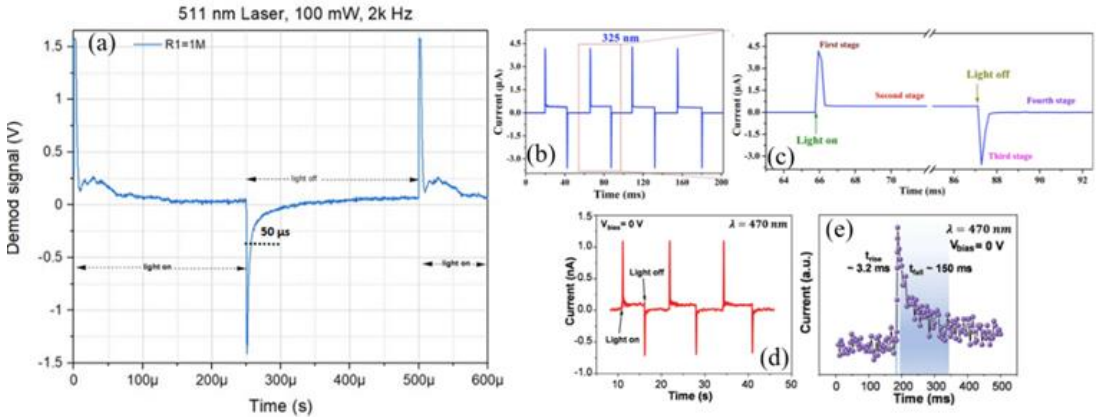

***Fig. 5.30**: **(a)** Unbiased TAC MoS_2 ~15 nm ('SS1A15' from tab. 5.1) measured under 511 nm laser of 100 mW and frequency modulated at 2 kHz. **(b)** Unbiased ZnO/ZnTe core/shell nanorods under 325 nm [57]. **(c)** Zoomed-n view of a peak in **(b)**. **(d)**, **(e)** Unbiased MoS_2 flake showing pyroelectricity peaks due to water adsorption [10].*

Clear evidence of this is also seen when measuring the time response of ~15 nm TAC MoS_2 films (sample 'SS1A15') under illumination of 511 nm laser where the amplitude of transient spikes is tuneable and the ratio of amplitude of transient peak to steady state peak can be controlled by changing the externally applied bias like in [10], [57]. A possible explanation of this occurrence in this case is that since these measurements were performed at room temperature and pressure, therefore MoS_2 is highly prone to adsorbing moisture from the air and upon illumination from a focused laser, it heats up the water-MoS_2 interface, thereby causing the transient spikes. ***Fig. 5.30(a)*** shows a plot of the time response

measurement of TAC based MoS_2 illuminated by frequency modulated laser (511) at 2 kHz. It clearly depicts this phenomenon and compares well with literature (***fig. 5.30(b-e)***).

Since 2D MoS_2 films have a high surface area and inherent defects, S-vacancies/dangling bonds not just adsorb oxygen but also adsorb water on their surface and edge sites. TAC MoS_2 has more vertical edge sites than horizontally oriented sheets (higher A_{1g} peak than E^1_{2g} peak from Raman measurements) which is especially favourable for efficient adsorption. In fact, monolayer MoS_2 is famous for its applications in catalysis [43], [44], [45], [46]. Also, water adsorption is enhanced with higher humidity [47] which is inevitable in Ireland throughout the year so there are enough reasons for water to be adsorbed on the MoS_2 surface.

Another reason for the observation of the transient peaks might also be due to the non-centrosymmetricity in an odd number layered thick MoS_2 causing an in-built electric field. Odd layer MoS_2 films show a high piezoelectric coefficient [48], [49] owing to their non-centrosymmetric structure. Raman spectroscopy and XRD results of TAC based multilayer MoS_2 hint at a possible 3R-phase which was discussed in ***2-2.3.1.3*** and ***2-2.6***. 3R - MoS_2 exhibits an out-of-plane spontaneous polarization [50] backed by modern Berry phase theory of polarization [51].

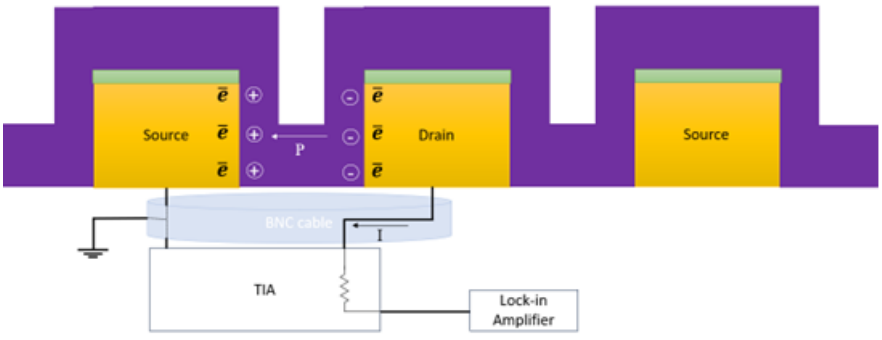

Fig. 5.31*: Schematic (not to scale) of polarization vector in MoS_2 sandwiched between Au electrodes and the electrical connection between the device and TIA and LIA.*

This net spontaneous polarization would decrease (increase) when there is a positive (negative) change in temperature. As shown in ***fig. 5.31*** change in polarization leads to change in polarization charges at the interface of MoS_2 and metal electrodes, further resulting in the flow of induced mirror charges (electrons) from one contact electrode to the other [52], [53] that is seen as the transient pyroelectric current (I_{Py}). Upon illumination, I_{Py}

is further accompanied by steady state photoconducting current (I_{PC}) resulting in total $I = I_{Py} + I_{PC}$.

N. Ma et al., report a very high PV effect in BTO with lateral interdigitated ITO contacts under 365 nm while in the vertical stack design where BTO was sandwiched between ITO (top electrode) and Ag (bottom electrode), no PV effect was observed under the same illumination [52]. PV effect could also arise here from the regions with Ti/Au backing due to the depolarization (DEP) field [54], [55]. DEP field induced PV effects are more prominent in up to a few-layer 3R- MoS_2 films but not in micrometre range thickness like in-plane devices [50], [56]. So, DEP field induced effects have a higher chance of occurring in the regions of MoS_2 on top of Au (***fig. 5.32***) since the MoS_2 thickness is restricted to less than 20 nm but in the region between a pair of Au electrodes (***fig. 5.31***), the distance is in the range of microns (inter-electrode spacing) and so this effect is less significant here.

Fig. 5.32*: Schematic (not to scale) showing MoS_2 on top of Au electrode surface - a region with possible formation of depolarization field.*

Finally, another possible source of such transient peaks can be due to photo-induced sliding ferroelectricity. Tuning of photo-induced sliding ferroelectricity is also studied in 3R-MoS_2 and is known to be of two types- 1) structural origin - light distorts the structure and leads to phase transition in phase change material (PCM). 2) charge origin- distribution of light induced carriers in the energy band as well as across MoS_2 layers [57], [58]. I-V sweeps of the samples presented previously showed a slight hysteresis many times in both dark and light conditions. This is a clear giveaway of sliding ferroelectricity occurring in TAC based 3R-MoS_2.

Fig. 5.33 shows 3 weeks apart status of sample 'SS1A15' from ***tab. 5.1***. ***Fig. 5.33(a)*** shows the microscopic image when it was a clean, new sample right out of the furnace with the electrodes showing a purple coloration due to interference between MoS_2 and Au while ***fig. 5.33(b)*** shows burnt-out electrodes (yellow instead of purple especially in D2, D4 and D5) after performing repeated I-V sweeps under large biases. These measurements damaged the

top MoS_2 on Au electrodes exposing them from beneath and resulted in an asymmetrical contacting where one electrode out of the pair contacted the MoS_2 from its edge as well as bottom (hybrid contact) while the burnt-out electrode is just an edge (or side) contact as depicted in ***fig. 5.33(c)***.

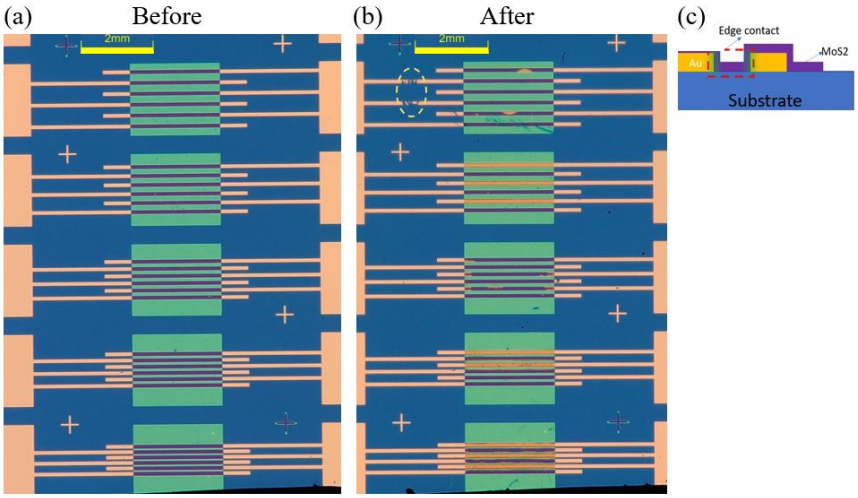

Fig. 5.33*: Optical image of ~15 nm MoS_2 on 50 nm Au S-D IDEs (SS1A15)* ***(a)*** *just after sample preparation and before any measurements and* ***(b)*** *after initial I-V sweeps under dark and light conditions.* ***(c)*** *pictorial depiction of damaged MoS_2 on electrodes seen from the cross-sectional view.*

D3 seems to be the most intact device in this sample but despite of the damage to electrodes on top surface of rest of the devices, they still form at least side contacts to the sandwich MoS_2 in between them. Only the ability of the Au electrodes in causing optical interference has reduced slightly but as conductors of electrical carriers they work fine. In short, this sample cannot be used to study any I-V sweep trends among its devices nor can it be used to compare a device of this sample to undamaged devices of other samples but it is an excellent demonstration of 1) reduced absorption capability due to damage of MoS_2 on top of the electrodes thereby changing their coloration, 2) reduction of light current compared to other devices of the same MoS_2 thickness and undamaged electrodes, 3) hysteresis in I-V sweeps under both dark and light conditions shown in ***fig. 5.34***. It is interesting to note that the most undamaged device (D3) with symmetrical electrode design does not show any hysteresis while all other devices where alternate electrodes behave as just edge contacts after having their top MoS_2 burn out, show significant hysteresis in their I-V sweeps. This hints at non-uniform polarization at different interfaces/regions of the device due to asymmetrical contacting with MoS_2.

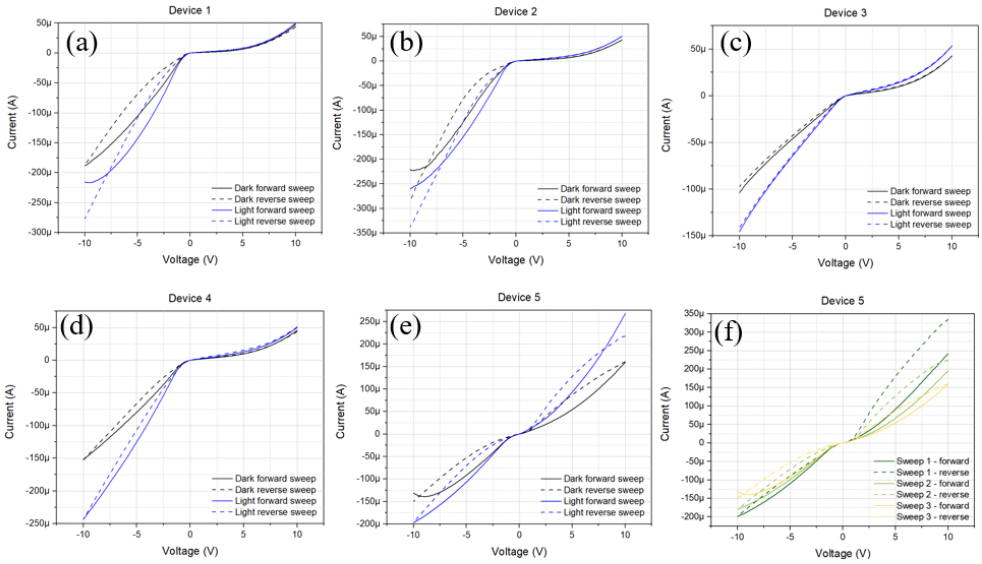

***Fig. 5.34**: **(a)-(e)** I-V sweeps under dark and light conditions of 15 nm MoS_2 film deposited on 50 nm Au S-D electrodes ('SS1A15') based devices (D1-D5) with varying inter-electrode spacing (as per Ossila design **sample set-1**) and **(f)** 3 repeated dark I-V sweeps of D5 right after measurement under light.*

Two electrodes on the left side of D1 in ***fig. 5.33(b)*** were purposely scratched out to electrically disconnect them from MoS_2 and act as non-biased metal backing just to cause optical interference with MoS_2. Photocurrent was measured in the optical interference part (MoS_2 on Au: purple) and compared to that of MoS_2 directly on the substrate (MoS_2 on SiO_2/Si: teal blue). ***Fig. 5.35*** shows I-t plots of D3 (***fig. 5.35(a)***) and D1 (***fig. 5.35(c)***) under 511 nm laser and a 405 nm laser turned on and off manually. D3 is entirely illuminated by a large laser spot covering the entire device while D1 is illuminated with a very focussed laser spot first placed on MoS_2 over Au (the disconnected electrode) region (***fig. 5.35(d)***) and then on MoS_2 region between a pair of Au electrodes and directly over SiO_2/Si (***fig. 5.35(e)***). The difference in photocurrent magnitude between ***fig. 5.35(a), (c)*** is most probably due to asymmetrical contacts in D1 (***fig. 5.35(d)***) leading to a larger intrinsic polarization and sliding ferroelectricity in MoS_2 which causes a higher photocurrent. But since D3 has stable symmetrical contacts, its photo-response is not as strong. Delving deeper into the comparison between photocurrent from the two regions in ***fig. 5.35(d), (e),*** the one corresponding to TAC MoS_2 on Au (referred to as J1) is lower than that corresponding to TAC MoS_2 directly on Si/SiO_2 substrate (referred to as J2). This experimental outcome seems counter-intuitive in the first glance if based on the assumption that MoS_2 backed with Au metal should cause zeroth order FP interference and should enhance absorption that would lead to an increased photocurrent. However, upon close inspection and analysis, this experimental outcome sits aligned with the previously discussed theory.

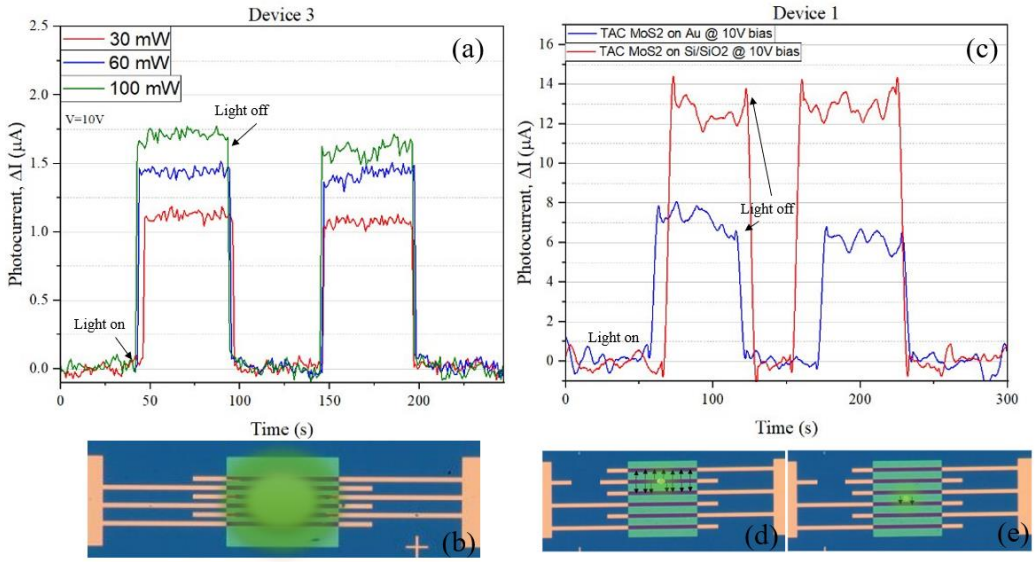

***Fig. 5.35**: **(a)** Photocurrent vs time plot of ~15 nm TAC based MoS_2 ('SS1A15') at 10 V under varying laser (511 nm) intensity and laser on/off. **(b)** Image depicting the way laser spot covers the device in experiment **(c)** Photocurrent vs time plot of 'SS1A15' at 10 V under manually modulated (on/off) 405 nm laser focussed at different regions on the device. TAC MoS_2 on **(d)** Au region corresponding to blue plot in **(c)** and **(e)** on Si/SiO_2 substrate region corresponding to red plot in **(c)**. Dark current is subtracted in all cases as baseline for a cleaner look and easier comparison.*

Firstly, according to TMM simulations shown in ***fig. 5.22***, 15 nm MoS_2 directly on Si/SiO_2 absorbs more strongly at 405 nm than on Au meaning that Salisbury effect overpowers zeroth order FP effect at 405 nm. Secondly, when light illuminated the region of MoS_2 on disconnected Au electrode, the photogenerated carriers have to travel a father distance (interelectrode spacing + half of electrode thickness) towards the next connected electrode while they have to cover a shorter distance (half of inter-electrode spacing) when light illuminates MoS_2 in between two adjacent pairs.

5.5 Conclusion

FET design is usually difficult to achieve for MoS_2 devices therefore, a simple source-drain design with MoS_2 as the active material was explored in this work. Transfer-free, photolithography compatible few-layer TAC based MoS_2 was used to achieve a greater photoresponsivity seen in MoS_2 monolayers previously [1]. MSM design was used by using IDE as bottom-edge hybrid contacts with dual purpose - firstly, to behave as electrical contacts to MoS_2 and secondly to create 0^{th} order FP regions to enhance optical absorption in MoS_2. To tune the photoresponsivity further, external electric bias was applied and MoS_2 active area was varied from mm^2 to μm^2 range. While the former behaved as expected, the

latter showed negative photoconductivity under a low power continuous wave laser of 405 nm wavelength which has its place for instance, in bio-inspired visuomorphic computing application [59]. For the large area (Ossila's IDE based design) samples, both continuous and frequency modulated illumination gave interesting results. Firstly, the I-V sweeps scaled with the interelectrode spacing as expected and interestingly, the sensitivity or photo-to-dark current ratio switched from being less than 1 to more than 1 after the thickness of MoS_2 reached 15 nm and above. Also, under the CW illumination, TAC based MoS_2 devices followed a typical 4 stage I-t response proving the persistent photoconductivity phenomenon seen in MoS_2 synthesised using other techniques previously. Generally, the devices with 50 nm Au IDE S-D contacts showed better I-t results. Based on TMM simulations which took into account the absorption enhancement by virtue of metal backing and MoS_2 thickness, a 6 nm device (D5) with symmetrical contacts (in design and contact material) had a photoresponsivity, R=0.015 A/W at 600 nm and at no gate bias. Though slightly lower than what has been reported by Tsai et. al., using a similar design (R = 0.57 A/W) [2], photoresponsivity in this work was calculated to be: R=0.4063 A/W for a 12 nm device (D5) with asymmetrical contacts. The results presented in this work are in the same order of magnitude while using 20 times less optical power and obtained under white light illuminated by Ossila Solar Simulator (AM 1.5G). This proves the broadband operation of these devices and future application under natural sunlight. These devices were fabricated to be back-compatible with Ossila solar testing kit which made them very easy to use.

Upon using a frequency modulated laser light source integrated with a LIA and a TIA, a significant photoinduced response was obtained at zero driving voltage for both thin and thick TAC based MoS_2 films. These signals showed a high transient peak in comparison to a steady state PC/PV signal that would be normally expected. However, the amplitude of these signals was found to be tuneable with laser modulation frequency, TIA gain settings, temperature change w.r.t time as well as gradient and externally applied bias. Fixing the laser modulation frequency, TIA settings and applied bias, time evolution of the photoresponse was studied to rule out any other possible effects and it can thus be concluded that TAC based MoS_2 shows very strong pyroelectric peaks at low (10 Hz) and high frequencies (up to 50 kHz) depending upon its thickness. Previously, these pyroelectric peaks have been utilised in several biomedical applications [26], [60], [61] and as pyro detectors.

Future studies can be carried out in vacuum and under controlled temperature conditions with an aim to enhance this design for space applications where this device will be subjected to vacuum, cold temperature and natural sunlight. Perhaps, operation in outer space will be the most appropriate since the environment will be least degrading to MoS_2 based devices.

In conclusion, the high absorption property of MoS_2 at excitonic resonances was enhanced by using 0^{th} order FP effect and Salisbury effect by incorporating both MoS_2 on Si/SiO_2 as well as on Au design in conjunction. This chapter showed that TAC process can successfully produce few-layer MoS_2 thin film-based devices on a 1.5 cm^2 substrate with the photoactive area spanning up to mm^2 range, without causing any damage to the underlying patterned layers while still being able to perform photoconductivity studies. These few layer MoS_2 devices can be used at room temperature, pressure and natural illumination without any post-deposition treatment or additional gate voltage.

References

[1] Z. Yin *et al.*, "Single-Layer MoS_2 Phototransistors," *ACS Nano*, vol. 6, no. 1, pp. 74–80, Jan. 2012, doi: 10.1021/nn2024557.

[2] D.-S. Tsai *et al.*, "Few-Layer MoS_2 with High Broadband Photogain and Fast Optical Switching for Use in Harsh Environments," *ACS Nano*, vol. 7, no. 5, pp. 3905–3911, May 2013, doi: 10.1021/nn305301b.

[3] M.-L. Tsai *et al.*, "Monolayer MoS_2 Heterojunction Solar Cells," *ACS Nano*, vol. 8, no. 8, pp. 8317–8322, Aug. 2014, doi: 10.1021/nn502776h.

[4] M. He *et al.*, "A flexible photo-thermoelectric nanogenerator based on MoS_2/PU photothermal layer for infrared light harvesting," *Nano Energy*, vol. 49, pp. 588–595, Jul. 2018, doi: 10.1016/j.nanoen.2018.04.072.

[5] A. Di Bartolomeo *et al.*, "Temperature-dependent photoconductivity in two-dimensional MoS_2 transistors," *Mater. Today Nano*, vol. 24, p. 100382, Dec. 2023, doi: 10.1016/j.mtnano.2023.100382.

[6] Y. Dong *et al.*, "Giant bulk piezophotovoltaic effect in 3R-MoS_2," *Nat. Nanotechnol.*, vol. 18, pp. 1–6, Nov. 2022, doi: 10.1038/s41565-022-01252-8.

[7] G. Cunningham *et al.*, "Photoconductivity of solution-processed MoS_2 films," *J. Mater. Chem. C*, vol. 1, no. 41, pp. 6899–6904, Oct. 2013, doi: 10.1039/C3TC31402B.

[8] A. Abnavi *et al.*, "Polarization-Sensitive and Self-Driven Pyro-Phototronic Photodetectors Based on MoS_2-Water Heterojunctions," *Adv. Opt. Mater.*, vol. 12, no. 11, p. 2302651, 2024, doi: 10.1002/adom.202302651.

[9] Y. Zhang *et al.*, "Photothermoelectric and photovoltaic effects both present in MoS_2," *Sci. Rep.*, vol. 5, no. 1, p. 7938, Jan. 2015, doi: 10.1038/srep07938.

[10] M. He *et al.*, "A flexible photo-thermoelectric nanogenerator based on MoS_2/PU photothermal layer for infrared light harvesting," *Nano Energy*, vol. 49, pp. 588–595, Jul. 2018, doi: 10.1016/j.nanoen.2018.04.072.

[11] P.-Y. Huang, H.-J. Chen, J.-K. Qin, L. Zhen, and C.-Y. Xu, "A polarization-sensitive photothermoelectric photodetector based on mixed-dimensional SWCNT–MoS_2 heterostructures," *Nanoscale Adv.*, vol. 4, no. 24, pp. 5290–5296, Dec. 2022, doi: 10.1039/D2NA00609J.

[12] M. Buscema, M. Barkelid, V. Zwiller, H. S. J. Van Der Zant, G. A. Steele, and A. Castellanos-Gomez, "Large and Tunable Photothermoelectric Effect in Single-Layer MoS_2," *Nano Lett.*, vol. 13, no. 2, pp. 358–363, Feb. 2013, doi: 10.1021/nl303321g.

[13] J. Gosciniak, "Integrated Bolometric Photodetectors Based on Transparent Conductive Oxides from Near- to Mid-Infrared Wavelengths," *Adv. Photonics Res.*, vol. 5, no. 2, p. 2300261, Feb. 2024, doi: 10.1002/adpr.202300261.

[14] C. Yang, G. Wang, M. Liu, F. Yao, and H. Li, "Mechanism, Material, Design, and Implementation Principle of Two-Dimensional Material Photodetectors," *Nanomaterials*, vol. 11, no. 10, p. 2688, Oct. 2021, doi: 10.3390/nano11102688.

[15] J.-Y. Wu *et al.*, "Broadband MoS_2 Field-Effect Phototransistors: Ultrasensitive Visible-Light Photoresponse and Negative Infrared Photoresponse," *Adv. Mater.*, vol. 30, no. 7, p. 1705880, 2018, doi: 10.1002/adma.201705880.

[16] Q. Wang *et al.*, "Preparation and Bolometric Responses of MoS_2 Nanoflowers and Multi-Walled Carbon Nanotube Composite Network," *Nanomaterials*, vol. 12, no. 3, p. 495, Jan. 2022, doi: 10.3390/nano12030495.

[17] X. Yang *et al.*, "An Ultrathin Flexible 2D Membrane Based on Single-Walled Nanotube–MoS_2 Hybrid Film for High-Performance Solar Steam Generation," *Adv. Funct. Mater.*, vol. 28, no. 3, p. 1704505, 2018, doi: 10.1002/adfm.201704505.

[18] E. R. Caley and J. F. C. Richards, *Theophrastus On Stones*. Columbus, Ohio: The Ohio state University, Columbus, 1956.
[19] M. D. Aggarwal and George C Marshall Space Flight Center, *Pyroelectric materials for uncooled infrared detectors processing, properties, and applications*. in NASA/TM, no. 2010. Huntsville], Ala: National Aeronautics and Space Administration, Marshall Space Flight Center, 2010.
[20] K. Zhang, S. Wang, and Y. Yang, "A One-Structure-Based Piezo-Tribo-Pyro-Photoelectric Effects Coupled Nanogenerator for Simultaneously Scavenging Mechanical, Thermal, and Solar Energies," *Adv. Energy Mater.*, vol. 7, no. 6, p. 1601852, Mar. 2017, doi: 10.1002/aenm.201601852.
[21] J. Tian, "An overview of pyroelectric photodetector: Photoresponse mechanisms and applications," *AIP Adv.*, vol. 13, no. 5, p. 050701, May 2023, doi: 10.1063/5.0146279.
[22] X. Wang *et al.*, "Multimechanism Synergistic Photodetectors with Ultrabroad Spectrum Response from 375 nm to 10 μm," *Adv. Sci.*, vol. 6, no. 15, p. 1901050, Aug. 2019, doi: 10.1002/advs.201901050.
[23] Y. Yang *et al.*, "Pyroelectric Nanogenerators for Harvesting Thermoelectric Energy," *Nano Lett.*, vol. 12, no. 6, pp. 2833–2838, Jun. 2012, doi: 10.1021/nl3003039.
[24] H. Ryu and S. Kim, "Emerging Pyroelectric Nanogenerators to Convert Thermal Energy into Electrical Energy," *Small*, vol. 17, no. 9, p. 1903469, Mar. 2021, doi: 10.1002/smll.201903469.
[25] M. Kumar, D.-K. Ban, and J. Kim, "Photo-induced pyroelectric spikes for neuromorphic sensors," *Mater. Lett.*, vol. 225, pp. 46–49, Aug. 2018, doi: 10.1016/j.matlet.2018.04.106.
[26] Y. Hu *et al.*, "Ultralow Power Optical Synapses Based on MoS_2 Layers by Indium-Induced Surface Charge Doping for Biomimetic Eyes," *Adv. Mater.*, vol. 33, no. 52, p. 2104960, 2021, doi: 10.1002/adma.202104960.
[27] M. A. Kats and F. Capasso, "Optical absorbers based on strong interference in ultra-thin films," *Laser Photonics Rev.*, vol. 10, no. 5, pp. 735–749, Sep. 2016, doi: 10.1002/lpor.201600098.
[28] U. Arad, E. Redmard, M. Shamay, A. Averboukh, S. Levit, and U. Efron, "Development of a large high-performance 2-D array of GaAs-AlGaAs multiple quantum-well modulators," *IEEE Photonics Technol. Lett.*, vol. 15, no. 11, pp. 1531–1533, Nov. 2003, doi: 10.1109/LPT.2003.818663.
[29] M. A. Kats and F. Capasso, "Optical absorbers based on strong interference in ultra-thin films," *Laser Photonics Rev.*, vol. 10, no. 5, pp. 735–749, Sep. 2016, doi: 10.1002/lpor.201600098.
[30] L. D. C. Folgueras and M. C. Rezende, "Multilayer radar absorbing material processing by using polymeric nonwoven and conducting polymer," *Mater. Res.*, vol. 11, no. 3, pp. 245–249, Sep. 2008, doi: 10.1590/S1516-14392008000300003.
[31] M. O'Brien *et al.*, "Transition Metal Dichalcogenide Growth via Close Proximity Precursor Supply," *Sci. Rep.*, vol. 4, no. 1, p. 7374, Dec. 2014, doi: 10.1038/srep07374.
[32] Y.-H. Lee *et al.*, "Synthesis of Large-Area MoS_2 Atomic Layers with Chemical Vapor Deposition," *Adv. Mater.*, vol. 24, no. 17, pp. 2320–2325, 2012, doi: 10.1002/adma.201104798.
[33] W. C. Cho, K. L. Wu, P. S. Yip, X. Wang, Y. Chai, and K. M. Lau, "Selectable Synthesis of 2-D MoS_2 and Its Electronic Devices: From Isolated Triangular Islands to Large-Area Continuous Thin Film," *IEEE Trans. Nanotechnol.*, vol. 15, no. 2, pp. 310–317, Mar. 2016, doi: 10.1109/TNANO.2016.2524044.

[34] M. Yuan *et al.*, “In-plane ferroelectrics enabling reduced hysteresis in monolayer MoS_2 transistors,” *Carbon Neutralization*, vol. 3, no. 4, pp. 700–709, 2024, doi: 10.1002/cnl2.148.
[35] V. K. Sangwan *et al.*, “Multi-terminal memtransistors from polycrystalline monolayer molybdenum disulfide,” *Nature*, vol. 554, no. 7693, pp. 500–504, Feb. 2018, doi: 10.1038/nature25747.
[36] I. Langmuir and V. J. Schaefer, “Activities of Urease and Pepsin Monolayers,” *J. Am. Chem. Soc.*, vol. 60, no. 6, pp. 1351–1360, Jun. 1938, doi: 10.1021/ja01273a023.
[37] T. Carey *et al.*, “High-Mobility Flexible Transistors with Low-Temperature Solution-Processed Tungsten Dichalcogenides,” *ACS Nano*, vol. 17, no. 3, pp. 2912–2922, Feb. 2023, doi: 10.1021/acsnano.2c11319.
[38] J. Neilson, M. P. Avery, and B. Derby, “Tiled Monolayer Films of 2D Molybdenum Disulfide Nanoflakes Assembled at Liquid/Liquid Interfaces,” *ACS Appl. Mater. Interfaces*, vol. 12, no. 22, pp. 25125–25134, Jun. 2020, doi: 10.1021/acsami.0c03794.
[39] N. M. Abdelazim *et al.*, “Lateral Growth of MoS_2 2D Material Semiconductors Over an Insulator Via Electrodeposition,” *Adv. Electron. Mater.*, vol. 7, no. 9, p. 2100419, Sep. 2021, doi: 10.1002/aelm.202100419.
[40] H. Jawa *et al.*, “Wavelength-Controlled Photocurrent Polarity Switching in BP-MoS_2 Heterostructure,” *Adv. Funct. Mater.*, vol. 32, no. 25, p. 2112696, 2022, doi: 10.1002/adfm.202112696.
[41] X. Xiao, J. Li, J. Wu, D. Lu, and C. Tang, “Negative photoconductivity observed in polycrystalline monolayer molybdenum disulfide prepared by chemical vapor deposition,” *Appl. Phys. A*, vol. 125, no. 11, p. 765, Nov. 2019, doi: 10.1007/s00339-019-3054-2.
[42] M. Moun, A. Singh, B. R. Tak, and R. Singh, “Study of the photoresponse behavior of a high barrier Pd/MoS_2 /Pd photodetector,” *J. Phys. Appl. Phys.*, vol. 52, no. 32, p. 325102, Aug. 2019, doi: 10.1088/1361-6463/ab1f59.
[43] Prof. Dr. I. Chorkendorff and Prof. Dr. J. W. Niemantsverdriet, *Concepts of Modern Catalysis and Kinetics*. John Wiley & Sons, Ltd, 2003. doi: 10.1002/3527602658.app1.
[44] B. Hinnemann *et al.*, “Biomimetic Hydrogen Evolution: MoS_2 Nanoparticles as Catalyst for Hydrogen Evolution,” *J. Am. Chem. Soc.*, vol. 127, no. 15, pp. 5308–5309, Apr. 2005, doi: 10.1021/ja0504690.
[45] T. F. Jaramillo, K. P. Jørgensen, J. Bonde, J. H. Nielsen, S. Horch, and I. Chorkendorff, “Identification of active edge sites for electrochemical H2 evolution from MoS_2 nanocatalysts,” *Science*, vol. 317, no. 5834, pp. 100–102, Jul. 2007, doi: 10.1126/science.1141483.
[46] Z. Gholamvand *et al.*, “Comparison of liquid exfoliated transition metal dichalcogenides reveals $MoSe_2$ to be the most effective hydrogen evolution catalyst,” *Nanoscale*, vol. 8, no. 10, pp. 5737–5749, Mar. 2016, doi: 10.1039/C5NR08553E.
[47] N. S. Bobbitt, J. F. Curry, T. F. Babuska, and M. Chandross, “Water adsorption on MoS_2 under realistic atmosphere conditions and impacts on tribology,” *RSC Adv.*, vol. 14, no. 7, pp. 4717–4729, Jan. 2024, doi: 10.1039/D3RA07984H.
[48] D. Zhang, Z. Yang, P. Li, M. Pang, and Q. Xue, “Flexible self-powered high-performance ammonia sensor based on Au-decorated $MoSe_2$ nanoflowers driven by single layer MoS_2-flake piezoelectric nanogenerator,” *Nano Energy*, vol. 65, p. 103974, Nov. 2019, doi: 10.1016/j.nanoen.2019.103974.

[49] W. Wu *et al.*, “Piezoelectricity of single-atomic-layer MoS_2 for energy conversion and piezotronics,” *Nature*, vol. 514, no. 7523, pp. 470–474, Oct. 2014, doi: 10.1038/nature13792.
[50] D. Yang *et al.*, “Spontaneous-polarization-induced photovoltaic effect in rhombohedrally stacked MoS_2_SI,” *Nat. Photonics*, vol. 16, no. 6, pp. 469–474, Jun. 2022, doi: 10.1038/s41566-022-01008-9.
[51] R. Resta and D. Vanderbilt, “Theory of Polarization: A Modern Approach,” in *Physics of Ferroelectrics: A Modern Perspective*, Berlin, Heidelberg: Springer, 2007, pp. 31–68. doi: 10.1007/978-3-540-34591-6_2.
[52] N. Ma, K. Zhang, and Y. Yang, “Photovoltaic–Pyroelectric Coupled Effect Induced Electricity for Self-Powered Photodetector System,” *Adv. Mater.*, vol. 29, no. 46, p. 1703694, 2017, doi: 10.1002/adma.201703694.
[53] K. Zhang, S. Wang, and Y. Yang, “A One-Structure-Based Piezo-Tribo-Pyro-Photoelectric Effects Coupled Nanogenerator for Simultaneously Scavenging Mechanical, Thermal, and Solar Energies,” *Adv. Energy Mater.*, vol. 7, no. 6, p. 1601852, 2017, doi: 10.1002/aenm.201601852.
[54] R. R. Mehta, B. D. Silverman, and J. T. Jacobs, “Depolarization fields in thin ferroelectric films,” *J. Appl. Phys.*, vol. 44, no. 8, pp. 3379–3385, Aug. 1973, doi: 10.1063/1.1662770.
[55] J. Wu *et al.*, “Ultrafast response of spontaneous photovoltaic effect in 3R-MoS_2-based heterostructures,” *Sci. Adv.*, vol. 8, no. 50, p. eade3759, Dec. 2022, doi: 10.1126/sciadv.ade3759.
[56] Y. J. Zhang *et al.*, “Enhanced intrinsic photovoltaic effect in tungsten disulfide nanotubes,” *Nature*, vol. 570, no. 7761, pp. 349–353, Jun. 2019, doi: 10.1038/s41586-019-1303-3.
[57] L. Gao and L. Bellaiche, “Large Photoinduced Tuning of Ferroelectricity in Sliding Ferroelectrics,” *Phys. Rev. Lett.*, vol. 133, no. 19, p. 196801, Nov. 2024, doi: 10.1103/PhysRevLett.133.196801.
[58] P. Meng *et al.*, “Sliding induced multiple polarization states in two-dimensional ferroelectrics,” *Nat. Commun.*, vol. 13, no. 1, p. 7696, Dec. 2022, doi: 10.1038/s41467-022-35339-6.
[59] L. Wang *et al.*, “Negative Photoconductivity Transistors for Visuomorphic Computing,” *Adv. Mater.*, vol. 36, no. 38, p. 2403538, Sep. 2024, doi: 10.1002/adma.202403538.
[60] S. Liu, J. Tian, S. Wu, W. Zhang, and M. Luo, “A bioinspired broadband self-powered photodetector based on photo-pyroelectric-thermoelectric effect able to detect human radiation,” *Nano Energy*, vol. 93, p. 106812, Mar. 2022, doi: 10.1016/j.nanoen.2021.106812.
[61] M. Kumar, D.-K. Ban, and J. Kim, “Photo-induced pyroelectric spikes for neuromorphic sensors,” *Mater. Lett.*, vol. 225, pp. 46–49, Aug. 2018, doi: 10.1016/j.matlet.2018.04.106.

Chapter 6. Conclusions and future work

6.1 Summary

Chapter 2 introduced our modified version of CVD method to produce TMD thin films which we refer to as thermally-assisted conversion (TAC). It was shown that TAC produces thickness controlled few-layer films of MoS_2 that are not just uniform and continuous over large area (up to cm^2) substrate but also compatible with photolithographic processes and therefore TAC based TMD films can be patterned into any shape at a designated area of interest and at any stage in a multilayer stack. This method of thin film synthesis gets rid of painstaking contacting of randomly deposited flakes of MoS_2 where all other pre or post synthesis processes need to be designed according to the placement of the deposited flake. Rather, with TAC based TMD thin films, deposition of the films can be adjusted to align to other process to fabricate a multilayer stack or device. This chapter proved the thickness control by utilising static coloration property of MoS_2 that occurs when it is backed by a metal. So, each thickness has a unique shade when backed by a reflecting metal layer. Here, MoS_2 deposited on a transparent quartz substrate was covered by Au reflector film and upon viewing from the flip side i.e., from the other side of the quartz substrate, the light that reflects off of the Au reflecting film after interaction with MoS_2, appeared as a distinct colour based on the MoS_2 thickness. Even slight difference in MoS_2 thickness leads to a different shade and colour of the TAC based MoS_2 which is easily observed on large 1 cm^2 quartz substrates with naked eyes without the use of optical microscopes due to the uniformity in thickness achieved by TAC based MoS_2 films as discussed previously.

Raman single spectrum measurements under 532 nm and 632.8 nm laser line were used to determine slight variations in thicknesses (qualitatively) of the few-layer MoS_2 films and to reveal 3R or mixed polytype being formed via TAC. Raman mapping on the other hand was used to show continuous and uniformly thick formation of MoS_2 via TAC across varying lateral areas (ranging from μm^2 to cm^2) directly on the substrate as well as in a multilayer patterned stack without damaging the layers beneath. This showed the compatibility of TAC based few-layer TMD films to be produced with any desired shape and size with precise control on the placement of the film directly on the substrate or as a part of a multilayer stack. This also makes metallization of contacts easy as compared to MoS_2 produced by other techniques like CVD, mechanical exfoliation, hot pick-up and stamp method and liquid

exfoliation where randomly placed flakes of MoS_2 are obtained. In these cases, MoS_2 is not continuous over a large area, cannot be patterned and poses problems of flake isolation to deposit metal contacts which can be a very time-consuming process and an impractical solution at for industries and commercial purposes. In a nutshell, TAC based TMD thin films mitigate all these issues.

Chapter 3 discussed all aspects of electrical characterization possible with TAC based MoS_2 thin films. I-V measurements were first performed using the four-point probe technique to screen large area, unpatterned MoS_2 thin films. Our TAC based MoS_2 films consistently showed an average sheet resistance (R_{sh}) in the order of 1E+9 ($\Omega/\square$) and average resistivity (ρ) in the order of 1E+10 ($\Omega \cdot m$) at 750℃ across film thicknesses ranging from 15 nm to 50 nm. These values tend more towards insulating nature. For 15 nm film thickness, both R_{sh} and ρ seem to be independent of the time of sulphurization in the TAC furnace and seem to depend more on the temperature at which starting Mo is sulphurised. For temperatures below 750℃, TAC films tend towards an upper range of semiconductor R_{sh} and ρ values but show much higher R_{sh} and ρ values indicating insulating nature when the temperature of sulphurization is 750℃ and above. Therefore, the optimum temperature to obtain semiconducting MoS_2 films of thicknesses 15 nm and above produced via TAC process as seen from the four-point probe method is therefore below 750℃ i.e., around 450℃ to 600℃. It can thus be concluded that TAC based MoS_2 thin films are capable of replacing Si as a semiconductor. Two terminal I-V sweeps gave similar results for 15 nm MoS_2 with the exception of IDE design-based samples of the same thickness due to a very different topology used in that case where MoS_2 was deposited on top of Au interdigitated contacts forming a bottom-side hybrid connection. Fermi level pinning at the Au-MoS_2 interface is inevitable and also adds a layer of complexity in the analysis. So other contact materials were also explored.

To quantify the effect of choice of contact material on TAC based MoS_2 thin films, TLM measurements were performed on electrodes deposited using different contact architectures on TAC based MoS_2 thin films and utilizing different contact materials. These included Mo, Sn-Au and Mo co-sulphurised top contacts out of which Sn-Au top contacts were found to have the lowest contact resistance (53.8 $k\Omega \cdot \mu m$) while forming Ohmic contacts at the interface with MoS_2.

Finally, temperature dependent resistance measurements were performed under vacuum from room temperature down to cryogenic temperatures that showed semiconducting behaviour of MoS_2 and a significantly high magnitude of temperature coefficient of resistance (1.724 $\%K^{-1}$). This also opens up avenues to use MoS_2 prepared by the TAC method to be used as bolometers and temperature sensitive detectors, perhaps in space exploration.

In ***chapter 4***, our in-house electro-optic characterization setup is introduced as CCD-DR tool that maps the change in reflectance in the region of interest as a response to an external stimulus that can be in the form of electricity (applied electric field or current injection) and/or heat (local heating due to focussed laser beam or large area heating by hotplate). This technique was used to obtain a direct visualisation of real time change in reflectance in response to an applied voltage on few layers TAC based MoS_2 films. Change in exciton oscillator strength upon gating manifests as change in absorption (or reflection) when light resonant with exciton energy illuminates the MoS_2 thin films. Leveraging the availability of room temperature excitons in visible range of the electromagnetic spectrum, the strong exciton confinement property of MoS_2 up to 4.5 nm thickness, and utilizing the ability to obtain patterned, stable, continuous and uniformly thick few-layer MoS_2 films via TAC on reflecting gold film thus forming a Fabry-Pérot cavity, a maximum change in reflectance around 0.32% was obtained upon externally gating the few-layer thick MoS_2 sample. Better result was obtained with MoS_2 deposited on Si/SiO_2 with almost double change in reflectance around 0.75% with the same magnitude of applied voltage of 200 V. A small change in reflectance was also obtained when MoS_2 was deposited on a plain transparent quartz substrate without using FP cavity advantage. In this case, an in-plane voltage of 5 V resulted in about 0.05% change in reflectance which is the smallest signal detected using our in-house CCD-DR setup in this work. This not just shows the impressive resolution of the CCD-DR setup but also reveals the potential of exciton tuning in few-layer MoS_2 films to be pushed beyond their monolayer limit.

Finally, ***chapter 5*** presented photo-induced response in TAC based MoS_2 films and compared with those prepared using CVD and liquid-liquid interface deposition (LLID). TAC based MoS_2 films outperform both CVD and LLID based MoS_2 films when illuminated by a broad white light source as well as focused 405 nm and 511 nm laser. The highest responsivity 'R' of 0.4 A/W was obtained from 12 nm TAC MoS_2 deposited on 50 nm Au IDEs on a Si/SiO_2 substrate. Interestingly, when illuminated by a high frequency modulated

511 nm focused light source, transient spikes were observed in the photo-induced current as a function of time along with a steady state component. The relative amplitude of the transient peaks corresponding to every 'on' cycle of the laser was tuneable with laser modulation frequency, intensity, local temperature, external bias and gain of any additionally amplifiers.

In summary, MoS_2 films produced by TAC which is a more industrially relevant and straightforward method of producing single to few layer TMD films was used to make devices for different applications. Its unique properties were exploited to fabricate devices such as active electro-optic modulator, broadband photodetector, pyro-detector and bolometric applications. In some cases, TAC based MoS_2 even outperformed its counterparts. For instance, higher photoconductivity when compared to CVD and LLID MoS_2 as discussed before and as a pyro-detector when compared to state of the art, commercially available pyroelectric sensors (Thorlabs ES4xxC fast sensors with repetition rate up to 10 kHz).

6.2 Additional results and future directions

While this work focuses on applications of TAC based MoS_2 films, other methods of MoS_2 synthesis were also tried. Etch free transfer of MoS_2 using PMMA and DI water [1] was used to exfoliate a thin film of MoS_2 on an Au coated substrate from a previously deposited sample using TAC on another substrate. The floating film on DI water surface is shown in ***fig. 6.1(a)***.

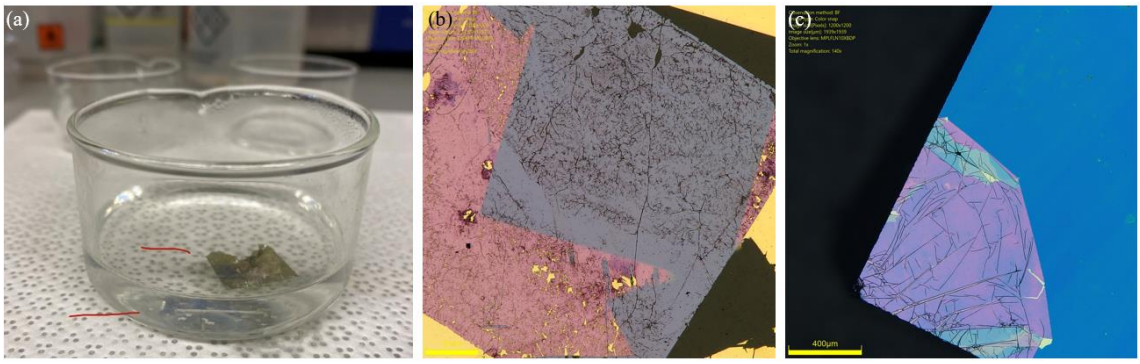

Fig. 6.1*: **(a)** Floating MoS_2 film on DI water after sonification according to the method outlined in [1]. **(b)** Floating MoS_2 transferred on a glass slide partially coated with gold. Purplish-pink region of MoS_2 was placed on the gold coating and the bluish-pink region lies directly on quartz. **(c)** MoS_2 transferred on Si/SiO_2 substrate.*

This was done to figure out a way to transfer TAC MoS_2 between different substrates like ITO coated glass and Au coated glass slide that cannot go into the TAC furnace for photovoltaic and electrochromic applications respectively.

The second method was hot pick up and stamp technique which produced WS_2 and MoS_2 flakes of arbitrary shape and position on different substrates as shown in ***fig. 6.2(a)*** and ***(b)*** respectively. Raman measurements show narrower characteristic peaks and close to equal peak heights indicating pristine, ordered and planar MoS_2. However, both the methods came with their own drawbacks. Extracting MoS_2 using just PMMA and DI water from a pre-existing MoS_2 deposited on another substrate leads to holey film which is neither fit for vertical solar cell applications nor for electrochromic devices due to shorting issues. Moreover, MoS_2 obtained by hot pick up and stamp technique from our collaborators in University of Salamanca, encapsulated the MoS_2 between bottom and top hBN films to protect them from degradation. This is also evident from Raman measurements that do not show any oxysulphide peaks.

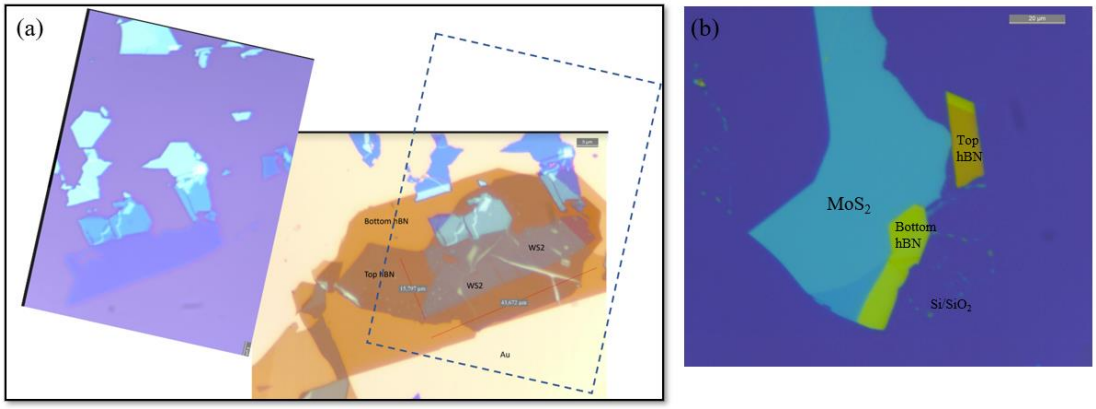

Fig. 6.2*: Mechanically exfoliated* ***(a)*** *WS_2 and hBN flakes on Au and* ***(b)*** *MoS_2 and hBN flakes on Si/SiO_2 via hot pick-up and stamp technique.*

Passive modulation of refractive index wherein apparent change in colour was observed in M-I-M structures comprising of a dielectric sandwiched between metal and TCO. Two separate stack designs were fabricated for this and shown in ***fig. 6.3***. The general stack structure for both remains the same as in ***fig. 6.3(c)*** but the choice of TCO and dielectric as well as their thicknesses vary in each case. Sample **S1** (shown in ***fig. 6.3(a)***) consists of 55 nm of SiO_2 sandwiched between 112 nm of RF sputtered TCO – zinc tin oxide (ZnSnO or ZTO in short) and 25 nm of Au bottom layer on 1.5 cm^2 quartz substrate. Top contacts were patterned in four circular pixels of increasing diameters by UV-lithography using OAI mask aligner and 100 nm Au was deposited after O_2 plasma cleaning. Both top and bottom Au

layers were deposited by thermal evaporation using Temescal tool. The custom mask was designed using CleWin software and fabricated using Heidelberg direct writing tool in our cleanroom. Sample **S2** (shown in ***fig.* 6.3*(b)***) was fabricated in the same way except that the TCO thickness was 125 nm and SiO_2 thickness was 127 nm in this case. TCO in both S1 and S2 were deposited by Dr. David Caffrey and Dr. Peter Callaghan from Prof. Igor Shvets' group in school of physics, Trinity College Dublin. ***Fig. 6.3(a), (b)*** show **S1** and **S2** when viewed from the quartz side. It is noteworthy that 55 nm of SiO_2 is not enough to cause a strong colour contrast in **S1** but 127 nm of SiO_2 leads to a significant change of colour of the gold pixels from mustard yellow to pink when viewed through quartz.

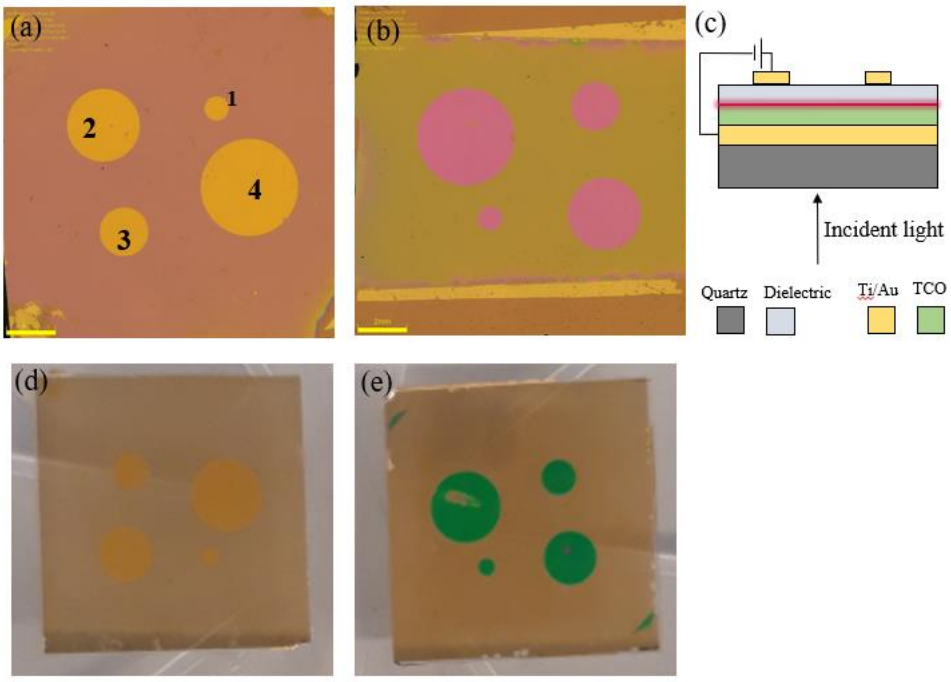

Fig. 6.3*: Top view TCO/dielectric-based stacks with 4 top pixel contacts marked as 1, 2, 3 and 4 with varying diameters as 1 mm, 2 mm, 3 mm and 4 mm.* ***(a)*** *S1: Quartz/Au 25 nm/ZnSnO 112 nm/ SiO_2 55 nm/Ti 1 nm/Au 100 nm and* ***(b)*** *S2: Quartz/Au 25 nm/ZnSnO 125 nm/ SiO_2 127 nm/Ti 1 nm/Au 100 nm viewwed through quartz.* ***(c)*** *General stack design of S1, S2 and S3.* ***(d)*** *Au pixel side and* ***(e)*** *flipped quartz side of S3: Quartz/Au 25 nm/ZnO:Al 100 nm/ Al_2O_3 100 nm/Ti 1 nm/Au 100 nm*

This is better seen in another sample – **S3** produced in the same way as **S1** and **S2** but ZTO was replaced by 100 nm of Al doped ZnO (19:1 Zn:Al ratio) and SiO_2 was replaced by 100 nm of Al_2O_3. Both the TCO and dielectric in this case were deposited using ALD and this sample was procured from Dr. Ian Povey's group in Tyndall National Institute, Cork. The top side of this sample with Au pixels facing up are shown in ***fig. 6.3(d)*** and the flipped side with Au pixels on the back side i.e., when viewed through quartz is shown in ***fig. 6.3(e)***. When viewed from the Au pixels facing up, the pixels appear as they should in colour –

mustard goldish but upon flipping and viewing through the quartz side, the same pixels appear green. This colour contrast is due to FP interference among the metal, TCO/dielectric interface. Previously active modulation has been achieved in a similar stack utilizing Indium Tin Oxide (ITO) as the TCO [2] and here this was achieved using **S3**. Applying a 3V bias between the top and bottom Au layers creates a charge accumulation at the TCO/dielectric interface which shifts the plasma frequency thereby changing 'n' and 'k' at the interface. This resulted in successful change in reflectance ~ 0.2 % under the CCD-DR setup at 670 nm for the 1 mm diameter pixel (shown in ***fig. 6.4***).

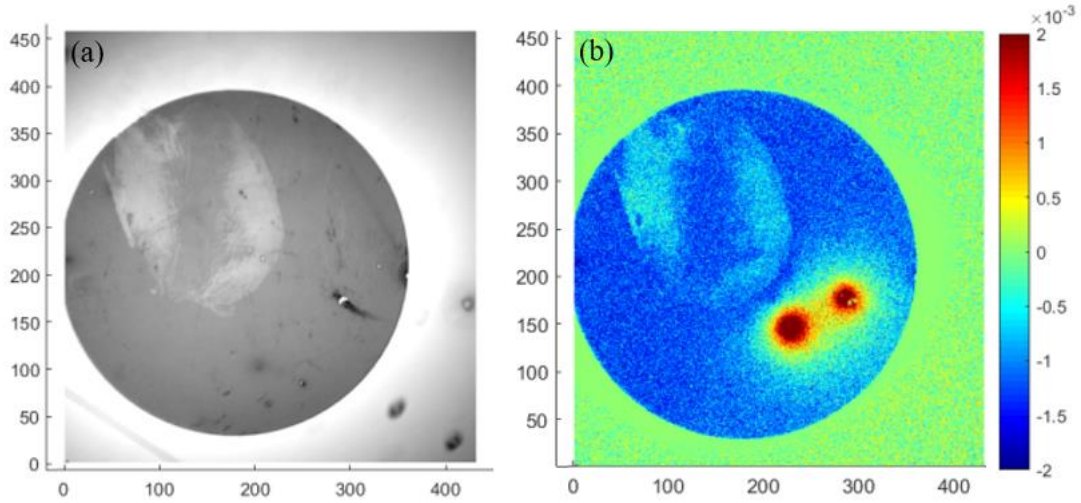

***Fig. 6.4**: **(a)** Grey-scale image under the CCD-DR microscope and **(b)** change in reflectance map of the region in **(a)** showing a clear 0.2 % change in reflectance when a 3 V bias is applied on the pixel while rest of the background stays neutral at 0%. The bright red regions correspond to current hotspots due to shorting.*

TCOs are definitely easier to fabricate and characterise but the modulation of reflectance and corresponding refractive index obtained is restricted by the thickness of accumulation formed at the TCO/dielectric interface which is around 5 nm. According to [2], the greater the carrier density and accumulation layer, the higher is the tuneability of refractive index. Thus, most of the TCO remain under-utilised. So to address the limitation of accumulation layer formation at only one interface, a better design that forms another TCO/dielectric interface at the bottom of the same TCO layer can be designed. So, replacing the metal/TCO/dielectric/metal stack with metal/dielectric/TCO/dielectric/metal stack, both interfaces of the TCO can be utilised to form a double accumulation layer on gating the stack.

Additionally, to enhance the FP effect and make use of the optical interference effects indicated by passive colour contrast upon flipping the stack, a thin absorbing layer of MoS_2 can be included along with the TCO especially when it is already encapsulated with dielectric which will also protect MoS_2. Perhaps, MoS_2 exfoliated via hot pick-up and stamp technique can be used in such devices. Since we utilised and integrated TCOs (ITO, ZTO, AZO) in multilayer stack successfully, it is very tempting to also use them for sensor applications especially as photo-bolometers [3] in future work.

References

[1] D. Ma *et al.*, "A universal etching-free transfer of MoS_2 films for applications in photodetectors," *Nano Res.*, vol. 8, no. 11, pp. 3662–3672, Nov. 2015, doi: 10.1007/s12274-015-0866-z.

[2] E. Feigenbaum, K. Diest, and H. A. Atwater, "Unity-Order Index Change in Transparent Conducting Oxides at Visible Frequencies," *Nano Lett.*, vol. 10, no. 6, pp. 2111–2116, Jun. 2010, doi: 10.1021/nl1006307.

[3] J. Gosciniak, "Integrated Bolometric Photodetectors Based on Transparent Conductive Oxides from Near- to Mid-Infrared Wavelengths," *Adv. Photonics Res.*, vol. 5, no. 2, p. 2300261, Feb. 2024, doi: 10.1002/adpr.202300261.